THE UNIVERSITY OF CHICAGO

FIRST ON-SKY DEMONSTRATION OF ULTRA-LOW NOISE SKIPPER CCDS FOR COSMOLOGY

A DISSERTATION SUBMITTED TO
THE FACULTY OF THE DIVISION OF THE PHYSICAL SCIENCES
IN CANDIDACY FOR THE DEGREE OF
DOCTOR OF PHILOSOPHY

DEPARTMENT OF PHYSICS

BY
EDGAR MARRUFO VILLALPANDO

CHICAGO, ILLINOIS
MARCH 2025

Copyright © 2025 by Edgar Marrufo Villalpando

All Rights Reserved

Dedication Text

To my parents whose life sacrifices opened the doors to a better future for their sons.

Epigraph Text

Este es un nuevo día
Para empezar de nuevo...

—Facundo Cabral

TABLE OF CONTENTS

LIST OF FIGURES viii

LIST OF TABLES xxii

ACKNOWLEDGMENTS xxiii

ABSTRACT xxvi

1 OVERVIEW 1

2 ASTROPHYSICAL STUDIES OF DARK MATTER 6
2.1 Standards of Cosmology 6
2.2 Dark Matter 7
2.2.1 The Vireal Theorem and the Coma Cluster 8
2.2.2 Galactic Rotation Curves 8
2.2.3 Gravitational Lensing and the Bullet Cluster 10
2.2.4 The Cosmic Microwave Background 11
2.3 Dark Matter Models 13
2.3.1 Warm Dark Matter 15
2.3.2 Self-Interacting Dark Matter 16
2.3.3 Wave-like Dark Matter 17
2.4 Dark Matter Probes 18
2.4.1 The Smallest Galaxies in the Milky Way 19
2.4.2 Stellar Stream Gaps 21
2.5 Cosmological Surveys 22
2.5.1 The Sloan Digital Sky Survey 23
2.5.2 The Dark Energy Survey 23
2.5.3 The Dark Energy Spectroscopic Instrument 25
2.5.4 The LSST Survey 26
2.5.5 Stage 5 Spectroscopic Surveys 27

3 CCDS AND ULTRA-LOW NOISE SKIPPER CCDS 29
3.1 CCDs 29
3.1.1 Charge Generation and the p-n Junction 30
3.1.2 The MOS Capacitor and the Pixel 32
3.1.3 Charge Transfer 34
3.1.4 Charge Measurement 35
3.2 The Skipper CCD 39
3.2.1 Skipper CCD Architecture 40
3.2.2 Skipper CCD Operating Principles 42
3.2.3 Fully-Depleted, Back-Illuminated Skipper CCDs 45

4 SKIPPER CCDS ON THE SKY: MOTIVATIONS AND FOCAL PLANE CONSTRUCTION . . . 48
4.1 Motivations . . . 49
4.2 SOAR Integral Filed Spectrograph (SIFS) . . . 52
4.3 Observational Improvements with Skipper CCDs . . . 54
4.4 Engineering Detectors . . . 58
4.4.1 Detector Architecture and Characteristics . . . 58
4.4.2 Detector Packaging . . . 59
4.5 Dewar and Focal Plane . . . 62
4.5.1 SIFS AstroSkipper Dewar . . . 62
4.5.2 Focal Plane Metrology . . . 64
4.6 Readout Electronics . . . 67
4.6.1 Synchronized LTA Readout . . . 67
4.6.2 Readout Electronics at SOAR . . . 69

5 SKIPPER CCD CHARACTERIZATION AND OPTIMIZATION FOR ASTRONOMY . . . 71
5.1 AstroSkipper: Detector Characteristics . . . 72
5.2 AstroSkipper Testing Procedures and Infrastructure . . . 74
5.2.1 Testing Equipment . . . 74
5.3 Time Optimization . . . 76
5.3.1 Skipper CCD Regions of Interest Time Optimization . . . 78
5.4 Skipper CCD Enabled Characterization Tests . . . 81
5.4.1 Readout Noise Characteristics and Photon-Counting . . . 81
5.4.2 Non-linearity . . . 84
5.5 Clock Induced Charge and Voltage Optimization . . . 88
5.5.1 CIC in the AstroSkipper . . . 89
5.5.2 Voltage Optimization . . . 94
5.6 Conventional Characterization Tests . . . 96
5.6.1 Dark Current (DC) . . . 96
5.6.2 Charge Transfer Inefficiency (CTI) . . . 97
5.6.3 Photon Transfer Curve (PTC) and Brighter-fatter Effect (BFE) . . . 98
5.6.4 Cosmetic Defects . . . 104
5.6.5 Charge Diffusion . . . 104
5.6.6 Absolute Quantum Efficiency . . . 107
5.7 Summary . . . 111

6 OBSERVING WITH SKIPPER CCDS . . . 113
6.1 Skipper Focal Plane Installation . . . 113
6.1.1 Other System Considerations . . . 118
6.2 Observation Strategy . . . 119
6.2.1 Astronomical Targets . . . 122
6.2.2 Sub-Electron Noise Regions of Interest . . . 125
6.2.3 Photon-Counting Region of Interest . . . 126

6.3 Observation Results . . . 126
6.3.1 System Performance . . . 126
6.3.2 Single-Photon Counting . . . 127
6.3.3 Signal-to-Noise Improvement . . . 132
6.4 Summary and Planned Science . . . 135

7 ASTRONOMICAL SPECTROSCOPY WITH SKIPPER CCDS . . . 138
7.1 Motivation . . . 139
7.2 Data Reduction Pipeline . . . 143
7.2.1 Image Correction . . . 143
7.3 Spectral Extraction Validation . . . 155
7.3.1 Wavelength Solution and Uncertainties . . . 155
7.3.2 Radial Velocity Standards . . . 163
7.4 Boötes II Candidate Member Star . . . 165
7.4.1 Outlook: UFD Science . . . 166

8 OUTLOOK: MAS CCDS . . . 170

9 SUMMARY . . . 180

A A PREDICTIVE FRAMEWORK FOR STELLAR STREAM GAPS . . . 184
A.0.1 Gap Evolution: A Qualitative Description . . . 184
A.0.2 Stream-Halo Kinematics . . . 186
A.0.3 Stream Gap Framework Definition . . . 188
A.0.4 Framework Implementation Results . . . 192
A.0.5 Outlook: Stellar Streams . . . 200

REFERENCES . . . 202

LIST OF FIGURES

2.1 Rotation curve for NGC 2841 and M31. The curves are comprised of three-components: the disc, bulge, gas (for NGC 2841), and halo. The different styled lines represent the best fit to the individual components of the galaxies. The back, solid line is the sum of all mass contributions. Note that the contribution of the DM "halo" is required to reconstruct the full velocity profile ("total"). Figure extracted from [1]. 9

2.2 Chandra space telescope X-ray data of the Bullet Cluster. The green, inner contours represent the weak lensing reconstructed mass. X-ray data, which traces the density of hot plasma in the galaxy clusters (colored regions, where blue indicates the least dense and white the most dense), reveal a clear discrepancy between the location of the plasma and the inferred location of the mass based on lensing. This discrepancy underscores that the bulk of the gravitational mass is not associated with the visible plasma but rather with an unseen component, strongly suggesting the presence of DM. Figure extracted from [2]. 11

2.3 CMB temperature power spectrum from Planck Collaboration (2018). The top panel shows the power spectrum intensity as a function of spherical harmonic modes (l). The blue line represents the best-fit ΛCDM model. The bottom panel shows residuals from the fit. Peaks correspond to acoustic oscillations at recombination, with the first peak at $l \sim 200$ representing the sound horizon scale. Odd peaks indicate compression, and even peaks indicate rarefaction phases. 12

2.4 Dimensionless linear matter power spectrum extrapolated to $z = 0$. Curves are derived from theoretical predictions. Four DM models that suppress structure formation are considered: Fuzzy DM for $M_\psi = 10^{-22}$ eV (magenta), SIDM for an interaction cross section proportional to $\sigma_0 v^{-4}$ (blue), WDM with $m_{WDM} \sim 40$ keV (orange), and weakly interacting massive particle with $m \sim 100$ GeV (black). There are four DM models that enhance power structure. 19

2.5 The Dark Energy Camera (DECam). The focal plane array is composed of 62, 2k $\times$ 4k CCDs for imaging and 12, 2k $\times$2k CCDs for targeting purposes. Image courtesy of the Dark Energy Survey [4]. 24

2.6 Number of galaxy redshifts as a function of time for the largest cosmological surveys. Stage 5 spectroscopic surveys maintain this trend into the 2030s. Figure adapted from [5]. 28

3.1 Light sensitive CCD MOS capacitor. The MOS capacitor has three components. The electrode (or gate) made from polysilicon, which serves as the conductive layer to apply an electric field across the insulating layer to control the movement and storage of charge in the silicon substrate beneath. The insulating film, which is made up of SiO_2, prevents direct current flow between the gate and the substrate while allowing the modulation of charge carriers within the substrate via the electric field. The silicon substrate serves as the photosensitive region of the CCD where e-h pairs are generated, and subsequently manipulated through the electric field applied via the gate. Note that the thickness between regions are not to scale. Diagram based on Figure 2.1 from [6]. 33
3.2 Charge transfer diagram for a non-Skipper readout configuration. 36
3.3 Electronic diagram of the output stage for a conventional CCD. Figure based on Figure 6.2 in [7]. 37
3.4 The raw pixel value in ADUs, measured at the SN, as a function of time for one of the Skipper CCDs tested at Fermilab. The signal in between both reset pulses define the components from which a single pixel value is determined. The pedestal value is measured after the RG pulse, and the signal is measured after the SW pulse. The final pixel value is determined by subtracting the pedestal integrated samples from the signal, i.e., CDS. 38
3.5 Top: diagram of the Skipper CCD output stage. As in conventional CCDs, H_1, H_2, H_3 are the serial-register clock phases that transfer the charge to the summing well, in this case SG. MR resets the SN to $V_{\rm ref}$ after a pixel read. M1 is the MOSFET in source follower configuration. For a Skipper, the SN is a floating amplifier, allowing for multiple, nondestructive measurements of the charge at SN. Image extracted from [8]. Bottom: Photograph of the out stage layout of a Skipper CCD. Image extracted from [9]. 41
3.6 Comparison of electronic noise contributions, coupled to the video signal, during pixel readout for conventional and Skipper CCDs. Both high-frequency Gaussian noise (light blue) and low-frequency $1/f$ noise (black) are shown. In the Skipper CCD, the noise profile is sampled 10 times per pixel (green dots), while the conventional CCD takes only a single sample (blue square). This multiple sampling in the Skipper CCD captures the complete $1/f$ noise profile in both the pedestal and signal regions, enabling more accurate noise cancellation during signal-pedestal subtraction. 43
3.7 First accurate electron-counting demonstration on a large format silicon CCD by Tiffenberg et al. (2017). The individual Gaussians represent the electron counts from the detector's pixels. Integer electron peaks can be distinctly resolved from 0 e^- (empty pixels) to the 779th electron peak. The readout noise was measured at $0th$ electron peak by fitting a Gaussian and calculating the standard deviation, $\sigma_{0e^-} = 0.068$ e^- rms/pixel. This noise level corresponds to $N_{\rm samp} = 4000$. Image extracted from [8]. 45

3.8 Diagram of the cross-section of a fully-depleted, backside-illuminated LBNL-designed CCD. DECam CCDs, DESI CCDs, and the Skipper devices in this work follow this design. The Skipper differs from the other two devices only on the output-stage which does not affect light-sensitivity performance. Image extracted from [10]. 47

4.1 Relative QE of the R&D Skipper CCD compared to the QE from DESI and DECam devices (all designed at LBNL, packaged and tested at Fermilab). . . . 50
4.2 Left: Backside-illuminated R&D Skipper CCD, similar to the one tested on [9], mounted in a picture frame adapter. Right: Experimental setup including a closed-cycle optical Dewar (gold; right) housing the Skipper CCD with attached LTA readout board and integrating sphere with attached photodiode (green; left). Behind the integrating sphere are a mechanical shutter, monochromator, filter wheel, and tungsten halogen lamp. Photographs presented in this thesis are taken by the author or are allowed for general use by the CCD group at Fermilab (otherwise the source is referenced). 51
4.3 The 4.1-m SOAR Telescope, located atop of Cerro Pachón, Chile. 53
4.4 The SIFS spectrograph The instrument consists of three subsystems: the fore-optics module, a 14-m. fiber bundle, and the bench spectrograph. 54
4.5 SIFS bench-top spectrograph. (1) Output unit support and fold mirror. (2) Collimator mirror. (3) Collimator lenses. (4) VPH grating mechanism. (5) Camera. (6) Cryostat containing detector (diagram taken from [11]). 55
4.6 Relative exposure times as a function of detector readout noise at a fixed S/N= 7. Curves represent 100%, 50%, and 5% of the detector being read out. 58
4.7 Left: Silicon wafer containing 16 Skipper CCDs for different Fermilab R&D projects. The prototype focal plane array uses the 6k × 1k pixel CCDs with four amplifiers (labeled "AstroSkipper"). Right: AstroSkipper flex cable with active components, i.e., two JFETs and resistors. The flex cable uses an Omnetics connector (right edge of the cable). 59
4.8 Skipper CCD packaging process. **(1)** Flex cable, with Omnetics connector at the end, is glued to the Si substrate. **(2)** The CCD, placed on the blue fixture, is attached to the flex-Si substrate assembly. **(3)** Wirebonding between CCD pads and flex cable. **(4)** CCD foot, gold-plated piece, is glued to the CCD. **(5)** CCD package is installed into a carrying box with removable lid for storage, testing, and transport. 60
4.9 Left: Cross section of a standard SOAR Dewar. It uses LN2 to cool the detectors. The detector mount is attached to the tank through a cold finger and a copper piece, with braids trimmed for thermal adjustment. Right: Original SIFS Detector mount, designed for a single e2v CCD44-82 (4k×4k). The image show the detector, and below it, the mount, which is a triangular aluminum plate that attaches to the Dewar through three posts. 61
4.10 Mount for the focal plane array of four Skipper CCDs. The three arms attach to the standard SOAR Dewar. The back holds an RTD and two heaters for temperature control. 63

4.11 Coordinate measuring machine used to measure individual packaged Skipper CCDs prior to shipping to CTIO. 63
4.12 Left: Laser profilometer configuration to measure the focal plane array. The instrument consists of a single-point profiling laser and a microscope head mounted over the x-y stage. Right: Dewar head with the window removed to measure tip/tilt. 65
4.13 Gap measurements between detectors. Gap variations between detectors are due to differences in individual packaging and possible inaccuracies when mounting the detectors (labeled with the yellow numbers). 66
4.14 Left: 2k × 4k, 16 amplifier Skipper CCD. Amplifiers are placed along the long sides of the detector in groups of 8 amplifiers. Right: LTA synchronized readout system used for CCD testing. LTAs are docked to the backplane, which receives the video signals (rainbow ribbon cable) and biases and clocks (gray ribbon cable). Hardware synchronization between boards is done through the cables on the top of the boards. 66
4.15 Glycol-cooled box to house the four synchronized LTAs. It provides a 200 W of dissipation power. 67
4.16 Preamplifier mounted inside the SIFS-Skipper Dewar. Each Skipper CCD connects to one of the Omnetic connectors and each pair of Positronics carry the signals for two of the detectors to each of the hermetic connectors on the Derwar. 68
4.17 Readout System Wiring: The wiring is designed so that two LTAs handle two AstroSkipper CCDs. This allows for symmetrical cables and independent operation, if required for testing purposes. Biases and clocks are shared among the two devices, except for VDD. 70

5.1 Fully packaged AstroSkipper housed in a carrier box. The package is a four-side-buttable pedestal package similar to DECam packages [12]. Refer to Section 4.4.2 for the detector packaging procedure. 73
5.2 Skipper CCD testing station. From the right, closed-cycle vacuum Dewar (vacuum cube), collimator, integrating sphere (photodiode mounted on top), shutter, monochomator, filter wheel, quartz tungsten halogen lamp. Light enters the vacuum Dewar through a fused-silica window. The Skipper CCD is mounted on a cold aluminium plate that faces the window. 75
5.3 Charge transfer diagram for the Skipper CCD output stage. This diagram is adapted from Figure 5 in Fernández Moroni et al. (2016). The total time for CDS to compute the pixel value is given by $t_{\rm pixel}$. 76
5.4 Top: measured single-sample readout noise versus CDS integration window time for the AstroSkipper. For each fixed integration window instance, we calculate the optimal noise for different $t_{\rm wt2}$, $t_{\rm PED}$, and $t_{\rm SIG}$ with $t_{\rm wt1} = 0$ μs. We note that the curve approaches the noise floor (3.5 e^- rms/pixel) at ~ 20 μs with a readout noise $\sigma_1 \sim 4.3$ e^- rms/pixel. Bottom: Readout speed in pixel/s as a function of the integration time while varying $N_{\rm samp}$ to achieve photon-counting resolution ($\sigma_N \sim 0.18$ e $^-$ rms/pixel). The optimal integration window time is ~ 20 μs for a readout speed of ~ 330 pixel/s. 79

5.5 Optimization of the integration time ($t_{\rm pixel}$) to achieve a noise of 0.5 e^- rms/pixel in 5% of the detector area and minimize the total readout time per frame. The optimal integration value is found to be $\sim$ 20 μs which allows the full frame to be read in $\sim$ 3.6 min. 80
5.6 Top: Single-sample image from one AstroSkipper quadrant (600 $\times$ 3200 pixels) with overscan region starting at the 3080 pixel. Middle: Average pixel value calculated per row in the overscan (blue) and active (black) regions of the detector. A large scale transient correlated with row number can be seen. Bottom: Same as the middle panel, but after row-by-row overscan pedestal subtraction. The algorithm corrects the slowly decaying transient associated with row number. . . 83
5.7 Readout noise characteristics and photon-counting for one of the AstroSkipper CCDs. Left: Histogram of the pixel values for one amplifier calculated from the average of 400 non-destructive measurements (samples) per pixel (cyan histogram). The low noise($\sigma_{0e-} \sim 0.18$ e^- rms/pixel) achieved after $N_{\rm samp}$=400 resolves single electrons/photons. We see photon-counting capabilities in all amplifiers from the six AstroSkippers. We fit the distribution of pixel values with a multi-Gaussian model. The gain of the detector can be directly calculated from the difference between the mean values in ADUs of adjacent electron peaks. Right: Readout noise for four amplifiers as a function of the number of non-destructive measurements of each pixel ($N_{\rm samp}$). The measurements deviate from the expectation from Eqn. 3.4 (dashed line) by as much as 20% and 10% for $N_{\rm samp} < 10$ and $N_{\rm samp} > 150$, respectively. 84
5.8 Variation in the noise characteristics of the four amplifiers in the six selected Skipper CCDs. Top: single-sample readout noise values for each amplifier. Bottom: noise performance per amplifier after taking 400 non-destructive measurements of the charge in each pixel. Dotted lines are the average readout noise for a given amplifier. 85
5.9 Gain measurements for all amplifiers for the six AstroSkipper CCDs. Gain calculated using separation between electron peaks in each detector's amplifier for all six AstroSkippers. We see variations of $< 6\%$ on average between gain values in all amplifiers; amplifiers 1 and 2 show the largest variation on average for all detectors. 85
5.10 Top: Gain values calculated from peak-to-peak separation of individual electron peaks, i.e., $\mu_{i+1} - \mu_i$. The average gain is $\sim$ 139 ADU/e^- (red dashed line) with a scatter about this mean of $< 4\%$. The blue dash-dotted line represents the gain value estimated from the slope of the signal variance vs. the signal mean in the PTC. Bottom: Ratio between the gain measured from the difference between the $0^{\rm th}$ and $i^{\rm th}$ electron peak, i.e., $(\mu_i - \mu_0)/i$, and the constant gain value from the PTC. We observe a $\sim$ 1% agreement between the two methods for determining the gain and $< 1\%$ variations in the gain as measured from electron peak. 87

5.11 Top: Pixel distribution from a pair of single-sample dark frames (no charge accumulation) acquired with a low and high voltage configuration of the horizontal clocks (serial register). The readout noise is calculated from a Gaussian fit to the distributions. The high voltage configuration exhibits an increase in noise (4.5 e^-rms/pix) compared to the expected baseline noise for the AstroSkipper (3.5 e^-rms/pix). Bottom: The "extra" noise contribution to the single-sample frame, in the high voltage configuration, comes exclusively from CIC electron rate as evident by the quantized electron peaks (red pixel distribution). 90
5.12 Modeling CIC generation. Left: Linear relationship between CIC and number of transfers in the serial register. Each data point corresponds to a different horizontal clock swing value. CIC increases linearly with number of transfers as seen from comparing CIC on two CCDs of different sizes (3200 versus 450 transfers). Right: Simulated and measured CIC for the AstroSkipper. The number of transfers (3200 per amplifier), the horizontal clock width, and the filter (RC filter with $\tau = 5.1\mu s$) are fixed. The model assumes Poisson statistics. We only consider variation in the horizontal clock swing which causes the highest electron rate generation compared to vertical and transfer gate clocks. We measure better than $\sim 10\%$ agreement between model and data for $\Delta H > 7.5$V. 92
5.13 Top: full-well capacity as a function of the horizontal clock voltage swing (ΔH). Bottom: CIC event rate versus full-well capacity. We measure an upper limit on the CIC (red arrow) with the SENSEI voltage configuration (1.45×10^{-3} e^-/pixel/frame), resulting in a full-well $\sim$ 900 e^-. Increasing the horizontal clock swing to $\Delta H = 6$ V increases full-well capacity to $\sim$ 10,000 e^- at a CIC rate of $\sim$ 1 e^-/pixel/frame and for $\Delta H = 9.5$ V we obtain a CIC rate of $\sim$ 3 e^-/pixel/frame and a full-well capacity $> 40,000$ e^-. 94
5.14 Average CTI versus signal for four amplifiers in one of the selected AstroSkippers. The average CTI for all 24 amplifiers is 3.44×10^{-7}. 97
5.15 Top: Measured a_{ij} from the electrostatic model (Eqn. 5.7). Bottom: Measured b_{ij} from Eqn. 5.7. Both matrices come from the fit to the electrostatic model using the method described in [14]. We measure $a_{00} = -6.78 \times 10^{-6} 1/e^-$. This factor dominates the pixel area change as charge accumulates (biggest contribution to the BFE). We note the asymmetric correlation between neighboring pixels ($a_{10}/a_{01} \sim 2.51$) due to difference in pixel boundaries between the row and column directions [15]. 99
5.16 Best fit values from the a and b matrices, averaged over all amplifiers, as a function of distance. a decreases sharply and behaves isotropically for > 3 pixels. Similarly to [14], we see that values for b are negative except for b_{01}. 102
5.17 PTC curve for a Skipper CCD. The Skipper CCD dynamic range is shown for single- and multi-sample ($N_{\rm samp}$) data sets. The multi-sample PTC shows that it is possible to dive down the noise floor from the single-sample data while maintaining a linear response. 103

5.18 Photon Transfer Curve for one AstroSkipper amplifier. The PTC follows the model described by Eqn. 5.8 [14] and gives the BFE strength factor, a_{00} from the covariance matrix. One can also calculate the detector's gain from the model fit, which is given by the slope of the curve. The full-well capacity, orange star, is defined as the last "surviving" data point after applying an outlier rejection algorithm. 105
5.19 Average full-well capacity for the six detectors. Full-well measurements are calculated by amplifier through the PTC; we average these full-well values from all amplifiers in a detector. 106
5.20 ^{55}Fe X-ray data frames. Top: AstroSkipper frame of low-energy ^{55}Fe X-rays taken with a substrate voltage of 40V. Bottom: Frame taken with a substrate voltage of 70V. Cosmetic defects become more apparent as the substrate voltage increases. This indicates physical damage to the CCD back side, which could be a result of the backside processing. 106
5.21 Silicon substrate (6k $\times$ 1k) on an AstroSkipper package. A Thorlabs NIST traceable Si photodiode is glued at the center of the substrate. The package-photodiode assembly is placed inside the AstroSkipper testing Dewar to measure the incident number of photons at the photodiode. 107
5.22 Absolute quantum efficiency for one AstroSkipper's amplifier compared to absolute QE from DECam detectors (dark gray line) [12] and relative QE from DESI detectors (grey line). Error bars in the AstroSkipper absolute QE represent the uncertainty in the absolute calibration at each wavelength. We see excellent agreement with DESI detector's QE (the AstroSkipper and DESI NIR detectors are $\sim$ 250 μm thick and have similar AR coating from LBNL Microsystems Laboratory). We measure QE $\gtrsim$ 80% for 450 nm and 980 nm and QE $>$ 90% for wavelengths from 600 nm to 900 nm for all AstroSkippers; this is an improvement from the first Skipper CCD relative QE measurements (QE $>$ 75% between 450 nm and 900 nm) we reported in [16]. 109
5.23 Extended QE for the AstroSkipper to the UV regime. The Vis-NIR measurements are the absolute QE values from Figure 5.22. The UV QE is measured separately with a Xenon UV lamp and normalized to the overlapping Vis-NIR QE values. . 110

6.1 **Left**: Skipper CCD focal plane prototype for SIFS. Four astronomy-grade Skipper CCDs are placed on a custom mount with three arms that attach to a standard SOAR Dewar. The focal plane spans an area of 6k $\times$ 4k pixels. The four devices are separated by gaps of $\sim$400 μm. **Right**: Focal plane inside the standard SOAR Dewar with a fused-silica window for exposure to light. 114
6.2 Left: SIFS bench spectrograph enclosure located on the lateral platform of the SOAR telescope. Right: The Dewar and the bench spectrograph equipment is located inside. 115
6.3 The diagram shows the three-point kinematic mount to align the Dewar to the optical path of the instrument. 116

6.4 Top: Orginal SIFS Dewar installed in the SIFS frame. The red circles indicate two of the three-point kinetic mounts for adjusting tip/tilt, and the red square highlights the rotation mechanism. Right: Installed Skipper Dewar and electronics. 117
6.5 example 118
6.6 Mapping of the signal from the SIFS optics to the Skipper CCD focal plane. The microlens array collects light from the astronomical target and channels the light into the fibers, which are arranged into a pseudo-slit following a serpentine mapping (red curved line). The fibers disperse the light onto the focal plane; the wavelength direction runs along the Skipper CCDs' rows and the fibers' spatial position runs along the detectors' columns. 120
6.7 Skipper CCD focal plane array data frames. The four frames show the full 6k × 4k physical pixels of the four Skipper CCDs. Each frame is composed of the four amplifiers in each detector. We show spectroscopic data from a CALSPEC [17] standard calibration star (HD101452); the fiber bundles span the 4k × 4k SIFS FoV. There are "hot" columns present outside the 4k × 4k FoV, which do not affect data reduction. The gaps between the Skipper CCDs are ∼400 μm (∼27 pixels) wide and are not shown to scale. 121
6.8 SIFS-Skipper CCD observation of quasar HB89 1159+123 using the 1/2 FoV ROI readout configuration. Top: The 1/2 FoV ROI consists of 50 repeated measurements of 1k × 2k contiguous physical pixels in the center of each AstroSkipper detector. The top panel shows the physical pixels from the four amplifier quadrants on a single AstroSkipper detector within the SIFS FoV and excludes overscan regions. The x-direction represents the SIFS spatial dimension over the SIFS FoV (∼ 2k pixels per amplifier, ∼ 4k pixels for the detector frame) and the y-direction is the spectral dimension (512 pixels per amplifier, ∼ 1k for the detector frame). This configuration was used to observe QSOs with sub-electron readout noise covering a focal plane region of 4k × 2k pixels. Bottom: The multi-sample and overscan regions for the bottom left amplifier quadrant from the 1/2 FoV ROI shown in the top image. The multi-sample active area (1k pixels in the x-direction) is followed by a 120-pixel-wide single-sample serial overscan and a 200-pixel-wide multi-sample serial overscan. The parallel overscan is 88 pixels wide in the row direction. These overscan sections are used in image reduction. . 123
6.9 Readout time for several ROI configurations. The plot gives the expected readout time given the target noise level (sub-electron and photon counting) for different percentages of the detector readout with the target noise. We note that the rest of the FoV is read out with single-sample noise. 124

6.10 Left: Readout noise from one of the detectors affected by correlated noise as a function of the number of samples per pixel ($N_{\rm samp}$). The single-sample readout noise is $\sim 17\,{\rm e}^-$ rms/pixel but rapidly decreases with increasing $N_{\rm samp}$, reaching ~ 4.6 e$^-$ rms/pixel at $N_{\rm samp} = 7$. The theoretical Gaussian noise is recovered for $N_{\rm samp} > 12$. These detectors are able to count photons at $N_{\rm samp} = 250$. Right: The pixel distribution from the multi-sample serial overscan. For small $N_{\rm samp}$, the pixel distribution exhibits a "double-Gaussian" feature, which suggests a temporal correlation between mixed sources of noise. 125
6.11 The total observation noise as a function of the exposure time. The total observation noise includes the background shot noise. In the configuration shown here, the background counts are dominated by the shutter-open dark rate. We note that for short exposure times (e.g., the $\sim 60\,{\rm s}$ exposure time used for some photon-counting readout configurations), the shot noise is subdominant to the readout noise. 128
6.12 Transition between single-sample to photon-counting readout noise level for a data frame containing the Ly-α line from HB89 1159+123. Each sequence shows an increasing number of non-destructive pixel measurements and decreasing readout noise. The faint spectral trace becomes increasingly visible as the readout noise decreases. Note that the spatial and spectral axes have been flipped relative to Figures 6.7 and 6.8. 129
6.13 Photon-counting demonstration on the sky with the SIFS Skipper CCD focal plane. Photon resolution is achieved at 128 and 250 measurements per pixel over the ROI shown in Figure 6.12. 130
6.14 Noise reduction sequence illustrating the Ly-α line from the data frame in Figure 6.12. Of particular interest for this demonstration is the ability to resolve features of interest in the spectra. The Ly-α line is completely hidden in the readout noise for low number of samples. As the noise decreases down to the photon-counting regime, one is able to identify and precisely fit the Ly-α line. 131
6.15 Top: Spectrum from a 600 s SIFS-Skipper CCD observation of an ELG identified in the DESI Early Data Release. The O III emission line is detected at $\lambda \sim 6628.8$ Å with different signal-to-noise ratios depending on the achieved readout noise (colored lines). Bottom: The signal-to-noise ratio as a function of $N_{\rm samp}$. In the readout-noise-dominated regime, it is possible to increase the SIFS signal-to-noise from ∼1.2 to ∼10.5 by achieving sub-electron readout noise levels. Note that this observations was taken by one of the Skipper CCDs that was affected by correlated noise. 133
6.16 Top: High signal level (∼70 e$^-$) spectrum around the Ly-α feature from a SIFS-Skipper CCD observation of QSO HB89 1159+123. Bottom: Signal-to-noise as a function of $N_{\rm samp}$ for the high signal QSO observation. The signal-to-noise improvement is minimal. The source and background contribution to the total noise is ~ 10 e$^-$, which dominates the noise budget in this observation. 134

6.17 Collection of selected constraints on the ALP mass/coupling parameter space. Previous results (gray) include integral-field spectroscopic data from MUSE [18] and VIMOS [19], HST optical background [20], and stellar evolution [21]. Projected constraints from observation of galaxy clusters with SIFS are shown in red, demonstrating the advantages of low-noise detectors, as well as observations of higher-redshift clusters. 136

7.1 Spatial distribution of Boötes II candidate member stars with metallicities [Fe/H < -1.5]. The dashed grey ellipses represent the half-life radii (r_h). Most star in the system lie within $2r_h$; however, there are two stars (solid black points) outside $5r_h$ that could be potential members. We acquired spectra from one of these candidates (red circled star). Figure extracted from [22]. 140
7.2 Image processing diagram. The first component of the pipeline performs image correction tasks. For a given data set, data products are first classified. Image correction proceeds with the user's choice of correction method. The algorithm models the spatial transients in ROI images and corrects for them in the parallel and serial ovserscans. The accuracy of the correction is validated by a series of tests that involved checking for noise increase and $0e^-$ shifts, introduction of linear correlations, and any other spatial patterns. Gain and flat-field (from a "combined flat") corrections are also applied. 144
7.3 Spectral Extraction diagram. After correction of science and arc-lamp data products, these pass to the spectral extraction step in the data reduction pipeline. First, individual channels (amps) are combined in groups of four to form a "detector image" (spectra and wavelength solutions are derived on a detector by detector basis). Fiber bundles are then selected and their pixel positions are used to extract spectral lines from the arc-lamps frames. The positions of these lines are used to derive the wavelength solution. The wavelength solution is validated and then applied to the combined spectra from science frames. 145
7.4 Baseline of the raw video signal. The flat signal profile (bottom left inset) corresponds to $N_{\rm samp} = 1$. A sharp exponential transient (bottom right inset) is induced in the video signal when changing to $N_{\rm samp} = 100$. The top insets indicate clock signals and their voltage swings Figure extracted from [23]. . . . 146
7.5 Raw AstroSkipper image for a single amplifier. The image has two ROIs with $N_{\rm samp} = 20$. The bias level variation between the single- and multi-sample regions is ~ 2000 ADUs (~ 15 e^-). 147
7.6 First step in the correction algorithm (Serial overscan correction). A model is derived to capture the bias shift as function of row number for for both the single- and multi-sample regions. The model is then applied to every region row by row (Bottom). Note that the image still exhibits pixel variations between regions. Subsequent steps are required to eliminate this residual. 148
7.7 Parallel overscan correction step. The leftover pixel transient, after serial ovsrscan correction, is modeled as a function of column number, using the parallel ovsrscan (Top). After column by column correction is applied to the ROI image, all bias shifts are fully eliminated (Bottom). 149

7.8 Statistical verification for the serial overscan. The pixel distributions from single-sample (SS) and multi-sample (MS) regions are shown. These correspond to images where the correction fitting algorithm (Fit) and the master bias (Combined) had been applied. Both correction methods perform similarly for all 16 amplifiers. 150
7.9 Linear correlation coefficients. Top: Raw ROI image corresponding to the Half-FoV ROI configuration. The horizontal direction (columns) show a strong positive and negative (1 and -1) linear correlation, which agrees with the alternating exponential model, e.g., Figure 7.7 (Top). The vertical direction shows a strong positive linear correlation. Center: The raw image has been corrected using the master bias. Bottom: The raw image has been corrected with the our fitting algorithm. In both instances, the linear correlations have been substantially reduced. We note that in the vertical direction there is a noticeable downward trend in the correlation coefficients. This might indicate leftover exponential residuals after image correction. However, we observe that the coefficient values are consistent with the master bias correction method (Center frame). 152
7.10 Frequency difference. Low frequency components have been shifted to the center of the images with higher frequencies in the outer edges. Top: Frequency difference for an image corrected with both the master bias and our fitting algorithm methods. Here a high-pass filter is applied, highlighting differences in the fine detail (high frequencies) between the two resulting corrected images. Center: Same as above but in this case we apply a low-pass filter to highlight differences from broad structures in the images. These would correspond to the exponential transients that cover large portions of the image. Bottom: Frequency difference for a corrected image (either method gives similar results) and a raw image using a low-pass filter. As expected the large frequency difference values across the image indicate the presence of substantial long-structure patterns in the raw image. 154
7.11 Spectral lines from the HgArNe lamp. Wavelength calibration images are taken after/before each science frame in order to account for any variation or shifts in fiber position. Note the curvature of the spectral line along the axis of the image, which needs to be corrected by the wavelength solution. 156
7.12 Identified spectral fiber bundles with signal level above ~ 10 electrons (colored) corresponding to a science detector frame. 157
7.13 Spectral features from the HgNeAr calibration lamp image. The user selects the peaks (blue arrows) to be used for the wavelength calibration. The red arrow indicates the next peak to be selected or discarded. Each peak has a known wavelength referenced from NIST. 157
7.14 Voigt profile fit for a spectral line in the HgArNe calibration frame. The center position is used to derive the wavelength calibration. 159
7.15 Wavelength solution. We assume a polynomial fit (e.g., Eqn. 7.7) for the lamp spectra center pixel positions and reference wavelengths. An independent fit is applied to each fiber bundle. In this case, five independent wavelength solutions are over-plotted. 160

7.16 Fit residuals for the wavelength calibration. Top: The residuals show a systematic parabolic pattern for a $m = 1$ fit, indicating the inability of the model to capture non-linear behavior. Bottom: Instead, if we implement a $m = 4$ fit the residuals improved by an order of magnitude and show a consistent scatter around 0. Fitting higher order polynomials does not improve the residuals. 162
7.17 Radial velocity standard stars spectra for the H-β and H-α lines. Top: BD-18 5550 H$-\beta$ spectra. We calculate $v_r = -126.05 \pm 2.02$ km/s. The referenced radial velocity value is -125.08 ± 0.25 km/s. The two values agree well within the uncertainties, i.e., $\Delta v = -0.97 \pm 2.04$ km/s. Center: We calculate $v_r = -125.35 \pm 1.54$ km/s for the same star from the H$-\alpha$ line. Bottom: $v_r = -85.73 \pm 1.67$ km/s for the Gaia DR3 2771566830179387776 star. These values pose no significant statistical variations from the referenced radial velocities. We validate the entire pipeline and show that our spectral extraction method gives reasonable answers. 168
7.18 Top: Boötes II candidate member star H$-\alpha$ spectra. Bottom: Spectra of the magnesium triplet. We show the Voigt profile fit to one of the magnesium lines. Radial velocities are derived following the same procedures as in the pipeline validation with radial velocity standards. 169

8.1 Picture of the output region of a MAS CCD with 8 independent floating-gate (skipper) amplifiers, labeled V_{out_1} to V_{out_8}. For a scale reference, the aluminum bond pads (white squares in the image above the labels) are 100 μm $\times$ 100 μm. As the charge is move from the active region to the serial register, charge packets are measured independently by each of the MAS amplifiers, providing a factor of $\frac{1}{\sqrt{M}}$ (where M is the number of amplifiers) after averaging. Picture adapted from [24]. 171
8.2 S/N as a function of readout time. The S/N is calculated for both a conventional Skipper CCD and MAS devices with increasing number of amplifiers. A typical SIFS observation is assumed with a fixed exposure time of 20 min. and a 20% ROI from 4k $\times$ 4k devices. We compare the time at which each configuration reaches a S/N of ~ 7. Mas devices reach S/N $\gtrsim 7$ in 8 seconds while the Skipper CCD requires 125 seconds which is equivalent to $N_{\rm samp} = 8$. 172
8.3 Relative observation time per exposure as a function of detector readout noise. The observation time is normalized to the baseline detector configuration (dashed-gray line in both plots), which is assumed to be a Skipper CCD operating with $N_{\rm samp} = 1$ and $\sigma_1 = 3.5 e^-$rms/pix. Top: Skipper and MAS ($M = 8$ and $M = 128$) comparison. MAS devices outperform the conventional Skipper CCD by a $\gtrsim 10\%$ increase in observation efficiency when targeting S/N=7 at SIFS. Bottom: Skipper and MAS comparison for IMACS. While the conventional Skipper cuts the nominal observation time (baseline detector configuration) by $\sim 47\%$ at a readout noise of $\sim 0.78 e^-$rms/pix , the MAS CCD can improve the instrument's efficiency by as much as $\sim 65\%$, resulting in lower observation times to reach S/N=5. 174

8.4 Comparison of the sensitivity to faint UFD stars between Skipper and MAS devices, assuming IMACS observations in the z-band. The three contour map plots show S/N bands for stars with magnitudes between 21.5 and 25; the exposure time is kept fixed at 40 minutes. For stars with magnitudes ~ 23, MAS devices ($M = 8$ and $M = 128$) achieve S/N ~ 5 while the Skipper system only reaches S/N $\lesssim 4$. For fainter stars, magnitudes $\gtrsim 23.5$, MAS devices retain sensitivity (S/N $\gtrsim 2$), while the Skipper CCD losses sensitivity entirely. 176
8.5 DESI and IMACS spectrographs throughput and sensitivity increase to faint stars from a Stage 5 survey. Top: Throughput for the IMACS and DESI spectrographs, extracted from [25] and [26], respectively. Measurements are not corrected for atmospheric effects. Bottom: Projections for the Spec-S5 system consisting of a thick ($\sim 250\mu$m) $M = 128$ MAS CCD (bright green curve). We take the baseline IMACS signal rate (0.00416e$^-$rms/pix) for observations of faint UFD stars at ~ 8400 Å [27] and rescale it assuming a 6-m telescope mirror and the DESI throughput at ~ 8400 Å. This measurement is compared to both the current IMACS configuration and an IMACS-MAS ($M = 128$, thin, blue-optimized MAS CCD). Notable, We note a factor of $\gtrsim 5$ improvement in the Spec-S5 system compared to the current IMACS system for all star magnitudes. Furthermore, for stars with magnitudes $\gtrsim 23$, the Spec-S5 system achieves a factor of $\gtrsim 4$ improvement in S/N compared to the IMACS-MAS system, highlighting the synergy between a stage-of-the-art spectrograph and ultra-low noise detectors. 177

A.1 Diagram of a stream gap creation and evolution. The dotted line denotes the direction of the stream motion, the solid lines show the point of closest approach. At each stage of gape evolution, the graphs illustrate density (ρ) as a function of the angle on the sky (ψ) from the perspective of an observer at the center of the galaxy. (1) Unperturbed stream with uniform density. (2) Compression of stream's particles to point of closest approach. (3) Changes in orbital period: particles kicked along their orbital direction gain kinetic energy, leading to a longer orbital period, which causes them to fall behind the impact point. particles kicked in the opposite direction lose kinetic energy, resulting in a shorter orbital period, causing them to move ahead of the impact point. As a result, compression is reversed. (4) Over time, the particles that were previously pulled together near the point of closest approach begin to spread out, forming an under-dense gap. (5) Expansion continues and eventually particles overtake each other, forming caustics. Figure extracted from [28]. 185
A.2 The geometry for the stream-halo interaction. The dotted line represents the stream and the dashed line is the halo's path. The interaction occurs in the $x-y$ where b is the point of closet approach. Figure taken from [28]. 186
A.3 Subhalo mass functions for CDM and different WDM models. In the halo-stream interaction realizations, the subhalo mass is drawn from the appropriate SHMF (i.e., CDM or WDM) via the inverse CDF method. Mass values are overplotted on the corresponding DM model (solid lines). 193

A.4 Gap size distribution for different density thresholds f. The gap sizes and dpeths are calculated from a population of ΛCDM subhalos with a mass range $10^5 - 10^9 M_\odot$. Calculations assumed a Plummer potential. 195
A.5 Left: the gap size distribution produced by a realization of ΛCDM subhalos with NFW and Plummer gravitational potentials. The distributions correspond to $f < 0.90$. Calculations are made with $10^5 - 10^9 M_\odot$ subhalos. In the NFW case, there is a suppression of small gaps, i.e., gaps produced by low-mass pertubers and a sharp cut-off of gaps $> 15^\circ$ produced by the most massive subahlos. These differences in gap sizes between NFW and Plummer subhalos are due to concentration effects in the NFW case. Right: the concetration-mass relation for NFW halos as described by Eqn. A.16. 197
A.6 The concentration-mass relation for the WDM models, as described by Eqn. A.17, explored in the simulations alongside the CDM concentration for comparison. . 198
A.7 Top: Gap size distributions for different realizations of WDM models. As expected, there is a pronounced suppression of all gap sizes, i.e., subhalo suppression, for WDM models with $m_{WDM} \lesssim 80$ keV. Bottom: The total number of gaps for various WDM models assuming both Plummer and NFW potentials. The CDM (Plummer and NFW) expected gaps are plot for reference. These calculations assume the properties of the Pal 5 stream in Table A.1. 199

LIST OF TABLES

4.1 SIFS Reference Parameters 57
4.2 Metrology requirements toe ensure optimal optical alignment and focus of the Skipper CCD focal plane array at SIFS. 64

5.1 Summary of the AstroSkipper characterization results for the six out of eight devices with best performance. 111

7.1 Uncertainties in radial velocity measurements for standard stars and the Boötes II candidate member star. The total systematic uncertainty is given by the RMS and frame-to-frame uncertainties. We assume the systematic and statistical uncertainties are independent. The combined uncertainty, σ_{COM}, is calculated with Eqn. 7.10 164

A.1 Properties of cold MW stellar streams. For this work, we test the gap predicting framework with the Pal 5 Stream. The gap predicting framework is fully generalized and thus the rest of the streams are good candidates for future implementations. The stream properties are extracted from [29]. 193

ACKNOWLEDGMENTS

An endeavor of this magnitude would have been next to impossible without the support of many people, who kindly took on the roles of academic, scientific, and life advisors, lab mates, friends, and believers in my ability to become a scientist. It truly takes a village to guide a PhD student to success. The following is an attempt, albeit inexhaustive, to acknowledge such people.

First and foremost, I extend my deepest gratitude to my advisor, Alex Drlica-Wagner. His exceptional mentorship, insightful guidance, and unwavering support have been pivotal to my growth as a scientist. Alex gave me the opportunity to take full ownership of my PhD project, empowering me to lead it from its inception to its successful completion. His encouragement and vision have allowed me to contribute meaningfully to the scientific community, and for that, I am profoundly grateful. I also thank Paolo Privitera, Abigail Vieregg, and Craig Hogan for being part of my committee and offering me valuable feedback on my PhD progress.

I would like to extend my special thanks to Juan Estrada, who became my "Fermilab advisor." I am indebted to Juan for all his support and mentoring. Most of the knowledge on CCDs I acquired throughout the years I learned from him. I want to thank Javier Tiffenberg for sharing his experience on the intricacies of Skipper CCDs; those lessons helped understand the details about how the detectors operate. Thanks to Dan Baxter for giving me the opportunity to participate and make meaningful contributions to a new project in the last year of my PhD. I am also appreciative of Andrew Lathrop for his help in the lab, his engaging conversations, and his outlook on current events. To everyone in the CCD group at Fermilab, thank you for your encouragement, collaboration, and friendship. You all played an integral role in making my PhD journey not only successful but also deeply rewarding. These years will remain among the most fruitful and memorable of my life.

I want to express my heartfelt gratitude to Marco Bonati, whose contributions were

pivotal to the success of my PhD project. Marco, your expertise and dedication were essential in making this project a reality. I am especially grateful for your warm hospitality during all my trips to Chile, which made my work there not only productive but also genuinely enjoyable.

I am deeply grateful to the friends who brought joy, camaraderie, and support to my PhD journey. Julian C.-Z., Lukas P., Mark L., Alec H., Joel F., Jonty P., Morgan L., Carly K., and Kenneth L.—thank you for being such an integral part of this chapter of my life. Your encouragement, the moments we shared, and the work we accomplished together enriched my experience and made this journey far more enjoyable and fulfilling.

I can never express enough gratitude for my family and their support. To my husband, Cuy: thank you for coming into my life and becoming my greatest source of strength and encouragement. You are the person who listens, who is always there for me, and who lifts me up when I need it most. I love you, and I could not have achieved this accomplishment without your steadfast support. Todo mi cariño y gratitud para mis padres y mi hermano, Socorro, Cipriano, y Cristian. Este logro se lo debo a ustedes y al sacrificio que hicieron para que mi hermano y yo tuviéramos un mejor futuro. Gracias por compartir mi sueño, por venir a un nuevo país y darme la oportunidad de seguir ese sueño, y por brindarme el apoyo necesario para crecer, aprender y, ultimadamente, alcanzar este anhelo. Este trabajo, este sacrificio, y este logro se los dedico a ustedes.

My work was supported by the U.S. Department of Energy, Office of Science, Office of Workforce Development for Teachers and Scientists, Office of Science Graduate Student Research (SCGSR) program. The SCGSR program is administered by the Oak Ridge Institute for Science and Education for the DOE under contract number DE-SC0014664. Also, this work was supported by the U.S. Department of Energy, Office of Science, Graduate Instrumentation Research Award (GIRA). Support was provided by the Fermilab Laboratory Directed Research and Development program (L2019.011 and L2022.053) under contract

No. DE-AC02-07CH11359 with the US Department of Energy, Office of Science, Office of High Energy Physics. Additionally, support was provided by NASA APRA award No. 80NSSC22K1411.

ABSTRACT

A precise understanding of the evolution of the universe and its constituents strongly depends on observations across both large and small cosmic scales. Over the past few decades, large cosmological surveys have expanded the number of galaxy redshifts available to probe cosmic expansion and dark matter (DM) by an order of magnitude every ten years. To sustain this growth into the 2030s and beyond, the next generation of surveys must look farther back in time while maximizing the discovery potential of the faintest objects within the Milky Way. Achieving these goals requires advancements in observational technology to improve sensitivity. Ultra-low readout noise detectors are fundamental to this effort, enabling greater sensitivity for high-density and high-redshift spectroscopic surveys to place tighter constraints on dark energy and DM, the two dominant components in the concordance model of cosmology.

In this thesis, I present the development and first on-sky demonstration of a novel detector technology, the Skipper CCD, integrated into a prototype focal plane array for the SOAR Telescope Integral Field Spectrograph (SIFS). These observations, carefully optimized to reduce readout times, achieved detector readout noise in the sub-electron ($\lesssim 1$ e^-rms/pixel) and photon-counting (~ 0.22 e^-rms/pixel) regimes. The SIFS-Skipper instrument demonstrated significant signal-to-noise (S/N) improvements for signal-starved astronomical targets, such as high-redshift quasars and emission-line galaxies. Additionally, I present radial velocity measurements of a candidate member star in the ultra-faint dwarf (UFD) galaxy Boötes II, at its periphery. These measurements are of particular interest for mapping the DM distribution in UFDs and for unraveling their formation and evolutionary history. Furthermore, I explore future advancements in Skipper CCD technology, focusing on readout architectures designed to drastically reduce readout times while maintaining ultra-low noise performance. These projections highlight the potential efficiency gains in observation time and S/N that can be achieved with these novel detectors for future large cosmological surveys.

CHAPTER 1

OVERVIEW

We begin in Chapter 2 with the central scientific motivation for this thesis: developing sensitive detector technology for next-generation cosmological surveys, specifically to study *dark matter* (DM). This chapter introduces the DM paradigm (Section 2.1), parting from a cosmological perspective and defining the wealth of cosmological evidence that supports the existence of DM (Section 2.2). In Section 2.3, we outline DM models that can be tested with observational signatures (e.g., suppression in the matter-power spectrum) at small scales. Intrinsically, these observations are in the starved-signal regime, where, for example, precise measurements of DM probes (Section 2.4) at these scales e.g., the MW population of faint satellite galaxies are crucial in constraining the microphysics of DM. Section 2.5 concludes with a technical description of large cosmological surveys and their instruments that have enabled scientific breakthroughs in DM physics. This section motivates the need for ultra-low-noise detectors such as the Skipper CCD.

Chapter 3 discusses the fundamentals of charge-coupled devices (CCDs) and Skipper CCDs, with an emphasis on their basic operational concepts, readout architectures, and hardware-level optimizations for astronomy. Section 3.1 introduces conventional CCDs and outlines the three fundamental operational processes common to all CCDs: charge generation, governed by silicon physics and the principles of metal-oxide-semiconductor structures; charge transfer, which relies on 3-phase voltage clocking; and charge measurement, which is performed using a sense node and associated techniques such as correlated double sampling to determine pixel values. Section 3.2 focuses on the readout architecture of Skipper CCDs, particularly the floating gate amplifier, enabling non-destructive measurements of the charge in each pixel, and how it differs from conventional readout architectures. The section concludes with a description of full-depleted, back-illuminated Skipper CCDs which have been processed for astronomical applications.

In Chapter 4, we present the motivation to construct a prototype Skipper CCD focal plane array for the Southern Astrophysical Research (SOAR) Telescope Integral Field Spectrograph (SIFS). Section 4.1 highlights the early characterization of astronomy-optimized Skipper CCDs, demonstrating promising performance results that motivate the development of a complete Skipper CCD imager for astronomical applications. Section 4.2 introduces SIFS, detailing its capabilities and synergies with a Skipper CCD focal plane. Section 4.3 discusses predictions for signal-to-noise improvements and reductions in observation time achievable with Skipper CCDs at SIFS, further justifying the project. The subsequent sections (Sections 4.4 through 4.6) describe the construction of the Skipper CCD focal plane array. These include detector packaging procedures, the assembly of the Dewar, focal plane array metrology to ensure precise optical alignment, and the integration of the readout electronics.

In Chapter 5, we present results from the extensive characterization and optimization of six astronomy-grade Skipper CCDs. Section 5.1 describes the Skipper detector characteristics (6k $\times$ 1k, 15 μm pixels, 250 μm thick, fully depleted, p-channel). Section 5.2 describes the laboratory setup used to test detectors and outlines characterization and optimization procedures. Section 5.3 outlines the process for optimizing readout time which resulted in a factor of five reduction, from 200 μs/pixel to 40 μs/pixel for a single amplifier. All amplifiers demonstrated consistent single-sample readout noise of < 4.3 e$^-$ rms/pixel. For $N_{\rm samp} = 400$ samples per pixel, all 24 amplifiers (four per detector) exhibited single-photon-counting capability with a readout noise of $\sigma_{N_{\rm samp}} \sim 0.18$ e$^-$ rms/pixel. Additionally, photon-counting capabilities allowed us to measure low-signal non-linearity ($\lesssim 1\%$) in the detector (Section 5.4). In Section 5.5, we explore the trade-off between full-well capacity and clock-induced charge (CIC). We achieved a CIC rate of $< 1.45 \times 10^{-3}$ e$^-$/pixel/frame for a full-well capacity of $\sim$ 900 e$^-$, which increased to a CIC rate of $\sim$3 e$^-$/pixel/frame for full-well capacities of $\sim$40,000–65,000 e$^-$. Section 5.6 reports results on conventional

characterization tests for astronomical CCDs which show that the Skipper devices retained the desirable properties of astronomy CCDs, such as charge transfer inefficiency (3.44×10^{-7} on average), dark current ($\sim 2 \times 10^{-4}$ e^-/pixel/s), cosmetic defects ($< 0.45\%$ "bad" pixels), and charge diffusion (PSF $< 7.5\mu$m). Furthermore, this work includes the first measurements of the brighter-fatter effect and absolute quantum efficiency ($\gtrsim 80\%$ between 450 nm and 980 nm; $\gtrsim 90\%$ between 600 nm and 900 nm) for Skipper CCDs. The chapter concludes in Section 5.7 by summarizing our findings, highlighting the viability of using Skipper CCDs for astronomy.

Chapter 6 provides a comprehensive description of the first on-sky demonstration of Skipper CCDs at SIFS, detailing the installation, commissioning, and observation strategy and results. The installation and commissioning of the Skipper CCD focal plane, described in Section 6.1, focused on achieving precise optical alignment and optimizing system performance, including focal plane array readout noise and backgrounds. The first observations, conducted on March 31, 2024, followed successful commissioning and implemented a novel observation strategy using regions of interest (ROIs), as outlined in Section 6.2. This strategy achieved sub-electron readout noise (~ 1 e^-/rms/pixel) for a 2k $\times$ 4k region and photon-counting noise (~ 0.22 e^-/rms/pixel) for a 220 $\times$ 4k region, each with a readout time of $\lesssim 17$ minutes. Astronomical targets included two high-redshift quasars (HB89 1159+123 and QSO J1621-0042), two galaxy clusters, an emission-line galaxy, a candidate star of the Boötes II ultra-faint dwarf (UFD) galaxy, and five CALSPEC standard stars. Section 6.3 presents the results, highlighting charge-quantized, photon-counting observations of HB89 1159+123 that demonstrated sensitivity improvements for faint spectral features and signal-to-noise enhancements in the low-background, readout-noise-dominated regime. Finally, Section 6.4 summarizes these achievements and introduces two science cases to be explored with SIFS-Skipper data: the study of decaying axion-like-particle dark matter and the study of a candidate member star from Boötes II. The latter will be explored in detail in this thesis.

Details on the data reduction pipeline and star radial velocity measurements are provided in Chapter 7. This chapter describes the data reduction pipeline developed for processing SIFS-Skipper data and presents the radial velocity measurement of a candidate member star from the UFD Boötes II, demonstrating the capability of the SIFS-Skipper system to acquire science-quality data. Section 7.1 serves as the scientific motivation for studying member stars at the periphery of UFDs. Here, we also review previous studies [22] on this particular Boötes II candidate member star. Section 7.2 outlines the data reduction pipeline, detailing the processing of raw images (including ROI images) and the extraction of spectra. The data reduction pipeline for image processing and spectral extraction is validated, in Section 7.3, using SIFS-Skipper data from two radial velocity standard stars: BD-18 5550 and Gaia DR3 2771566830179387777. For BD-18 5550, we measure radial velocities of -126.05 ± 2.02 km/s and -125.35 ± 1.54 km/s from the H-β and H-α lines, respectively. For Gaia DR3 2771566830179387777, we measure -85.73 ± 2.19 km/s from the H-β line. Uncertainties in all radial velocity measurements include contributions from systematic effects, such as fluctuations in pixel position due to the wavelength solution, and statistical errors in fitting the spectral features. The calculated radial velocities for the standard stars are consistent with the referenced values of -125 ± 0.25 km/s (BD-18 5550) [30] and -85.86 $\pm$0.42 km/s (Gaia DR3 2771566830179387777) [31]. Finally, Section 7.4 presents the results obtained by applying the validated data reduction pipeline to the Boötes II candidate member star. This study aims to confirm whether the candidate star's velocity is consistent with the UFD's mean systematic radial velocity, $139.4^{+1.4}_{-1.1}$ km/s [32]. From the H-α spectral line, we measure a radial velocity of 177.88 ± 1.97 km/s, and from one of the magnesium triplet spectral features, we obtain 177.09 ± 2.42 km/s. These results suggest that the candidate member star is likely a MW foreground star, e.g., a MW halo star.

Chapter 8 provides an outlook on the future implementation of Skipper amplifiers with the multi-amplifier sensing (MAS) architecture. We explore the potential improvements

MAS CCDs can contribute to astronomical observations, demonstrating over a 15% increase in observation efficiency when targeting faint sources, with gains as high as 65% in specific scenarios, such as with the IMACS instrument on the Magellan-Baade telescope. Sensitivity studies show that MAS CCDs can achieve a S/N of ~ 5 for stars with magnitudes $\gtrsim 23$, enabling unprecedented exploration of UFDs. These capabilities significantly enhance the potential of future Stage 5 survey [5] instruments, addressing the primary limitations of conventional Skipper CCDs and facilitating the broader adoption of ultra-low-noise detectors. This thesis concludes with Chapter 9, which summarizes the efforts leading to the first on-sky demonstration of the Skipper CCD. We reflect on the maturity of Skipper CCD technology and its demonstrated viability for cosmological applications, as evidenced by significant improvements in observation performance and science-quality data acquisition.

CHAPTER 2

ASTROPHYSICAL STUDIES OF DARK MATTER

2.1 Standards of Cosmology

Modern cosmology extends beyond the classical framework of localized motion, e.g., the solar system or the Milky Way (MW) to describe the evolution of space over time. Observational cosmology, particularly with the work of Henrietta Levitt [33], Vest Slipher [34], Edwin Hubble, and Milton Humason [35] provided compelling evidence that the universe itself is expanding. Their groundbreaking observations opened the door for decades of transformative discoveries that have come to define the standards of modern cosmology. The discovery of the cosmic microwave background (CMB) in 1964 [36] provided critical evidence for the Big Bang model, offering a snapshot of the universe 380,000 years after the Big Bang. The CMB reveals the early distribution of matter and energy, allowing precise determinations of the universe's composition and geometry [3].

In the domain of large scales, cosmology is primarily concerned with the time evolution of structure and energy under the influence of gravity. To this end, general relativity provides the essential framework to describe how space changes—expands or contracts—over time. At the heart of relativistic cosmology is the Friedman-Lemaître-Robertson-Walker (FLRW) metric [37, 38, 39, 40]:

$$ds^2 = dt^2 - a^2(t)\left[\frac{dr^2}{1-\kappa r^2} + r^2(d\theta + \sin^2\theta d\phi^2)\right], \tag{2.1}$$

where $a(t)$ is the scale factor, and κ represents the spatial curvature. The Friedmann equations govern the time evolution of $a(t)$:

$$\left(\frac{\dot{a}}{a}\right)^2 = \frac{8\pi\rho}{3M_{Pl}^2} - \frac{\kappa}{a^2}, \tag{2.2}$$

$$\frac{\ddot{a}}{a} = -\frac{4\pi}{3M_{Pl}^2}\left(\rho + 3p\right). \tag{2.3}$$

The first equation relates the Hubble parameter, $H(t) = \dot{a}/a$, to the energy density ρ, which includes contributions from matter, radiation, and dark energy. The second equation describes the acceleration of the universe's expansion, influenced by the pressure p of its components. The curvature κ depends on the total energy density relative to the critical density $\rho_{crit} \equiv \frac{3H^2M_{Pl}^2}{8\pi}$. The density parameter $\Omega_i = \rho_i/\rho_{crit}$ determines the universe's geometry: flat ($\kappa = 0$) if $\rho = \rho_{crit}$, spherical ($\kappa = +1$) if $\rho > \rho_{crit}$, and hyperbolic ($\kappa = -1$) if $\rho < \rho_{crit}$.

Observations (e.g., [3, 41, 42]) show that our universe is flat ($\kappa = 0$), with current energy densities of $\Omega_M = 0.315$ (matter), $\Omega_{\rm rad} = 9.26 \times 10^{-5}$ (radiation), and $\Omega_\Lambda = 0.685$ (dark energy). Most of the universe's energy density resides in dark energy (Ω_Λ), driving accelerated expansion. Only 5% of the total matter-energy density is baryonic matter, while 25% is dark matter (DM), which interacts primarily through gravity and has low velocity dispersion, critical for structure formation. These components define the standard ΛCDM cosmological model, incorporating dark energy (Λ) and cold dark matter (CDM).

2.2 Dark Matter

The term *dark matter* might evoke concepts from science fiction but in reality, it precisely encapsulates one of the greatest mysteries of modern cosmology. Over the decades, astronomical observations have accumulated an enormous amount of evidence supporting the conclusion that most of our universe is composed of an exotic substance that neither radiates, reflects, nor absorbs light. In fact, 80% of the matter in the universe is DM [3], with the remaining 20% composed of Standard Model (SM) particles. In this section, I will summarize some of the astronomical and cosmological evidence, accumulated over many years,

for the existence of DM.

2.2.1 The Vireal Theorem and the Coma Cluster

The first evidence for DM was presented by Fritz Zwicky in 1933 through his study of the Coma Cluster [43, 44]. Zwicky observed that the velocities of galaxies within the cluster were much higher and exhibited much more dispersion than expected [43, 44]. Assuming equilibrium and isotropic galaxy distribution, he applied the virial theorem, $2T + V = 0$, to relate the cluster's velocity distribution to its mass profile. For a gravitationally bound system, the cluster mass depends on velocity dispersion σ_v, projected radius R_G, and Newton's constant G [45]:

$$M = \frac{3\pi R_G \sigma_v^2}{2G} = 1.1 \times 10^{15} M_\odot \left(\frac{\sigma_v}{1000\text{km/s}}\right)^2 \left(\frac{R_G}{1\text{Mpc}}\right). \tag{2.4}$$

Using a velocity dispersion of 700 km/s and a radius of 2×10^6 light-years, Zwicky calculated a total cluster mass of $4.5 \times 10^{13} M_\odot$, corresponding to an average galaxy mass of $4.5 \times 10^{10} M_\odot$. This resulted in a mass-to-light ratio of $\sim 500 M_\odot L_\odot^{-1}$, far exceeding the expected value from stars and luminous gas. Zwicky attributed this discrepancy to "missing mass," or DM. Despite its groundbreaking nature, this idea did not gain widespread acceptance until the late 20th century.

2.2.2 Galactic Rotation Curves

The 1970s brought new insights into the question of the "missing matter" through the findings of astronomers such as Vera Rubin and Kent Ford [46, 47], who provided much more precise measurements of the rotation curves of galaxies. From Newtonian mechanics, the velocity of a star from the galactic center (r) is given by

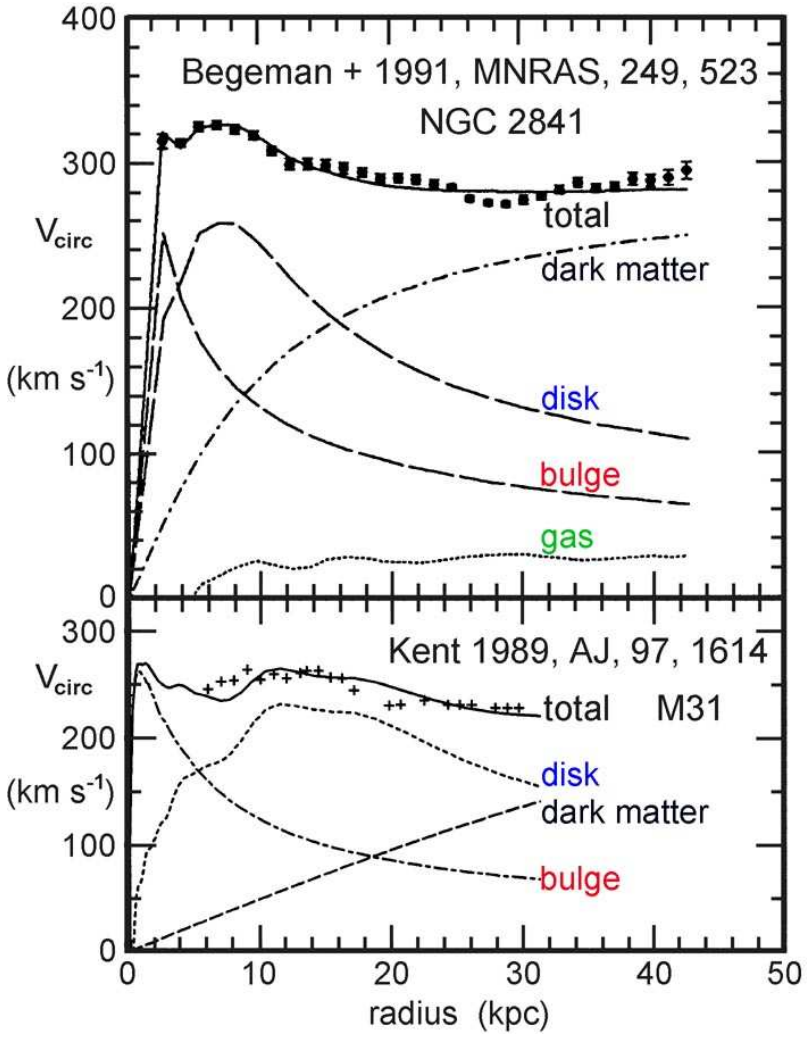

Figure 2.1: Rotation curve for NGC 2841 and M31. The curves are comprised of three-components: the disc, bulge, gas (for NGC 2841), and halo. The different styled lines represent the best fit to the individual components of the galaxies. The back, solid line is the sum of all mass contributions. Note that the contribution of the DM "halo" is required to reconstruct the full velocity profile ("total"). Figure extracted from [1].

$$v(r) = \sqrt{\frac{GM(r)}{r}}. \tag{2.5}$$

The galaxy rotation curve data compiled by Rubin and Ford, based on Doppler shifts of atomic spectral lines of known wavelengths (e.g., the singly ionized Nitrogen line at $\lambda = 6583$ Å), intended to probe the mass distribution within galaxies. According to the Newtonian

model (Eqn. 2.5), the orbital velocity $v(r)$ of stars and gas should scale as $r^{-1/2}$, predicting an exponential drop-off in velocity with increasing distance from the galactic center. However, the hundreds of rotation curves collected by Rubin and others [47] revealed a different pattern: the velocities plateaued at large radii instead of decreasing. This indicated that the velocity of stars at the edges of galaxies was too high to remain gravitationally bound if the only source of gravity were the visible mass within the galaxy. This discrepancy suggested the presence of a significant amount of unseen, or "dark," matter extending well beyond the visible boundaries of galaxies. Figure 2.1 shows rotation curves for NGC 2841 and M31; the best fit to the date is given by the combination of all of the visible and dark (the DM halo) constituents.

2.2.3 Gravitational Lensing and the Bullet Cluster

Gravitational lensing is a phenomenon predicted by general relativity where the gravity of a massive object, such as a galaxy or galaxy cluster, bends the path of light from a more distant source. This effect acts like a cosmic lens, magnifying, distorting, or even multiplying the images of the background object [48, 49, 50]. Gravitational lensing directly probes the total mass distribution that a light ray encounters; hence, the lens does not have to be luminous or baryonic [50]. Techniques in weak and strong lensing look for for distortions due to diffuse or single gravitational sources, which can be applied to objects such as the Bullet Cluster to probe DM distribution.

The Bullet Cluster originated from the merger of a pair of galaxy clusters, separated by a distance of about 720 kpc. During the merger, the galaxies within each subcluster, due to their relatively small size compared to the overall cluster, largely passed through one another without colliding, continuing along their original paths. In contrast, the gas clouds surrounding each subcluster, which constitute the bulk of the visible matter, did collide, resulting in significant deceleration. This interaction caused the X-ray emitting gas, which

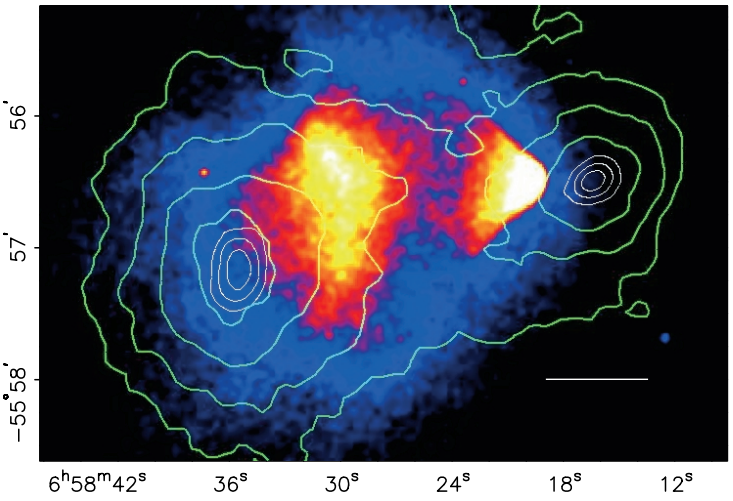

Figure 2.2: Chandra space telescope X-ray data of the Bullet Cluster. The green, inner contours represent the weak lensing reconstructed mass. X-ray data, which traces the density of hot plasma in the galaxy clusters (colored regions, where blue indicates the least dense and white the most dense), reveal a clear discrepancy between the location of the plasma and the inferred location of the mass based on lensing. This discrepancy underscores that the bulk of the gravitational mass is not associated with the visible plasma but rather with an unseen component, strongly suggesting the presence of DM. Figure extracted from [2].

accounts for most of the visible mass in the system, to lag behind the galactic centers of each cluster after the collision. X-ray maps (Figure 2.2) were compared to the mass distribution inferred through weak lensing, leading to the conclusion that the mass within the Bullet Cluster does not follow the distribution of visible matter. This discrepancy indicates that another source of gravitational potential, such DM, must be present and dominating the system.

2.2.4 The Cosmic Microwave Background

The CMB was first detected by Penzias and Wilson in 1965 as a "3.5 K excess temperature" [36]. Formed during the recombination era, $\sim 380,000$ years after the Big Bang, the CMB represents photons that decoupled from baryonic matter as the universe cooled enough for neutral hydrogen to form. These photons have since redshifted due to cosmic expansion,

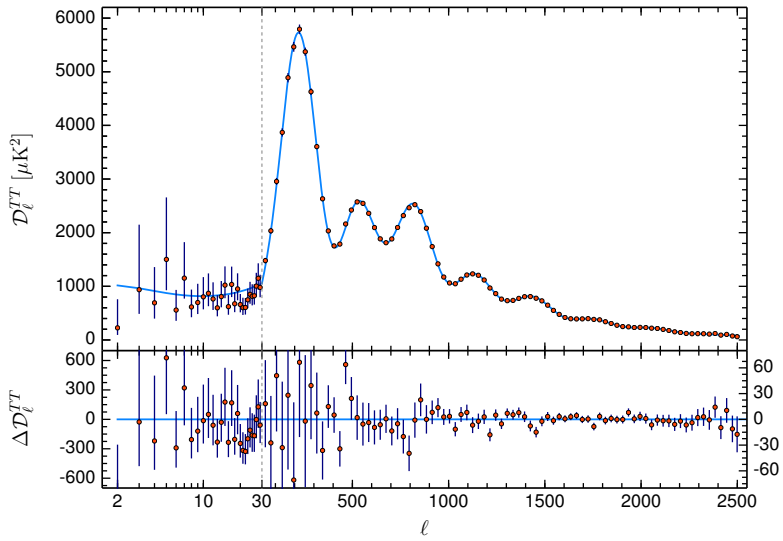

Figure 2.3: CMB temperature power spectrum from Planck Collaboration (2018). The top panel shows the power spectrum intensity as a function of spherical harmonic modes (l). The blue line represents the best-fit ΛCDM model. The bottom panel shows residuals from the fit. Peaks correspond to acoustic oscillations at recombination, with the first peak at $l \sim 200$ representing the sound horizon scale. Odd peaks indicate compression, and even peaks indicate rarefaction phases.

creating a nearly perfect blackbody spectrum with a current temperature of 2.72548±0.00057 K, measured by COBE's FIRAS instrument [51].

The CMB's temperature fluctuations, about 1.5×10^{-5}, reveal anisotropies arising from acoustic oscillations in the photon-baryon plasma. These fluctuations can be decomposed into spherical harmonics $Y_{lm}(\hat{n})$, forming the angular power spectrum (Figure 2.3). The first peak in the spectrum corresponds to the largest oscillations that reached maximum compression at recombination, while subsequent peaks represent higher harmonics of compression and rarefaction phases.

DM influences the CMB through its gravitational effects. While DM did not participate in acoustic oscillations of the photon-baryon fluid, its gravitational influenced suppressed the amplitudes of these oscillations, particularly at low multipoles. During the radiation-dominated era, photon pressure resisted compression, allowing density fluctuations to decay. After transitioning to DM dominance, gravitational potentials stopped decaying, enhancing

only modes that compressed before this transition. By measuring the ratio of the first two acoustic peaks to higher peaks, the abundance of DM can be precisely determined [3].

2.3 Dark Matter Models

Astrophysical observations probe the nature of DM by examining its impact on the formation and evolution of cosmic structures throughout history. On large scales, current observational data is well-explained by the CDM paradigm. However, many viable theoretical models of DM predict deviations from this CDM framework, which can be tested with both current and future observations. The fundamental properties of DM—such as particle mass, self-interaction cross-section, coupling to the SM, and time evolution—can manifest in the macroscopic distribution of DM, leading to detectable signals. To explore these variations, I first provide a summary of the concepts of the matter power spectrum and the transfer function, both of which are crucial for discussing distinct classes of DM models, including examples like particle DM and wave-like DM. For a complete, detailed derivation, I refer the reader to Hooper (2024).

Statistically, we can express the distribution of matter density variations in the limit of a large spatial direction as

$$\delta(\boldsymbol{x}) = \frac{V}{(2\pi)^3} \int \delta(\boldsymbol{k}) e^{i\boldsymbol{k}\cdot\boldsymbol{x}} d^3k \tag{2.6}$$

where $\delta(\boldsymbol{k})$ is the Fourier transform of the density contrast, $\delta(\boldsymbol{x})$, which tells us how much of each wavevector $\boldsymbol{k}$ contributes to the density perturbation. The coefficients or Fourier components of $\delta(\boldsymbol{k})$ are given by $\delta_{\boldsymbol{k}} = \frac{1}{V}\int \delta(\boldsymbol{x}) e^{i\boldsymbol{k}\cdot\boldsymbol{x}} d^3x$. Effectively, the Fourier expression allows us to write the distribution of the density variations, $\delta(\boldsymbol{x})$, in terms of an infinite series of sine waves, of comoving wavevector, $\boldsymbol{k}$, and comoving wavelength, $\lambda = 2\pi/k$. In the regime where the density variations are small (i.e., $|\delta_{\boldsymbol{k}}| \ll 1$), the evolution of these

perturbations can be treated using linear theory. This means that the modes do not interact with each other; they evolve independently. This simplifies the analysis significantly because the evolution of the density field can be understood by studying each mode separately.

Now, we can write an expression to measure the mean squared amplitude of the Fourier coefficients (i.e., the matter power spectrum), $\delta_{\boldsymbol{k}}$, to quantify the variance of density fluctuations at different spatial scales

$$P(k) = \left\langle |\delta_{\boldsymbol{k}}|^2 \right\rangle \tag{2.7}$$

where the average is taken over a large space or a large ensemble of realizations. Here, we have dropped the vector nature of $\boldsymbol{k}$ due to the assumption of isotropy, i.e., $P(\boldsymbol{k}) \Rightarrow P(k)$. The primordial power spectrum describes the initial distribution of density perturbations in the early universe. As the universe evolves, the power spectrum is shaped by several processes. Gravity enhances the growth of structures, pressure influences the evolution of perturbations, and cosmic expansion dilutes matter and induces variations in density. The transfer function, T_k, encapsulates the combined effects of these processes, effectively describing how the initial density perturbations evolve over time, such that the current power spectrum is given by

$$P(k) \propto k^{n_s} T_k^2 \tag{2.8}$$

where k^{n_s} is the primordial power spectrum. The transfer function depends on cosmological parameters such as Ω_b and Ω_{DM}. Therefore, measurements of the transfer function can be used to probe observable predictions, on structure formation, of CDM itself, and deviations from CDM.

2.3.1 Warm Dark Matter

Warm dark matter (WDM) was proposed as a potential solution to the "small-scale crisis" or "missing satellite problem," which highlights a discrepancy between the observed MW satellites and model predictions [53]. In the WDM model, the free-streaming scale—the distance a particle travels while it is relativistic—is significant. This implies that WDM particles have non-negligible velocities at high redshifts, which suppress the growth of structures on scales below the free-streaming length. This length scale is directly related to the mass of the WDM particle, typically in the keV range, and affects how structure formation occurs in the early universe [54].

The quantitative effects of WDM on the transfer function can be written as follows:

$$T_{k,WDM} \sim T_{k,CDM} \left[1 + (\alpha k)^{2.24}\right]^{-4.46} \tag{2.9}$$

where $T_{k,CDM}$ is the transfer function for the CDM model, and $\alpha = 0.7\text{Mpc} \times \left(\frac{m_{\text{DM}}}{1\text{keV}}\right)$. The WDM free-streaming nature leads to a CDM-like power spectrum with a sharp cutoff in the spatial frequency at small scales, i.e., structures smaller than $k \sim 8$ Mpc^{-1} are suppressed, corresponding to masses $\sim 3 \times 10^8 M_\odot$ [55, 52]. While WDM behaves like CDM on large scales, allowing for the formation of large cosmic structures, it introduces a damping mechanism on smaller scales. This damping effectively washes out small-scale overdensities, delaying the formation of the lowest mass galaxies. Figure 2.4 (orange curve) illustrates this sharp cutoff in the power spectrum from the WDM model.

Measurements of the Lyman-α forest and ultra-faint satellite galaxies provide constraints on the lower bound of thermally produced produced WDM particles at $\sim 3 - 5$ keV, corresponding to DM halo masses of $\sim 10^8 - 10^9 M_\odot$. Future large-scale surveys (see Section 2.5) seek to enhance sensitivity to subhalo mass functions down to $\sim 10^6 M_\odot$, allowing to probe WDM particle masses $m_{\text{WDM}} \gtrsim 18$ keV, [1] effectively testing signatures of keV-mass sterile

1. The thermal-relic WDM particle mass is related to the half-mode halo mass—the scale at which the

neutrinos.[2]

2.3.2 Self-Interacting Dark Matter

SIDM proposes interactions between DM particles mediated by new forces within the dark sector [59, 60]. The key parameter is the self-interaction cross-section per unit mass, $\sigma_{\rm SIDM}/m_\chi$, which influences energy and momentum exchange in DM halos. Cross-sections on the order of $\sim$ 1 cm^2/g can thermalize inner halo regions, leading to cored density profiles in low-surface brightness galaxies and altered rotation curves in spiral galaxies [61].

SIDM effects vary across scales. For example Observations of merging systems like the Bullet Cluster constrain $\sigma_{\rm SIDM}/m_\chi \lesssim 2$ cm^2/g for high relative velocities ($\sim$ 1000–4000 km/s) [62]. These limits suggest weak self-interactions at cluster scales. At galactic sacles, rotation curves indicate $\sigma_{\rm SIDM}/m_\chi \gtrsim 1$ cm^2/g for low velocities ($\sim$ 50–200 km/s). This implies stronger interactions in small systems, resulting in cored density profiles and reduced central densities in DM-dominated regions [63].

SIDM can also introduce dark acoustic oscillations in the early universe, caused by interactions with a massless or light mediator. These oscillations suppress and oscillate the power spectrum at small scales, with features appearing at wave numbers $k \gtrsim 10$ Mpc^{-1} (Figure 2.4, "Interacting DM", blue curve):

$$k \sim a(T_{\rm kd})H(T_{\rm kd}), \tag{2.10}$$

where $T_{\rm kd}$ is the temperature at which DM kinetically decouples. These interactions in-

DM transfer function decreases by half—by $m_{\rm WDM} = 3.33 \left(\frac{M_{hm}}{10^9 M_\odot}\right)^{-3.33}$ keV. The half-mode scale is useful as it represents a characteristic halo mass scale at which observables can manifest as a result of halo abundance suppression [56].

2. The sterile-neutrino is a well-motivated DM particle candidate with a mass range (keV range) consistent with WDM. Possible signatures of sterile neutrinos include X-ray emissions resulting from their decay via interactions with the SM neutrinos. One such example is the elusive 3.5 keV X-ray line, which has been proposed as a potential signal of sterile neutrino decay (e.g., see [57, 58]).

hibit structure formation on small scales by transferring momentum between DM particles and mediators, while oscillations arise from pressure-like effects analogous to photon-baryon acoustic oscillations.

In the early universe, when DM particles are still interacting frequently with massless or light particles in the dark sector, these interactions can create a pressure that counteracts gravitational collapse, much like how radiation pressure creates sound waves in the photon-baryon plasma. These distinctive features in the power spectrum provide a potential observational signature of SIDM models (e.g., [64, 65]), distinguishing them from the standard CDM paradigm.

2.3.3 Wave-like Dark Matter

Here, I describe axion-like particles, a paradigm inspired by the quantum chromodynamics (QCD) axion, which originally arose as a by-product of the solution to the strong CP problem [66]. From an astrophysical perspective, axion-like particles are of particular interest due to their potential detectability. Sikivie and Yang (2009) argue that because of the scalar nature of axions and their high abundance in the early universe, these particles could settle into a Bose-Einstein condensate. As a result, axions could be modeled as a coherent ground state function. The implications of this model suggest a Hubble-scale correlation length, leading to significant observational consequences, such as kpc-scale caustic structures in galactic halos [68]. These caustics, or regions of enhanced density, could provide observable signatures that help distinguish axion-like particles from other DM candidates, making them a compelling subject for further theoretical and observational studies.

Astrophysical observations place the only lower bound constraint on the mass of axion-like DM or ultralight bosonic DM, also known as fuzzy dark matter (FDM). For example, relationships derived between the FDM and WDM models,[3] which is well-suited to the

3. Armengaud et al. [69] define the relationship between the FDM and WDM particle mass as $m_{\rm WDM} =$

Lyman-α forest data, have been used to exclude FDM masses, m_ψ, in the range $10^{-22} \lesssim m_\psi < 2.3\times10^{-21}$eV at 95 % confidence. Competitive WDM mass constraints are also placed by the MW satellite galaxy population (see Section 2.4.1).

The connection between FDM and WDM models leads to a sharp cutoff in the matter power spectrum for small scales (Figure 2.4, "Fuzzy DM", black curve). This feature, also seen in the WDM model, relates to the apparent lack of structure at small scales. In the case of FDM, the structure suppression is due to quantum interference effects, as the de Broglie wavelength of the FDM particle is of the order of galactic scales [69].

2.4 Dark Matter Probes

The DM models described above produce observable deviations from the expected CDM predictions. In this section, I do not attempt to provide a comprehensive overview of all DM probes but instead focus on systems where one can probe DM halo abundances at small scales using the MW small structures (e.g., MW dwarf galaxies and stellar streams)—where deviations from CDM are most pronounced. These scales are represented in Figure 2.4 where structure formation suppression can be proved with halos $< 10^{12}M_\odot$ for Fuzzy DM models down to Earth-mass or below ($\lesssim 10^{-8}M_\odot$) subhalos for weakly interacting massive particle (WIMP) models. Small-scale structures offer a pristine environment to study the microphysics of DM. From this point onward, the cosmology-centered topics, including DM probes, will be motivated by the study of small-scale structure through the lens of near-field cosmology.

While existing observations provide evidence for subhalo masses in the range $\sim 10^8M_\odot - 10^9M_\odot$ [70, 71, 72], probing below this mass threshold remains challenging due to the limited observational sensitivity to the faintest galaxies. Moreover, halos with mass $\lesssim 10^8M_\odot$

$0.79\left(\frac{m_\psi}{10^{-22}\text{eV}}\right)^{0.42}$ keV. The FDM particle mass can then be expressed in terms of the halo half-mode mass as $m_\psi = 3.1\times10^{-21}\left(\frac{M_{\rm hm}}{10^9M_\odot}\right)^{-0.71}$ eV [50].

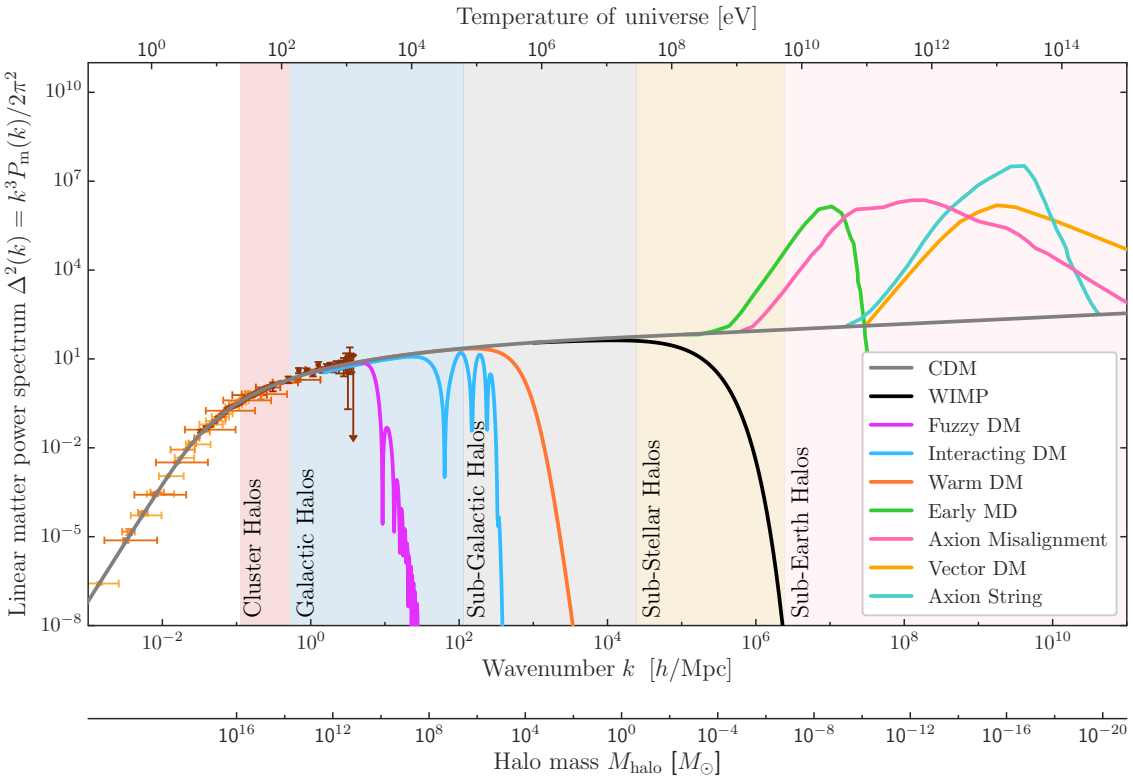

Figure 2.4: Dimensionless linear matter power spectrum extrapolated to $z = 0$. Curves are derived from theoretical predictions. Four DM models that suppress structure formation are considered: Fuzzy DM for $M_\psi = 10^{-22}$ eV (magenta), SIDM for an interaction cross section proportional to $\sigma_0 v^{-4}$ (blue), WDM with $m_{WDM} \sim 40$ keV (orange), and weakly interacting massive particle with $m \sim 100$ GeV (black). There are four DM models that enhance power structure.

generally host few or no stars [73, 74], necessitating novel detection techniques that do not rely on the baryonic content of halos. In this section, I focus on DM probes that target systems with small halos down to halos below the threshold of galaxy formation, which are crucial for testing the fundamental predictions of the CDM model and possible deviations from it.

2.4.1 The Smallest Galaxies in the Milky Way

Galaxies form within host DM halos, with the properties of these galaxies largely reflecting the characteristics of their surrounding halos. To a first approximation, galaxies with large

stellar masses are hosted by massive DM halos, while faint, small galaxies are expected to occupy DM halos with progressively lower masses. Importantly, smaller galaxies are predicted to be more numerous in the universe [75]. Therefore, studying the microphysics of DM in low-mass halos is inherently connected to understanding the properties and distribution of the faintest galaxies. Probing the extreme faint end of the galaxy luminosity function thus becomes a valuable approach for studying galaxy distribution and constraining DM models. For instance, a key scientific objective of future large cosmic surveys is to determine how well the population of MW satellites can be used to constrain the minimum DM halo mass necessary for galaxy formation. This minimum halo mass is influenced by factors such as the details of reionization and other forms of baryonic feedback that prevent gas from accreting and cooling in low-mass subhalos [50]. However, it may also indicate a cutoff in the subhalo mass function determined by the particle nature of DM, such as the suppression of the matter power spectrum at small scales.

The discovery and study of ultra-faint dwarf galaxies have expanded significantly in recent years, although our understanding remains incomplete. These galaxies, which contain only a few hundred stars, are primarily detected in the inner regions of the MW. The census of MW dwarf galaxies has increased from ~ 25 to over 50, largely due to large cosmological surveys [76, 77, 78] (e.g., the Dark Energy Camera; see Section 2.5.2). However, a large number of faint galaxies remain undetected, particularly those at greater distances and with even lower luminosities. For instance, the Hyper Suprime-Cam Subaru Strategic Program (HSC-SSP) collaboration identified two ultra-faint galaxy candidates in just the first 300 $\deg^2$ of the survey [79, 80]. These galaxies were too faint and distant to be detected in previous optical surveys, indicating that more comprehensive surveys could drastically increase the sample of galaxies.

Upcoming surveys such as the Legacy Survey of Space and Time (LSST) (see Section 2.5.4) will observe an area 60 times larger than the HSC-SSP footprint with similar depth,

potentially resulting in tens to hundreds of new detections of faint MW satellites [81]. New techniques, such as using correlated phase-space motion of stars [80, 82] and the clustering of variable stars [83], have the potential to expand the sample of ultra-faint galaxies further. Current measurements of MW satellite abundances, luminosity functions, and the radial distribution of MW satellites have already placed competitive constraints on WDM particle masses at the level of 3-4 keV [71, 72]. In the coming years, new measurements from larger surveys will expand the sample of ultra-faint galaxies even more, allowing us to explore alternative DM paradigms.

2.4.2 Stellar Stream Gaps

A recurring theme from the cosmological DM probes described in the previous sections is that probing DM microphysics from the smallest DM halos either requires advances in instrumentation sensitivity to detect the faintest galaxies or the development of new techniques sensitive to these sub-DM structures. The gravitational effects exerted by DM halos, including low-mass ones, remain one of the most valuable tools for studying DM. For instance, fluctuations in the gravitational tidal field can be used to detect subhalos with masses down to $10^{-6} M_{\odot}$ [84]. As previously discussed, gravitational lensing is one of the most sensitive methods available for detecting these subtle gravitational perturbations. However, the search for truly dark, lower-mass subhalos—those without stars—continues.

Stellar streams are long, dynamically cold formations of stars that originate from dwarf galaxies and globular clusters. These streams form gradually as their progenitor systems orbit within the halos of larger host galaxies, with stars being stripped away due to tidal forces [85, 86, 87]. The cold, kinematic nature of these streams—due to adiabatic cooling—results in very low velocity dispersions, typically just a few km/s. This makes them highly sensitive to small perturbations from external gravitational sources, which can significantly alter the structure of the streams. One of the most notable effects of such perturbations is the for-

mation of gaps, regions of lower stellar density, caused by changes in the orbital periods of the stars within the stream [28]. These gaps are often created by interactions with nearby gravitational sources, leading to the natural question: can DM halos act as perturbers and induce the formation of gaps in stellar streams? The answer is that these gaps can serve as forensic tools [28, 29], allowing us to infer the characteristics of these subhalo "flybys" by analyzing the size and distribution of the gaps. By studying the gravitational perturbations, it is possible to statistically infer the population of DM subhalos, which in turn puts to test the observable predictions of different DM models at small scales [88]. I refer the reader to Appendix A for more details on building statistical models to derive observable predictions on the distribution of gap sizes expected from CDM and WDM paradigms.

2.5 Cosmological Surveys

The understanding we have developed about the composition and evolution of the Universe is derived from a wide range of observations across the electromagnetic spectrum, collected by large-scale cosmological experiments [3, 89, 90, 91]. The topics discussed in this chapter have highlighted the importance of cosmological surveys in the study of DM, allowing to further constrain DM properties and rule out models that do not agree with observations. The goal of this section is to briefly outline a few important cosmic surveys that probe the visible to near-infrared (Vis-NIR) portion of the electromagnetic spectrum. In addition to introducing the scientific cases for each survey, I will highlight the instrumentation technologies—such as detectors and cameras—that have enabled groundbreaking scientific contributions. This discussion will serve to motivate the need for improved survey sensitivity, which can be achieved by leveraging current research and development (R&D) efforts in new detector technologies, such as the Skipper CCD.

2.5.1 The Sloan Digital Sky Survey

The Sloan Digital Sky Survey (SDSS), with its first light in May 1998, was described as the "most ambitious digital database on the sky." Using a 2.5m telescope, a large format camera, and multi-fiber spectrographs at Apache Point, New Mexico, SDSS has conducted continuous observations of stars, galaxies, and quasars. SDSS-I imaged over 800 $\deg^2$ of the sky in the *ugriz* filters[4] and obtained spectra for more than 70,000 objects [92]. SDSS-II expanded this effort with a supernova imaging survey and a spectroscopic survey of $\sim 230,000$ MW stars [93, 94].

Currently in its fifth generation, SDSS-V includes 18 data releases and three programs. The MW Mapper studies stellar populations and chemical dynamics, focusing on the MW and Magellanic Clouds in the Vis-NIR regime. The Black Hole Mapper studies black hole growth through time-domain spectroscopy, targeting extragalactic X-ray sources from the eROSITA survey [95]. The Local Volume Mapper (LVM) explores gas emission and energy exchange within the MW and nearby galaxies using ultra-wide-field optical integral field unit (IFU) spectroscopy [96].

SDSS has evolved through advancements in instrumentation and telescopes. Early surveys used 30 Tektronix CCDs[5] and fiber-fed spectrographs with 3800–9200 Å coverage and resolution of 1800 [92]. SDSS-V's LVM, for instance, employs four 16-cm telescopes at Las Campanas Observatory, feeding spectrographs with ~ 4000 resolution and STA4850 detectors featuring 15 μm pixels and $3e^- - 4e^-$ readout noise [97].

2.5.2 The Dark Energy Survey

In Section 2.4.1, the Dark Energy Camera (DECam), a key component of the Dark Energy Survey (DES) [98], was highlighted for its role in increasing the population of dis-

4. *ugriz* filters are sensitive at 3590 Å, 4810 Å, 6230 Å, 7640 Å, and 9060 Å [92].

5. See Chapter 3 for details on Charge-coupled Devices.

covered dwarf galaxies. DES is a photometric survey aimed at characterizing dark energy and DM using DECam on the 4-m. Blanco Telescope in Chile. It imaged 5000 $\deg^2$ in *grizY* filters over six years, completing observations in 2019 [99]. The current Y3 data release covers $\sim$ 4132 $\deg^2$, with the Wide Survey targeting weak lensing, and galaxy clusters. The Supernovae Survey has enabled the discovery of 1635 supernovae in the redshift range $0.10 < z < 1.13$, meeting quality selection criteria sufficient to constrain cosmological parameters. [100, 101, 102].

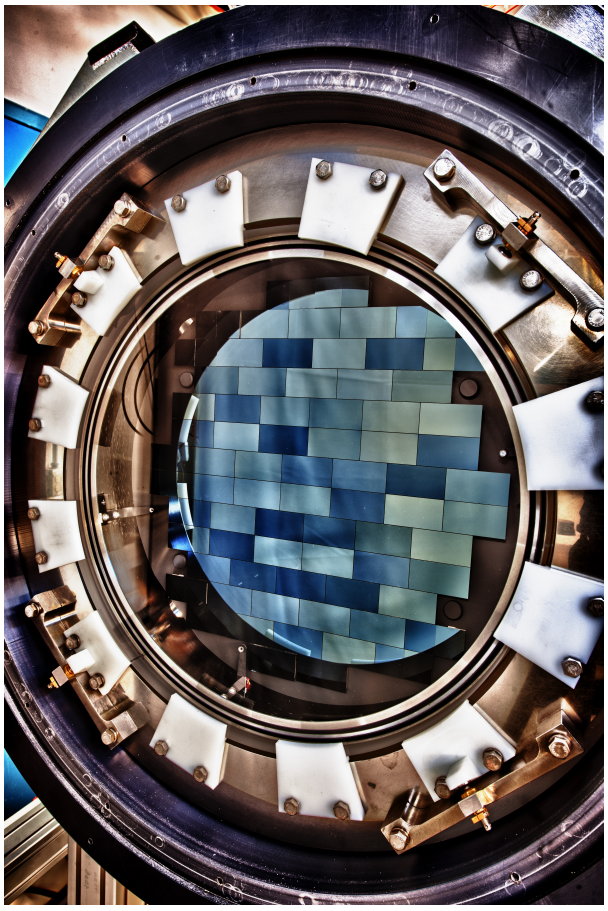

Figure 2.5: The Dark Energy Camera (DECam). The focal plane array is composed of 62, 2k $\times$ 4k CCDs for imaging and 12, 2k $\times$2k CCDs for targeting purposes. Image courtesy of the Dark Energy Survey [4].

DECam, a 570-megapixel camera with a 2.2-degree field-of-view, was designed for high sensitivity in the near-infrared, low readout noise, and excellent image quality to meet the

survey's scientific demands. Its 5-lens optical corrector and filters cover 400–1065 nm. The focal plane (Figure 2.5) includes 62, 2k × 4k CCDs for imaging and 12, 2k × 2k CCDs for guiding and alignment [103].

The DES technical requirements demanded CCDs with low noise, low backgrounds, and high sensitivity to both visible and near-infrared photons. To meet these requirements, Lawrence Berkeley National Laboratory (LBNL) developed back-side illuminated, red-sensitive CCDs [104, 10]. These devices are p-channel CCDs fabricated on high-resistivity n-type substrates. The CCDs are 250 μm thick with 15 μm pixels and are fully-depleted by a 40V substrate voltage. In these CCDs, positively charged holes are collected in the depletion region within buried channels located a few microns below the gate electrodes. To enhance light sensitivity, an anti-reflective coating made from indium-tin oxide and SiO_2 is applied to the back side of each CCD. Each CCD has two serial registers and corresponding output amplifiers, enabling simultaneous readout from both sides. The detectors are read out in $\sim$ 17 seconds with 6-9 electrons RMS readout noise. The packaging of the CCDs, design of the focal plane, and testing and validation of the devices were all performed at Fermi National Accelerator Laboratory (Fermilab) [103].

2.5.3 The Dark Energy Spectroscopic Instrument

The Dark Energy Spectroscopic Instrument (DESI) is a Stage IV spectrograph on the Mayall 4-m. Telescope at Kitt Peak, AZ, designed for a spectroscopic survey of 40 million galaxies and quasars over 14,000 deg^2 in five years [105, 106]. DESI uses 5000 robotic fiber positioners across an 8 deg^2 focal plane, feeding 10 triple-arm spectrographs with 360–980 nm coverage and spectral resolutions of 2000 in the UV and $\gtrsim$ 4000 in the red/infrared bands [107].

DESI aims to trace cosmic expansion to redshift $z = 3.5$ using baryonic acoustic oscillations (BAO) as a standard ruler and to study cosmic structure growth, neutrino masses, primordial density fluctuations, and potential modifications to general relativity [106]. Dur-

ing the Survey Validation phase (completed May 2021), DESI released spectra for ∼1.8 million targets, including MW stars, galaxies, and quasars, covering $\sim 7,500$ deg^2 [91]. Results include a 9.1σ BAO detection at $z = 0.93$ and a combined precision of 0.52%, a 1.2-fold improvement over prior studies [108].

A detailed description of the technical systems that have enabled DESI science can be found here [26]. All DESI spectrographs use 15μm pixel, back-illuminated CCDs. The blue channel devices are 4096 × 4096 STA4150 CCDs developed by STA, with a sensitivity of 75% from 360 nm to 400 nm with a readout noise of 3 e$^-$ rms. The red and NIR spectrograph channels use LBNL thick, fully-depleted devices similar to those employed in DECam. These CCDs are 4114 × 4128 and operate with a readout noise $\lesssim$ 3 e$^-$ rms. Their sensitivity to red wavelengths is excellent, with 85% from 600-900 nm and $\gtrsim$ 60% from 900-980nm. This improved sensitivity, compared to DECam devices, is due to different anti-reflective (AR) coating processes, e.g., higher-index, ZrO_2 multi-layer coating. The Skipper CCDs described later in this work retain this desirable characteristic (see Chapter 5).

2.5.4 The LSST Survey

The Vera C. Rubin Observatory, under construction at Cerro Pachón in Chile, will conduct the 10-year Legacy Survey of Space and Time (LSST) using the Simonyi Survey Telescope. LSST will image 18,000 deg^2 of the Southern Hemisphere in six optical bands (320–1050 nm). The Simonyi Telescope features an 8.4-meter primary-tertiary mirror and a 3.4-m. secondary mirror. The LSST Camera, the observatory's sole instrument, includes a 3.2-gigapixel CCD mosaic, a three-element optical corrector, and an out-of-plane filter exchange mechanism for rapid filter transitions. Its data acquisition system digitizes images in 2 seconds, supporting the survey's rapid imaging pace [81, 109, 110].

The LSST Camera uses n-channel CCDs, 100 μm thick with 10 μm pixels. The science CCD mosaic comprises 189 4k × 4k CCDs, with 8 CCDs for guiding and 4 for wavefront

sensing. Each CCD has 16 segments with independent readouts, enabling low-noise parallel processing for 3024 image frames. Two CCD types are used: Teledyne e2v CCD250 and ITL STA3800C, with $\lesssim 6$ e^- rms noise for most devices, though some amplifiers exhibit higher noise than the 9 e^- rms requirement. This slightly impacts u-band depth but does not affect overall survey goals. CCD light efficiency is comparable to DESI devices, with minor differences between the e2v and ITL CCDs. Camera testing at SLAC National Accelerator Laboratory concluded in March 2024, and the camera was shipped to Rubin Observatory in May 2024. Installation on the Simonyi Survey Telescope is planned for late 2024, with the 10-year LSST survey starting in mid-2025 [110, 111].

2.5.5 Stage 5 Spectroscopic Surveys

A Stage 5 spectroscopic survey represents an evolution of current efforts, such as DESI, aiming to increase the number of observed astronomical objects by probing farther back in time. For example, a Stage 5 survey will measure over 40 million redshifts, enabling unprecedented precision in dark energy measurements. Spectroscopic surveys have exhibited linear growth over time, increasing by an order of magnitude each decade (e.g., Figure 2.6) [5]. Stage 5 surveys continue this trend, facilitating groundbreaking discoveries about cosmic expansion mechanisms and providing more precise constraints on dark matter through Milky Way matter distribution tracers [5, 112].

The MegaMapper is a proposed Stage 5 spectroscopic facility designed to measure inflation parameters and dark energy from galaxy redshifts at $2 < z < 5$. To achieve the scientific breakthroughs expected from a Stage 5 survey, MegaMapper would leverage existing technologies—such as spectrograph designs from DESI and SDSS-V—while introducing innovations in other areas, like fiber positioners, to maximize cost effectiveness [112]. MegaMapper would feature a 6.5-meter telescope, similar to the Magellan telescopes, equipped with DESI-like spectrographs but with an increased number of fibers, expanding from 500 to $\gtrsim 600$ fibers

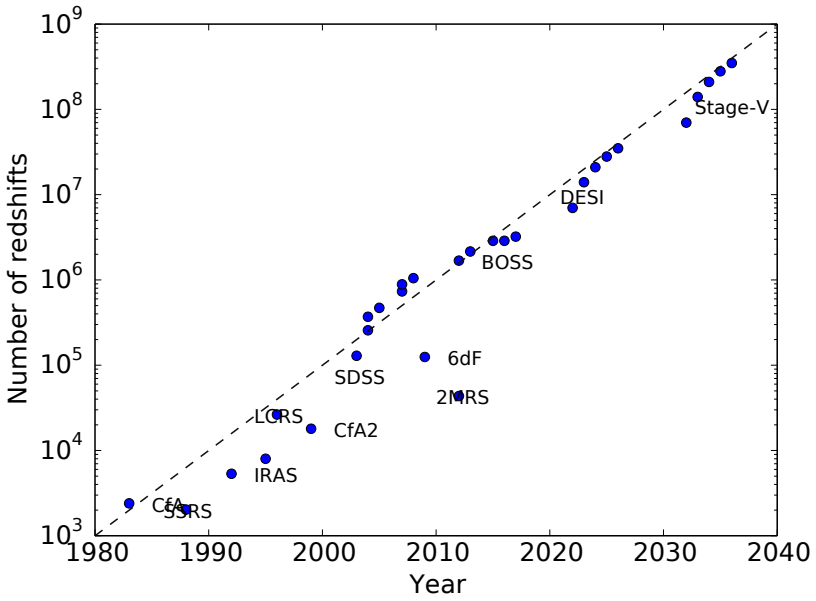

Figure 2.6: Number of galaxy redshifts as a function of time for the largest cosmological surveys. Stage 5 spectroscopic surveys maintain this trend into the 2030s. Figure adapted from [5].

per spectrograph. These improvements, combined with the telescope's increased mirror collecting area, would result in a 15-fold increase in survey speed compared to current-generation facilities [113].

A key characteristic of Stage 5 spectroscopic surveys is their focus on observing more distant objects, bolstering high-redshift datasets to measure cosmological conditions in the early universe. This requirement places strong demands on the technological capabilities of Stage 5 surveys: the survey must be sensitive to these distant, faint objects, capable of achieving sufficient signal-to-noise to measure critical spectral features, e.g., the Lyman-alpha (Ly-α) forest from high-redshift quasars. As outlined throughout this section, a crucial factor in achieving high survey sensitivity is the detector technology. Currently, early stages of Stage 5 survey planning are exploring potential ultra-low noise detectors with sub-electron readout noise and even sensitivity to individual photons. From this point onward, I will focus on describing the efforts to develop and demonstrate this technology for astronomical measurements in preparation for future large cosmological surveys.

CHAPTER 3

CCDS AND ULTRA-LOW NOISE SKIPPER CCDS

In this chapter, I discuss the fundamental concepts of charge-coupled devices (CCDs) and ultra-low noise Skipper CCDs, with an emphasis on devices optimized for astronomical measurements. I begin by outlining the basic operational and architectural principles of CCDs, including the mechanisms of charge generation, storage, transfer and readout. Following the overview of CCDs, I introduce the concept of the Skipper CCD, a novel device capable of making precise measurements of the charge in each pixel by performing multiple non-destructive reads. The operational performance of the CCD and Skipper CCD technology is compared, highlighting their shared astronomical capabilities while emphasizing how Skipper CCDs outperform conventional scientific CCDs in charge detection sensitivity. Finally, I introduce astronomical CCD fabrication and configuration schemes (e.g., backside-illuminated and full depletion CCDs) that enable high light sensitivity performance in an ample wavelength range.

3.1 CCDs

The CCD was invented in 1969 by Willard S. Boyle and George E. Smith at Bell Telephone Laboratories [114]. The invention was inspired by pre-existing technologies: the magnetic bubble memory, the silicon diode array camera tube, and the metal-oxide-semiconductor (MOS) transistor. The latter becoming an essential component in making a cohesive, functional device. As George E. Smith recalls [115], the basic functional design of the CCD was brainstormed on a backboard in less than one hour. The device would use closely placed MOS capacitors, where each capacitor not only stores charge but also allows for the manipulation of that charge by transferring it between capacitors. To achieve this, a sequence of capacitors is arranged so that, for example, when one capacitor holds a charge and the

adjacent one is empty, applying a more attractive voltage to the empty capacitor causes its depletion region to overlap with the first, allowing the charge to flow from one to the other. The original design, which employed a three-phase voltage source to facilitate the charge transfer, remains a fundamental principle in modern CCDs (e.g., [104]).

3.1.1 Charge Generation and the p-n Junction

Central to the operation of CCDs is the charge generation process, which relies on the photoelectric effect. When photons interact with the bulk material of the CCD, typically silicon, they generate electron-hole (e-h) pairs. The efficiency of this process is quantified by the quantum efficiency (QE), which represents the fraction of incident photons that produce a detectable charge in the silicon (for a detailed discussion on QE, see Section 5.6.6). The charge generation by interacting photons is highly dependent on the properties of the semiconductor material [7, 116].

Semiconductors, such as silicon, exhibit a unique property of transitioning between insulating and conductive states depending on temperature or external energy inputs, such as photon absorption. At low temperatures, semiconductors act as insulators because their energy bands are either completely filled (valence band) or completely empty (conduction band). Conduction requires the presence of partially filled bands, which is absent at $T = 0$ K. The band gap is the energy difference between the top of the valence band (highest filled energy level) and the bottom of the conduction band (lowest empty energy level). This energy gap represents the minimum energy required to excite an electron from the valence band to the conduction band. When sufficient energy is provided—either thermally or by absorbing photons—electrons are promoted to the conduction band, leaving behind holes in the valence band. These electrons and holes act as charge carriers, enabling conduction within the semiconductor material [116].

In the case of silicon, which behaves as an insulator at $T = 0$ K but has a relatively

small band gap (∼1.14 eV), photons with energies > 1.14 eV can excite electrons from the valence band to the conduction band, generating a detectable charge. Photons below < 1.4 eV, such as those in the far-infrared, pass through the silicon without interacting, as the material is transparent to them. However, some of these low-energy photons may still interact through a process called free-carrier absorption, though this does not generate usable signal carriers. Photons with energies $1.1 - 3.1$ eV (400-1100 nm) will produce a single e-h pair. For astronomical measurements, this range covers the Vis-NIR regime. In contrast, photons with energies > 3.1 eV can generate multiple e-h pairs when the energetic conduction band electron collides with other valence electrons. The average number of electrons generated for a photon with energy $E(eV) > 10$ eV is [7]

$$\eta_i = \frac{E(eV)}{E_{e-h}} \tag{3.1}$$

where η_i is the ratio between electrons and incident photons, i.e., the quantum yield and E_{e-h} is the energy required to generate a single e-h pair.

In a CCD, precise control over doping levels during manufacturing is essential for creating key structures that enable the storage and manipulation of the generated charge. One of the most critical components is the p-n junction, which is formed by doping different regions of the semiconductor with acceptor atoms (to create a p-type region rich in holes) and donor atoms (to create an n-type region rich in electrons). When the p-type and n-type regions are brought together, they naturally reach thermal equilibrium. During this process, free electrons from the n-type region diffuse into the p-type region, where they combine with holes. This diffusion leaves behind immobile, positively charged donor ions in the n-type region and negatively charged acceptor ions in the p-type region. As a result, a depletion region forms at the interface, which is devoid of free charge carriers (i.e., electrons and holes). Although the overall material remains electrically neutral, the depletion region generates an internal electric field. This field points from the positively charged n-type side (where donor

ions remain) to the negatively charged p-type side (where acceptor ions are located). The internal electric field of the depletion region plays a key role in CCD operation, as it acts like a diode: it allows charge carriers to move across the junction in only one direction, preventing unwanted recombination of electrons and holes [7, 117].

3.1.2 The MOS Capacitor and the Pixel

The MOS capacitor in a CCD plays a critical role in the device's operation by serving as the primary component for information storage—specifically, the storage of photoelectrons. The MOS structure is composed of three layers: the semiconductor (typically silicon), an insulating oxide layer, usually silicon dioxide (SiO_2), and a conductive layer that forms the "metal" contact (though in practice, for CCDs highly doped polysilicon is often used instead of metal), e.g., Figure 3.1.

To create a MOS structure, a thin layer of SiO_2 is grown on top of the silicon substrate through thermal oxidation. This process involves exposing the silicon to an oxygen-rich environment at high temperatures (around 1000°C). The duration of this exposure determines the thickness of the oxide layer, which acts as the insulating layer in the MOS structure. Polysilicon (heavily doped to ensure sufficient electrical conductivity) is deposited on top of the oxide layer. When a voltage is applied to the polysilicon gate, it creates an electric field across the SiO_2 and into the underlying silicon substrate. This electric field induces a depletion region beneath the SiO_2/Si interface [7]. Similar to the depletion region in a p-n junction, this area is devoid of free charge carriers (electrons and holes), leaving behind ionized dopants. The depletion region expands into the semiconductor as the voltage increases, creating a zone where charge can be collected and stored.

The notion of a pixel structure in a CCD becomes clear as we incorporate the MOS capacitor, which acts as a potential well for storing charge. Based on the basic structure of the MOS, the p-type buried channel is introduced to enhance efficiency of charge collection

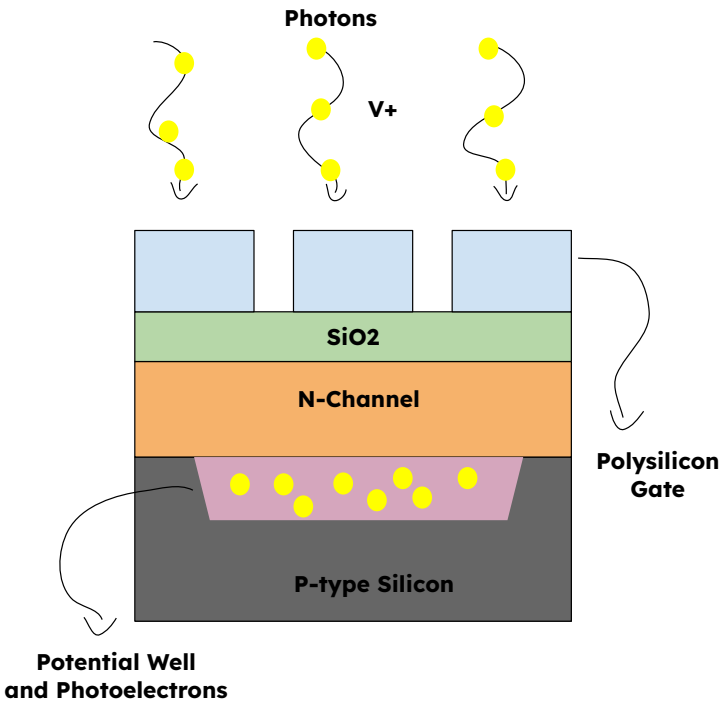

Figure 3.1: Light sensitive CCD MOS capacitor. The MOS capacitor has three components. The electrode (or gate) made from polysilicon, which serves as the conductive layer to apply an electric field across the insulating layer to control the movement and storage of charge in the silicon substrate beneath. The insulating film, which is made up of SiO_2, prevents direct current flow between the gate and the substrate while allowing the modulation of charge carriers within the substrate via the electric field. The silicon substrate serves as the photosensitive region of the CCD where e-h pairs are generated, and subsequently manipulated through the electric field applied via the gate. Note that the thickness between regions are not to scale. Diagram based on Figure 2.1 from [6].

and transfer. This buried channel is created by doping the surface of the silicon with p-type impurities, while maintaining an p-type bulk substrate beneath. The buried channel provides a region where charges can accumulate and move efficiently while keeping them away from the SiO_2/Si interface. This design is crucial because the SiO_2/Si interface often contains defects and energy states that can trap charges, potentially degrading the CCD's charge transfer efficiency (CTE). In parallel, channel-stops are implemented as heavily doped n-type regions located between the pixel columns, running beneath the SiO_2 layer. These channel-stops create a depletion region that serves to electrically isolate adjacent pixels by repelling mobile charges that might otherwise spill over into neighboring columns [7]. Together, the buried

channel and the channel-stops define the physical boundaries and operational independence of each pixel.

3.1.3 Charge Transfer

With the concepts of the MOS capacitor and the CCD pixel structure established, we can now explore the process of charge manipulation in a CCD, i.e., charge transfer. The charges generated and accumulated in the potential wells of the CCD's photosensitive area are transferred vertically, pixel by pixel, by changing the voltages in a specific sequence. This process is particularly well illustrated in the operation of a 3-phase CCD, a common architecture for charge transfer. In a 3-phase CCD, each pixel is associated with three closely spaced polysilicon gate electrodes, referred to as phases. These gates are connected to independent clock lines, each driven by an external clock signal that modulates the voltage levels on each gate in a specific sequence.

Consider Figure 3.2 which illustrates the process of charge transfer in one of the CCDs described later (see Chapter 5). After a complete vertical transfer, the charges generated in the top row are stored beneath the pixels in the horizontal register or serial register, which uses three independent horizontal clocks (H_1, H_2 and H_3) to move the charge packets to the output stage. At $t = 0$, H_1 is kept in the raised voltage sate while H_2 is lowered, causing the charge to flow to the lower potential, where it remains trapped in the potential well created by H_1, with H_3 serving as a barrier. At $t = 1$, H_3 is lowered and thus the charge is free to flow to a new phase where at $t = 2$, H_2 is raised, preventing the charge from flowing back. The summing well (SW) remains at a lower potential than H_3, causing the charge to move further down into the SW. From $t = 3$ to $t = 12$, this sequence of raising and lowering voltages is repeated to continue moving the charge along the serial register toward the output gate (OG). Once the charge reaches the output gate, it is measured. After the charge is processed, it is passed to the drain gate (DG), where it is discarded to prepare the

register for the next set of charges.

Figure 3.2 not only illustrates the process of moving the charge to the output stage but also highlights two important components of CCD readout: the sequence and voltage parameters. The charge transfer diagram depicts the processes of moving charge packets as outlined by the sequencer. In a sequencer, the user can define specific instructions for how the charge packets will be moved within the CCD, including the timing for each phase of the transfer. For more details on sequencers, see Chapter 6. Equally important are the voltage parameters, which play a crucial role in the efficient transfer of charge from one phase to another, i.e., CTE. These voltages must be carefully optimized to ensure that charge is moved effectively through the CCD while preserving critical voltage-dependent characteristics e.g., full-well capacity (see Chapter 5).

3.1.4 Charge Measurement

Once the charge packets are moved to the serial register, they are transferred to the SW via the horizontal clocks (H_1, H_2 and H_3) and finally to the sense node (SN), where the charge is measured. The SN is a small capacitor connected to an output MOSFET at the end of the horizontal register. The output amplifier generates a voltage proportional to the signal charge for each pixel. Figure 3.3 shows the electronic design of the output stage for a conventional CCD, which consists of two MOSFET transistors (M1 and MR) connected by the SN [7]. The sensitivity of the output amplifier is defined as

$$S_V = \frac{q}{C_s} \tag{3.2}$$

where S_V is given in $(\frac{V}{e^-})$ and C_s is the sense capacitance, which includes both the capacitance associated with the output MOSFET and neighboring parasitic capacitances [7]. It is clear that reducing the capacitance of the amplifier will increase its sensitivity—i.e., the smaller the capacitance, the higher the amplifier's gain, resulting in a greater output signal.

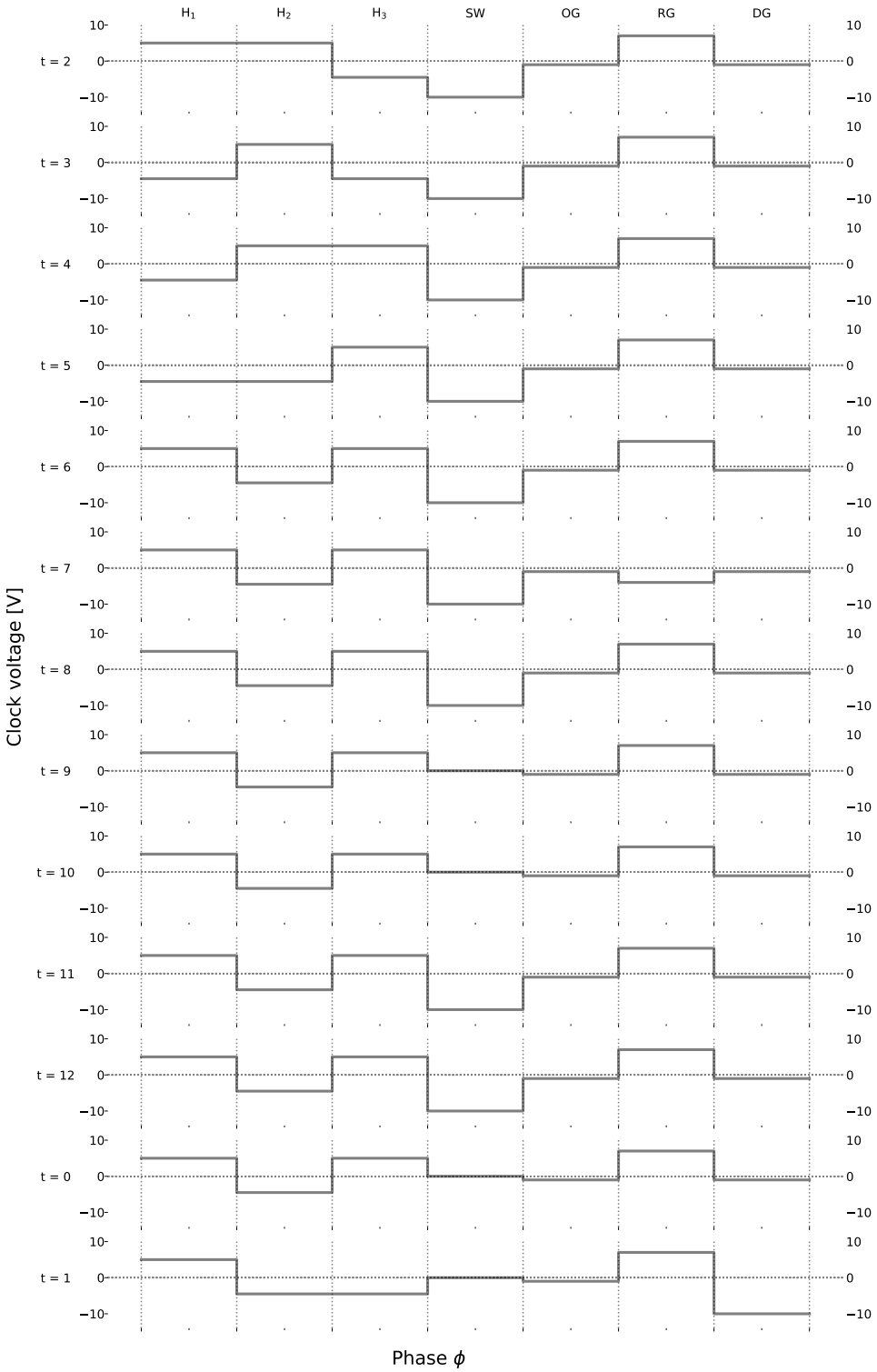

Figure 3.2: Charge transfer diagram for a non-Skipper readout configuration.

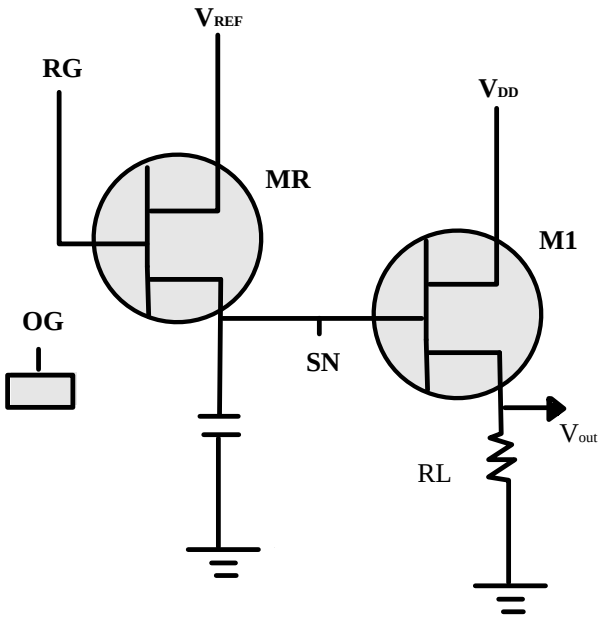

Figure 3.3: Electronic diagram of the output stage for a conventional CCD. Figure based on Figure 6.2 in [7].

In addition to increasing CCD sensitivity by optimizing the output amplifier capacitance, reducing the noise associated with reading out the CCD pixel array is critical in CCD R&D. Noise rms fluctuations inhibit the ability to make precise measurements of charge packets, limiting the sensitivity of the device. For instance, in conventional CCDs, noise levels make it impossible to distinguish single photoelectrons. The essential CCD operations of generating, collecting, and transferring charge are mostly noiseless processes [7]. However, the output amplifier can add a considerable amount of noise to the charge packet measured during readout. To reduce noise in the readout process, particularly low-frequency noise ($1/f$), the correlated double sampling (CDS) technique is implemented in CCD readout. CDS is an integration method that relies on the assumption that most of the noise is white and Gaussian and thus the noise reduction is proportional to to the square root of the integration time. During readout the pixel value is determined by [118]:

$$P_i = \frac{1}{t_i}\left(\int_{t_i+\tau}^{2t_i+\tau} x(t)dt - \int_0^{t_i} x(t)dt\right) \tag{3.3}$$

where P_i is the final pixel value, τ is the time spent to transfer the charge to the SN after the reset pulse (see Fig. 3.4) has been applied, and t_i is the integration time.

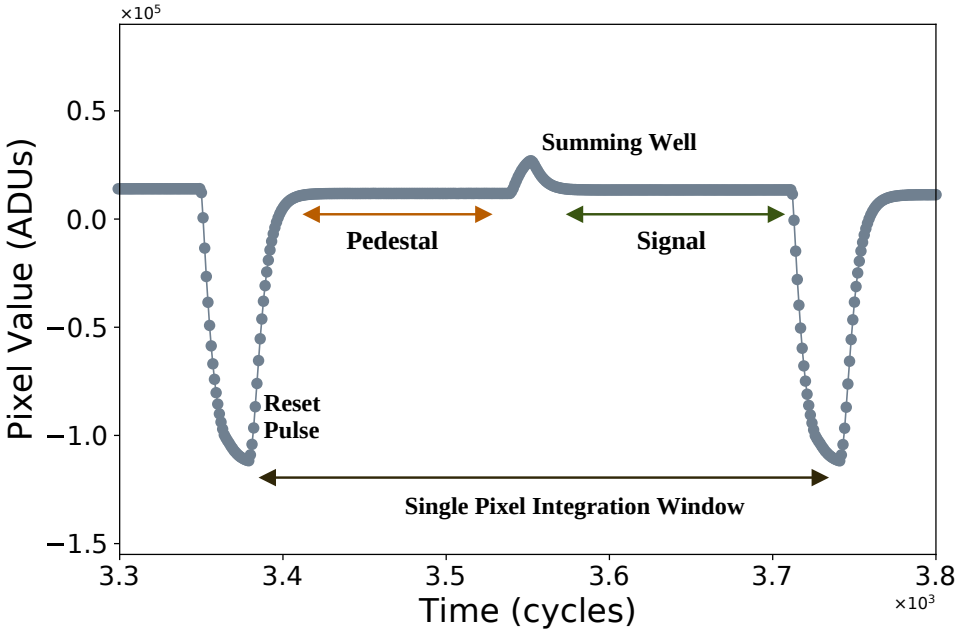

Figure 3.4: The raw pixel value in ADUs, measured at the SN, as a function of time for one of the Skipper CCDs tested at Fermilab. The signal in between both reset pulses define the components from which a single pixel value is determined. The pedestal value is measured after the RG pulse, and the signal is measured after the SW pulse. The final pixel value is determined by subtracting the pedestal integrated samples from the signal, i.e., CDS.

Figure 3.4 shows a CCD output amplifier video signal, from which a pixel value is determined using CDS. The process begins with a pulse sent from the reset gate (RG in Figures 3.2 and 3.3) to establish a reference voltage at the SN. This reference voltage is sensed through the source of the transistor M1, [1] resulting in in V_{out}. This reference voltage measurement is called the pedestal and it is measured for a period of time, t_i, i.e., the second integral in Eqn. 3.3. Next, the charge packets are transferred from OG to the SN, and the voltage is

1. M1 is configured in source follower mode.

measured again for the same period of time, t_i. This second measurement includes both the pedestal and the signal generated by the charge present in that pixel, i.e., the first integral in Eqn. 3.3. By subtracting the pedestal from the signal measurement, the result is proportional to the number of electrons stored in the SN, which corresponds to the pixel value (P_i). After the signal is measured, the charge packet is discarded when a new RG pulse is sent to the SN, repeating the process for each pixel in the serial register until the entire array is read out. By integrating the pedestal and signal components, correlated noise sources (e.g., $1/f$ noise and reset noise) are capture and effectively cancel out during signal-pedestal subtraction, reducing the readout noise [119].

Modern scientific CCDs have made significant advancements in design and readout techniques, reaching readout noise levels $\lesssim 2$ e$^-$ rms. For example, the DESI detectors underwent developmental changes, including the addition of a buried contact, which provides a direct connection between the SN and the polysilicon gate electrode of the source-follower transistor. This buried-contact technology, with its more compact design, reduces the capacitance at the SN, resulting in noise levels as low as 1.7 e$^-$ rms [120]. Such design improvements, coupled with low-noise readout techniques like CDS, have significantly enhanced the sensitivity of CCDs. While modern devices have pushed the noise down to levels approaching single-electron precision, low-frequency noise remains a significant limitation. This $1/f$ noise, typically generated by the output transistor, couples to the video signal preventing conventional CCDs to achieve the sensitivity to count individual photoelectrons and thus being sensitive to the faintest signals.

3.2 The Skipper CCD

The Skipper CCD is an ultra-low noise, photon-counting capable CCD that offers a significant advantage over conventional CCDs by enabling multiple non-destructive reads of the charge in each pixel. This unique feature allows the Skipper CCD to significantly reduce readout

noise, particularly $1/f$ noise. By performing multiple reads of the same pixel and averaging the results, the Skipper CCD can achieve sub-electron noise levels, effectively allowing for precise charge detection, even at the single-photon level. The Skipper CCD concept as a photosensitive detector was proposed in 1990 by Janesick and Chandler [121, 122]; however, in early demonstrations of this technology, the readout noise improvement deviated from the theoretical expectation at ~ 0.5 e^- rms/pixel after 512 measurements per pixel [121]. Additional measurements did not yield further noise improvements, implying that systematic noise effects were preventing single photon-counting [121, 24]. In contrast, modern Skipper CCDs have achieved an order of magnitude lower readout noise and stable performance over a large area detector [8]. This section introduces the Skipper CCD, outlining its key architectural differences compared to conventional scientific CCDs and describing its basic operating principles. I will explain how the Skipper capabilities lead to ultra-low noise characteristics, enabling single-electron sensitivity and how these attributes can be leveraged to improve the precision of astronomical measurements. The discussion in this chapter serves as motivation for the central theme of this thesis: demonstrating the Skipper CCD technology in astronomical observations for the first time.

3.2.1 Skipper CCD Architecture

In a Skipper CCD, the overall structure and functions are similar to conventional CCDs, particularly in terms of how charge is collected stored, and transferred from the Si photosensitive region to the serial register. The major difference in the Skipper CCD lies in the design of the output stage. A conventional CCD uses a floating diffusion gate architecture while the Skipper CCD uses a floating gate. The concept of the floating gate design, to perform non-destructive charge measurements, for a CCD was first described by David Wen in 1974 [123]. Nevertheless, modern Skipper CCDs implement the floating gate design proposed by Janesick [121], which electronic schematic is similar to Figure 3.5 (Top). In this case, M1

is a floating gate and it is separated from the SiO_2 channel, which transfers the charge. The floating gate is electrically isolated, surrounded by highly restive materials. The MR transistor allows for charging the floating gate directly and set M1's operation state.

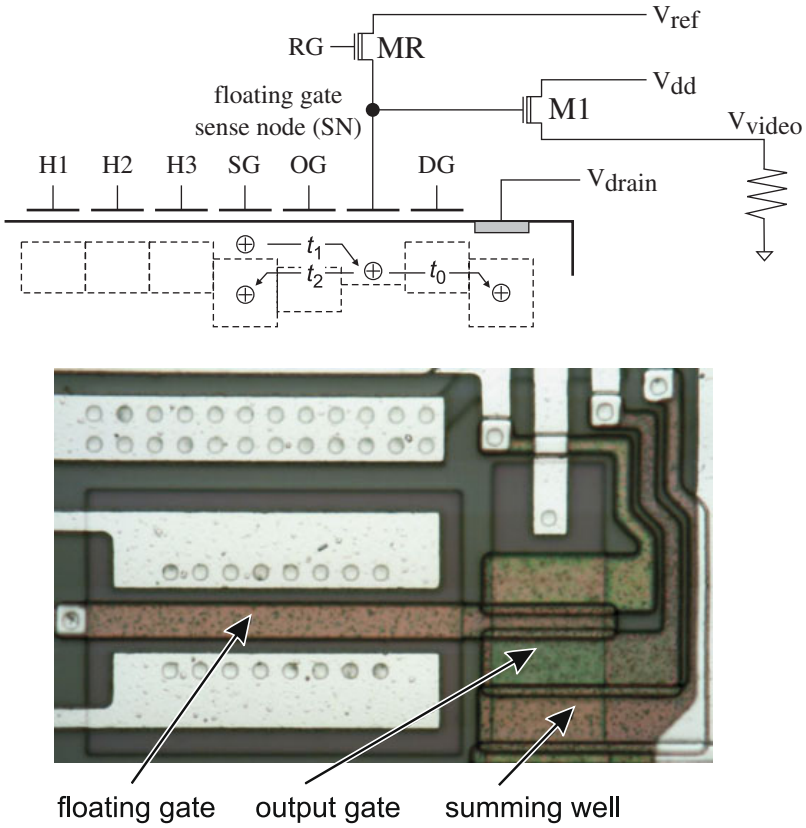

Figure 3.5: Top: diagram of the Skipper CCD output stage. As in conventional CCDs, H_1, H_2, H_3 are the serial-register clock phases that transfer the charge to the summing well, in this case SG. MR resets the SN to V_{ref} after a pixel read. M1 is the MOSFET in source follower configuration. For a Skipper, the SN is a floating amplifier, allowing for multiple, nondestructive measurements of the charge at SN. Image extracted from [8]. Bottom: Photograph of the out stage layout of a Skipper CCD. Image extracted from [9].

As we discussed in the previous section, in a conventional CCD, after the charge has been measured by the SN, RG is triggered, and SN is set to V_{REF} (see Figure 3.3) destructively flushing out the charge, and readying SN for the next charge measurement. In the Skipper case, however, the floating SN is treated as another gate. When charge is transferred from the serial register to the region under the floating gate, it does not come into direct contact

with the measurement node. Instead, the charge electrostatically induces a potential on the floating gate, which modulates the behavior of the output amplifier. This induced potential allows the charge to influence the output signal indirectly, facilitating the readout process. Since the charge is not physically drained or altered during the measurement, the surrounding gate potentials can be adjusted to drive the charge back out from under the floating gate, repeating the process N_{samp} times, thereby, allowing noise reduction through averaging.

To manage the flow of charge through the floating gate, the Skipper CCD introduces a few additional components: the dump gate (DG) and the drain potential (V_{drain}). DG is used to clear out the charge after the measurement is complete. V_{drain}, then, represents the potential that is applied to discard the charge. After the charge is cleared, the floating gate must be reset via RG to a nominal potential (V_{ref}) to prepare for the next cycle of charge measurement. Figure 3.5 (Bottom) shows the micrograph of the output stage of a Skipper CCD where various components, including the floating gate, are highlighted.

3.2.2 Skipper CCD Operating Principles

A defining operational feature of Skipper CCDs is the capability for non-destructive charge measurement, which allows repeatedly measuring the charge in the same pixel without disturbing the stored charge. For any given pixel, the measurement during the $i-th$ readout consists of the true charge (C), representing the actual number of electrons collected in the pixel, and a Gaussian noise component ($Gauss(0, \sigma_{pix})$ with a mean of 0 and a standard deviation σ_{pix}, which is the random noise introduced during the readout process (i.e., the detector noise that couples to the video signal). Thus, the measurement of the $i-th$ readout can be expressed as $P_i = C + Gauss(0, \sigma_{pix}) = Gauss(C, \sigma_{pix})$.

By reading the same pixel N_{samp} times and averaging the results, the contribution of the noise to the final measurement can be reduced. Since the noise is uncorrelated for each measurement, the variance of the averaged result decreases by a factor of N_{samp}. Mathematically,

this can be expressed as:

$$
\begin{aligned}
\bar{P} &= \frac{1}{N_{\text{samp}}^2} \sum_{i=1}^{N_{\text{samp}}} P_i \\
Var(\bar{P}) &= \frac{1}{N_{\text{samp}}^2} \sum_{i=1}^{N_{\text{samp}}} Var(\bar{P}_i) \\
Var(\bar{P}) &= \frac{1}{N_{\text{samp}}^2} N_{\text{samp}} \sigma_{pix} \rightarrow \frac{\sigma_{pix}^2}{N_{\text{samp}}} \\
\sigma_{\bar{P}} &= \frac{\sigma_{pix}}{\sqrt{N_{\text{samp}}}}.
\end{aligned}
\tag{3.4}
$$

The readout noise is reduced by a factor of $1/\sqrt{(N_{\text{samp}})}$, allowing the noise level to be tuned by adjusting N_{samp} [8]. This enables the possibility of achieving sub-electron readout noise and even single-photon counting.

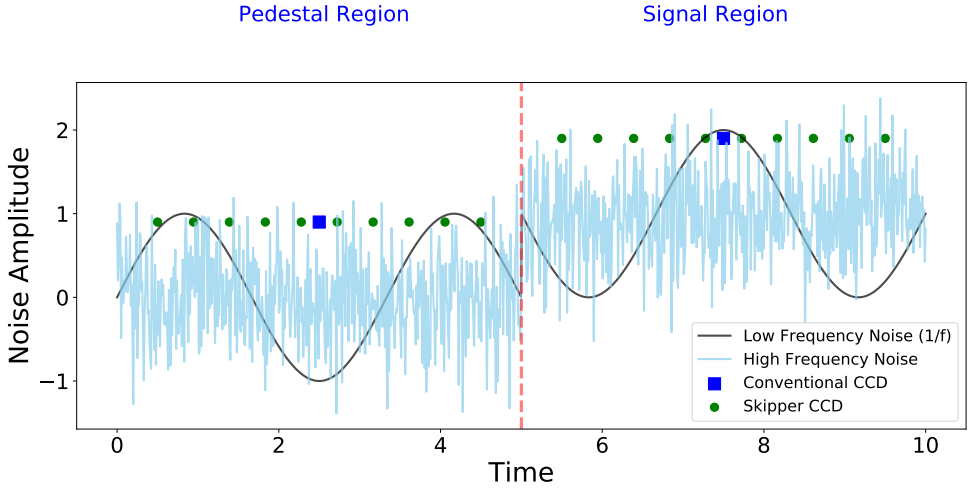

Figure 3.6: Comparison of electronic noise contributions, coupled to the video signal, during pixel readout for conventional and Skipper CCDs. Both high-frequency Gaussian noise (light blue) and low-frequency $1/f$ noise (black) are shown. In the Skipper CCD, the noise profile is sampled 10 times per pixel (green dots), while the conventional CCD takes only a single sample (blue square). This multiple sampling in the Skipper CCD captures the complete $1/f$ noise profile in both the pedestal and signal regions, enabling more accurate noise cancellation during signal-pedestal subtraction.

To gain insight for how the Skipper CCD overcomes the $1/f$ noise barrier through multi-

sample averaging, let us revisit the concept of CDS. Similar to Eqn. 3.3, the pixel value from a Skipper readout is given by:

$$P_i = \frac{1}{N_{\text{samp}}} \sum_{t_i}^{N_{\text{samp}}-1} \frac{1}{t_i} \left(\int_{t_i+\tau+t_j}^{2t_i+\tau+t_j} x(t)dt - \int_{t_j}^{t_i+t_j} x(t)dt \right) \tag{3.5}$$

where t_j is is the initial time of each measurement of the pixel charge. One of the key insights from the Skipper CCD's readout mechanism is the trade-off between readout time and achieving low noise. Increasing the number of samples reduces the noise in the final measurement, but it also extends the total readout time. Optimizing this balance is essential for applications where fast readout times are required (see Section 5.4 for details on readout time optimization). Additionally, the Skipper CCD's multi-sampling strategy allows it to average over a wide range of frequency domains, capturing both high-frequency noise and, more importantly, $1/f$ noise.

Figure 3.6 provides a qualitative schematic for how the Skipper CCD's multi-sampling technique effectively mitigates the effects of low-frequency noise. In conventional CCD readout, a single pedestal-signal measurement may not capture a full cycle of the low-frequency noise, leading to uneven noise contributions between the pedestal and signal readings. In contrast, Skipper sampling over the pedestal and signal regimes significantly improve noise cancellation. The repeated sampling allows for averaging over several cycles of the low-frequency noise, effectively neutralizing the noise contributions. As the noise fluctuates over time, the noise measured in one pedestal-signal pair is counteracted by subsequent measurements, resulting in a reduction of readout noise as all the samples are averaged.

Modern advancements in Skipper CCD R&D have led to unprecedented reduction in readout noise for large-format devices, e.g., achieving noise levels < 0.4 e^- rms/pixel in Skipper CCDs with ~ 5.5 Mpixels [118]. The capability for single-photon counting in this ultra-low noise regime—where the probability of misestimating the charge per pixel by more than 0.5 e^- is $p \sim 10^{-13}$—was first demonstrated by Tiffenberg et al. (2017). In this work,

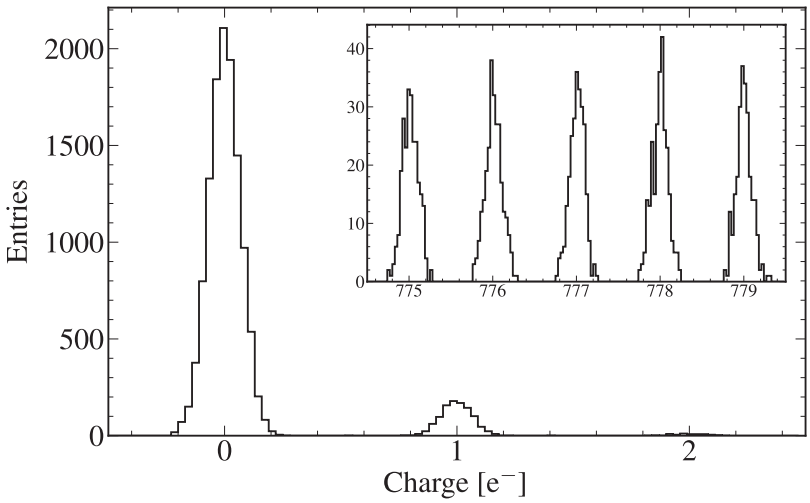

Figure 3.7: First accurate electron-counting demonstration on a large format silicon CCD by Tiffenberg et al. (2017). The individual Gaussians represent the electron counts from the detector's pixels. Integer electron peaks can be distinctly resolved from 0 e^- (empty pixels) to the 779th electron peak. The readout noise was measured at $0th$ electron peak by fitting a Gaussian and calculating the standard deviation, $\sigma_{0e^-} = 0.068$ e^- rms/pixel. This noise level corresponds to $N_{\text{samp}} = 4000$. Image extracted from [8].

Tiffenberg et al. showed that Skipper CCDs designed at LBNL, fabricated by Teledyne DALSA, and packaged at Fermilab could implement a floating gate output stage, a small-capacitance sense node, and isolation from parasitic noise sources to perform thousands of independent, non-destructive measurements of the charge in a pixel. This architecture allows for the drastic reduction of low-frequency readout noise, and the device achieved a readout noise of 0.068 e^- rms/pixel, demonstrating the first accurate single-electron counting on a large-format (4126 × 866 pixels) silicon detector (see Figure 3.7).

3.2.3 Fully-Depleted, Back-Illuminated Skipper CCDs

The key advantage of the Skipper CCD over conventional scientific CCDs lies in its ability to tune the readout noise to achieve sub-electron noise levels. However, for astronomical applications, it is crucial that Skipper CCDs not only provide this ultra-low noise capability but also match or exceed the performance of conventional CCDs when measuring photons

from astronomical objects. To this end, it is important to experimentally validate that the Skipper CCD's unique output stage—designed for ultra-low readout—does not, in any way, affect other detector characteristics that are desirable in astronomy. For example, characterizing detector linearity at all signal levels (from photon-counting to thousands of electrons) can indicate variations in the floating-gate response as a function of signal. Moreover, understanding the connection between V_{ref} and the detector's signal saturation is critical for increasing the full-well capacity.

The highest light sensitivity that can be achieved by a CCD is accomplished by removing the substrate-layer to allow direct illumination on the epitaxial layer from the back-side of the device. This back-side illumination technique allows to bypass the CCD gate-structure, resulting in the highest QE possible [7]. Therefore, development of CCD detectors for astronomical telescopes such as the DECam and DESI devices are thinned and back-illuminated to enhance QE, especially in the blue. Thinning reduces the thickness of the CCD, which is necessary because the low-resistivity silicon used in CCD fabrication limits the depth of the depletion region—the region where charge carriers are collected. A shallow depletion region can lead to the formation of field-free regions, which degrade spatial resolution. To address this, scientific CCDs are typically thinned to about 20 μm [104, 10].

However, this thinning process introduces challenges in the red and near-infrared regions. Silicon's absorption length increases rapidly at longer wavelengths (red/NIR). As a result, thinned CCDs exhibit lower QE at these wavelengths. LBNL CCDs overcome this limitations by using high-resistivity silicon substrates, which allows for a much ticker depleted region. This extended depletion depth enables better photon capture in the red and NIR regions, achieving high QE across the entire wavelength spectrum, including the extended red response. CCDs with QE$>$ 50% in the near-infrared are critical for observations of high-redshift ($z > 1$) galaxies, a key requirement for DES cosmology. [10, 99, 104].

The LBNL-designed Skipper CCDs describe in this work retain the astronomical per-

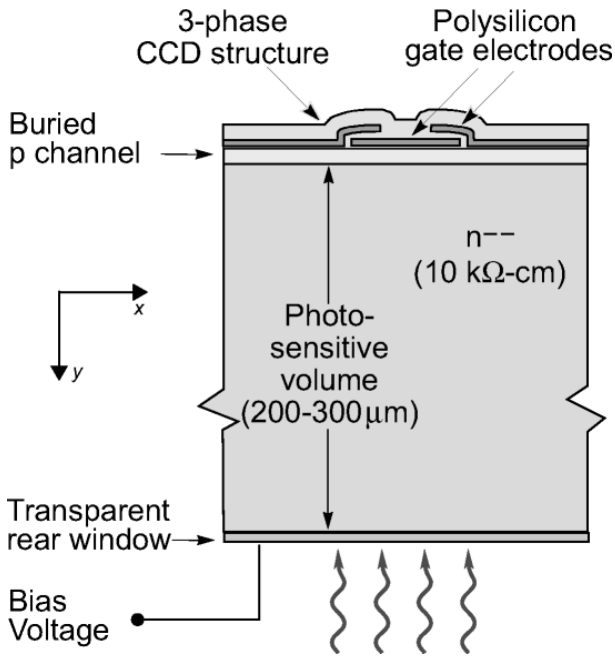

Figure 3.8: Diagram of the cross-section of a fully-depleted, backside-illuminated LBNL-designed CCD. DECam CCDs, DESI CCDs, and the Skipper devices in this work follow this design. The Skipper differs from the other two devices only on the output-stage which does not affect light-sensitivity performance. Image extracted from [10].

formance of other fully-depleted, back-illuminated LBNL CCDS (e.g., DECAm and DESI devices). These devices are conventional three-phase, triple polysilicon gate CCDs with a buried channel, fabricated on a high-resistivity (> 10 KΩcm) n-type silicon substrate (see Figure 3.8). The high resistivity of the substrate results in a low donor density of ($\sim 10^{-11}$) cm^{-3}, allowing the device to be fully depleted with a relatively low bias potential of around 40V. Fully depleted, back-illuminated operation is achieved by applying a bias voltage to an ohmic contact on the wafer's backside. This contact consists of a thin, in situ doped poly-crystalline silicon layer, capped by indium tin oxide (ITO) and SiO_2. The thin contact layer enables a strong response to short wavelengths, while the large depleted thickness of the silicon substrate provides excellent sensitivity to near-infrared light. As a result, fully-depleted, backside-illuminated CCDs maintain a high QE across a broad range of wavelengths [104, 10].

CHAPTER 4

SKIPPER CCDS ON THE SKY: MOTIVATIONS AND FOCAL PLANE CONSTRUCTION

In Section 2.5.5, we discussed the aims of future, Stage 5 cosmological surveys to significantly increase the catalog of high-redshift quasars and emission line galaxies as well as the number of MW faint objects (dwarf galaxies). By probing deeper into the universe and identifying the faintest objects, these surveys will provide more precise measurements of large and small-scale structure, improving constraints on cosmic expansion and refining DM models (see Section 2.5). As I have alluded, a critical component of achieving these objectives is the development of detector technology that maximizes signal-to-noise (S/N) in the readout noise-dominated regime. Therefore, advancing such technology is a priority. For instance, plans to upgrade DESI (see Section 2.5.3) include the development of Skipper CCDs. Here, I focus on our efforts to develop astronomy-optimized Skipper CCDs specifically for astronomical spectroscopy applications.

Astronomical spectrographs disperse light over a large detector area. For faint astronomical sources, this results in low signal-to-noise in each detector pixel. In the low-signal-to-noise regime, detector readout noise can be an important contribution to the overall noise in an observation, affecting the sensitivity of spectroscopic measurements. Skipper CCDs offer tuneable readout noise, potentially increasing S/N for these low-light observations. In particular, medium to high resolution spectroscopy at blue wavelengths has low sky-background levels and significant gains could be achieved by reducing the readout noise to $\lesssim 1$ e^- rms/pixel (sub-electron readout noise) [16].

While modern ultra-low noise, photon-counting Skipper CCDs have seen abundant use as particle detectors, particularly in DM searches [e.g., 124, 125, 126, 127], prior to this thesis work they had not been applied to astronomical observations. In 1994, NASA's Cosmic Unresolved X-ray Background Instrument Using CCDs (CUBIC) mission aimed to

make moderate-resolution X-ray spectral measurements at spatial scales of a few degrees. The satellite payload featured Loral Fairchild 1024 × 1024 CCDs that incorporated both floating diffusion amplifiers and floating gate-"skipper"-amplifiers. However, the skipper amplifiers were not planned to be used [128]. Specific details were not given but one can only speculate that the performance issues, discussed earlier, that plagued early Skippers might have influenced the decision.

In this chapter, I outline plans to conduct the first on-sky demonstration of the Skipper CCD for acquiring astronomical spectra. Specifically, I describe the construction of a prototype Skipper CCD focal plane array for use with the Southern Astrophysical Research (SOAR) Telescope Integral Field Spectrograph (SIFS), located on Cerro Pachón in the Coquimbo Region of Chile. This demonstration aims to validate the Skipper CCD's ultra-low noise performance of observations in the readout noise dominated regime, demonstrate that this technology retains the well-characterized performance of the thick, fully depleted, *p*-channel CCDs developed by LBNL for astronomy (i.e., stability, linear response, large dynamic range, high QE in the near infrared regime, and radiation tolerance), and motivate further Skipper development for Stage 5 surveys.

4.1 Motivations

We performed early measurements to characterize the astronomical performance of a R&D Skipper CCD (see Figure 4.2, Left) similar to the one used in [9]. In the study, we characterized the response of a novel 250μm thick, fully-depleted Skipper CCD to visible/near-infrared light with a focus on potential applications for astronomical observations. We achieved stable, single-electron resolution with readout noise $\sigma \sim 0.18$ e^-rms/pixel from 400 non-destructive measurements of the charge in each pixel. We verified that the gain derived from photon transfer curve (see Section 5.6.3) measurements agrees with the gain calculated from the quantized charge of individual electrons to within $\lesssim 1\%$ and showed that the detector

could achieve a full-well capacity of $34,000$ e^-. We also performed relative quantum efficiency measurements and demonstrate high relative quantum efficiency (QE $>$ 75% from 450 nm to 900 nm) at optical/near-infrared wavelengths (see Figure 4.1), as is expected for a thick, fully depleted detector. For details on optimization and characterization of Skipper CCDs for astronomy, see Chapter 5.

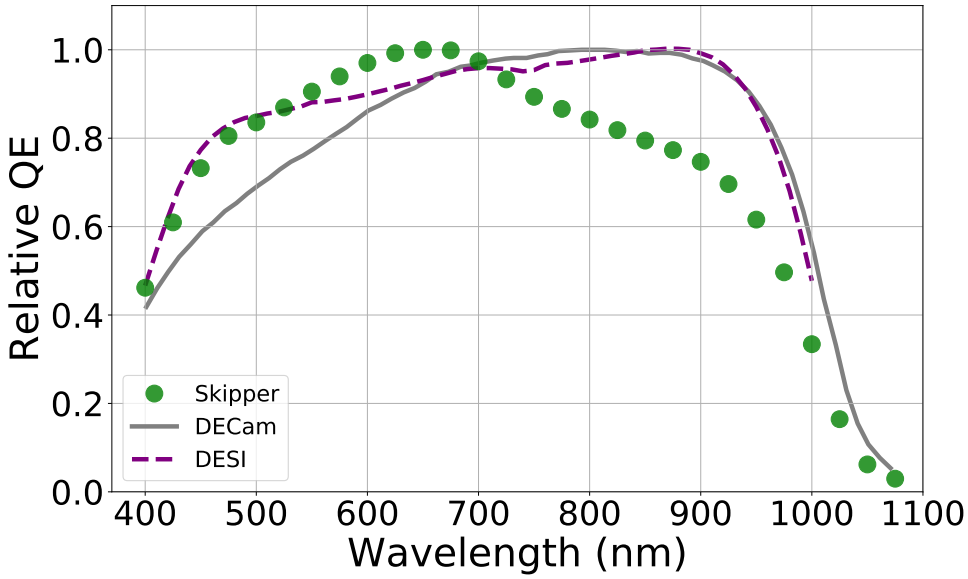

Figure 4.1: Relative QE of the R&D Skipper CCD compared to the QE from DESI and DECam devices (all designed at LBNL, packaged and tested at Fermilab).

This work served as the first step for demonstrating the viability of using Skipper CCDs for astronomical applications. In a more practical sense, it represented the opportunity to learn about Skipper operation and testing. In particular, we setup a vacuum Dewar and cooling system consisting on a closed-cycle vacuum Dewar with a fused silica window manufactured by Infrared Laboratories Inc. The system is cooled by a closed-system cryocooler. A 40 W cartridge heater is installed in the copper block and is controlled by a Lakeshore temperature controller to maintain a stable operating temperature of 140 K. We also assembled the optical equipment which includes a tungsten arc lamp, motorized filter wheel, monochromator, shutter, and integrating sphere (Figure 4.2, Right). This setup provided uniform illumination to the CCD surface with configurable wavelength and exposure time.

The shutter, filter wheel, and monochromator were controlled using GPIB through a TCL interface.

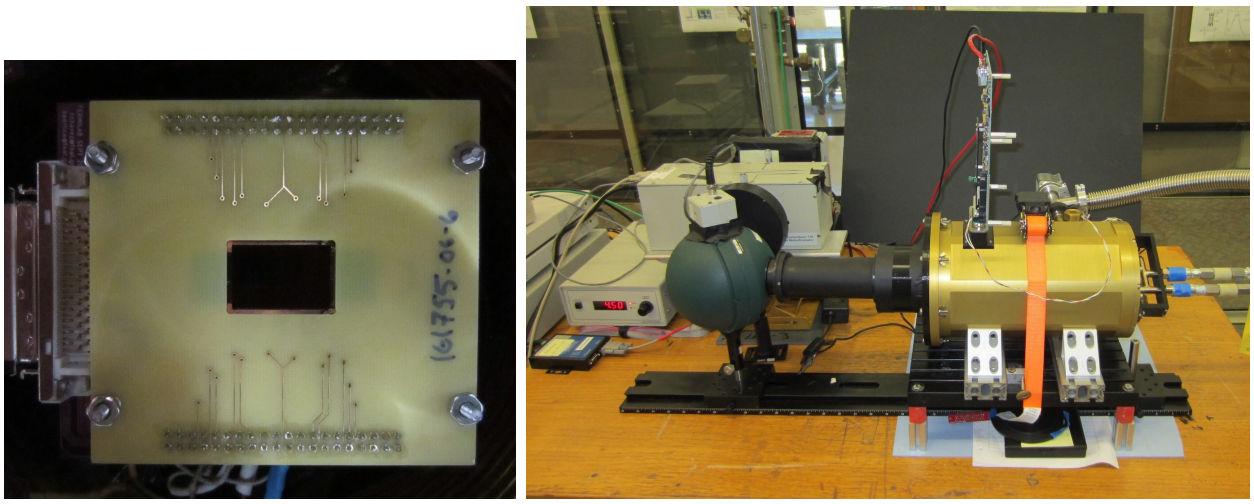

Figure 4.2: Left: Backside-illuminated R&D Skipper CCD, similar to the one tested on [9], mounted in a picture frame adapter. Right: Experimental setup including a closed-cycle optical Dewar (gold; right) housing the Skipper CCD with attached LTA readout board and integrating sphere with attached photodiode (green; left). Behind the integrating sphere are a mechanical shutter, monochromator, filter wheel, and tungsten halogen lamp. Photographs presented in this thesis are taken by the author or are allowed for general use by the CCD group at Fermilab (otherwise the source is referenced).

The first demonstration of the desirable optical properties of Skipper CCDs for astronomical measurements incentivized our group to form a collaboration with NSF's National Optical-Infrared Astronomy Research Laboratory (NOIRLab), the premier U.S. national center for ground-based, nighttime optical and infrared astronomy. This collaboration aimed to test the Skipper CCD for the first time on the sky using SIFS. This effort would not only serve as a technology demonstration but also provide an opportunity to acquire science-quality data, showing the potential of Skipper CCDs for making scientifically relevant measurements (see Chapters 6 and 7 for more details on science with Skipper CCDs). Furthermore, this demonstration would serve as a precursor to developing analysis tools for astronomical data collected with Skipper CCDs, enabling the exploration of unique features—such as implementing regions of interest (see Section 6.2)—that are possible with these devices.

4.2 SOAR Integral Filed Spectrograph (SIFS)

The SOAR Telescope is a 4.1-m Ritchey-Chretien alt-azimuth telescope (Figure 4.3) that provides high-precision pointing with a large instrument payload capacity and excellent angular resolution with tip-tilt correction [129, 11]. SIFS (Figure 4.4) is a fiber-fed integral field spectrograph consisting of 1300 fibers covering a 15 $\times$ 7.8 arsec^2 field-of view with an angular resolution of 0.30 arsec/fiber. This allows SIFS to perform spatially resolved 2D spectroscopy of complex extended objects and crowded fields. SIFS has wide wavelength coverage, from 350 nm to 1000 nm, while allowing for simultaneous spectra to be taken of all parts of moderately extended objects such as H II regions. Furthermore, SIFS uses volume phase holographic (VPH) transmission gratings that offer a range of spectral resolution ($R = \delta\lambda/\lambda$) from $5000 < R < 30000$, which, for example, is sufficient to measure stellar metallicities at $R > 6000$ and abundance ratios, such as Hα/Fe, at $R > 15000$ [130, 129, 11].

Typical applications of SIFS include studies of star-forming regions and active galactic nuclei (AGN). For example, Palumbo et al. (2020) used SIFS to measure redshifts, velocity fields, which were constructed by sampling object spectra at many discrete points, specific start formation rates, and surface mass densities of compact dwarf starburst galaxies in the Local Volume [131]. Patrícia da Silva at al. (2020) presented a multi-wavelength study of the nuclear region of NGC 613, which contains an AGN. In this study, SIFS is used to obtain a data cube of the central region of NGC 613 with a spatial resolution of 0.3 arsec $\times$ 0.3 arsec; the data is used to study H II star-forming regions in the circumnuclear ring of the galaxy [132].

SIFS is composed of three main subsystems: the fore-optics, the IFU, and the bench spectrograph. The fore-optics consist of a magnification lens group followed by a field lens, which magnifies the focal plane of the telescope to the scale that is required by the micro lens array [129]. SIFS employs a lenslet, fiber IFU system which consists of 1300 lenslets and optical fibers arranged into a 50×26 array and encapsulated in 26 furcation tubes. The

Figure 4.3: The 4.1-m SOAR Telescope, located atop of Cerro Pachón, Chile.

optical fibers (Polymicro “blue" fiber) have a spectral transmission $> 70\%$ for wavelengths between 350 nm and 950 nm [129, 11]. The bench spectrograph (Fig. 4.5) is installed on the platform of the SOAR telescope, supported by six sets of pneumatic supports for vibration isolation. The bench spectrograph includes the output unit support, the collimator lens group and a spherical mirror, the VPH gratings exchanging mechanism, the camera and detector [11]. The SIFS Skipper CCD focal plane is mounted in a replacement cryostat that matches the mechanical dimensions and focal distance of the original (item 6 in Fig. 4.5). The modular design of the cryostat simplifies the time, cost and risk of installation since no mechanical or optical modifications are required; furthermore, there is not need to replace any other components of the bench spectrograph.

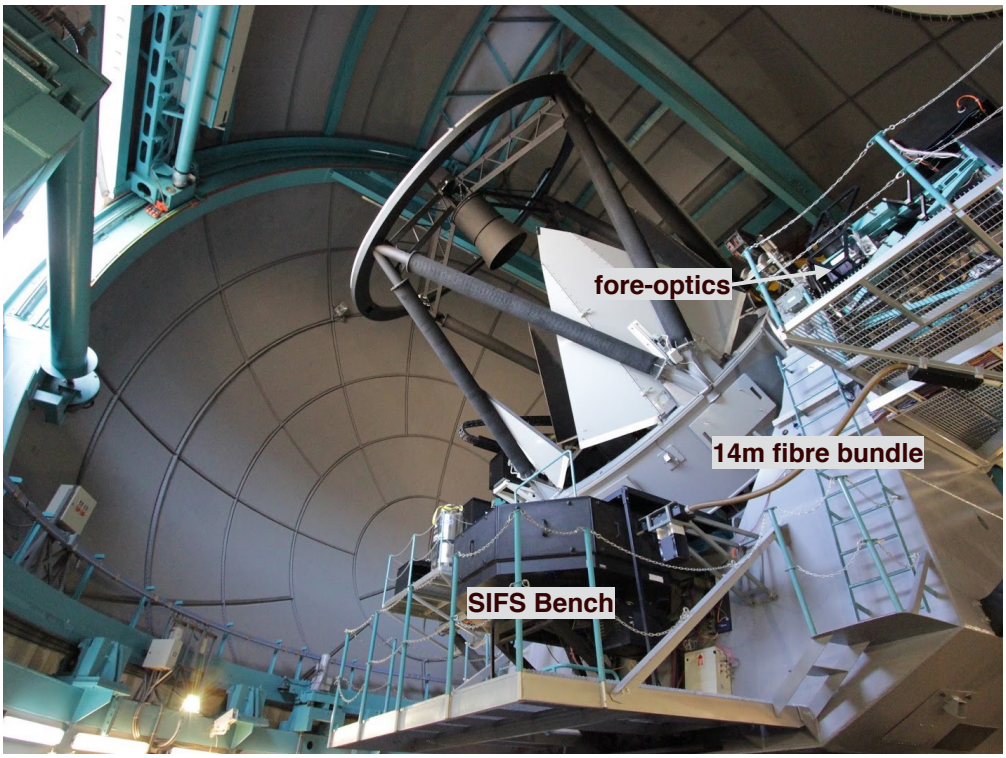

Figure 4.4: The SIFS spectrograph The instrument consists of three subsystems: the fore-optics module, a 14-m. fiber bundle, and the bench spectrograph.

4.3 Observational Improvements with Skipper CCDs

The SIFS bench spectrograph currently uses a thinned CCD231-84 from Teledyne e2v that has a format of 4096 $\times$ 4112 pixels and a pixel size of 15 μm. The detector is read through two channels in 22s with a readout noise of 5.2e$^-$rms/pix and a gain of 2.0e$^-$/ADU. Table 4.1 shows some characteristic parameters that influence the SIFS performance, including the SIFS detector performance. We note that an evident improvement from the Skipper CCD focal plane is the single sample per pixel readout noise. Assuming the Skipper CCD can reach a single sample readout noise of 3.5 e$^-$rms/pix there is a $\sim$ 40% improvement in readout noise when comparing with SIFS's current detector. However, we note that the goal is to demonstrate sub-electron readout noise.

We consider improvements to the S/N and observation time possible with Skipper CCDs. First, let us consider the S/N from an astronomical observation. The noise per pixel can be

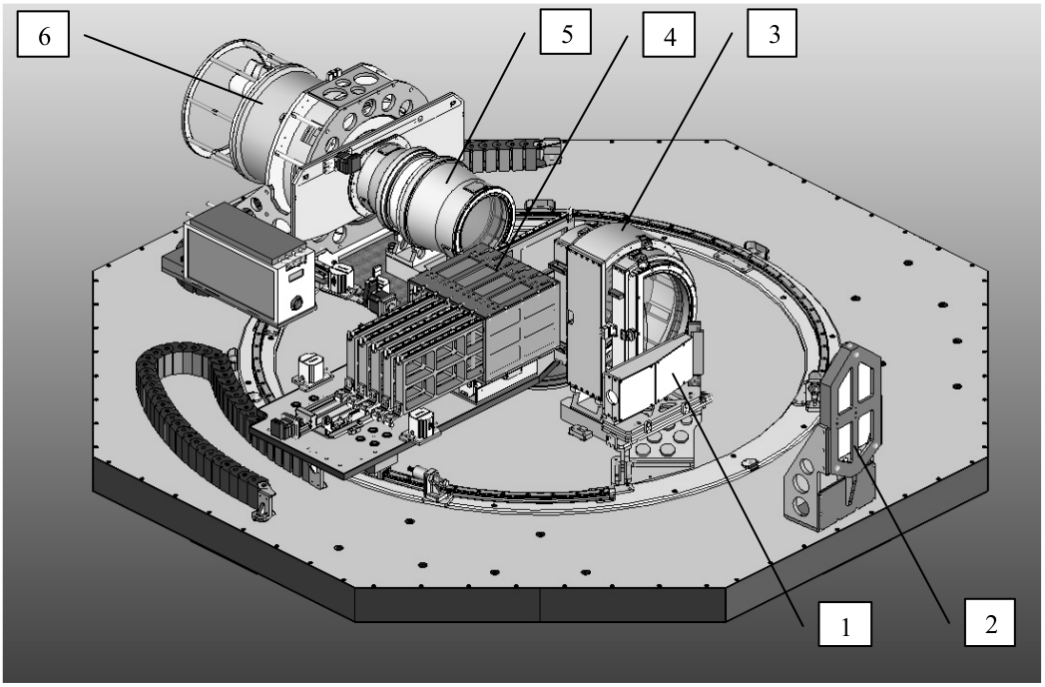

Figure 4.5: SIFS bench-top spectrograph. (1) Output unit support and fold mirror. (2) Collimator mirror. (3) Collimator lenses. (4) VPH grating mechanism. (5) Camera. (6) Cryostat containing detector (diagram taken from [11]).

broadly decomposed into two components:

$$\sigma^2 = \sigma^2_{\text{shot}} + \sigma^2_{\text{read}}. \tag{4.1}$$

Here, σ_{shot} is the Poisson shot noise contributed by the source of interest, contaminating background light (e.g., scattered light, sky background, zodiacal light, etc.), and detector dark current[1]. The total shot noise can be derived from the rate, r ($\text{e}^{-}\text{pix}^{-1}\text{s}^{-1}$), for each contributing component and the integration time, t_{exp} (s), of the exposure,

$$\sigma^2_{\text{shot}} = (r_{\text{src}} + r_{\text{bkg}} + r_{\text{dark}})t_{\text{exp}}. \tag{4.2}$$

1. CCD dark current, produced by thermal fluctuations or environmental factors generate charge counts that contribute to the 'noise' as these add to the true counts from the astronomical object. See Chapter 5 for details on dark current.

In contrast to the shot noise, the readout noise is independent of the exposure time and is generally expressed in terms of the rms fluctuations in the number of electrons per pixel (e^-rms/pix).

Observationally, the counts from a source will be spread over several pixels. Assuming uncorrelated pixel measurements, the noise components add in quadrature. Thus, the total noise integrated over the pixels of interest will be,

$$\Sigma^2_{\rm tot} = N\sigma^2_{\rm tot} = N(r_{\rm src} + r_{\rm bkg} + r_{\rm dark})t_{\rm exp} + N\sigma^2_{\rm read} \tag{4.3}$$

$$= (R_{\rm src} + R_{\rm bkg} + R_{\rm dark})t_{\rm exp} + N\sigma^2_{\rm read}, \tag{4.4}$$

where in the second line we have defined the total source, background, and dark contributions integrated over pixel elements ($R_{\rm src}, R_{\rm bkg}, R_{\rm dark}$), since these numbers are commonly provided by astronomers.

The sensitivity to a given source is generally expressed by the S/N, which we define it as the ratio between the number of counts contributed by the source and the total noise in the observation,

$$S/N = \frac{R_{\rm src}t_{\rm exp}}{\Sigma_{\rm tot}} = \frac{R_{\rm src}t_{\rm exp}}{\sqrt{(R_{\rm src} + R_{\rm bkg} + R_{\rm dark})t_{\rm exp} + N\sigma^2_{\rm read}}}. \tag{4.5}$$

From this formulation, it is clear that the total noise will be dominated by the readout noise only in cases where $N\sigma^2_{\rm read} \geq (R_{\rm src} + R_{\rm bkg} + R_{\rm dark})t_{\rm exp}$. When the readout noise dominates then $S/N \propto t_{\rm exp}$ as opposed to the familiar behavior $S/N \propto \sqrt{t_{\rm exp}}$. Most astronomical observations are designed to avoid the readout-noise dominated regime. In particular, for bright sources $R_{\rm src} \gg R_{\rm bkg} \gg R_{\rm dark}$, and any moderate exposure time yields $R_{\rm src}t_{\rm exp} \gg N\sigma^2_{\rm read}$. In contrast, for faint sources $R_{\rm src} < R_{\rm bkg}$ and achieving a reasonable signal-to-noise requires a long exposure time such that $R_{\rm bkg}t_{\rm exp} > N\sigma^2_{\rm read}$. Thus, the readout-noise dominated regime occurs only in scenarios where both the signal and

Table 4.1: SIFS Reference Parameters

Characteristic	Value	Unit
Signal Rate	0.01191	$e^{-}pix^{-1}s^{-1}$
Background Rate	0.0079	$e^{-}pix^{-1}s^{-1}$
Dark Current	3.2×10^{-3}	$e^{-}pix^{-1}s^{-1}$
Readout Noise	5.2	e^{-}rms/pix
Npix	3.2×2.1	pix
Readout Time	22	secs

background rates are small and the exposure time is constrained such that longer integration times are not possible. Such observations are necessarily in the low signal-to-noise regime. For ground-based imaging of the static sky, Poisson shot noise from the source of interest and the sky background generally dominate over the readout noise of current detectors. However, for spectroscopic measurements from the ground (especially at short wavelengths where the sky background is greatly reduced), space-based imaging and spectroscopy of faint sources (e.g., extra-solar planets), and very high-cadence imaging for short duration transients (e.g., fast radio bursts), readout noise can be an important contribution to the overall noise budget. In these cases, reducing readout noise can achieve higher signal-to-noise with shorter observation times.

For SIFS, the signals are faint, and the background contributions to the noise are small, as evident in Table 4.1. Fig. 4.6, constructed with the values from Table 4.1, shows the expected improvement in the reduction of observation time (exposure + readout time) to reach a target signal-to-noise (S/N=7, the typical S/N reached by SIFS with the e2v CCD.) for different percentages of the detector being read out, i.e., region of interest functionality (see Section 5.3.1). It is clear that if the noise is decreased to the sub-electron level, i.e., ~ 0.7 e^{-}rms/pix it would be possible to improve the instrument observational efficiency by $\sim 30\%$.

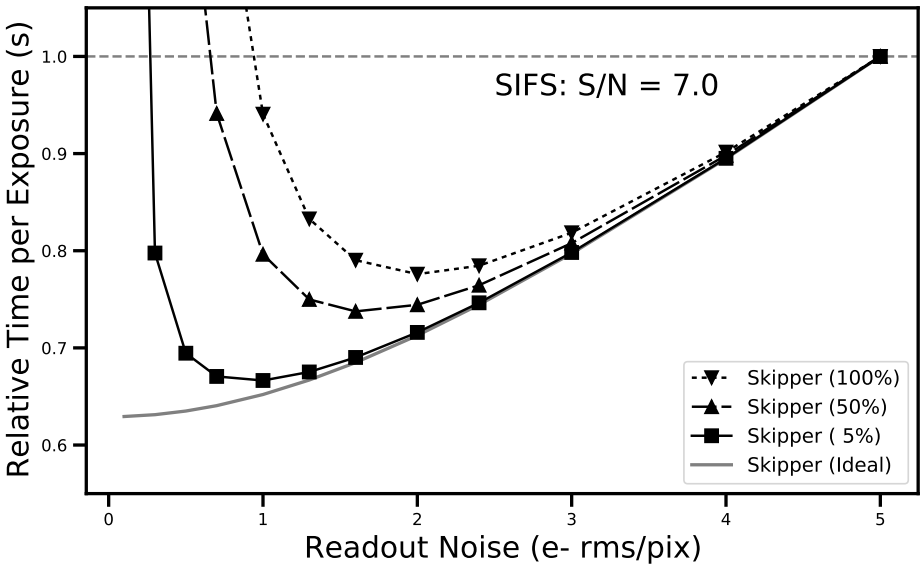

Figure 4.6: Relative exposure times as a function of detector readout noise at a fixed S/N= 7. Curves represent 100%, 50%, and 5% of the detector being read out.

4.4 Engineering Detectors

As outlined earlier, the prototype Skipper CCD focal plane for SIFS consists of four Skipper CCDs, designed to preserve the original optical alignment between the spectrograph and the e2v detector. The detector characterization and optimization process begins with the characterization of "engineering-grade" detectors. Although these engineering grade detectors are not optimized for light detection (e.g., they lack the substrate thickness and AR coatings necessary for maximizing QE)[2], they provide a critical testing platform. These detectors allow us to measure readout noise performance, develop and validate the readout electronics, construct testing stations, and refine detector packaging procedures.

4.4.1 Detector Architecture and Characteristics

The four backside illuminated Skipper CCDs that were used for SIFS come from a fabrication run for Fermilab R&D projects. The Skipper CCDs are *p*-channel detectors fabricated on

2. "Science-grade" Skipper CCDs are thinned to 250 nm and AR coated to maximize light sensitivity.

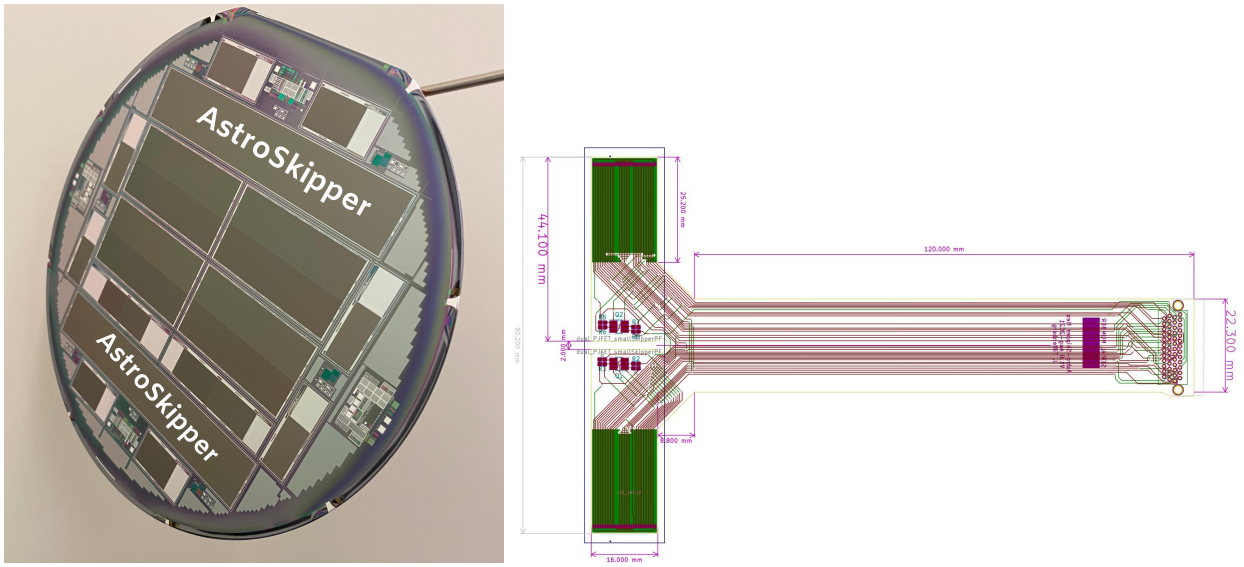

Figure 4.7: Left: Silicon wafer containing 16 Skipper CCDs for different Fermilab R&D projects. The prototype focal plane array uses the 6k × 1k pixel CCDs with four amplifiers (labeled "AstroSkipper"). Right: AstroSkipper flex cable with active components, i.e., two JFETs and resistors. The flex cable uses an Omnetics connector (right edge of the cable).

high resistivity (∼5 kΩcm), n-type silicon. The wafers are fabricated at a thickness of ∼ 650μm. For a description on the thinned detectors see Chapter 5. Each silicon wafer contains 16 Skipper CCDs (Fig. 4.7) with different readout and size configurations. For the SIFS Skipper CCD focal plane, we used standard wide-format Skipper CCDs (6k × 1k, 15 μm pixels) with four amplifiers ("AstroSkipper" in Fig. 4.7). The pixel scale of these detectors matches that of the existing SIFS e2v detector, and a mosaic of four 6k × 1k Skipper CCD detectors covers the full ∼4k × 4k pixel area of the original SIFS detector.

4.4.2 Detector Packaging

We packaged a total of 4 engineering-grade and 8 Science-grade Skipper CCDs at Fermilab. The AstroSkipper CCD detector package has two main components: a flexible cable for carrying electrical signals to/from the CCD and a mechanical foot for mounting the CCD to the focal plane. The flexible cable carries the bias voltages, clock voltages, and video signals,

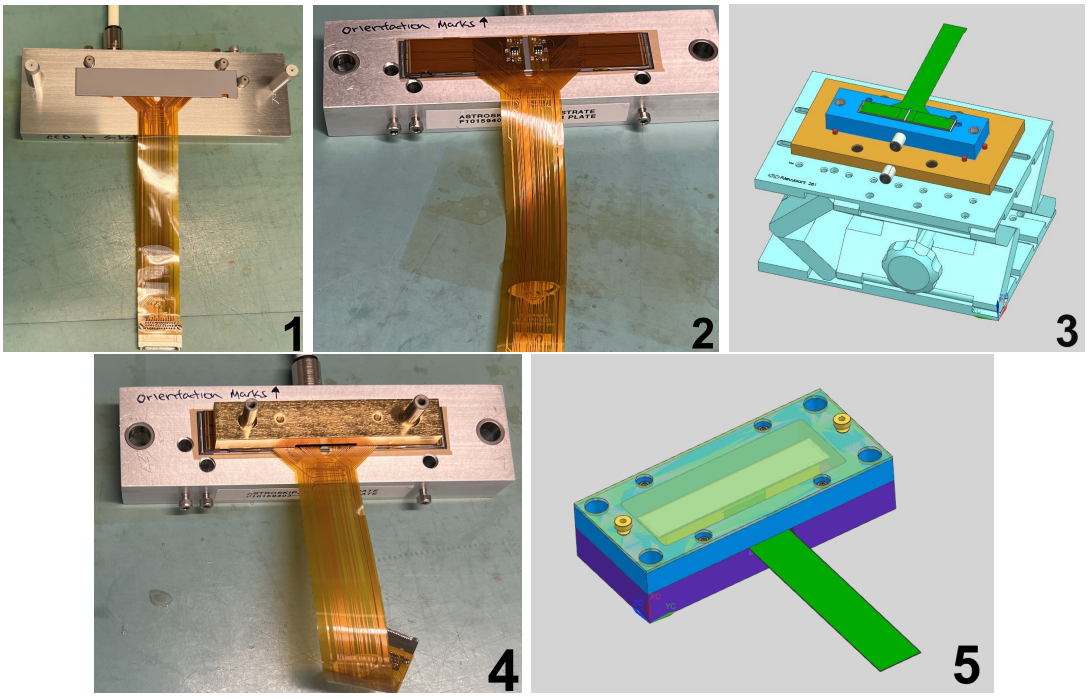

Figure 4.8: Skipper CCD packaging process. **(1)** Flex cable, with Omnetics connector at the end, is glued to the Si substrate. **(2)** The CCD, placed on the blue fixture, is attached to the flex-Si substrate assembly. **(3)** Wirebonding between CCD pads and flex cable. **(4)** CCD foot, gold-plated piece, is glued to the CCD. **(5)** CCD package is installed into a carrying box with removable lid for storage, testing, and transport.

and it has two junction-gate field-effect transistors (JFETs), four 20 kΩ resistors, and a 51-pin Omnetics connector. We use two high performance dual LSJ689-SOT-23, p-channel JFETs that provide ultra-low noise ($\sim 2.0\text{nV}/\sqrt{\text{Hz}}$).

The mechanical packaging process (Fig. 4.8) starts by **(1)** attaching the flex cable to a 90.74mm × 16.36mm × 1.00mm silicon (Si) substrate piece. A mechanical fixture is used to align the Si substrate and a vacuum system that runs through the fixture is used to apply suction and hold the substrate in place. The flex cable is attached to the Si substrate using two pyralux sheets. The Si substrate–pyralux–flex cable assembly is cured at 191° C for 3.5 hours under vacuum. **(2)** The CCD is attached to the Si substrate–flex cable assembly. Another fixture is used to align the CCD with the the Si substrate, and double-sided tape is used to secure the CCD to the Si substrate while epoxy is applied [133]. Epotek 301-2

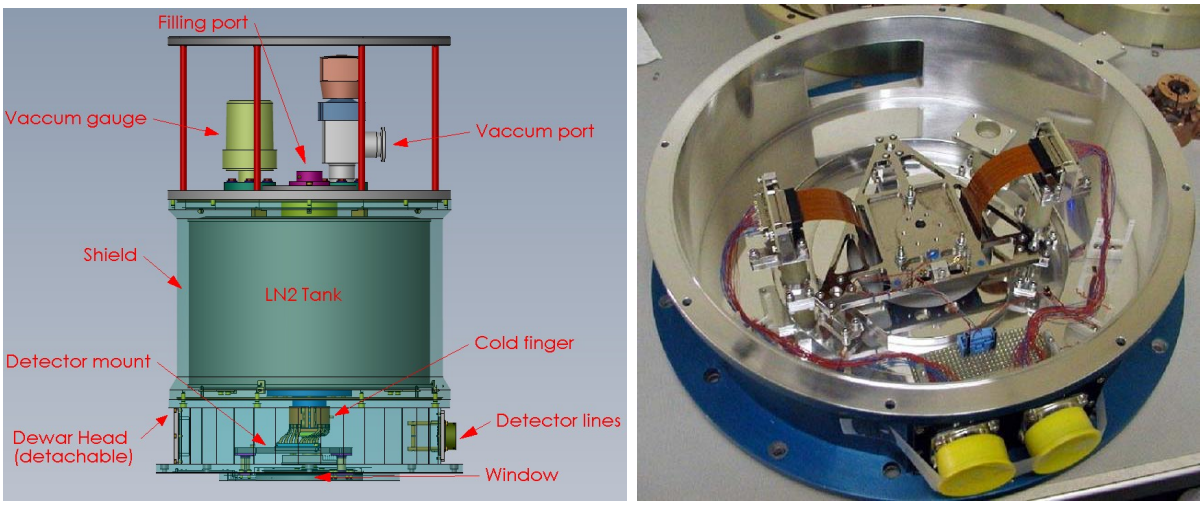

Figure 4.9: Left: Cross section of a standard SOAR Dewar. It uses LN2 to cool the detectors. The detector mount is attached to the tank through a cold finger and a copper piece, with braids trimmed for thermal adjustment. Right: Original SIFS Detector mount, designed for a single e2v CCD44-82 (4k×4k). The image show the detector, and below it, the mount, which is a triangular aluminum plate that attaches to the Dewar through three posts.

epoxy is dispensed through a small cutout in the edge of the Si substrate near one of the corners and is allowed to fill the region between the CCD and the Si substrate. The epoxy is allowed to cure for 48 hours. **(3)** Wirebonding is performed between the pads on the CCD and flex cable. **(4)** We attach the CCD assembly to a gold-plated invar foot that serves as the structure for mounting the packaged Skipper CCDs on the focal plane. The fixture holding the CCD is placed onto the foot gluing plate; Masterbond EP21TCHT-1 epoxy is used to attach the CCD assembly and the foot and is allowed 18 to 24 hours to cure. **(5)** The packaged AstroSkipper is placed within an aluminium carrying box for storage and transport. The carrying box has a removable cover and is compatible with our CCD testing stations. The storage box can be directly mounted to the cold-finger plate inside the testing vacuum chambers and the storage box cover can be removed for CCD testing.

4.5 Dewar and Focal Plane

SOAR employs a standard Dewar design for most of its visible-light instruments, a design that is also used by several instruments at the Cerro Tololo Inter-American Observatory (CTIO). This Dewar features a single liquid nitrogen (LN2) tank and achieves a typical vacuum level of $\sim 10^{-6}$ Torr. When fully filled, the Dewar has a holding time exceeding 30 hours, ensuring extended periods of stable operation without frequent refilling [134]. Additionally, the Dewar is equipped with a molecular sieve, which helps maintain a stable vacuum for several months without requiring maintenance or intervention. Figure 4.9 (Left) shows a cross section of a SOAR Dewar.

4.5.1 SIFS AstroSkipper Dewar

The SIFS Dewar has a customized mount designed specifically for its e2v detector. Figure 4.9 (Right) shows the SIFS Dewar head with the current detector mount. The mount, which is the triangular aluminum piece in Figure 4.9 (Right), mounts to the Dewar head through three posts.

Since in SIFS the Dewar is independent of the rest of the instrument, by replacing the current detector and mount with one that holds the AstroSkipper CCDs and ensuring the same spatial coverage and back focal distance, there is no need to make any modification to the instrument itself. However, given that SIFS is a operational instrument and the AstroSkipper focal plane is a prototype, it is impossible to modify the SIFS Dewar itself. Instead, we use an unfinished SOAR Dewar with original parts built for the COSMOS red side (but never actually implemented), manufacture the missing pieces, and fit a spare Dewar head identical to that of SIFS (this was kept in the detector laboratory for testing purposes). In this way, it would be possible to remove the current SIFS Dewar and install the one with the AstroSkipper CCDs without making any mechanical change to the instrument. This would also facilitate returning to the original Dewar configuration, since this operation does

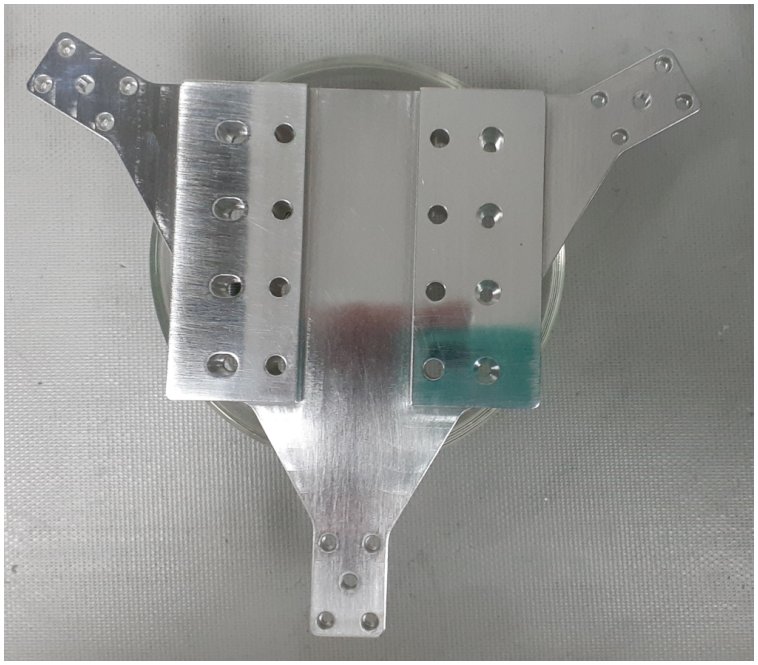

Figure 4.10: Mount for the focal plane array of four Skipper CCDs. The three arms attach to the standard SOAR Dewar. The back holds an RTD and two heaters for temperature control.

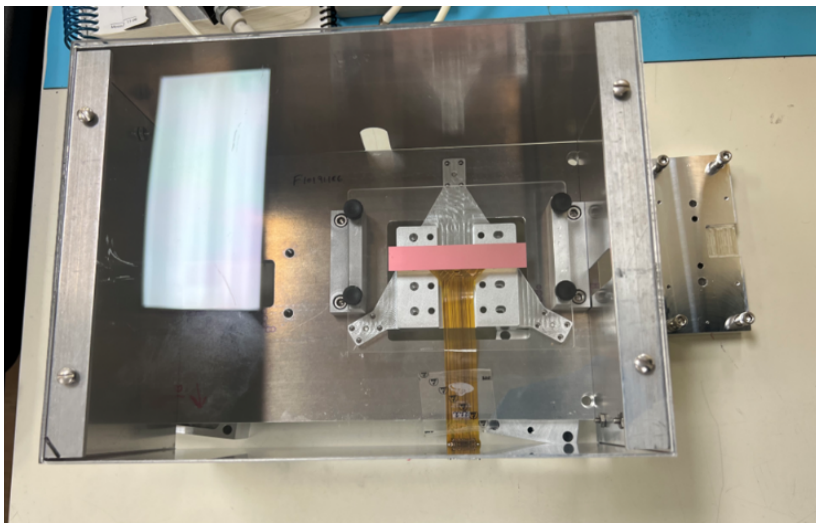

Figure 4.11: Coordinate measuring machine used to measure individual packaged Skipper CCDs prior to shipping to CTIO.

not take more than a couple of hours during the day.

Having a Dewar and a head identical to that of SIFS, we needed to design and fabricate a new detector mount (Figure 4.10) to hold the AstroSkipper CCDs. The mount was designed

Table 4.2: Metrology requirements toe ensure optimal optical alignment and focus of the Skipper CCD focal plane array at SIFS.

Parameter	Target	Measured	Units
Focal distance	6.8	6.9	mm
Detector height difference	50	< 10	μm
Intra and inter tip/tilt	< 50	< 35	μm
Gap	< 900	< 630	μm

at Laboratório Nacional de Astrofísica (LNA) and machined at CTIO. The mount is made of aluminum 6061 and holds four Fermilab-packaged AstroSkipper detectors using rods to place the detectors on the mount. The mount has three ears that are identical to those of the current mount, allowing it to use the same mounting holes. Special posts were manufactured so that the mount can be placed at a height that ensures the same back focal distance than the current detector.

4.5.2 Focal Plane Metrology

For specific details on focal plane metrology, I refer the reader to Bonati et al. (2024). Detector focal plane alignment is a critical step in the focal plane assembly as the spectrograph optical alignment with respect to the focal plane depends on the flatness of the detectors on the mount. Each packaged CCD was placed in a dummy focal plane and measured using an Optical Gaging Product (OGP) for $x-y$ alignment (Figure 4.11). Multiple points along the edge of the CCDF were measured with respect to the alignment pins installed on the invar foot. Each individual package was measured to be $\lesssim 100\mu$m of its nominal x-y location. The resultant peak to peak flatness was measured to be $\sim 30\mu$m.

The focal plane array of four Skipper CCDs was assembled and measurements verified at the CTIO lab in La Serena, Chile. We selected Skipper CCDs $\#2, \#4, \#5, \#6$ based on performance. Table 4.2 shows the required tolerances (for optical focus across the focal plane array) for the tip/tilt and back focal distance for all detectors. Moreover, the inter detector gap was also measured to be within the acceptable tolerance. Given that the instrument

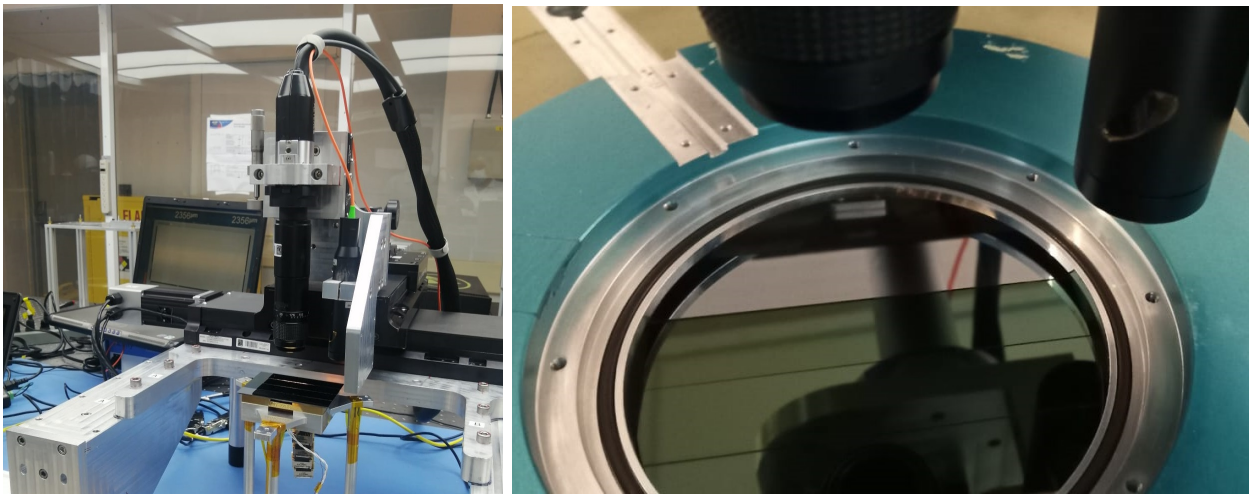

Figure 4.12: Left: Laser profilometer configuration to measure the focal plane array. The instrument consists of a single-point profiling laser and a microscope head mounted over the x-y stage. Right: Dewar head with the window removed to measure tip/tilt.

has a focus mechanism that allows for a 10 mm movement, the back focal distance for the mount was the less restrictive, yet the target goal was to replicate the 6.8 mm of the original system. The requirement of $\lesssim 5$ % difference in focus across the focal plane constraints the hight between detectors and tip/tilt inter- and intra- detector to be < 50 μm.

The focal plane was measured using a laser profilometer/microscope to assess the precise alignment and positioning of the detectors. Initially, we removed the mount from the Dewar to simplify the measurement process for intra- and inter-detector tip, tilt, and height. Following this, the focal plane was measured while mounted on the Dewar head with the window removed. This configuration enabled us to assess the mount's overall tip, tilt, and back focal distance, using the Dewar head's front flange as the reference point. The measurement configuration is illustrated in Figure 4.12 and the results are recorded in Table 4.2. All intra- and inter-detector measurements were within the required specifications. The only deviation was found in the general tip/tilt of the mount, i.e., ~ 200 μm outside the acceptable range. This issue was corrected by shimming the three posts of the mount. Additionally, the gap between the detectors varied from 200 μm to 600 μm, as illustrated in Figure 4.13.

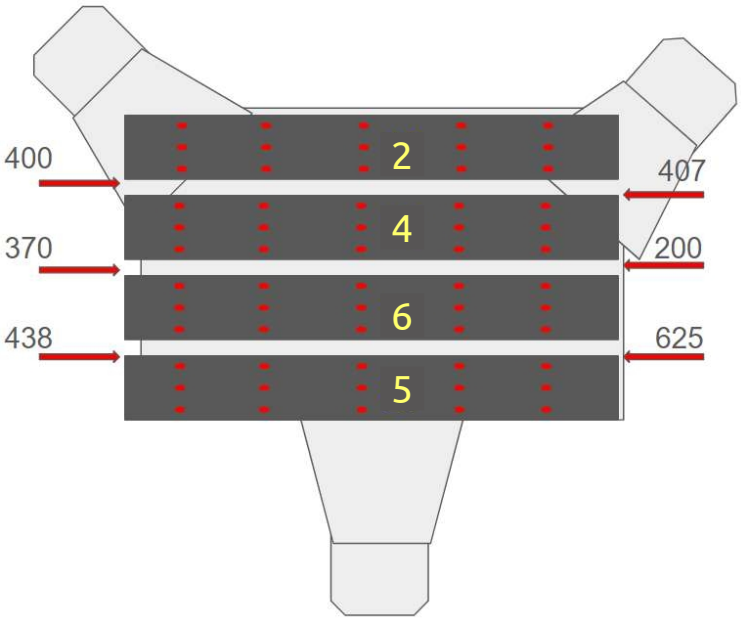

Figure 4.13: Gap measurements between detectors. Gap variations between detectors are due to differences in individual packaging and possible inaccuracies when mounting the detectors (labeled with the yellow numbers).

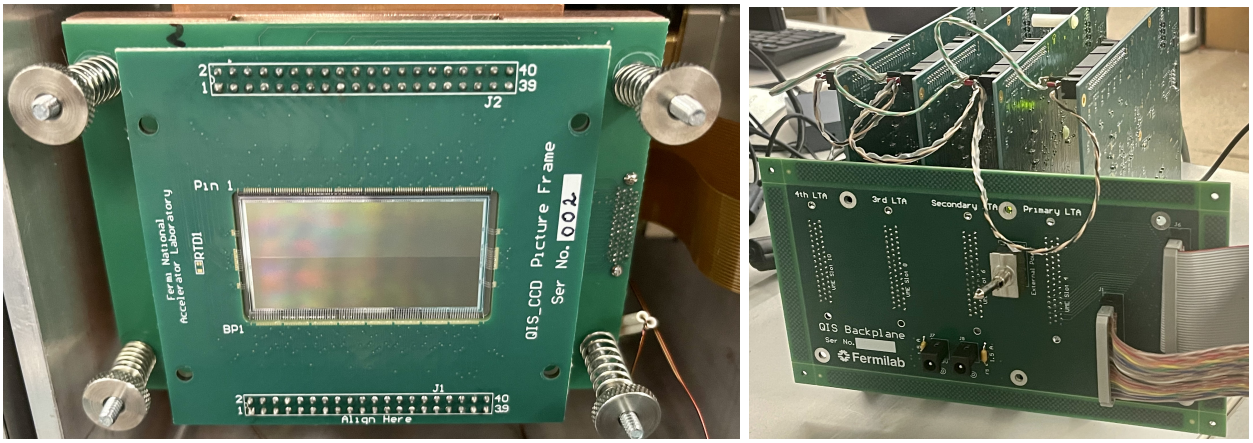

Figure 4.14: Left: 2k × 4k, 16 amplifier Skipper CCD. Amplifiers are placed along the long sides of the detector in groups of 8 amplifiers. Right: LTA synchronized readout system used for CCD testing. LTAs are docked to the backplane, which receives the video signals (rainbow ribbon cable) and biases and clocks (gray ribbon cable). Hardware synchronization between boards is done through the cables on the top of the boards.

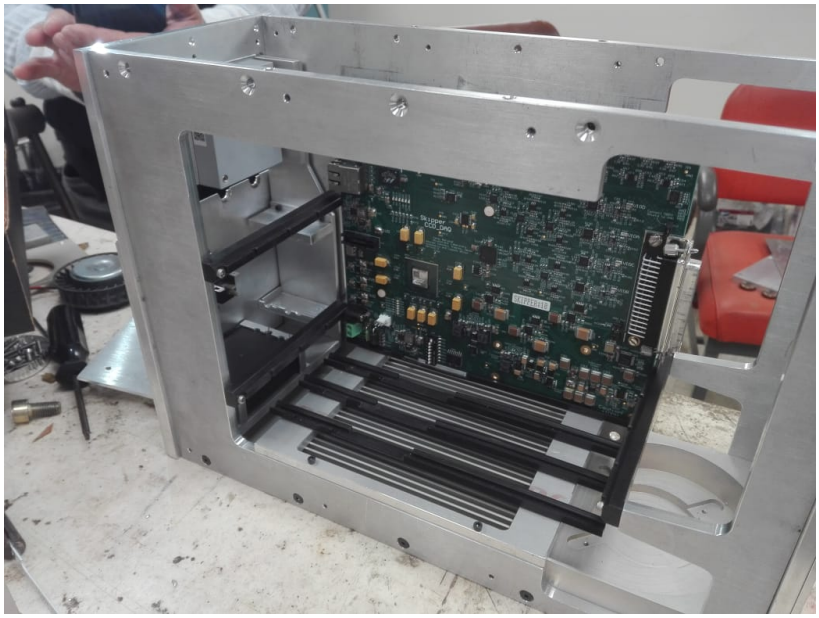

Figure 4.15: Glycol-cooled box to house the four synchronized LTAs. It provides a 200 W of dissipation power.

4.6 Readout Electronics

4.6.1 Synchronized LTA Readout

The Low-Threshold Acquisition (LTA) readout board was designed at Fermilab for performing the readout of Skipper CCDs [136]. We implemented 4 LTAs to read out the 4 detectors on the focal plane. The LTA is a single PC board hosting 4 video channels for readout, plus CCD bias and control. The board was designed and optimized to work with p-channel, thick, high resistivity Skipper CCDs. The LTA is controlled by a Xilinx Artix XC7A200T FPGA, which sets up the programmable bias voltages/clocks, to move the charge along the CCD pixel array, video acquisition, telemetry, and data transfer from the board to the PC. The LTA software is written in C++ and allows for communication using UDP over IP through the computer's gigabit Ethernet port. The user can communicate with the LTA via terminal commands to perform board configuration, readout and telemetry requests, and sequencer uploading. The data acquisition comes in the form of images in FITS and other formats.

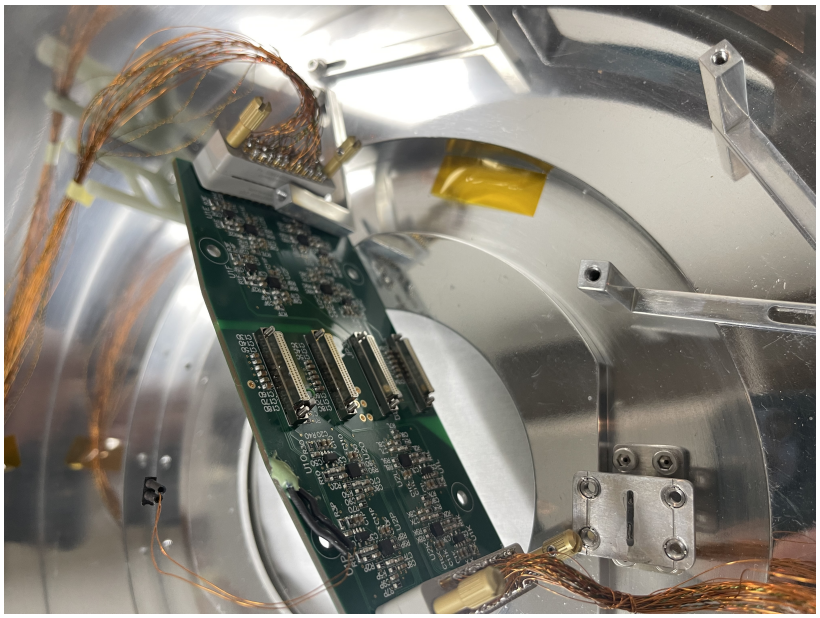

Figure 4.16: Preamplifier mounted inside the SIFS-Skipper Dewar. Each Skipper CCD connects to one of the Omnetic connectors and each pair of Positronics carry the signals for two of the detectors to each of the hermetic connectors on the Derwar.

A synchronized readout system was required to read out the four detectors at the same time. The LTA allows for easy scaling to several CCDs in parallel. A synchronized LTA system consists of connected boards where the "Leader" LTA provides a start signal to the LTAs in "Follower" mode; this configuration ensures that all boards commence the readout sequence in parallel with independent synchronized clocks. Each board is responsible for reading out one detector (4 amplifiers per detector; 16 amplifiers total). We extensively tested the LTA synchronized readout system, consisting of four LTAs, with a set of engineering 16-amplifier, 2k $\times$ 4k detectors (Figure 4.14, Left), fabricated on the same wafers as the AstroSkipper CCD. For this synchronized system (Figure 4.14, Right), each of the four LTAs reads out a quadrant of the detector, containing four amplifiers; the LTAs connect to a backplane, which can provide power to the boards and distributes biases and video signals.

4.6.2 Readout Electronics at SOAR

The original SIFS readout electronics use an SDSU-III controller. Given the thermal constrains, the housing is being cooled using glycol provided by the telescope facilities. The AstroSkipper CCDs, on the other hand, were readout by 4 synchronized LTA boards. Due to the same environmental constrain, they were enclosed in a glycol-cooled box. This box (Figure 4.15) was designed at CTIO. The box has a fan for air re-circulation and a heat exchanger plate cooled with glycol which was designed to dissipate at least 200 W. The box also includes two 12 V supplies (6 amps each) and a 5 V supply, used for the preamps on the electronic box inside the Dewar.

Due to the nature of the application and the space available inside the Dewar, CTIO designed a special preamplifier board (Figure 4.16) that fit on the envelope of the Dewar and provide preamplification that is more suitable for an astronomical application. The electronic preamplifier PCB consists of a 12.49 cm $\times$ 6.15 cm, eight layer, two-sided PCB board with 16 preamplifier circuits, i.e., 4 preamplifiers per AstroSkipper CCD. The board has one Omnetics connector per CCD, and two Positronics connectors that route the signals in and out of the preamp (two Omnetics per Positronics). The preamplifier board amplifies and converts to differential the output signal from the LSJ689 JFET, which allows it to isolate the video output signal from external noise sources. Finally, the differential output signals from the preamplifier board are connected to the input amplifiers at the LTA.

The preamp board routes the signals for two of the detectors on each Positronics, which in turn get routed internally to one of the two 41-pin Bendix hermetic connectors, as shown in Figure 4.17. Two identical, 1.7 m long external cables were made to route the signals from the hermetic to two of the LTAs. The clock and biases for those two detectors are shared and are provided by one of the LTAs. We then read all four detectors (16 channels) by running the four LTAs synchronized.

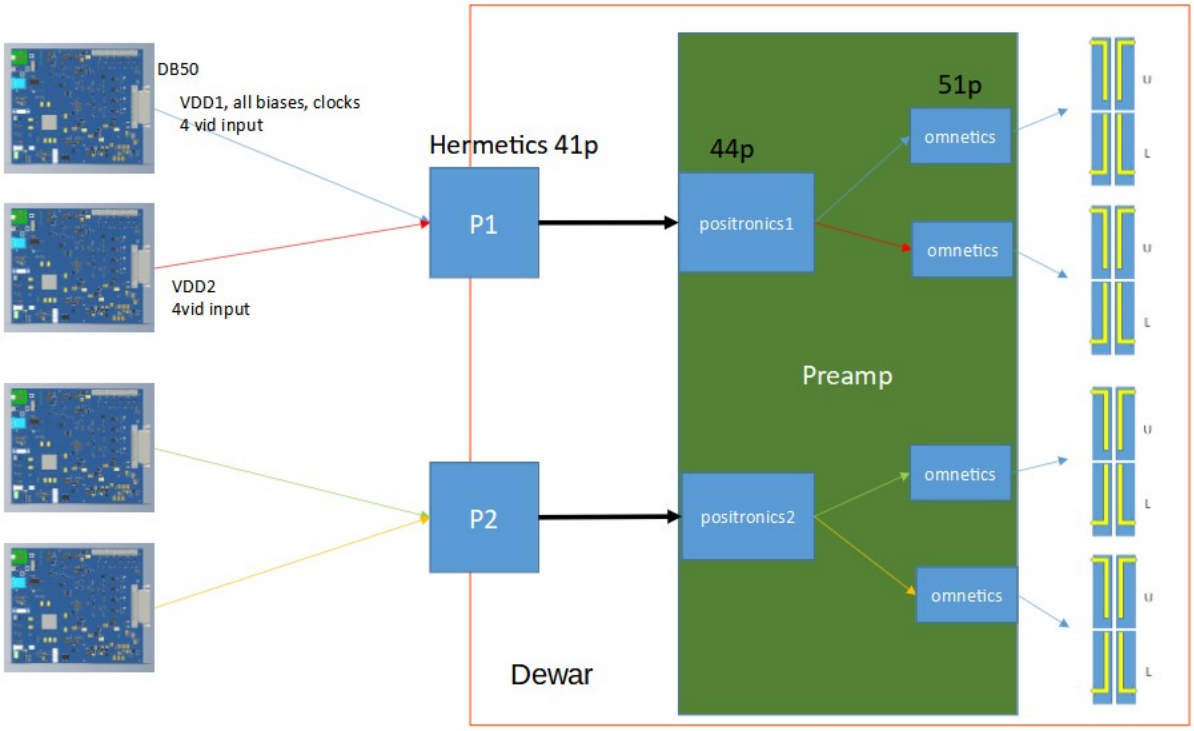

Figure 4.17: Readout System Wiring: The wiring is designed so that two LTAs handle two AstroSkipper CCDs. This allows for symmetrical cables and independent operation, if required for testing purposes. Biases and clocks are shared among the two devices, except for VDD.

CHAPTER 5

SKIPPER CCD CHARACTERIZATION AND OPTIMIZATION FOR ASTRONOMY

While the primary implementation of ultra-low noise Skipper CCDs has been in direct DM detection experiments, their application in astronomy requires distinct operational parameters. Skipper CCDs have demonstrated exceptional performance across various detector formats, packages, and operating conditions. For example, they have achieved single- and multi-sample readout noise levels of 2.5e^-rms/pix and 0.039 e^-rms/pix, respectively, dark current levels of 6.82×10^{-9} $e^-pix^{-1}s^{-1}$, and clock induced charge of 1.52×10^{-4} e^-/pixel/frame [137, 138]. These performance metrics are achieved with specific detector configurations optimized for DM searches, which are suboptimal for astronomical measurements. For instance, operating AstroSkipper CCDs with these parameters yields full-well capacities < 1000 electrons and readout times can be on the order of $\sim$ few hours to reach sub-electron readout noise.

It is important to note that the SIFS-Skipper technology demonstration intends to highlight the increase in S/N when observing in the readout noise dominated regime, and thus we target faint objects where signals are < 1000 electrons. However, a detector that posseses a high dynamic range while maintaining exquisite sensitivity to low signals is required for most astronomical applications. For instance, a detector with low dynamic range can easily become saturated by bright nearby objects, potentially compromising measurements of faint targets. In the case of astronomical spectroscopy, even when focusing on faint spectral features, a detector must be capable of handling high signal levels during calibration measurements. These measurements, often performed with bright sources, e.g., HgArNe arc lamps, can result in signal levels $> 20,000$ electrons in exposures as short as one second.

The goal of this chapter is to describe the characterization and optimization procedures aimed at demonstrating the viability of using Skipper CCDs at the SIFS. We intended to

better understand the performance and challenges of Skipper CCDs when they are configured for astronomy, as this had never been explored before. Here, I perform a suite of characterization and optimization studies with a specific focus on optimizing readout time, readout noise, full-well capacity, and clock induced charge (CIC). I present several measurements that are uniquely enabled by the single-photon resolution of the Skipper CCD (i.e., photon counting performance and low-signal-level non-linearity) as well as a suite of conventional CCD measurements that confirm that Skipper CCDs perform similarly to other thick, fully-depleted p-channel CCDs. While reducing readout time and CIC at large full-well capacity remain challenging, our results verify the readiness of the AstroSkipper CCDs for on-sky testing.

5.1 AstroSkipper: Detector Characteristics

In Section 4.4.1, I outlined the architectural characteristics of the 6k $\times$ 1k, thick, engineering-grade detectors. The AstroSkipper (Figure 5.1) shares the same format and architecture as these engineering-grade detectors, but it has been processed to meet astronomy-grade standards. We fabricated eight backside illuminated AstroSkipper CCDs for the SIFS focal plane prototype. The wafers, from which the AstroSkipper comes from, were processed following the same procedures used for DECam and DESI detectors. [104, 120, 103, 139]. Factors such as thickness and CCD surface coatings were developed to reach high QE from the NIR to the near-ultra-violet (NUV), which are desirable for astronomical observations [120]. The wafers were thinned from a standard thickness of 650–675 μm to 250 μm at a commercial vendor and then backside processed at the LBNL Microsystems Laboratory. A thin (20–25 nm) *in situ* doped polysilicon (ISDP) layer was applied to form a backside n^+ contact (refer to Section 3.2.3 for more details on LBNL-designed astronomy detectors) [10, 140].

High QE in the Vis-NIR makes the AstroSkipper detectors candidates for ground- and

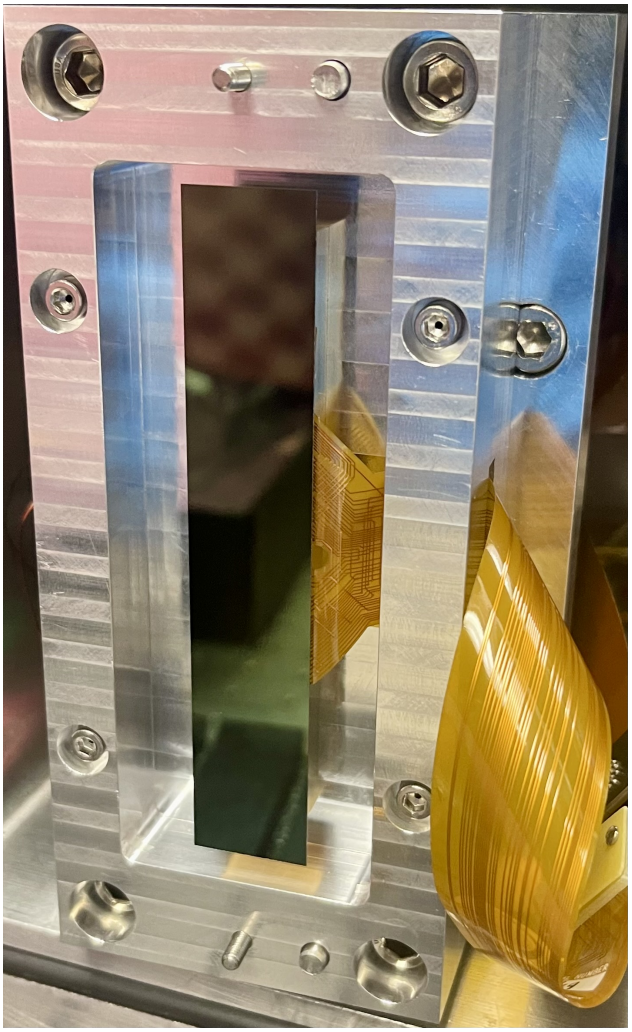

Figure 5.1: Fully packaged AstroSkipper housed in a carrier box. The package is a four-side-buttable pedestal package similar to DECam packages [12]. Refer to Section 4.4.2 for the detector packaging procedure.

spaced-based astronomical spectroscopy. To reach QE $>$ 80% in the Vis-NIR, our eight AstroSkipper CCDs were treated with an AR coating at the LBNL Mycrosystems Laboratory. The AR coating was developed for the DESI detectors and consists of a 20 nm layer of indium tin oxide (ITO), 38 nm ZrO_2, and 106 nm of SiO_2. This three-layer AR coating resulted in substantial QE improvements at shorter wavelengths ($<$ 600 nm) than the two-layer ITO/SiO_2 coating that was used for the DECam detectors [139, 140]. This result is reproduced in QE measurements of the AstroSkippers (Section 5.6.6).

5.2 AstroSkipper Testing Procedures and Infrastructure

We packaged, tested, and optimized eight AstroSkipper CCDs. The four best performing devices were selected for the prototype focal plane. Two of the AstroSkipper devices were found to have cosmetic and photon-counting performance issues in at least one amplifier, leaving six high-quality AstroSkipper CCDs suitable for the SIFS focal plane. This corresponds to a detector yield of 75% and a Skipper amplifier yield of 97% (i.e., we define a working amplifier as an amplifier that can register a charge measurement and can count photons).

First, I optimize the AstroSkipper readout time (see Section 5.3) by minimizing the pixel integration window and the horizontal sequence times to reach a total pixel time of $\sim 40\,\mu$s/pixel for a single-sample. Subsequent characterization tests are performed with this optimized readout time. I developed a streamlined procedure for testing detectors: I collect single and multi-sample bias and dark frames, flat fields at different illumination levels, and ^{55}Fe X-ray data. Based on the results of each test, I determined whether each detector passed the requirements for inclusion in the SIFS focal plane. I refer to the performance metrics used to evaluate the DESI red and NIR CCDs tested at Fermilab to asses the AstroSkippers [141]; these metrics are also similar to DECam performance requirements [12].

5.2.1 Testing Equipment

The AstroSkipper CCDs undergo testing employing the optical setup shown in Figure 5.2. Characterization of DECam and DESI detectors utilized a similar optical setup [12, 141]. This optical testing station is a derivative of the optical bench described in Section 4.1; the automated scripts for collecting data and operating the equipment were refined for the AstroSkipper testing. This setup is located in a “dark room" in order to reduce external light contamination. A single AstroSkipper CCD is housed in a thermally controlled vacuum Dewar with a fused silica window for illumination purposes.

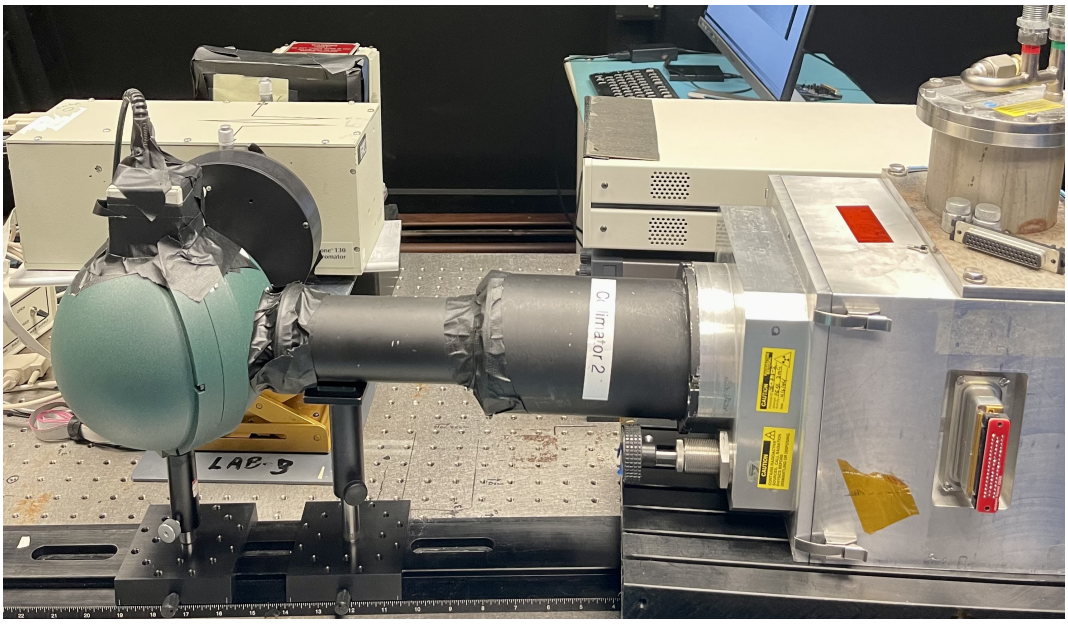

Figure 5.2: Skipper CCD testing station. From the right, closed-cycle vacuum Dewar (vacuum cube), collimator, integrating sphere (photodiode mounted on top), shutter, monochomator, filter wheel, quartz tungsten halogen lamp. Light enters the vacuum Dewar through a fused-silica window. The Skipper CCD is mounted on a cold aluminium plate that faces the window.

The AstroSkipper carrier box (Figure 5.1) attaches to an aluminum plate that is screwed to a copper cold finger inside the vacuum Dewar. The system is cooled by a closed-cycle cryocooler to an operating temperature of 140 K, which is maintained by a LakeShore temperature controller. A standard set of optical devices consisting of a quartz tungsten halogen lamp, motorized filter wheel, monochromator, shutter, and integrating sphere are used to provide uniform illumination of the AstroSkipper surface in the targeted wavelength. Light intensity is measured independently by an National Institute of Standards and Technology (NIST)-traceable Oriel photodiode mounted on the integrating sphere. This first photodiode, in conjugation with a second Thorlabs NIST-traceable photodiode mounted at the position of the CCD, allows us to calibrate the photon flux for absolute QE measurements. The shutter, filter wheel, and monochromator are controlled using a serial-to-Ethernet interface.

5.3 Time Optimization

The Skipper CCD's ability to achieve ultra-low noise comes at the cost of readout time. When taking a large number of non-destructive measurements of the charge in each pixel, the readout time scales approximately as $t_{\text{readout}} \propto N_{\text{samp}} \propto 1/\sigma_N^2$. In applications that require ultra-low noise, data taking can take several hours [e.g., 125]. In astronomical applications, the readout and exposure time need to be optimized to maximize the S/N of a faint astronomical source in a fixed observation time [16]. Therefore, it is a priority to reduce the AstroSkipper's readout time while maintaining relatively low single-sample noise performance. Readout time optimization is independent of the detector's processing (e.g., backside thinning), and we expect that time performance optimizations can be applied to other Skipper CCDs intended for astronomy or applications that require fast readout.

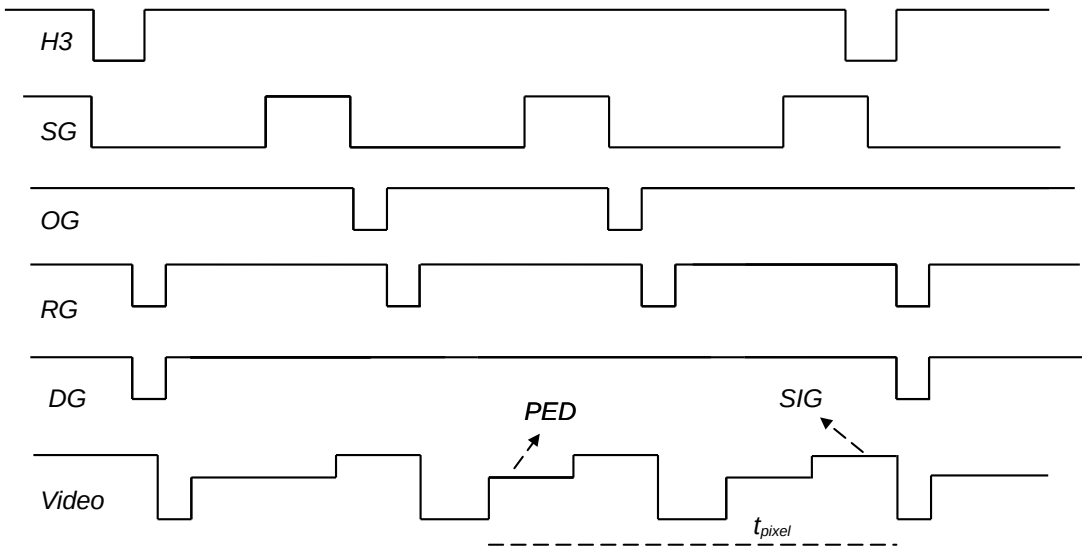

Figure 5.3: Charge transfer diagram for the Skipper CCD output stage. This diagram is adapted from Figure 5 in Fernández Moroni et al. (2016). The total time for CDS to compute the pixel value is given by t_{pixel}.

The total readout time for a single amplifier, in a given sequence, is as follows:

$$t_{\text{readout}} = N_{\text{ROW}}\Big[\Big((t_{\text{pixel}}N_{\text{samp}} + t_{\text{H}})N_{\text{COL}}\Big) + t_{\text{V}}\Big] \tag{5.1}$$

where t_{pixel} is the pixel integration time window including both the pedestal and signal components (Figure 5.3), N_{samp} is the number of non-destructive measurements, t_{H} is the time required for the horizontal sequence, i.e., serial register clocking during the charge transfer to the summing well, t_{V} is the time for the vertical clocking, i.e., the time to move the charge toward the serial register, N_{ROW} and N_{COL} define the CCD dimensions (CCD rows and columns).

From Eqn. 5.1, we can see that t_{pixel} and t_{H} have the greatest contribution to the total readout time (t_{readout}); therefore, we attempt to optimize these two times in the sequence. In Section 3.1.3, we outline the charge transferring process for a three-phase CCD. In Sections 3.2.1 and 3.2.2, we describe the multi-sample readout procedure, enabled by the floating gate amplifier, and the role of CDS in determining a pixel value from the pedestal (PED) reference value and the signal (SIG) level. Figure 5.3 depicts the process of charge transferring in the Skipper CCD output stage. The time for computing the pixel value, i.e., the pixel integration window time (t_{pixel}) is given by:

$$t_{\text{pixel}} = t_{\text{wt1}} + t_{\text{PED}} + t_{\text{wt2}} + t_{\text{SIG}} \tag{5.2}$$

where t_{wt1} and t_{wt2} represent the wait times in the pedestal and signal integration periods; these are resting times with samples that are not being integrated either in the pedestal (t_{wt1} + t_{PED}) or signal (t_{wt2} + t_{SIG}) integration intervals. The addition of these waiting times improves noise characteristics as the system does not integrate noise-dominated samples from the transients in the video signal after the sense node is reset.

Optimizing the readout time consists of fixing the integration window in the sequence, and varying $t_{\rm PED}$ and $t_{\rm SIG}$ for each integration window instance with the condition that $t_{\rm PED} = t_{\rm SIG}$ for a series of $t_{\rm wt1}$ and $t_{\rm wt2}$. For each configuration, i.e., an instance of a fixed integration window, we measure the readout noise. To perform the readout noise scan, we take single-sample images without integrating charge (charge-less readout), i.e., we clock the charge in the opposite direction to the amplifiers, enabling measurements of the noise properties of the system, and ignoring contributions due to charge accumulation. We find that $\rm t_{wt1}$ can be set to $0\,\mu$s while $\rm t_{wt2}$ can be set to values $0\,\mu{\rm s} < t_{\rm wt2} < 2\,\mu$s.

Figure 5.4 (top panel) shows the optimal readout noise for different integration window time instances for one AstroSkipper. We find that it is possible to shorten the integration window to $20\,\mu$s while maintaining a readout noise $\sigma_1 < 4.3$ $\rm e^-$ rms/pixel for the six AstroSkippers. This is a factor of two reduction in the integration time compared to the original configuration used for the SENSEI DM direct detection experiment [124]. In Figure 5.4 (bottom panel), we calculate the readout speed, using Eqn. 5.1, as a function of the integration window time while varying $N_{\rm samp}$ to reach photon-counting resolution (e.g., $\sigma_N \sim 0.18$ $\rm e^-$ rms/pixel). The optimal integration window time is $t_{\rm pixel} \sim 20\,\mu$s for a readout speed of $\sim$330 pixel/s for $N_{samp} = 400$. Furthermore, we reduced $t_{\rm H}$ from $100\,\mu$s to $20\,\mu$s, the limit set by the time constant of the horizontal clocks RC filters for reducing CIC (Section 5.5). These time optimization improvements result in a total pixel readout of $\sim 40\,\mu$s/pixel for one sample (i.e., 25 kpixels/s per amplifier) or $\sim$1.28 min. to read the whole detector with $N_{\rm samp} = 1$. This is compared to $\sim 200\,\mu$s/pixel for a single amplifier and pixel sample commonly used for DM experiments [124].

5.3.1 Skipper CCD Regions of Interest Time Optimization

Despite the timing optimization described in the previous section, it is clear from Figure 5.4 that it would still take several hours to achieve photon-counting resolution over the

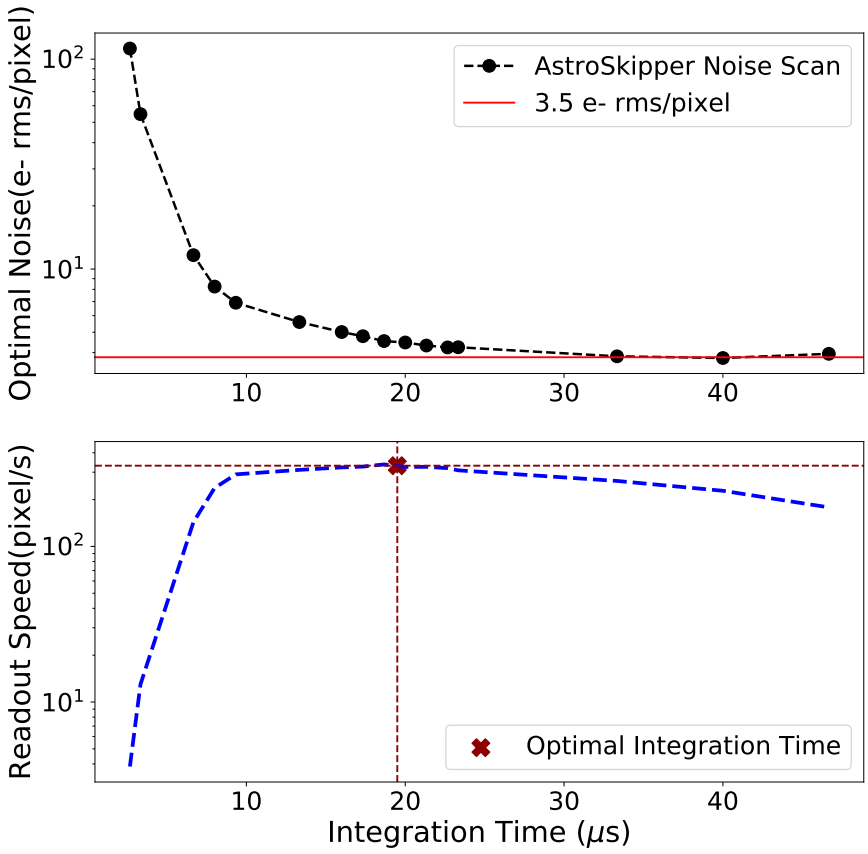

Figure 5.4: Top: measured single-sample readout noise versus CDS integration window time for the AstroSkipper. For each fixed integration window instance, we calculate the optimal noise for different t_{wt2}, t_{PED}, and t_{SIG} with $t_{\mathrm{wt1}} = 0$ μs. We note that the curve approaches the noise floor (3.5 e^- rms/pixel) at $\sim$ 20 μs with a readout noise $\sigma_1 \sim 4.3$ e^- rms/pixel. Bottom: Readout speed in pixel/s as a function of the integration time while varying N_{samp} to achieve photon-counting resolution ($\sigma_N \sim 0.18$ e $^-$ rms/pixel). The optimal integration window time is $\sim$ 20 μs for a readout speed of $\sim$ 330 pixel/s.

entire detector. These long readout times are unacceptable for astronomical applications. For astronomical observations, there is a minimum at which the S/N improvements due to reducing readout noise is overcome by the lost exposure time during long readout times, i.e., time used for readout could alternatively be used to collect more signal. Therefore, it is a priority to explore readout noise configurations for a particular application and optimize the AstroSkipper parameters (e.g., N_{samp}) to reach the desired noise performance in the least amount of time.

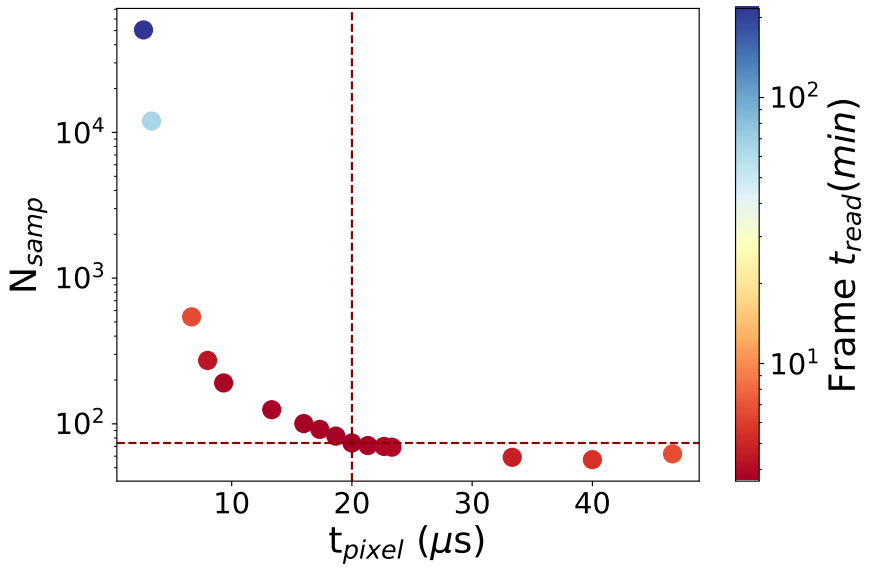

Figure 5.5: Optimization of the integration time ($t_{\rm pixel}$) to achieve a noise of 0.5 e$^-$ rms/pixel in 5% of the detector area and minimize the total readout time per frame. The optimal integration value is found to be $\sim$ 20 μs which allows the full frame to be read in $\sim$ 3.6 min.

We can explore the readout time improvement possible by exploiting the region of interest (ROI) capability of the Skipper CCD [23, 16, 23] (see Section 6.2 for a complete description of the ROIs implemented in the observations with the SIFS-Skipper). In Figure 4.6 we showed that by reducing the readout noise to levels $\sim$ 0.7 e$^-$rms/pix, we would expect a $\sim$ 30% improvement of the instrument efficiency. We conducted a similar study in [16] and showed similar improvements, with sub-electron readout noise, for Lyman-α observations with DESI. It would take $\sim$ 40 min to reach $\sim$ 0.7 e$^-$rms/pix in all detector pixels, considering a 4k $\times$ 6k area coverage for the entire prototype focal plane. We can define a geometrical area on the Skipper CCD (e.g., 5% of the detector area) that is read with multiple samples. For our implementation, this ROI corresponds to a specific wavelength range produced by the SIFS spectrograph. The ROI can be read with reduced noise while the rest of the detector is read once with single-sample noise.

As an example, we use each integration window instance time and single-sample readout noise (top panel in Figure 5.4) to find the optimal configuration of pixel integration time

and number of samples (N_{samp}) to reach $\sim$ 0.7 e$^-$ rms/pixel in 5% of the detector area and minimize the readout time per frame. From Eqn. 3.4, which describes the relationship between readout noise and number of non-destructive read samples (N_{samp}), one sees that $N_{\text{samp}} = (\frac{\sigma_1}{\sigma_N})^2$ where σ_N is the target sub-electron readout noise and σ_1 is the optimal single-sample readout noise in Figure 5.4 top panel. For each N_{samp} and integration time (t_{pixel}), we use Eqn. 5.1 to calculate the total readout time. Figure 5.5 shows the optimal pixel integration time ($\sim$ 20 μs) that minimizes the total readout time for a frame with $\sigma_N = 0.7$ e$^-$ rms/pixel in 5% of the pixels. We can then calculate the total readout time for a full frame where 5% of the detector is readout with $\sim$ 0.7 e$^-$ rms/pixel and the remaining 95% with single-sample readout noise, which comes out to $t_{\text{readout}} \sim 3.6$ min.

5.4 Skipper CCD Enabled Characterization Tests

The ultra-low noise capability of the Skipper CCD enables several interesting measurements of detector performance in the photon-counting regime. For instance, the capability to resolve individual electrons, allows for a precise measurement of the detector's gain, the conversion between Analog-to-Digital Units (ADUs) and electrons. Furthermore, resolving individual electrons allows for non-linearity measurements at low signals, which can be challenging to perform with conventional scientific CCDs.

5.4.1 Readout Noise Characteristics and Photon-Counting

The readout noise of a Skipper CCD is tunable through multiple non-destructive measurements of the charge in each pixel. For uncorrelated Gaussian noise, the effective readout noise distribution from averaging N_{samp} non-destructive measurements scales as $\sigma_N \propto 1/\sqrt{N_{\text{samp}}}$ (Eqn. 3.4). We note that the readout noise is a combination of intrinsic electronic noise and external noise sources, which are dependent on specific testing stations and factors such as electronic grounding. We measure the readout noise from processed images, i.e., overscan

subtracted images. To account for non-uniformities in the overscan pedestal level, the overscan subtraction algorithm fits the pixel distribution of each row in the overscan region with a multi-Gaussian model and subtracts the mean of the 0 e^- peak to that row. Similarly to [16] and [142], the readout noise we measure is given by the standard deviation of the 0 e^- peak. Figure 5.6 shows a 600 $\times$ 3200 pixel image where the overscan region starts at pixel 3080. The middle panel plots the structure of the pedestal in the overscan and activated regions in a single-sample image. We observe a slowly decaying transient that is correlated with row number; this same behavior is present in both multi- and single-sample images. The pedestal subtraction algorithm is able to correct for this row-dependent variation as observed in the bottom panel (pedestal subtracted traces).

We measure the readout noise for all 32 AstroSkipper amplifiers (eight detectors with four amplifiers per detector) and find values ranging from 3.5 e^- rms/pixel to 5 e^- rms/pixel; the six astronomy-grade detectors maintain a readout noise $< 4.3\,e^-$ rms/pixel for all 24 amplifiers. In Figure 5.7, we show an example of photon-counting (Left) and noise reduction (Right) achieved by one of the AstroSkippers with 400 samples per pixel. To simplify the calculation of the readout noise as function of $N_{\rm samp}$, we again implement the charge-less readout by not integration charge to measure only the noise characteristics of the system. The measured noise varies from the expected Gaussian noise model (Eqn. 3.4) by $\lesssim 20\%$ for $N_{\rm samp} < 10$ and 10% for $N_{\rm samp} > 150$ (Figure 5.7, Right).

We note that the greatest contribution to variations in the noise model comes from instabilities in the first few samples. Similar behavior was seen in early testing of Skipper CCDs [13], where it was postulated that variations in the readout noise at low $N_{\rm samp}$ are produced by residual low-frequency noise and fluctuations at large samples might be due to external or unidentified sources of noise coupling to the readout electronics. At low sample numbers, fluctuations in the clock induced transients can dominate the noise behavior; however these transients settle as $N_{\rm samp}$ increases. For instance, if the averaging starts from $N_{\rm samp} = 5$,

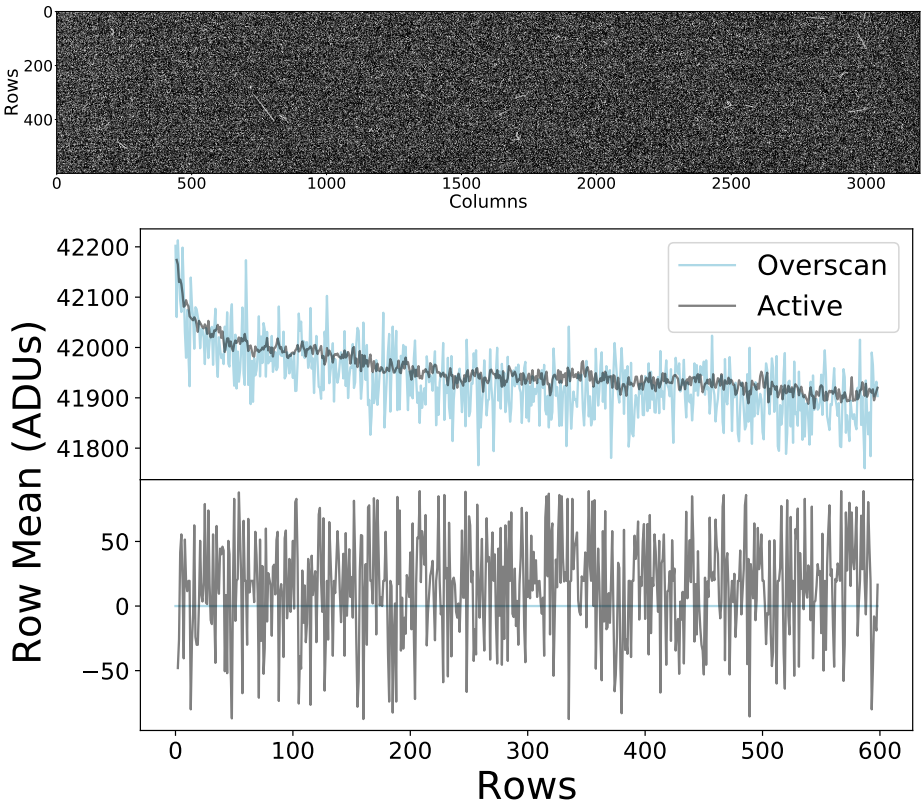

Figure 5.6: Top: Single-sample image from one AstroSkipper quadrant (600 × 3200 pixels) with overscan region starting at the 3080 pixel. Middle: Average pixel value calculated per row in the overscan (blue) and active (black) regions of the detector. A large scale transient correlated with row number can be seen. Bottom: Same as the middle panel, but after row-by-row overscan pedestal subtraction. The algorithm corrects the slowly decaying transient associated with row number.

the variation in the noise measurements with respect to the Gaussian noise model reduces to $< 3\%$ for all sample numbers. Figure 5.8 shows the single (σ_1) and multi-sample (σ_{400}) noise performance for each amplifier and detector.

Since each peak in the pixel distribution histogram (Figure 5.7) differs from its neighbor by a single electron, we can obtain a direct measurement of the detector's gain by calculating the difference between adjacent electron peaks, i.e., the gain would be given by $\Delta_{i,i+1}$ where $\Delta_{i,i+1} = \mu_{i+1} - \mu_i$ is the difference between the means of the Gaussians fits to the i and $i+1$ adjacent electron peaks. Figure 5.9 shows gain measurements per amplifier from the six AstroSkippers; gain measurements depend on resolving electron peaks in each amplifier,

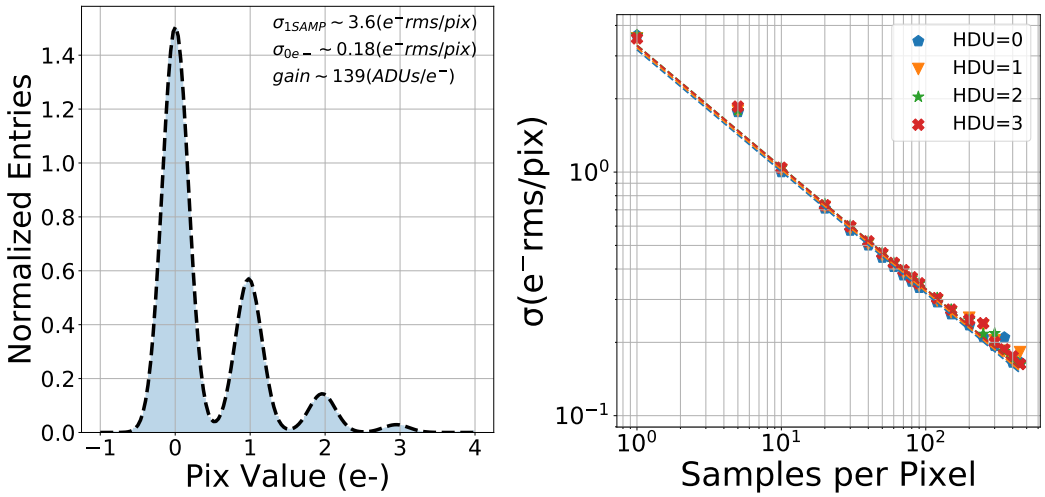

Figure 5.7: Readout noise characteristics and photon-counting for one of the AstroSkipper CCDs. Left: Histogram of the pixel values for one amplifier calculated from the average of 400 non-destructive measurements (samples) per pixel (cyan histogram). The low noise($\sigma_{0e-} \sim 0.18$ e$^-$ rms/pixel) achieved after N_{samp}=400 resolves single electrons/photons. We see photon-counting capabilities in all amplifiers from the six AstroSkippers. We fit the distribution of pixel values with a multi-Gaussian model. The gain of the detector can be directly calculated from the difference between the mean values in ADUs of adjacent electron peaks. Right: Readout noise for four amplifiers as a function of the number of non-destructive measurements of each pixel (N_{samp}). The measurements deviate from the expectation from Eqn. 3.4 (dashed line) by as much as 20% and 10% for $N_{\text{samp}} < 10$ and $N_{\text{samp}} > 150$, respectively.

and applying the method described above. We use the 0 e$^-$, 1 e$^-$, and 2 e$^-$ electron peaks ($\Delta_{0,1}$, $\Delta_{1,2}$) and take the average between both $\Delta_{i,i+1}$ to calculate these gain values for all amplifiers. We measure gain values ranging from $\sim$123 ADU/e$^-$ to $\sim$143 ADU/e$^-$ (left) for amplifiers on all six of the astronomy-grade AstroSkippers with average variations of $< 6\%$ between gain values from all amplifiers. We do not see any clear correlation between amplifier gain and amplifier noise.

5.4.2 Non-linearity

The AstroSkipper's large dynamic range and ability to count individual charge carriers enables a unique avenue to measure linearity at both low and high illumination levels. At high

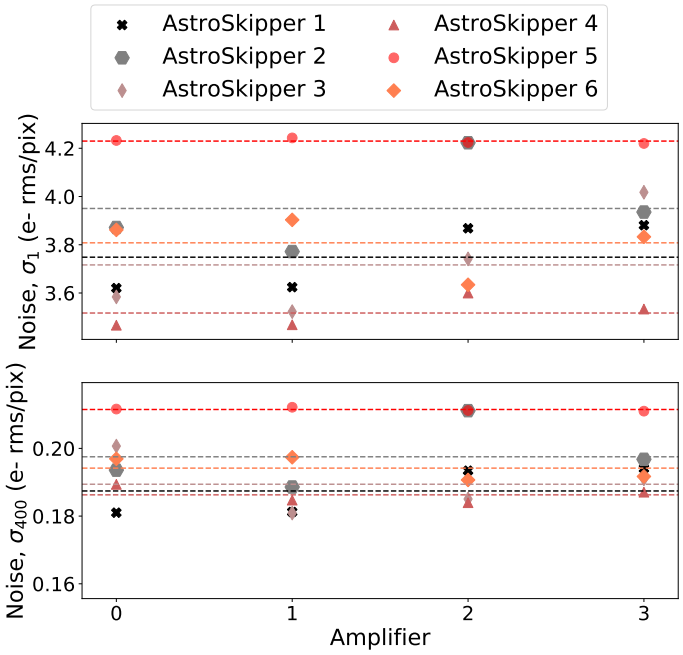

Figure 5.8: Variation in the noise characteristics of the four amplifiers in the six selected Skipper CCDs. Top: single-sample readout noise values for each amplifier. Bottom: noise performance per amplifier after taking 400 non-destructive measurements of the charge in each pixel. Dotted lines are the average readout noise for a given amplifier.

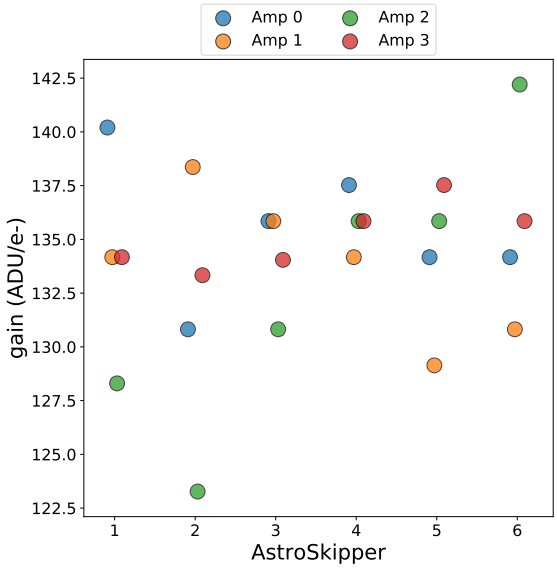

Figure 5.9: Gain measurements for all amplifiers for the six AstroSkipper CCDs. Gain calculated using separation between electron peaks in each detector's amplifier for all six AstroSkippers. We see variations of $< 6\%$ on average between gain values in all amplifiers; amplifiers 1 and 2 show the largest variation on average for all detectors.

illumination levels, we follow a conventional approach to measure non-linearity by increasing exposure times. We study a wide range of images taken with high illumination levels from 1500 e^-/pixel to values near saturation. The data taking procedure consists of taking ~ 20 flat-fields with increasing illumination; we perform bias subtraction and sigma clipping to eliminate cosmic rays on each frame.

We calculate non-linearity following the procedure implemented by Bonati et al. 141 to measure the non-linearity of the DESI detectors. To compute the non-linearity over our data set of 20 flat-field images, we implement a least-squares fit to minimize the sum of the squares of the error $E(\alpha, \beta) = \sum_{n=1}^{20}(y_n - (\alpha x_n + \beta))^2$. Here n indexes over the images, y_n is the mean of the pixel values for image n, x_n is the exposure time for image n, and α and β are the parameters of the linear fit. We find the values of α and β that minimize $E(\alpha, \beta)$, i.e., $\partial E/\partial\alpha = 0$, $\partial E/\partial\beta = 0$. The non-linearity factor is then given by the mean value of the square-root of the residuals $E(\alpha, \beta)$. We find non-linearity values $< 0.05\%$ for all of the amplifiers in the six AstroSkipper CCDs.

In conventional CCDs, low-signal level non-linearities are poorly understood since these CCDs lack the precision to quantize charge in the single-electron regime. In contrast, Skipper CCDs can quantify non-linearties for all electron occupancies, i.e., they can resolve electron peaks for the full range. For instance, in [143] non-linearity measurements for a subset of DECam devices show poorly understood behavior at low illumination levels (few tens of electrons). The AstroSkipper allows us to precisely characterize non-linearity in this regime of a few tens of electrons following a procedure similar to the one described in [144]. In the photon-counting regime, one can probe non-linearities by measuring variations in the relationship between the number of electrons in each pixel and the signal readout value in ADUs (i.e., the gain).

We take several flat-field images with 400 samples per pixel to reach single-electron resolution with $\sigma_{400} \sim 0.18$ e^-/rms/pixel. Images are taken with increasing exposure time

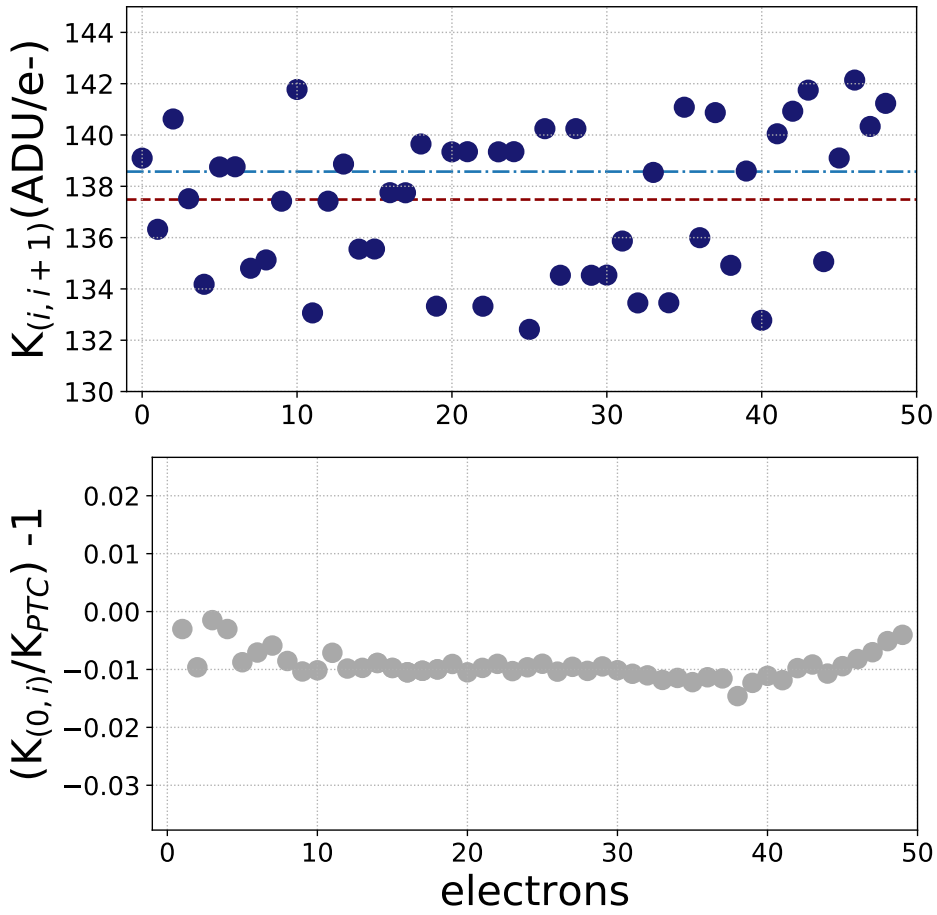

Figure 5.10: Top: Gain values calculated from peak-to-peak separation of individual electron peaks, i.e., $\mu_{i+1} - \mu_i$. The average gain is ~ 139 ADU/e$^-$ (red dashed line) with a scatter about this mean of $< 4\%$. The blue dash-dotted line represents the gain value estimated from the slope of the signal variance vs. the signal mean in the PTC. Bottom: Ratio between the gain measured from the difference between the 0^{th} and i^{th} electron peak, i.e., $(\mu_i - \mu_0)/i$, and the constant gain value from the PTC. We observe a $\sim 1\%$ agreement between the two methods for determining the gain and $< 1\%$ variations in the gain as measured from electron peak.

where the set of images produced different overlapping Poisson distributions with increasing mean number of electrons [144]. We resolved up to 50 e$^-$, i.e., it is possible to count individual peaks up to the 50^{th} electron peak in the set of images. To perform the non-linearity measurement, we fit each electron peak with a Gaussian and compute the gain from each peak by dividing the mean value of the difference between the electron peak and the 0 e$^-$ peak in ADU by the peak's assigned electron number, $(\mu_i - \mu_0)/i$. For example

the gain calculated from the 10^{th} electron peak would be given by $(\mu_{10} - \mu_0)/10\text{e}^-$ where $(\mu_{10} - \mu_0)$ is the difference (in ADU) between the means of Gaussian fits to the 0 e^- and 10 e^- peaks and 10 e^- is the assigned number of electrons for that peak. We note that this method for charge quantization results in increased variability when computing gain values at low electron counts and diminishes for higher electron counts since variations in the mean get divided by the amount of charge. If we instead calculate the gain from the peak-to-peak separation, i.e., $\mu_{i+1} - \mu_i$, we find a consistent gain with a scatter of $< 4\%$ between individual electron peaks (though we note that adjacent points are highly correlated).

Figure 5.10 (Top) shows peak-to-peak gain calculations and as expected, we observe a greater spread between gain values. The bottom panel shows a low-signal non-linearity measurement for one of the AstroSkippers where we represent the non-linearity as the deviation from unity of the ratio between the gain calculated as $(\mu_i - \mu_0)/i$ and the fixed, conventional gain value measured from the slope of the variance versus the signal in the PTC (Section 5.6.3). We find non-linearity values that are $< 1.5\%$ at this low-signal regime of a few tens of electrons which agrees with values reported in [144] ($< 2.0\%$). Furthermore, this method for calculating non-linearity also shows the agreement between PTC and charge quantization gain calculations. Similar to Drlica-Wagner et al. (2019), we find that the gain measurements from the two methods agree within $\sim 1\%$ (Figure 5.10, Bottom).

5.5 Clock Induced Charge and Voltage Optimization

CIC can be an appreciable background for measurements in the single-photon/single-electron regime [e.g., 7, 145]. The SENSEI direct DM detection experiment measures a CIC rate of $\sim 1.52 \times 10^{-4}$ e^-/pixel/frame with a low-voltage configuration for a Skipper CCD similar in pixel and readout configuration to the AstroSkipper [146]. Implementing this low-voltage configuration under the AstroSkipper testing conditions, we measure an average electron rate of $\sim 1.45 \times 10^{-3}$ e^-/pixel/frame, which sets an upper limit on the CIC contribution. The

full-well capacity in this configuration is ~ 900 e$^-$. Considering the AstroSkipper application, it is important to study the trade-off between CIC and full-well capacity. Achieving full-well capacities suitable for the anticipated signal levels from calibration and data products for SIFS requires using higher voltages than SENSEI; however, higher voltage swings, specially in the serial register, increase CIC. Thus, CIC can become an important background for astronomical measurements with the AstroSkipper. Therefore, we study CIC production in the AstroSkipper and optimize voltages to reach high full-well capacities for the SIFS application while minimizing CIC and maintaining photon-counting capabilities.

5.5.1 CIC in the AstroSkipper

CIC is generated during the clocking sequence when inverting clocks between the high and low-voltage states. When switching the clock to the non-inverted state, holes that become trapped at the Si-SiO_2 interface during clock inversion are accelerated with sufficient energy to create electron-hole pairs through impact ionization [7]. Released electrons are then collected in the summing well and contribute to the overall readout signal. In conventional CCDs, where the noise floor can be > 5 e$^-$ rms/pixel, CIC is not apparent, i.e., the charge produced by CIC can be characterized as shot noise with a contribution of $N_{\rm CIC} = \sqrt{\mu_{\rm CIC}}$ where $\mu_{\rm CIC}$ is the average CIC in electrons [7] and for $\mu_{\rm CIC} = 3$ e$^-$/pixel/frame (typical value observed with an AstroSkipper at high operating voltages) the CIC noise contribution of ~ 1.7 e$^-$ rms/pixel would be lower than the noise floor and thus undetectable. However, for ultra-low-noise detectors operating in the photon-counting regime, CIC is an important source of background for observations of faint sources [e.g., 147].

As a demonstration of the potential noise increase due to Clock-Induced Charge (CIC), consider Figure 5.11. The top panel in Figure 5.11 shows the pixel distribution for a single-sample dark frame (where no charge accumulation occurs), captured using two different voltage configurations for the serial register: low voltages ($\Delta H = 2.5$ V) and high voltages

(ΔH = 9 V). It is evident that the high voltage configuration produces a higher readout noise level (4.4 e$^-$rms/pix) compared to the expected baseline noise level (3.5 e$^-$rms/pix) of the AstroSkipper.

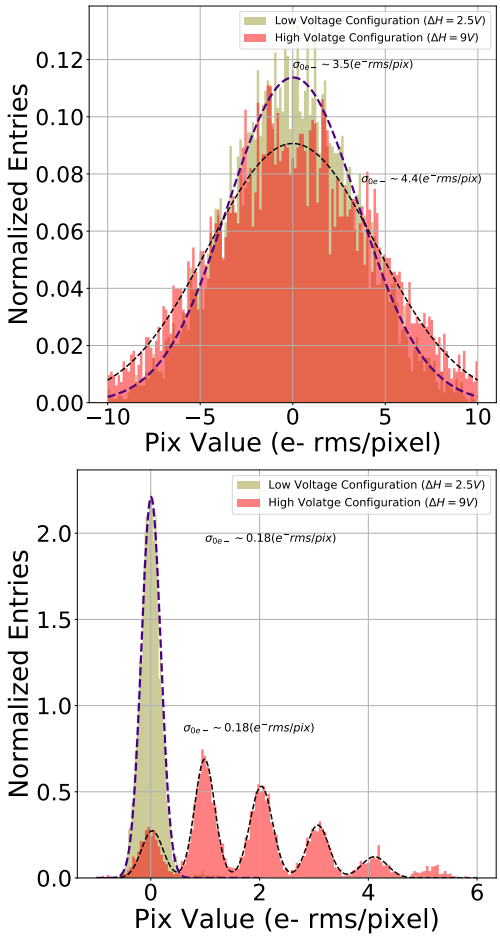

Figure 5.11: Top: Pixel distribution from a pair of single-sample dark frames (no charge accumulation) acquired with a low and high voltage configuration of the horizontal clocks (serial register). The readout noise is calculated from a Gaussian fit to the distributions. The high voltage configuration exhibits an increase in noise (4.5 e$^-$rms/pix) compared to the expected baseline noise for the AstroSkipper (3.5 e$^-$rms/pix). Bottom: The "extra" noise contribution to the single-sample frame, in the high voltage configuration, comes exclusively from CIC electron rate as evident by the quantized electron peaks (red pixel distribution).

One might initially suspect that the increase in readout noise is related to a correlation between full-well capacity and noise. However, it becomes clear (as shown in the bottom panel of Figure 5.11) that CIC is the true cause of this noise increase. In a pair of electron-

resolution frames, taken with both low and high voltage configurations, the readout noise calculated from the standard deviation of the 0 e^- peak remains consistent between the two configurations. However, in the high voltage configuration pixel distribution, extra "charge" is observed, quantized in the form of electron peaks, which contributes to the overall increase in readout noise seen in the single-sample case.

We focus on optimizing the CIC with respect to the horizontal clock swings since we find that CIC produced in the activated area is negligible compared to CIC generated in the serial register. First, we build a statistical model to predict the electron event rate from CIC as a function of the horizontal clock voltage swings. Since CIC can be characterized as shot noise, we assume it obeys Poisson statistics and therefore the expected CIC electron rate is given by the Poisson probability mass function (PMF):

$$P(X = k) = \frac{\exp(-\mu)\mu^k}{k!} \tag{5.3}$$

where $P(X = k)$ gives the probability of observing k events (CIC electron rate) in a given interval, and μ is the average rate of CIC electron events for the full readout sequence.

Furthermore, we assume that the average rate of CIC electron events (μ) can be modeled with an exponential, which describes the growth of CIC electron events with respect to the horizontal clock swings,

$$\mu = a \exp(b\Delta H) + c. \tag{5.4}$$

Here ΔH is the horizontal clock voltage swing and a, b, and c are fit parameters. To calculate the best fit for μ, we take several dark frames with increasing ΔH and electron resolution ($N_{\text{samp}} = 400$, $\sigma_{400} \sim 0.18$ e^- rms/pixel) in order to resolve single electron rates from CIC. To get μ, we fit a single Gaussian model to the pixel distribution, containing CIC electron rate peaks, and subtract the background, which is calculated with the low-voltage configuration that generates minimum CIC (i.e., $\lesssim 1.45 \times 10^{-3}$ e^-/pixel/frame). We fit an

exponential model to find the values of a, b, and c in Eqn. 5.4.

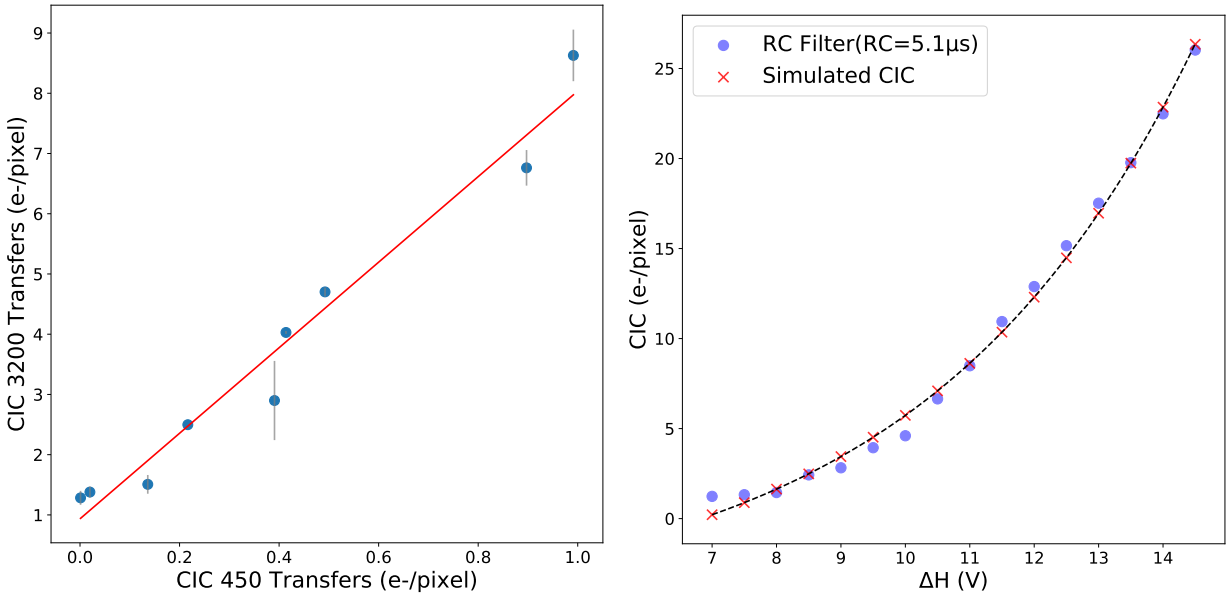

Figure 5.12: Modeling CIC generation. Left: Linear relationship between CIC and number of transfers in the serial register. Each data point corresponds to a different horizontal clock swing value. CIC increases linearly with number of transfers as seen from comparing CIC on two CCDs of different sizes (3200 versus 450 transfers). Right: Simulated and measured CIC for the AstroSkipper. The number of transfers (3200 per amplifier), the horizontal clock width, and the filter (RC filter with $\tau = 5.1\mu s$) are fixed. The model assumes Poisson statistics. We only consider variation in the horizontal clock swing which causes the highest electron rate generation compared to vertical and transfer gate clocks. We measure better than $\sim 10\%$ agreement between model and data for $\Delta H > 7.5$V.

The number of transfers in the serial register is closely related to CIC [7]; the probability of generating a CIC electron event increases as the pixel is clocked more times in the serial register. To investigate how the number of transfers (NT) affect our probabilistic model, we calculate CIC for one quadrant of the smaller format (1248 $\times$ 724, 15 μm $\times$ 15 μm pixels) Skipper CCD characterized in [16]. We use the voltage configurations tested in the AstroSkipper and repeat the same data taking procedure, i.e., dark frames ($\sigma_N \sim 0.18$ e$^-$rms/pixel). We consider CIC_{1i} and CIC_{2i}: the average CIC electron rate per pixel per frame from the smaller Skipper CCD and the AstroSkipper, respectively. Assuming a linear relationship between both data sets (informed by CIC production in Janesick 7), the linear

regression model is

$$CIC_{2i} = \beta_0 + \beta_1 \cdot CIC_{1i} + \epsilon_i \tag{5.5}$$

where β_0 is the rate of CIC generation, related to the relative NT between both detectors, β_1 is the intercept, and ϵ_i is the error term associated with the ith observation in CIC_{2i}. We perform a linear regression to find β_0 and β_1, minimizing the sum of squared residuals, $\sum \epsilon_i^2$. Figure 5.12 (Left) shows the linear relationship between CIC_{1i} and CIC_{2i} with $\beta_0 \sim 7.1$ (a factor of 7 increase in CIC for the AstroSkipper with 3200 transfers compared to 450 transfers for the smaller Skipper CCD).

Figure 5.12 (Right) shows the simulated CIC rate from the statistical model, i.e., random draws from the Poisson PMF, and the measured data; we see better than ∼10% agreement, for $\Delta H > 7.5$V, between the model and the measured data. We note that this model assumes a fixed horizontal clock filtering solution, and horizontal clock width. In future work, we will generalize the statistical model formalism to include the effect from varying clock pulse width, i.e., the time the clock spends in the non-inverted state immediately after inversion, and the CIC reduction from different clock shaping solutions [7, 148, 149].

Because CIC is closely linked to horizontal clock voltage swing (ΔH) and the full-well capacity is also dependent on ΔH, we must optimize CIC and full-well capacity for the expected signal levels in the application. To mitigate CIC, we have implemented a simple filtering solution consisting of a first-order low-pass filter with a time constant $\tau = 5.1$ μs placed between the pre-amplification stage and the LTA. This allows for a factor of ~ 2 reduction in CIC electron events for $\Delta H > 9$V, which yields the highest full-well capacity.

5.5.2 Voltage Optimization

The small voltages used for these rare particle searches limit the dynamic range of the Skipper CCD, which can be problematic for most astronomical applications. We perform a voltage optimization for the AstroSkipper in order to increase the dynamic range while maintaining low CIC, stable readout noise, and photon-counting capabilities.

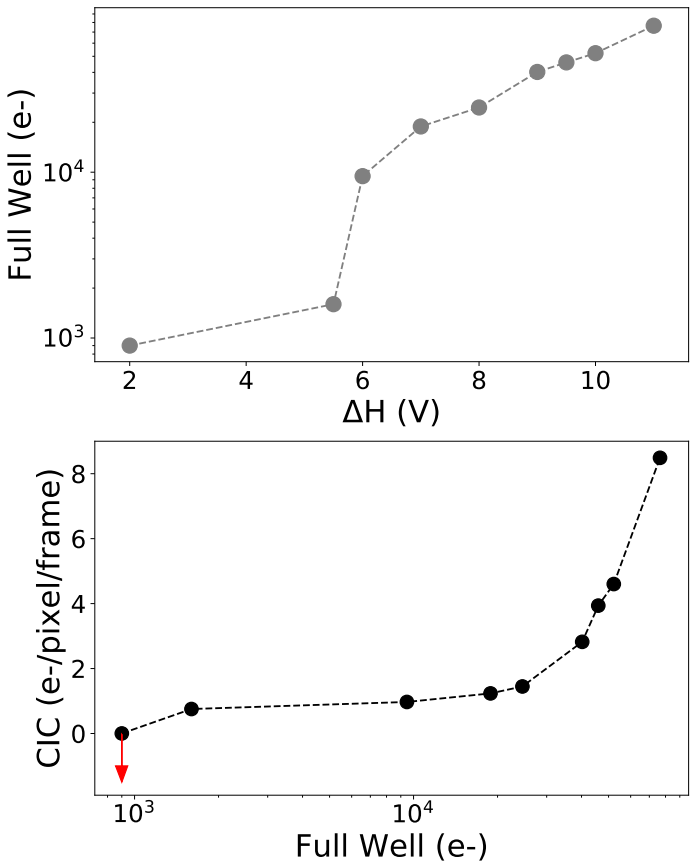

Figure 5.13: Top: full-well capacity as a function of the horizontal clock voltage swing (ΔH). Bottom: CIC event rate versus full-well capacity. We measure an upper limit on the CIC (red arrow) with the SENSEI voltage configuration (1.45×10^{-3} e$^-$/pixel/frame), resulting in a full-well $\sim$ 900 e$^-$. Increasing the horizontal clock swing to $\Delta H = 6$ V increases full-well capacity to $\sim$ 10,000 e$^-$ at a CIC rate of $\sim$ 1 e$^-$/pixel/frame and for $\Delta H = 9.5$ V we obtain a CIC rate of $\sim$ 3 e$^-$/pixel/frame and a full-well capacity $> 40,000$ e$^-$.

The full-well capacity is derived from the PTC. Due to the CIC and full-well dependence on the horizontal clocks swing voltage, we optimize ΔH for reducing CIC while maintaining

a full-well capacity suitable for the expected signal levels from SIFS ($\lesssim 1000$ e$^-$ for science images and $> 40,000$ e$^-$ for calibration products). Figure 5.13 shows the full-well capacity for increasing ΔH (top), which approaches levels comparable to other thick, fully-depleted CCDs [103], and the CIC levels expected for each full-well (bottom). We measure an upper limit on the CIC using the low-voltage configuration from SENSEI (red arrow in Figure 5.13, bottom panel); however, the full-well capacity at these voltages (~ 900 e$^-$) is inadequate for the SIFS application.

In our optimization tests, we find that a CIC rate of ~ 1 e$^-$/pixel/frame is possible with a corresponding full-well of $\sim 10,000$ e$^-$, which is adequate for the expected signal levels in science data products. However, we expect signals of $\sim$40,000 to 50,000 e$^-$ in calibration data products. Configuring voltages for these signal levels results in a CIC rate of ~ 3 e$^-$/pixel/frame. The achieved CIC rate for the high-voltage configuration is an unacceptable source of noise if the expected signals are in the order of a few electrons. We note that it might be possible to maintain a large full-well capacity while retaining low CIC to levels ($\lesssim 10^{-3}$ e$^-$/pixel/frame) by employing waveform shaping [e.g., 138]. Shaping the clock pulse rise time and sharpness, which play a critical role in CIC generation, has been shown to reduce CIC in EMCCDs [150, 147].

This is the first time that full-well capacities of $\sim 40,000$ to $50,000$ e$^-$ have been demonstrated with a Skipper CCD. This was achieved in a configuration with a horizontal clock swing, $\Delta H = 9.5\,$V, a vertical clock voltage swing, $\Delta V = 5\,$V, and a transfer gate clock voltage swing, $\Delta T = 5\,$V. We discovered that the floating sense node reference voltage can be a limitation in increasing the dynamic range. Furthermore, it is important to optimize this reference voltage for both full-well and "skipping" functionality. As we have discussed in a Skipper CCD the charge packet is readout in the floating node. To move the charge back the SW voltage is set to a value lower than the S/N reference voltage, repeating $N_{\rm samp}$. If the voltage gradient between the SN and SW is not "extreme" enough, the charge will not

flow back. We optimized the sense node reference voltage to achieve the targeted full-well while maintaining the ability for photon-counting.

5.6 Conventional Characterization Tests

The implementation of conventional CCD characterization tests is important to evaluate the performance of the AstroSkipper CCDs. These tests not only allow us to assess the performance of individual AstroSkipper detectors in order to select the best detectors for SIFS, but also serve the broader purpose of comparing the AstroSkipper to other thick, fully-depleted CCD devices used in astronomical applications. For example, we demonstrate comparable metrics for CTI, DC, BFE, detector cosmetics, charge diffusion and QE between the AstroSkipper and well-characterized detectors used for DECam and DESI.

5.6.1 Dark Current (DC)

We use DC to refer to the electron events generated in the CCD during exposure and readout phases of data collection. These electron events are unrelated to the transfer of the charge between pixels (CIC). We note that the DC value reported for the AstroSkipper is an upper bound as it includes contributions from light leaks and other environmental sources.

The measurements of DC consists of acquiring 10 single-sample dark exposures with 400 seconds of exposure time. A combined dark, consisting of the median from 10 images, is calculated to remove cosmic rays and any transient effect; the combined dark is overscan subtracted and the signal mean is calculated over the activated area, divided by the exposure time, and normalized by the detector's gain. We measure DC values of $\sim 2 \times 10^{-4}$ e^-/pixel/s for the six astronomy-grade AstroSkippers. Despite the fact that we tested the AstroSkippers in a dark room, light leaks dominate the electron event rates in our DC measurement and increase linearly with exposure and readout time. Previous DC measurements for astronomy performed with a similar setup in ambient lighting yielded DC values an order of magnitude

higher ($\sim 10^{-3}$ e$^-$/pixel/s; Villalpando et al. 142).

Barak et al. (2020) reports a significantly lower DC value of 6.82×10^{-9} e$^-$/pixel/s for a Skipper CCD operating underground. In contrast to our measurements, the DC measurements reported in Barak et al. 125 are performed underground with a Skipper CCD that is shielded from environmental radiation. For detectors with single-photon capabilities, external effects that increase the dark rate even by a small amount can be a problematic source of noise in the low-signal regime.

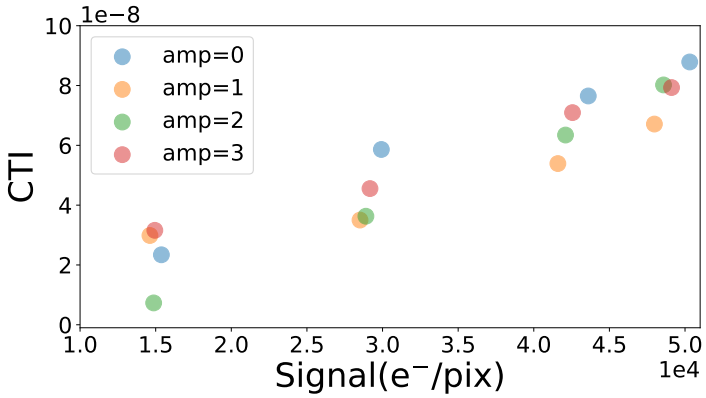

Figure 5.14: Average CTI versus signal for four amplifiers in one of the selected AstroSkippers. The average CTI for all 24 amplifiers is 3.44×10^{-7}.

5.6.2 Charge Transfer Inefficiency (CTI)

To characterize CTI, we implement the extended pixel edge response method (EPER). EPER consists of measuring the amount of deferred charge found in the extended pixel region or overscan of a flat-field at a specific signal level. CTI is calculated from the EPER as

$$CTI = \frac{S_D}{S_{LC} N_P}, \tag{5.6}$$

where S_D is the total deferred charge measured in the overscan in electrons, S_{LC} is the signal level (e$^-$) of the last column in the detector's activated area and N_P is the number of pixel transfers in the serial register [7]. For our CTI measurement, we take a number of

flat-fields at increasing illumination levels (∼10,000 e^- to ∼ 50,000 e^-); Figure 5.14 shows the average CTI for all of the amplifiers in one of the AstroSkippers versus signal level. We calculate an average CTI value of 3.44 $\times 10^{-7}$ from the 24 amplifiers on the six astronomy-grade AstroSkipper CCDs, which is about an order of magnitude lower compared to the one we reported previously in [16].

5.6.3 Photon Transfer Curve (PTC) and Brighter-fatter Effect (BFE)

The PTC characterizes the response of a CCD to illumination and can be used to measure the detector's gain and dynamic range. A PTC is constructed by taking several flat-fields at increasing illumination level, which then can be used to show how the variance in the signal changes with the mean flux level of uniformly illuminated images. To eliminate non-uniformities, e.g., variations in the illumination and CCD cosmetic defects, the PTC is calculated with the difference between pairs of flat-fields.

It is assumed that charge collection in pixels exactly follows Poisson statistics, and therefore, pixels are independent light collectors. In this idealized case, the variance versus the signal mean should be linear, once the readout noise is negligible, with a 1/gain slope until pixel saturation. However, at high signal levels this assumption breaks, causing a loss in variance as the PTC linear behavior flattens out. Furthermore, binning neighboring pixels improves the linearity of the PTC [151, 14]. This indicates that correlation arises between neighboring pixels as charges migrate from one pixel to another, producing transverse electric fields on incoming photocharges [152]. The repulsion effect between photocharges in a pixel's potential well causes quasistatic changes in the effective pixel area, for astronomical observations, biasing the light profile from a bright source.

This effect is known as the brighter-fatter effect (BFE), which can bias the point-spread function (PSF) from a source by ∼ 1% and the shear of faint galaxies, posing an unacceptable systematic for large imaging surveys if not corrected [153, 154, 15, 14, 155]. At the

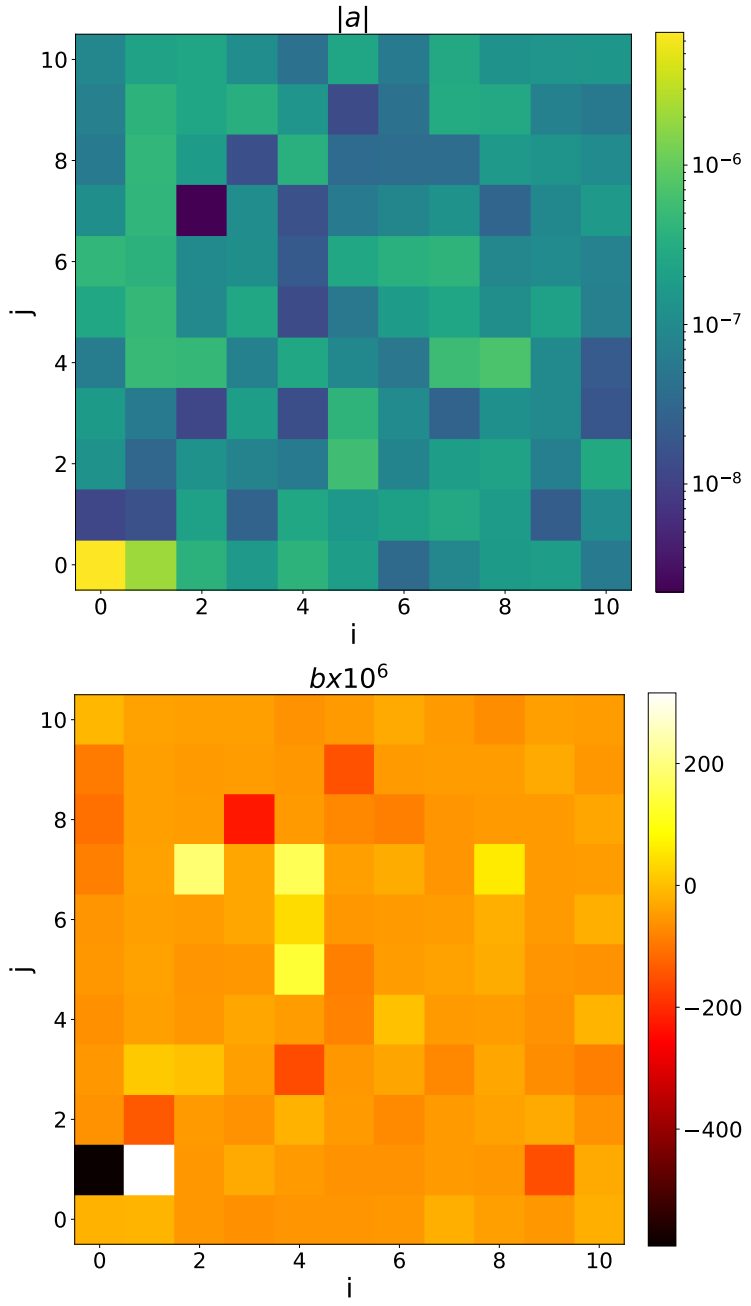

Figure 5.15: Top: Measured a_{ij} from the electrostatic model (Eqn. 5.7). Bottom: Measured b_{ij} from Eqn. 5.7. Both matrices come from the fit to the electrostatic model using the method described in [14]. We measure $a_{00} = -6.78 \times 10^{-6} 1/e^-$. This factor dominates the pixel area change as charge accumulates (biggest contribution to the BFE). We note the asymmetric correlation between neighboring pixels ($a_{10}/a_{01} \sim 2.51$) due to difference in pixel boundaries between the row and column directions [15].

detector level the BFE has been observed on DECam, Hyper Suprime-Cam, and LSSTCam fully-depleted CCDs [153, 14, 155]. Astier et al. (2019) proposes an electrostatic model to characterize the time-dependent build-up of correlations in flat-fields. The model describes the resulting correlation between pixels that grow with increasing flux and decay rapidly as photocharges migrate to neighboring pixels, resulting in a loss of covariance. The covariance function, that describes the change in effective area as a result of BFE, for a given signal level (μ) is given by:

$$C_{ij}(\mu) = \frac{\mu}{g}\Big[\delta_{i0}\delta_{j0} + a_{ij}\mu g + \frac{2}{3}(\mathbf{a}\otimes\mathbf{a} + \mathbf{ab})_{ij}(\mu g)^2 + \frac{1}{6}(2\mathbf{a}\otimes\mathbf{a}\otimes\mathbf{a} + 5\mathbf{a}\otimes\mathbf{ab})_{ij}(\mu g)^3 + ...\Big] + \frac{n_{ij}}{g} \tag{5.7}$$

where a_{ij} describes the strength of the changes in pixel area due to the accumulated charge and has units of $1/\mathrm{e}^-$, b_{ij} describes other contributions to the pixel area change, e.g., shortened drift time and asymmetries in how charges are stored in pixels, g is the detector's gain, n_{ij} is a matrix that contains noise components with n_{00} being the traditional readout noise, and $\otimes$ refers to the discrete convolution. We follow the method in Planck Collaboration [3] and perform the fit for our covariance function up to signal values close to saturation ($\sim 8 \times 10^6$ ADUs) up to $O(\mathrm{a}^{10})$ terms, resulting on a 11×11 covariance matrix as a function of mean signal from the difference of flat-field pairs, taken at increasing illumination level. Figure 5.15 shows the recovered 11×11 a_{ij} and b_{ij} pixel matrices.

We note that $|a_{00}| > a_{ij}$ and therefore a_{00} is the biggest contributor to pixel are change, i.e., the quantity that describes the strength of the BFE [14, 155]. In Figure 5.16, we show the a and b matrices best fit values averaged over all amplifiers from an AstroSkipper detector as a function of distance with error bars representing the uncertainty from all the averages. We see that a decays rapidly and becomes isotropic; similarly to [14], we see that b is negative except for b_{01}, which might indicate a parallel distance increase in the charge cloud as charge

accumulates.

Astier et al. (2019) fit the electrostatic model (Eqn. 5.7) for a LSST Teledyne e2V 250 device with a thickness of 100 μm, operated at a substrate voltage of 70 V. They find $|a_{00}| = 2.377 \times 10^{-6}$. Astier and Regnault (2023) perform a BFE analysis for the CCDs in the Hyper Supreme-Cam, which uses deep-depleted, 200 μm thick Hamamatsu CCDs, operated with a substrate voltage of < 50 V [156]; they measure $|a_{00}| = 1.24 \times 10^{-6}$. We measure an average value of $|a_{00}| = 6.153 \times 10^{-6}$. We note that the AstroSkipper a_{00} higher value might be due to the thickness (250 μm) and the operating substrate voltage (40V) as explained by a physics-based model from [152], which shows that the PSF size depends on detector thickness and substrate voltage.

For spectroscopy, especially applications where the line's structure profile is important, i.e., radial velocity structure of radiative transfer effects in an object [157], the BFE can be an important systematic. Furthermore, as part of spectroscopic data reduction, sky subtraction and wavelength calibration depend on sky lines and calibration lamp data, which often have a signal level that is significantly higher than the science data, sometimes approaching the detector's full-well capacity. This situation could potentially bias science measurements due to the BFE. We note that further studies of the BFE in the context of spectroscopy are needed to fully determine how the BFE may bias various spectroscopic measurements, e.g., redshift recovery, equivalent widths, velocity dispersion, etc. For instance, assuming that DESI detectors have similar BFE characteristics to those measured in the AstroSkipper, it would be possible to use DESI data to measure the impact of the BFE on DESI science and predict the potential impact of the BFE on future spectroscopic cosmology surveys (e.g., a Stage 5 spectroscopic survey [5]).

The shape of the PTC curve (variance vs. signal mean) can be approximated by considering the first element (the variance) in the covariance matrix, i.e., C_{00} and a_{00} in the Taylor expansion of Eqn. 5.7. The PTC curve as a function of μ with g, n_{00}, and a_{00} as fit

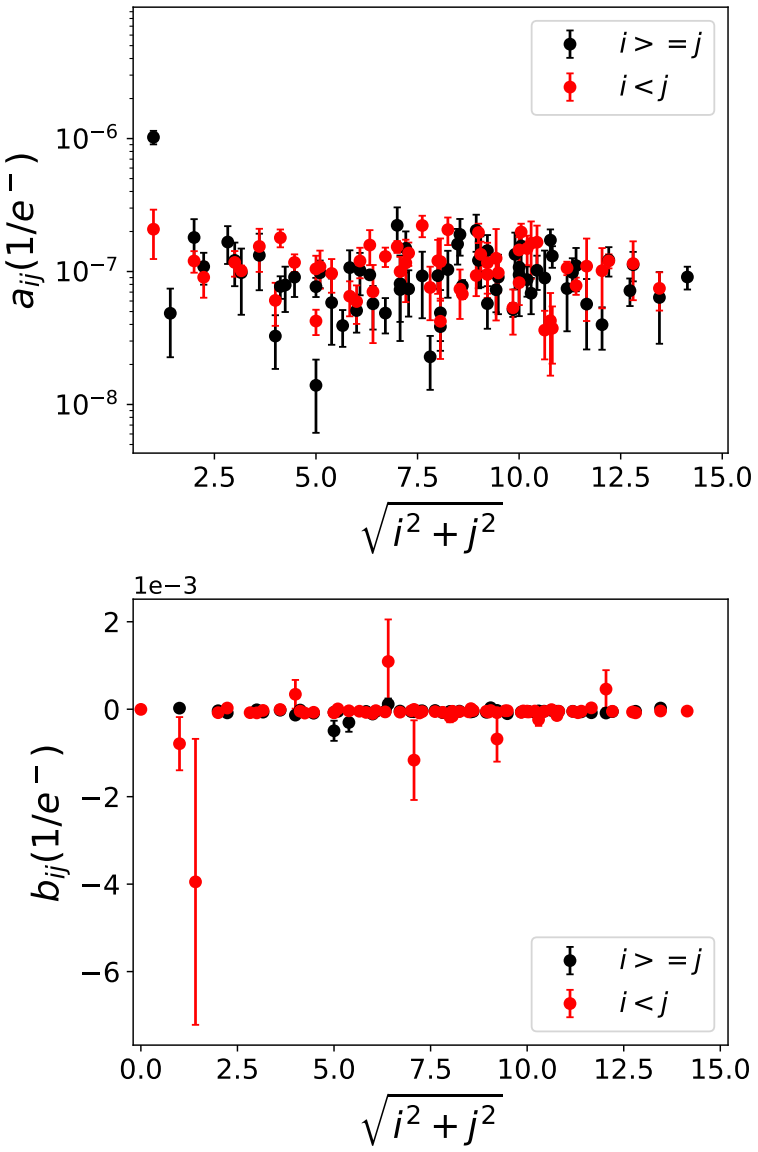

Figure 5.16: Best fit values from the a and b matrices, averaged over all amplifiers, as a function of distance. a decreases sharply and behaves isotropically for > 3 pixels. Similarly to [14], we see that values for b are negative except for b_{01}.

parameters is given by

$$C_{00}(\mu) = \frac{1}{2g^2 a_{00}} \Big[\exp(2a_{00}\mu g) - 1 \Big] + \frac{n_{00}}{g^2}. \tag{5.8}$$

For a Skipper CCD, the PTC can also serve as a useful tool for probing the detector's

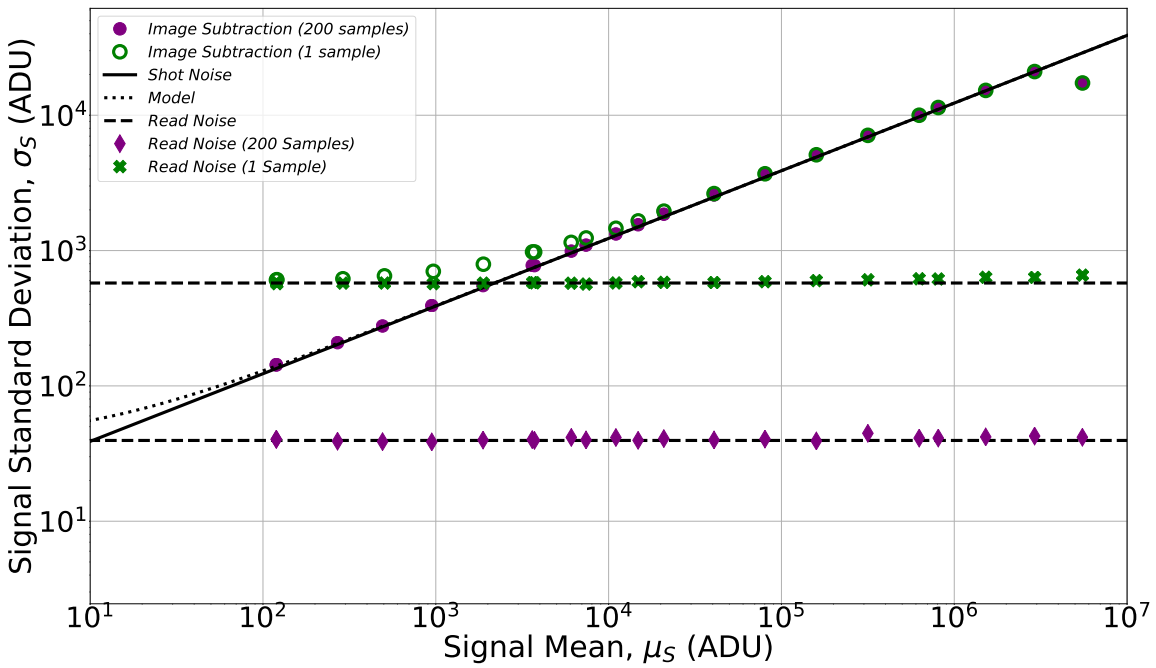

Figure 5.17: PTC curve for a Skipper CCD. The Skipper CCD dynamic range is shown for single- and multi-sample (N_{samp}) data sets. The multi-sample PTC shows that it is possible to dive down the noise floor from the single-sample data while maintaining a linear response.

linearity response across different readout noise levels. For example, consider Figure 5.17, where we show the PTC curve for a Skipper CCD, overlaying single-sample data with data acquired using $N_{\text{samp}} = 200$, where photon-counting is achieved. As expected, the single-sample data (green dots) follows the expected linear behavior in the shot-noise dominated regime, with a noise floor of 3.5 e^-rms/pix. However, by reducing the readout noise through the averaging of 200 readout samples, it is possible to dive below the single-sample noise floor while maintaining linearity (purple dots). This illustrates that the Skipper CCD's performance, even at ultra-low noise levels, preserves the expected linear relationship between signal variance and mean signal level, as captured in the PTC. Therefore, the PTC remains a valuable diagnostic tool for Skipper CCDs in astronomical applications. It can be used to measure the detector's light response across all operational regimes, from the sub-electron noise regime up to saturation.

Figure 5.18 shows a PTC curve for one of the AstroSkippers calculated with Eqn. 5.8.

We implement public code from the LSST Science Pipelines for calculating and fitting the PTC [158]. We use 135 pairs of flat-fields, to compute the difference between them, taken at increasing signal rates from a few electrons to saturation ($\sim$ 50,000 e^- for the AstroSkipper PTC shown in Figure 5.18). PTCs are constructed using $\Delta H = 9.5$ V and the full-well capacity is determined by the last data point that is not cut by the outlier rejection algorithm; the algorithm assigns weights to data points based on residuals from deviations to the model. Figure 5.19 shows the full-well capacity averaged across amplifiers for the six astronomy-grade AstroSkipper detectors; we measure full-well values ranging from $\sim$ 40,000 e^- to 65,000 e^- which is suitable for the SIFS application.

5.6.4 Cosmetic Defects

Cosmetic defect tests consist of characterizing pixels that are "hot" in dark exposure frames and "cold" in flat-fields at different illumination levels. We take 10 dark exposure frames with 400 seconds of exposure in the dark to measure bright pixels. Images are overscan-subtracted and sigma clipped to eliminate cosmic rays. We flagged bad pixels as those with mean values $\mu \pm 3.5\sigma$. The same statistical discrimination is applied for "cold" pixels in flat-fields, which also eliminates "hot" pixels that might be present ($\mu + 3.5\sigma$). We use different illumination levels up to $\mu \sim 30,000$ e^-/pixel. We create a mask to include these pixels ("cold" and "hot") and apply it to the images for subsequent tests. We find cosmetic defects affect $< 0.45\%$ of the pixels for all amplifiers.

5.6.5 Charge Diffusion

To characterize charge diffusion, we implement the method described in [159] which is suitable for thick, backside illuminated, fully-depleted CCDs. The method consists of exposing the CCD to low-energy X-rays from a ^{55}Fe source and statistically characterizing the charge clouds that result from the X-ray photon generating charge carriers in tight clusters. The

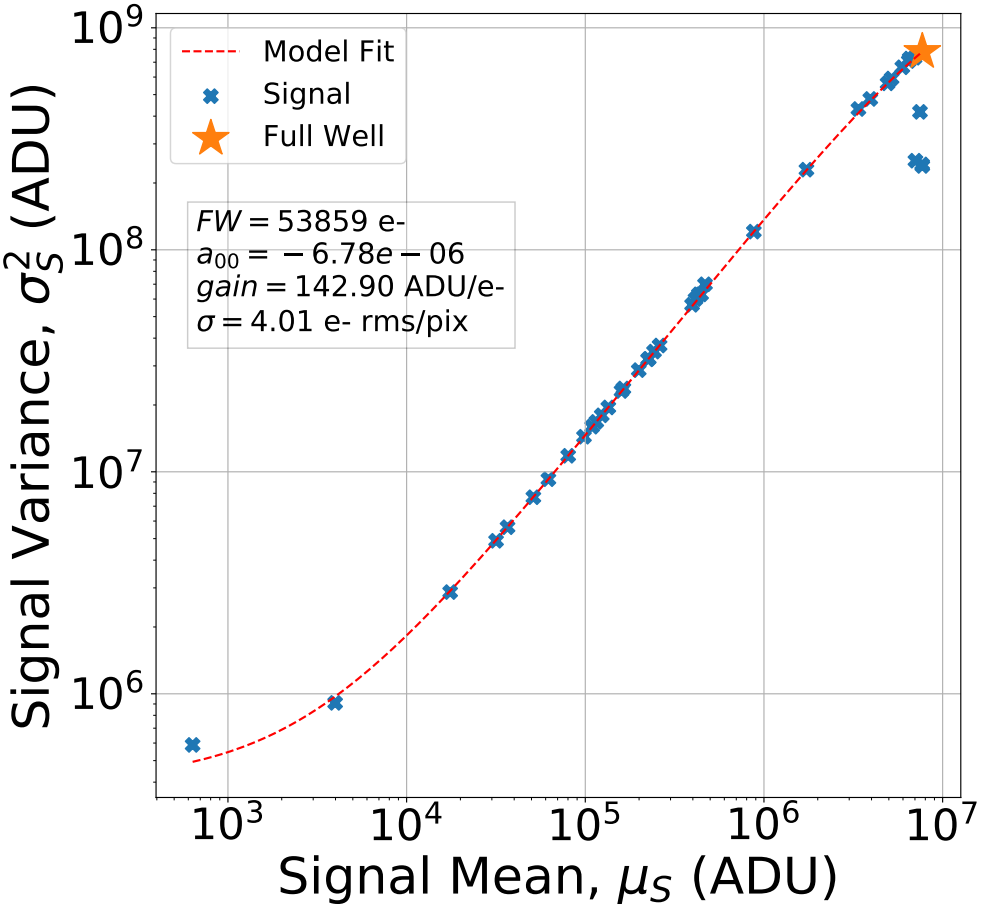

Figure 5.18: Photon Transfer Curve for one AstroSkipper amplifier. The PTC follows the model described by Eqn. 5.8 [14] and gives the BFE strength factor, a_{00} from the covariance matrix. One can also calculate the detector's gain from the model fit, which is given by the slope of the curve. The full-well capacity, orange star, is defined as the last "surviving" data point after applying an outlier rejection algorithm.

charge diffuses laterally, producing a cloud with a Gaussian profile. The method uses the profile of the two-dimensional, Gaussian PSF to measure diffusion from these charge clouds. The pixel selection algorithm reconstructs events and selects those originating from conversions of 5.988 keV Mn Kα photons, producing 1590 electron-hole pairs. The algorithm (1) defines a "box" that is 2 $\times$ 2 pixels and calculates the charge in that region, (2) calculates local maxima by rejecting the box with minimum charge between two intersecting regions, (3) histograms remaining boxes, and (4) centers the window on the Mn Kα peak position with upper bound at the Kα and Kβ peaks.

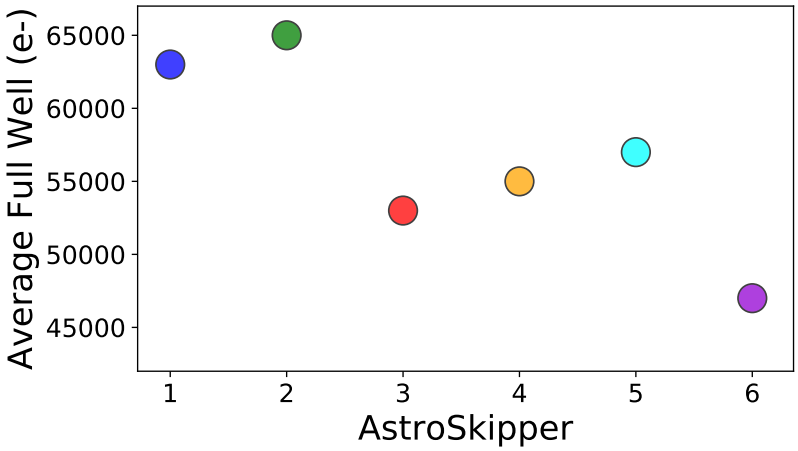

Figure 5.19: Average full-well capacity for the six detectors. Full-well measurements are calculated by amplifier through the PTC; we average these full-well values from all amplifiers in a detector.

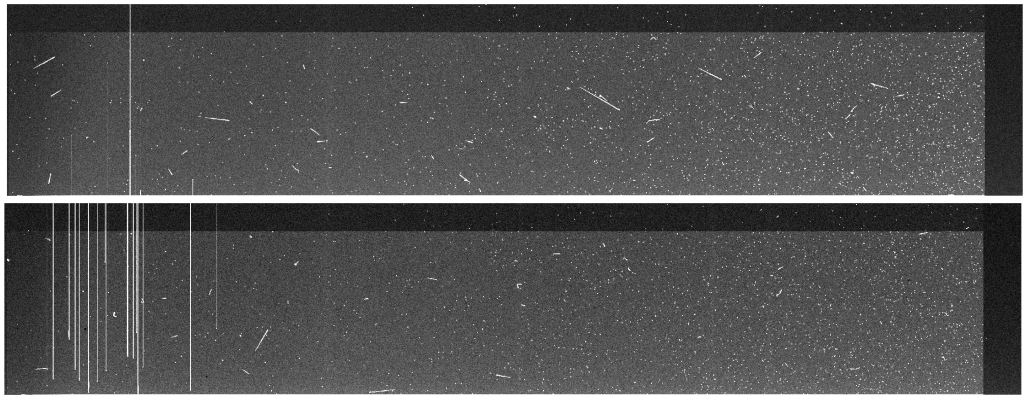

Figure 5.20: ^{55}Fe X-ray data frames. Top: AstroSkipper frame of low-energy ^{55}Fe X-rays taken with a substrate voltage of 40V. Bottom: Frame taken with a substrate voltage of 70V. Cosmetic defects become more apparent as the substrate voltage increases. This indicates physical damage to the CCD back side, which could be a result of the backside processing.

We take 10 images each with 5 min. exposure to ^{55}Fe radiation, which are combined to measure the PSF of the charge clouds using the method described above. We test different bias substrate voltages ranging from 30 V to 70 V and compute the PSF as a function of the substrate voltage. We decide to operate the AstroSkipper CCD at 40 V [similar to DECam; 12], since we find that cosmetics defects, such as hot columns, grow with increasing substrate voltage (>40 V), e.g., Figure 5.20. We measure PSF values for all amplifiers $< 6.75\,\mu$m for

the six AstorSkippers, operating with a substrate voltage of 40 V. This is comparable to DECam charge diffusion requirements: PSF $< 7.5\,\mu$m with a substrate voltage of 40 V [12].

5.6.6 Absolute Quantum Efficiency

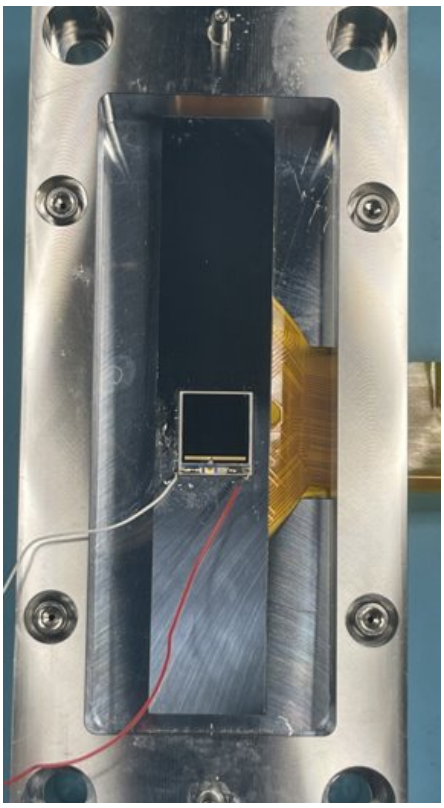

Figure 5.21: Silicon substrate (6k × 1k) on an AstroSkipper package. A Thorlabs NIST traceable Si photodiode is glued at the center of the substrate. The package-photodiode assembly is placed inside the AstroSkipper testing Dewar to measure the incident number of photons at the photodiode.

The LBNL Mycrosystems Laboratory CCD backside treatment and AR coating provides excellent (QE $> 80\%$) long wavelength (NIR) and acceptable (QE $> 60\%$) g-band response for $250\,\mu$m thick detectors [e.g., 12, 139]. In [16], we demonstrated that a $250\,\mu$m thick, backside illuminated Skipper CCD can achieve relative QE $> 75\%$ for wavelengths 450 nm to 900 nm. Here we report the first absolute QE measurements for astronomy-grade Skipper CCDs and demonstrate better QE than previous measurements.

We define the absolute QE as the ratio of the number of electrons generated and captured per incident photon at a given wavelength for a given unit area,

$$\mathrm{QE}(\lambda) = (N_{\mathrm{ADU}} K) \frac{hc}{P t_{\mathrm{exp}} \lambda}, \tag{5.9}$$

where N_{ADU} is the signal from the detector in ADU, g is the detector's gain in ADU/e$^-$, h is the Planck constant, c is the speed of light, P is the incident optical power at the CCD surface, t_{exp} is the exposure time used to take the flat-fields, and λ is the incident light wavelength. An accurate measurement of the absolute QE depends on an accurate determination of the incident optical power at the AstroSkipper, housed in the vacuum Dewar (Figure 5.2). To measure the absolute incident power at the detector, we mount a Thorlabs NIST traceable calibrated Si photodiode, with a 10 mm $\times$ 10 mm activated area, on a AstroSkipper package (Figure 5.21). The photodiode plus AstroSkipper package is mounted inside the vacuum Dewar at the same location that the AstroSkipper CCDs are mounted when testing.

We then measure the ratio of the incident optical power in the Thorlabs photodiode relative to the Oriel NIST traceable photodiode on the integrating sphere (Figure 5.2) as a function of wavelength. We repeat the process of mounting the photodiode, assembling the optical system for illumination, and measuring the ratio of the incident optical power to account for uncertainties and prove reproducibility. We then replace the photodiode with an AstroSkipper, measured the optical power at the integrating sphere, and adjust this measurement by the absolute calibration factor to get the expected incident power at the detector's surface. Figure 5.22 shows the absolute QE for one quadrant of an AstroSkipper and the comparison with DECam and DESI detectors. We see good agreement with the QE of the DESI detectors, which is expected given that the AstroSkipper has a similar AR coating [139]. For all amplifiers in the six AstroSkippers, we see QE $\gtrsim$ 80% between 450 nm and 980 nm, and QE $>$ 90% for wavelengths from 600 nm to 900 nm.

We note that the absolute calibration, i.e., the ratio of the incident optical power in

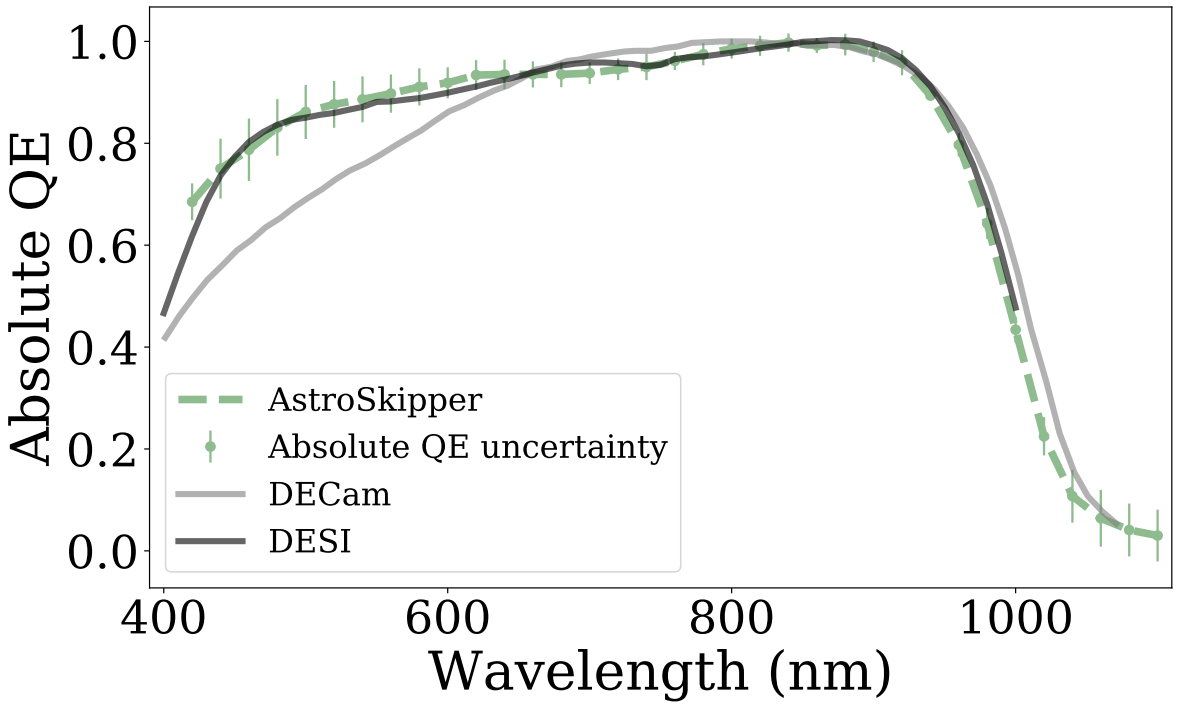

Figure 5.22: Absolute quantum efficiency for one AstroSkipper's amplifier compared to absolute QE from DECam detectors (dark gray line) [12] and relative QE from DESI detectors (grey line). Error bars in the AstroSkipper absolute QE represent the uncertainty in the absolute calibration at each wavelength. We see excellent agreement with DESI detector's QE (the AstroSkipper and DESI NIR detectors are ~ 250 μm thick and have similar AR coating from LBNL Microsystems Laboratory). We measure QE $\gtrsim 80\%$ for 450 nm and 980 nm and QE $> 90\%$ for wavelengths from 600 nm to 900 nm for all AstroSkippers; this is an improvement from the first Skipper CCD relative QE measurements (QE $> 75\%$ between 450 nm and 900 nm) we reported in [16].

the Thorlabs photodiode relative to the Oriel NIST traceable photodiode on the integrating sphere (Figure 5.2) is the greatest source of uncertainty; therefore, we take multiple absolute calibration measurements. We derive an uncertainty in the absolute QE at each wavelength; we find uncertainties $< 6\%$ in the absolute QE values for all wavelengths. Error bars in Figure 5.22 represent the uncertainty at each wavelength calculated from the absolute calibration measurements.

Motivated by measuring the sensitivity of the AstroSkipper in the UV for applications related to direct DM detection [160], we extend the QE to wavelengths < 400 nm. To

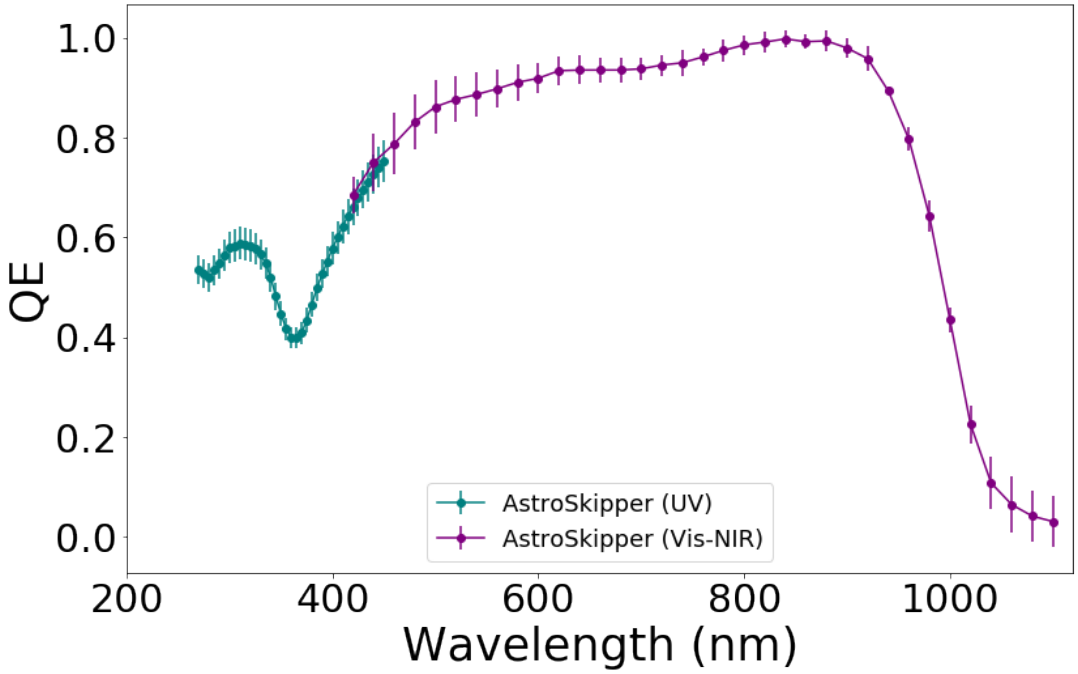

Figure 5.23: Extended QE for the AstroSkipper to the UV regime. The Vis-NIR measurements are the absolute QE values from Figure 5.22. The UV QE is measured separately with a Xenon UV lamp and normalized to the overlapping Vis-NIR QE values.

perform the measurements, we replaced the conventional lamp in the testing station (Figure 5.2) with a 75 W Xenon lamp. Figure 5.23 shows the extended QE. The visible/near-infrared values correspond to the absolute QE in Figure 5.22. The UV QE is then measured from 270 nm to 450 nm, so that we have overlapping values between the Vis-NIR and UV regimes. We then normalized the UV QE using the overlapping values from the Vis-NIR data set.

UV photons with energies > 3.65 eV (wavelengths $\lesssim 340$) have a non-zero probability of producing more than one electron-hole pair in a silicon detector [161, 162]. We observe an increase in QE for wavelengths $\lesssim 300$ nm which can be explained by 2-electron event production rate for UV incident with wavelengths between 270 nm and 340 nm. Multi-electron-hole pair production has been observed in other astronomy-grade CCDs, e.g., the Hubble Space Telescope Wide Field Camera 3 (WFC3) e2v CCDs. For instance, the WFC3 CCD exhibits the characteristic drop in QE at $\sim$360 nm and the sharp QE increase, reaching $\sim 60\%$ at 300 nm [163] similarly to what we observe in the AstroSkipper.

Table 5.1: Summary of the AstroSkipper characterization results for the six out of eight devices with best performance.

Parameter	Goal	Measured	Units
$N_{\text{samp}} = 1$ noise	3.5	< 4.3	e^- rms/pixel
$N_{\text{samp}} = 400$ noise	0.18	0.18	e^- rms/pixel
Cosmetic Defects	10%	$< 0.45\%$	...
DC	$< 8 \times 10^{-3}$	2×10^{-4}	e^-/pixel/s
CIC	1.52×10^{-4}	3	e^-/pixel/frame
Full-Well Capacity	$> 40,000$	$\sim 40,000 - 60,000$	e^-
Non-linearity	$< 1.5\%$	$< 0.05\%$ and $< 1.5\%$ (low signals)	...
CTI	$< 1 \times 10^{-5}$	3.44×10^{-7}	...
Charge Diffusion (PSF)	< 15	< 7.5	μm
Absolute QE	$> 80\%$	$\gtrsim$ 80% (450nm to 980nm); $\gtrsim$ 90% (600nm to 900nm)	...

5.7 Summary

This Chapter presents the results from characterizing and optimizing eight AstroSkipper CCDs developed for a prototype Skipper CCD focal plane for SIFS. Six astronomy-grade Skipper CCDs were identified as potential candidates for the focal plane. These were shipped to CTIO and devices #2, #4, #5, and #6 were ultimately selected for the focal plane with the remaining two exhibiting performance degradation as they arrived to CTIO. Table 5.1 summarizes characterization measurements derived from all amplifiers on the six detectors. Measurements satisfied targeted goals, which were set by previous characterization of DESI detectors [141].

An important conclusion from these results is that CIC is a critical issue when large full-well capacities are required. While we achieve a low CIC of $< 1.45 \times 10^{-3}$ e^-/pixel/frame at a full-well capacity of $\sim$900 e^-, this rises to $\sim$ 1 e^-/pixel/frame at a full-well capacity of $\sim$10,000 e^- and $\sim$ 3 e^-/pixel/frame at a full-well capacity of $> 40,000$ e^-. This prompts a

nuanced consideration of the trade-off between full-well capacity and CIC, especially when optimizing the system for the expected signal level in the SIFS application. For this technology demonstration, we opted to use a dynamic voltage configuration for the observation where we applied high voltages when calibrating the focal plane, e.g., calibration lamps, and switching to a low voltage configuration when acquiring science data.

We highlight the absolute QE measurements (QE $\gtrsim$ 80% between 450 nm and 980 nm, and QE $>$ 90% for wavelengths from 600 nm to 900 nm). This is an improvement relative to previous Skipper CCD QE measurements and is comparable to the QE of the DESI red-channel detectors [139]. Furthermore, we achieved a factor of five reduction in the readout time (from 200 μs/pixel to 40 μs/pixel for the entire pixel sequence). We emphasize that readout time reduction is critical in Skipper CCD astronomy applications. The results presented here demonstrate that the AstroSkipper CCD retains all the desirable characteristics of conventional astronomical CCDs while providing optimal performance across a wide range of operational regimes. This includes the ultra-low noise sub-electron regime, which was probed using novel techniques, as well as the regime of thousands of electrons, which is expected from any high-performance astronomy-grade detector.

CHAPTER 6

OBSERVING WITH SKIPPER CCDS

This chapter describes key aspects of the observation planning, and the first on-sky observations with Skipper CCDs at SIFS. I summarize the installation and commissioning procedures, including focal plane alignment, and system testing. I outline the ROI observation strategy developed to achieve sub-electron readout noise and on-sky photon-counting, for the first time on a CCD, while limiting the readout times to < 20 minutes. I present results from the observations, demonstrating S/N improvements and describing limitations of the as-built system.

The observation targets S/N improvements in the readout noise dominated regime. To this end, we observed two quasars (HB89 1159+123 and QSO J1621–0042) at redshifts $z \sim 3.5$, two high-redshift galaxy clusters (CL J1001+0220 and SPT-CL J2040−4451), an emission line galaxy at $z = 0.3239$, a candidate member star of the Boötes II ultra-faint dwarf galaxy, and five CALSPEC spectrophotometric standard stars (HD074000, HD60753, HD106252, HD101452, HD200654). This technology demonstration presents charge-quantized, photon-counting observations of the quasar HB89 1159+123 and show the detector sensitivity increase for faint spectral features. Furthermore, I introduce two science cases that would be pursued with the galaxy cluster data and the Boötes II candidate member star spectra. The latter would be explained in detail in Chapter 7 as part of this thesis.

6.1 Skipper Focal Plane Installation

After the AstroSkipper CCDs were fully characterized and optimized for the SIFS application, they were shipped to CTIO for focal plane assembly and metrology (see Section 4.5.2). The laboratory system integration involved conducting cold testing and thermal cycling of the Dewar along with assembling and externally testing the preamplifier board and cables.

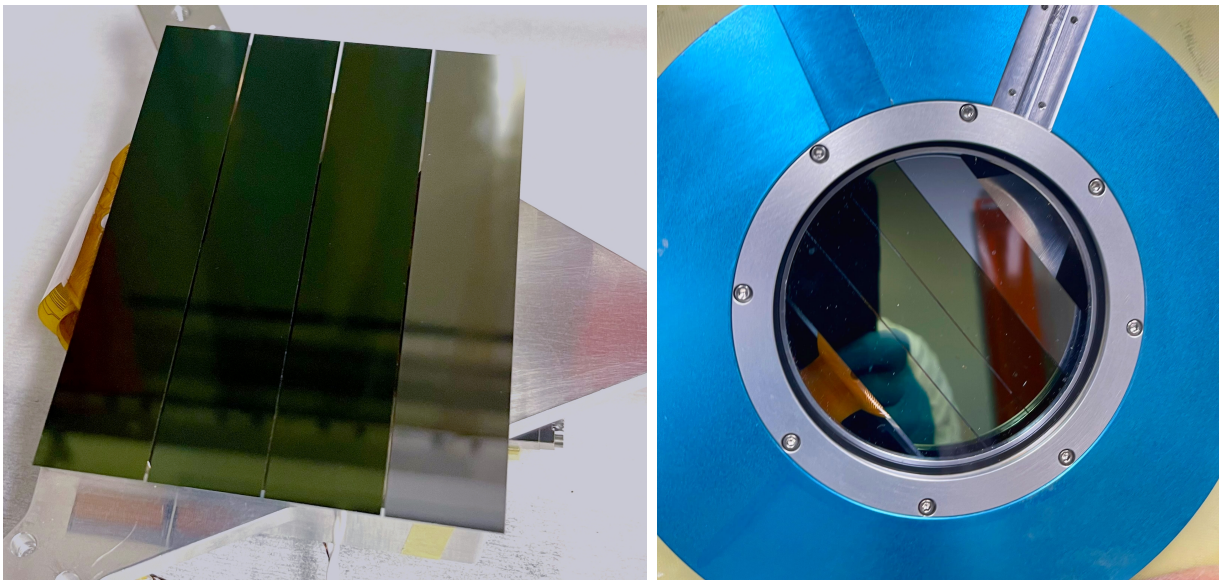

Figure 6.1: **Left**: Skipper CCD focal plane prototype for SIFS. Four astronomy-grade Skipper CCDs are placed on a custom mount with three arms that attach to a standard SOAR Dewar. The focal plane spans an area of 6k × 4k pixels. The four devices are separated by gaps of ∼400 μm. **Right**: Focal plane inside the standard SOAR Dewar with a fused-silica window for exposure to light.

After this, The preamplifier board was mounted inside the Dewar, connected to internal cabling, and linked to the LTAs via pre-tested cables. Each preamp output was checked using a break-board, ensuring all signals and output impedance were correct across the four CCD connectors. Video signals were tested with sinusoidal injections to verify gain and continuity. Once confirmed, the engineering-grade Skipper CCD was installed, and its performance was evaluated after cooling the Dewar to 140 K. Following successful tests, the four astronomy-grade Skipper CCDs were installed and the focal plane was assembled and transported to SOAR for the on-sky demonstration (Figure 6.1).

Installation and commissioning (refer to Bonati et al. (2024)) of the SIFS Skipper CCD focal plane prototype took place March 25–29, 2024 in advance of the first on-sky observations on March 31, 2024. The SIFS instrument is positioned on a platform adjacent to the telescope, as illustrated in Figure 6.2 (Left). The enclosure houses the rotating bench, grat-

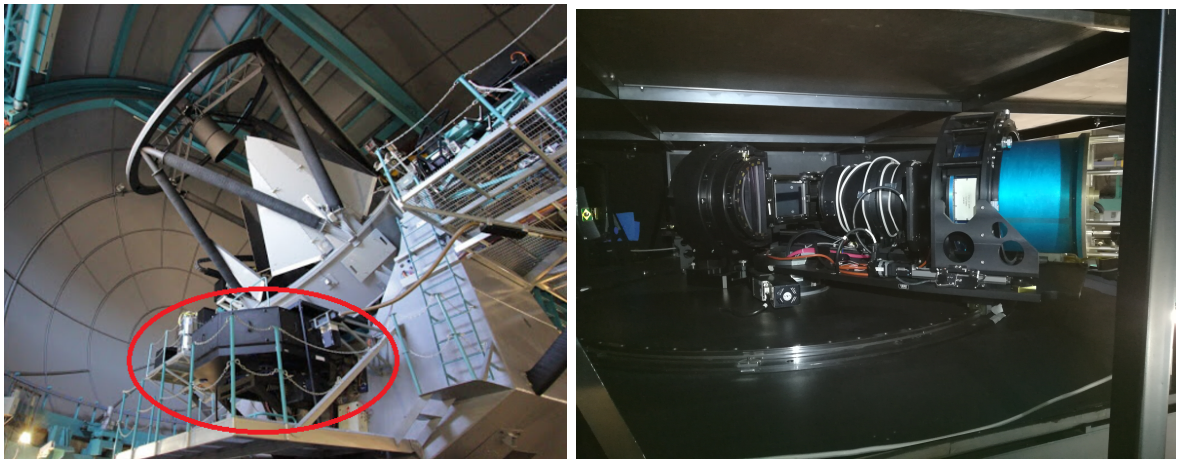

Figure 6.2: Left: SIFS bench spectrograph enclosure located on the lateral platform of the SOAR telescope. Right: The Dewar and the bench spectrograph equipment is located inside.

ings, and the Dewar, all of which are mounted on a frame to ensure precise alignment with the instrument's light path (Figure 6.2, Right). Optical alignment was a critical concern, as it can be a delicate process. The SIFS Dewar had been aligned years earlier, and any adjustments required for the Skipper Dewar would need to be reversible to accommodate the re-installation of the SIFS Dewar. The SIFS frame, which supports the Dewar, is equipped with a three-point kinematic mount (see Figures 6.3 and 6.4), along with a mechanism for Dewar rotation.

The goal was to install the Skipper Dewar without disturbing the settings of the kinematic mount, providing a solid baseline for alignment if the Skipper focal plane was close to optimal. We removed the SIFS Dewar and its kinematic frame, then replaced the Dewar with the Skipper Dewar, carefully reassembling everything onto the instrument. Once the Dewar and its frame were securely in place, we proceeded to replace the SIFS detector controller (an SDSU-III) with our own electronics. This included installing the detector box with the four LTAs, the Lakeshore controller, and the shutter control box (Figure 6.4, Right).

After completing the installation, we verified communication with the LTA electronics from the computer room, and ensured connectivity to the Lakeshore controller, pressure gauge, and shutter. We also tested the shutter's reliability. Once both the mechanical and

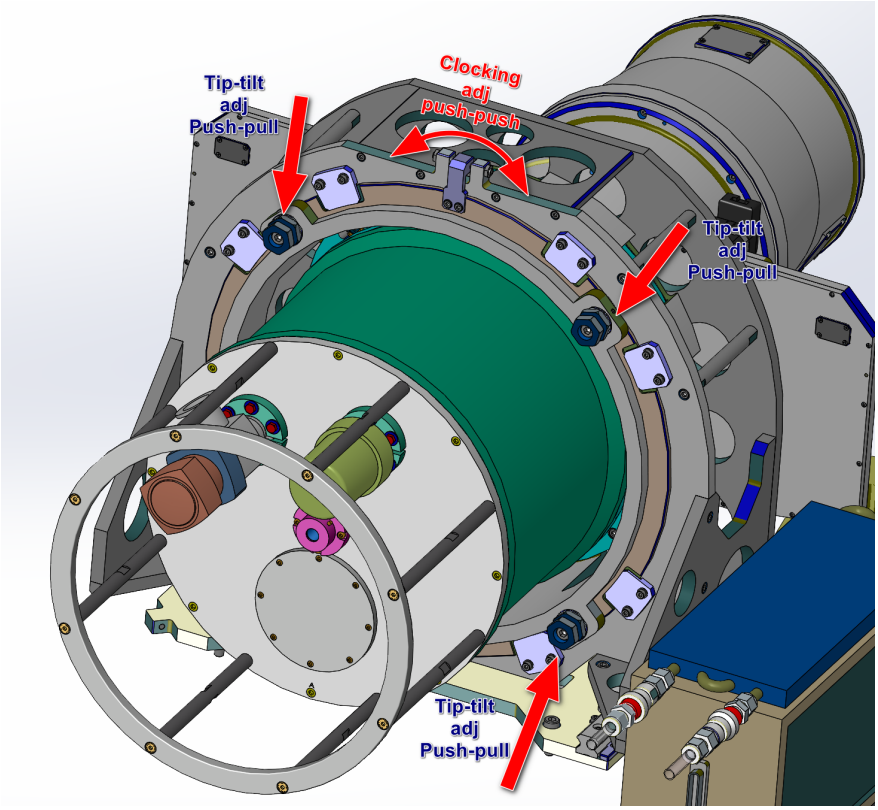

Figure 6.3: The diagram shows the three-point kinematic mount to align the Dewar to the optical path of the instrument.

electrical installations were finished, the Dewar was pumped down and cooled. With the Dewar cold, we planned to take calibration spectra using the instrument's calibration lamps and measure the Full Width at Half Maximum (FWHM) across the field. Based on the results, we would adjust focus, tip, tilt, and rotation if necessary. Prior to making any adjustments, we carefully marked the positions of the kinematic mount's knobs to ensure we could revert to the original settings if needed.

The first spectra (Figure 6.5) captured with the Skipper CCD focal plane showed that the system was nearly in focus across the entire field of view. We measured the Full Width at Half Maximum (FWHM) at various points, especially at the edges, and found only slight variation, ranging from 3.2 to 2.8 pixels—a variation of $\sim$13%. This was well within acceptable limits, eliminating the need for complex optical alignment procedures, which would have required

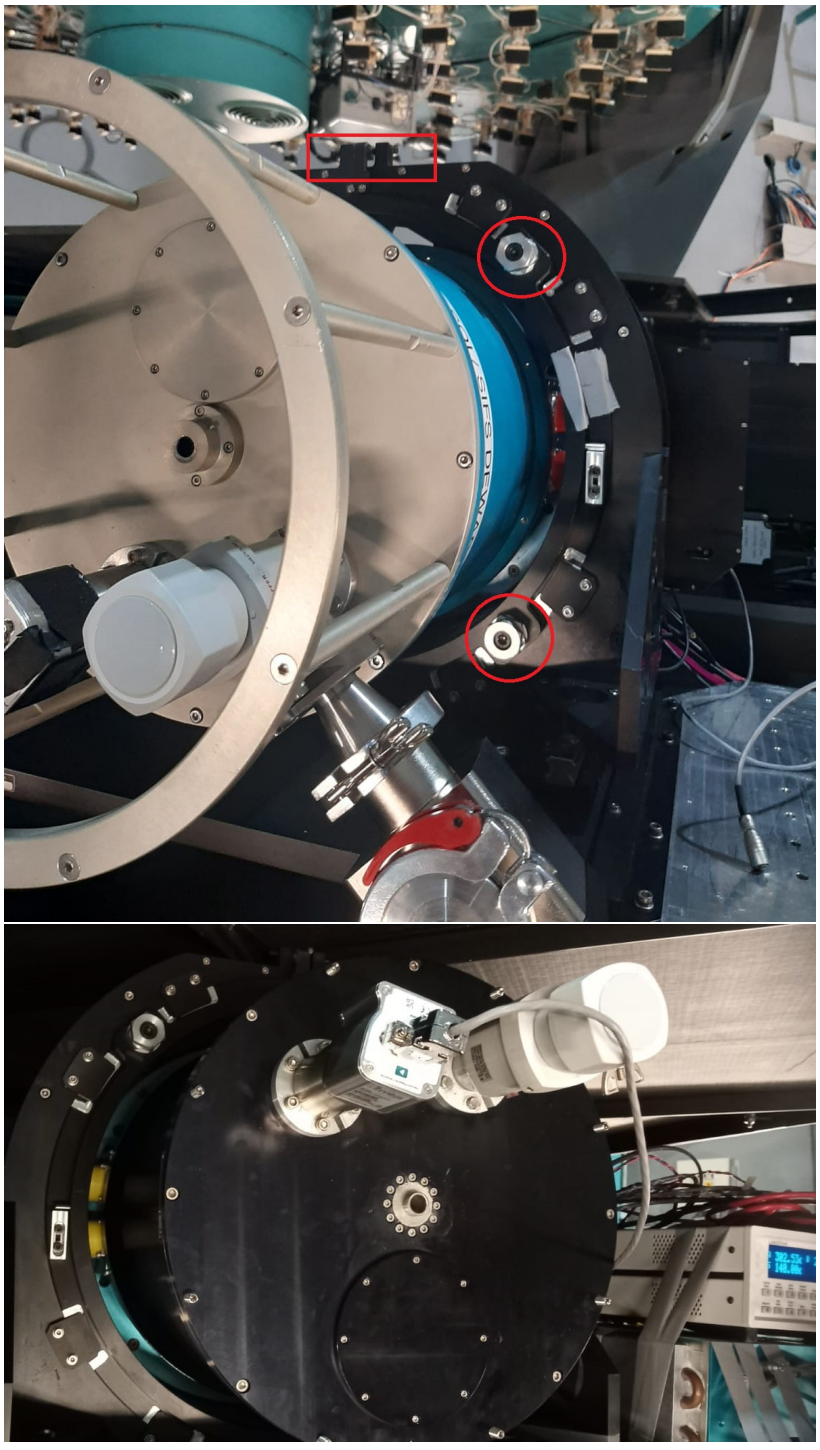

Figure 6.4: Top: Orginal SIFS Dewar installed in the SIFS frame. The red circles indicate two of the three-point kinetic mounts for adjusting tip/tilt, and the red square highlights the rotation mechanism. Right: Installed Skipper Dewar and electronics.

modifying the current kinematic mount settings. A dedicated focus sequence confirmed that the optimal position for the Skipper Dewar was close to the original—5 mm for the original and 5.5 mm for the Skipper Dewar.

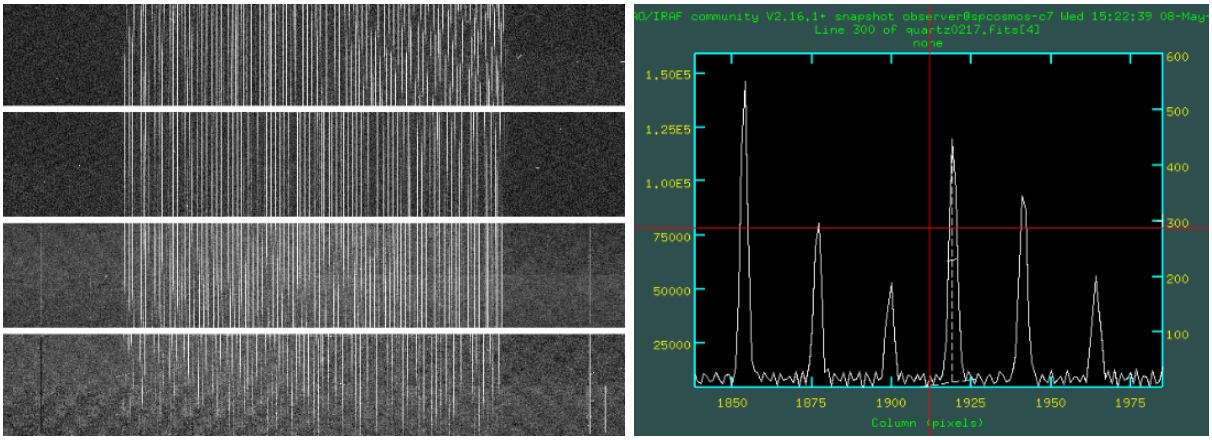

Figure 6.5: Left: First spectra acquired with the Skipper array of a quartz calibration lamp. Right: FWHM calculation of the fiber traces from the first calibration spectra.

6.1.1 Other System Considerations

Here, we address additional system challenges that were resolved to achieve science-quality data. Initially, we planned for the Dewar's orientation such that the spectral direction would align with the CCD columns, ensuring continuous wavelength coverage—given that the four detectors are separated by gaps of approximately 400 μm—and for the spatial direction to run along the rows. However, the focal plane array was inadvertently rotated by 90°, placing the wavelength direction along the rows, which introduced gaps of approximately $\sim$275 Å in wavelength coverage. This issue, however, can be overcome by segmenting the data analysis in a detector-by-detector basis.

Laboratory tests of the fully assembled Skipper CCD array revealed correlated noise ($\sim$ 17 e^-rms/pix) on two detectors, despite symmetric readout electronics outside the Dewar. We discovered that reading multiple samples per pixel reduced the noise faster than

expected for uncorrelated Gaussian noise (i.e., $\sigma_N < \sigma_1/\sqrt{N_{\text{samp}}}$). After approximately 12 samples per pixel, we recovered Gaussian noise behavior (see Section 6.3). During commissioning, stray light within the SIFS enclosure contributed to a shutter-open dark rate of $\mathcal{O}(10^{-1})$ $\text{e}^{-}\text{pix}^{-1}\text{s}^{-1}$. This stray light affected observations on March 31, 2024, but was reduced by an order of magnitude for subsequent observations.

6.2 Observation Strategy

Science-quality observations were acquired with the SIFS-Skipper CCD focal plane on March 31 and April 9, 2024 during time allocated to Brazilian collaborators on SOAR. The science verification program was intended to demonstrate the performance of Skipper CCDs on the sky for the first time. The observational parameters were chosen to demonstrate the S/N improvement possible from the reduced readout noise of the Skipper CCD in the low-signal regime. Therefore, we chose astronomical targets that satisfy our science case (see Section 6.4) and prioritized reducing readout noise over a detector region-of-interest in order to minimize readout times. In several cases, we reduced integration times to several minutes in order to artificially reduce the signal strength and place the observations in the readout noise dominated regime.

SIFS is equipped with a 1300-element Integral Field Unit (IFU) that operates through two main components: the fore-optics and the bench spectrograph. The fore-optics consists of a 26 $\times$ 50 array of 1 mm $\times$ 1 mm square microlenses, which channel light into the fibers. The bench spectrograph receives these aligned fibers arranged into a pseudo-slit. The IFU has a fiber scale of 0.30 arcsec/fiber which produces a field of view of 15 $\times$ 7.8 arsec^2 [130, 129]. Figure 6.6 shows the spatial and wavelength mapping from the microlens array to the Skipper CCD focal plane. The gap between detectors causes $\sim$2% of the wavelength coverage to be lost. Therefore, object targeting becomes important to ensure that important features are mapped to an active region on the focal plane.

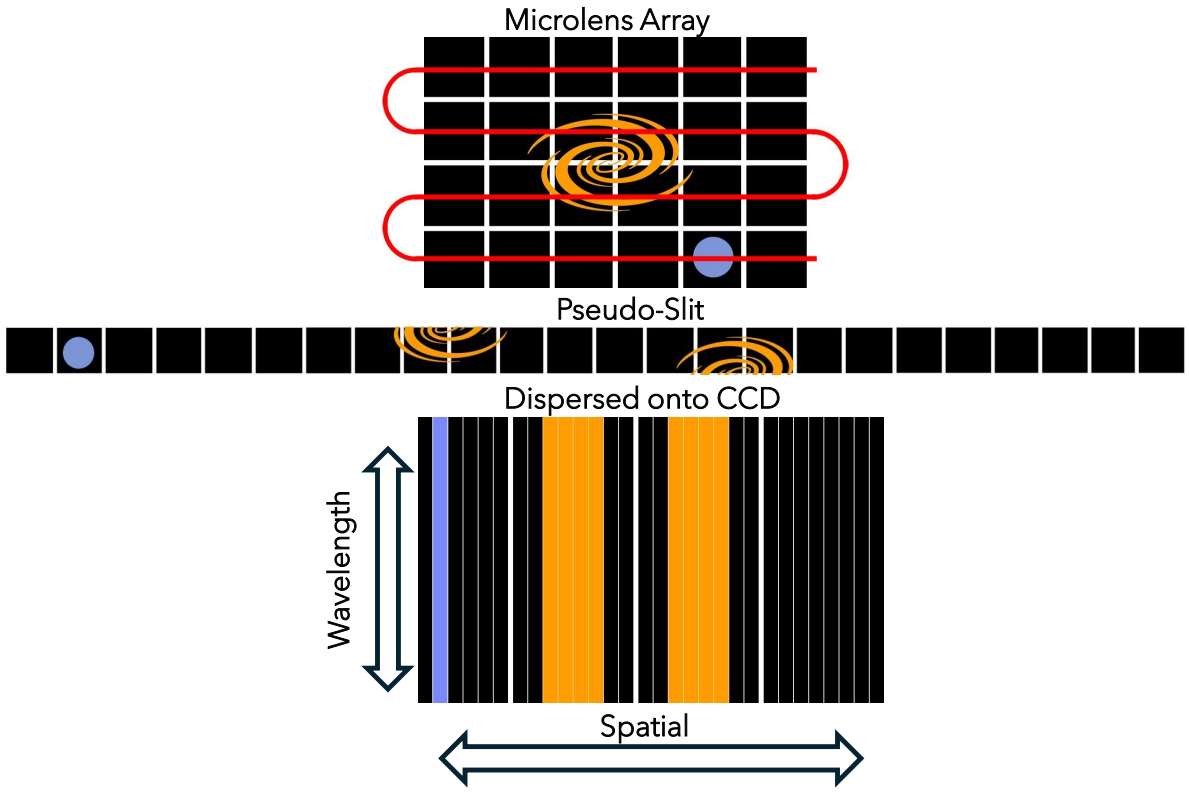

Figure 6.6: Mapping of the signal from the SIFS optics to the Skipper CCD focal plane. The microlens array collects light from the astronomical target and channels the light into the fibers, which are arranged into a pseudo-slit following a serpentine mapping (red curved line). The fibers disperse the light onto the focal plane; the wavelength direction runs along the Skipper CCDs' rows and the fibers' spatial position runs along the detectors' columns.

The Skipper CCD focal plane spans an area of 6k $\times$ 4k pixels (Figure 6.1); however, the active area where the SIFS spectra are dispersed onto the focal plane is only 4k $\times$ 4k pixels (the "field of view", FoV). Figure 6.7 shows the complete focal plane array (6k $\times$ 4k) formed by the four Skipper CCDs; the illuminated fiber bundles correspond to the signal from HD101452, a bright ($V = 8$) CALSPEC standard star [17]. The bright fiber bundles span the SIFS FoV (pixel $\sim$1000 to $\sim$5000 in the spatial direction). The readout strategy takes advantage of ROIs to readout different regions of the FoV with different readout noise configurations suitable for the astronomical targets. Nominally, the ROIs are defined per detector amplifier quadrant and span 512 physical pixels in the wavelength direction (4k pixels

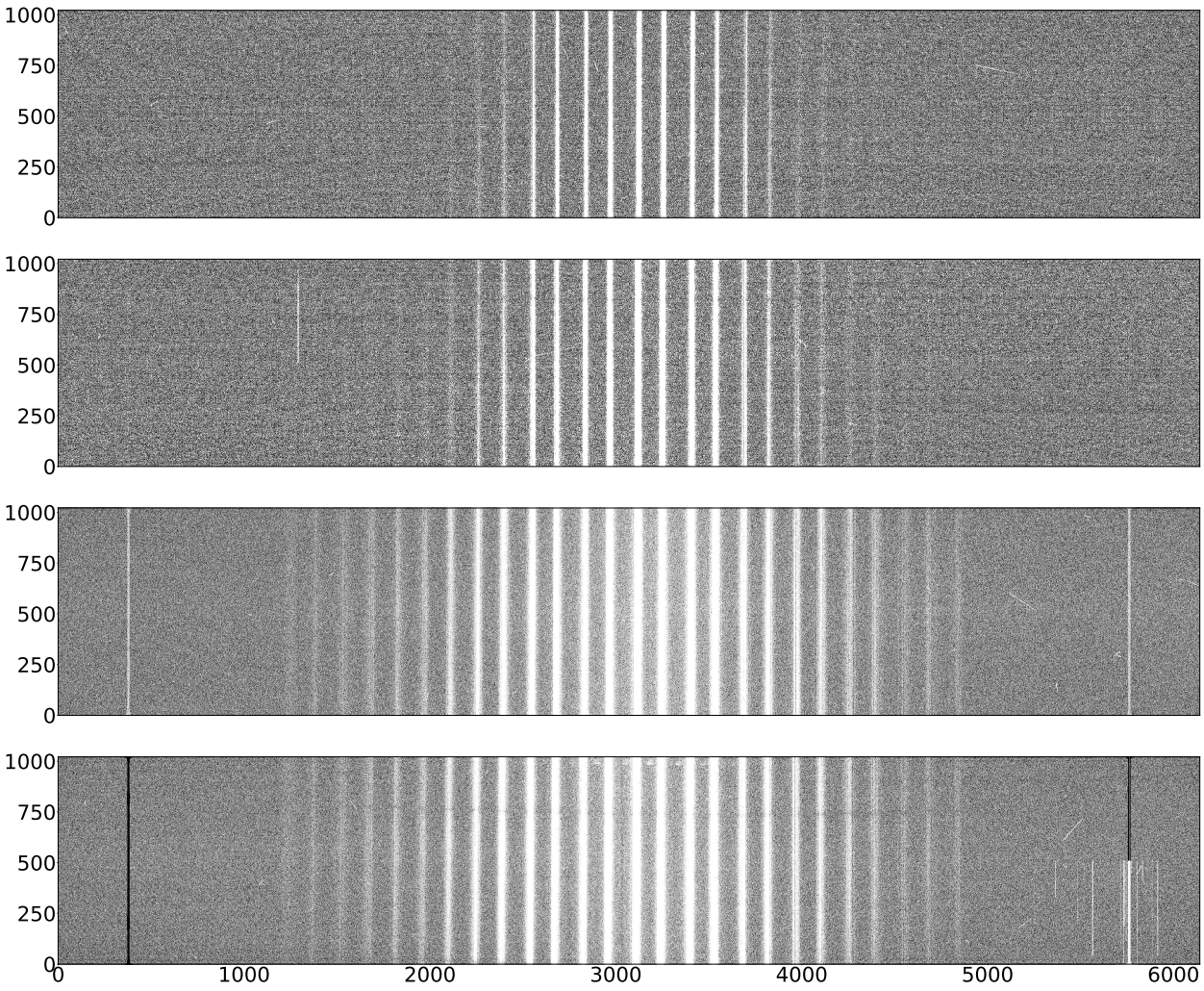

Figure 6.7: Skipper CCD focal plane array data frames. The four frames show the full 6k × 4k physical pixels of the four Skipper CCDs. Each frame is composed of the four amplifiers in each detector. We show spectroscopic data from a CALSPEC [17] standard calibration star (HD101452); the fiber bundles span the 4k × 4k SIFS FoV. There are "hot" columns present outside the 4k × 4k FoV, which do not affect data reduction. The gaps between the Skipper CCDs are ∼400 μm (∼27 pixels) wide and are not shown to scale.

for the whole detector array) and the spatial direction is left as a configurable parameter. The combination of the ROI size and the number of Skipper samples that are collected set the readout time and the readout noise in the ROI (Figure 6.9).

The observation sequence begins with a series of calibration products. We take ∼ 5 flat-

field frames illuminating the instrument with a quartz lamp. The instrument focus is set to zero to produce a uniform image and avoid localized imperfections. Flat-field data taking is followed by a series of arc-lamp calibrations using mercury (Hg), argon (Ar), and neon (Ne) lamps to derive the wavelength solution for our spectroscopic data. The full calibration sequence is performed again at the midpoint and end of the night to account for shifts in the fiber positions. The LTA readout electronics do not perform clock shaping, and we found a strong dependence between the amplitude of the horizontal clock voltage swings and the CIC rate (see Section 5.5) [164]. To maintain a high full-well capacity for the calibration images (where the expected signals are $> 20{,}000$ e^-), the detector clock voltages are set to a high voltage configuration. The CIC rate for these high voltages (~ 3 e^-/pixel/frame) is negligible compared to the signal. When observing science targets, we switch to an intermediate set of clock voltages with a CIC rate of $\lesssim 1$ e^-/pixel/frame, which contributes $< 10\%$ of the total noise for sources contributing tens of electrons.

6.2.1 Astronomical Targets

Quasars: We identified two quasars, HB89 1159+123 ($z = 3.522$) and QSO J1621˘0042 ($z = 3.711$) that were observed with the X-shooter spectrograph on the European Southern Observatory Very Large Telescope as part of the XQ-100 legacy survey [165]. XQ-100 provides high-quality echelle spectra of 100 quasars at redshifts $z \simeq 3.5 - 4.5$ with high signal-to-noise (median S/N = 30). These high-quality spectra can be compared to the SIFS-Skipper CCD data. We also acquired spectra of these QSOs with the original SIFS Teledyne e2v detector, which serves as another baseline for comparison.

Galaxy Clusters: We identified moderate-redshift ($z \sim 1 - 2$) galaxy clusters intended for a search of axion-like particle (ALP) decay (see Section 6.4). We acquired spectroscopic data with Skipper CCDs from two galaxy clusters: CL J1001+0220 ($z = 2.5$) and SPT-CL J2040−4451 ($z = 1.48$). These observations are paired with observations of CALSPEC

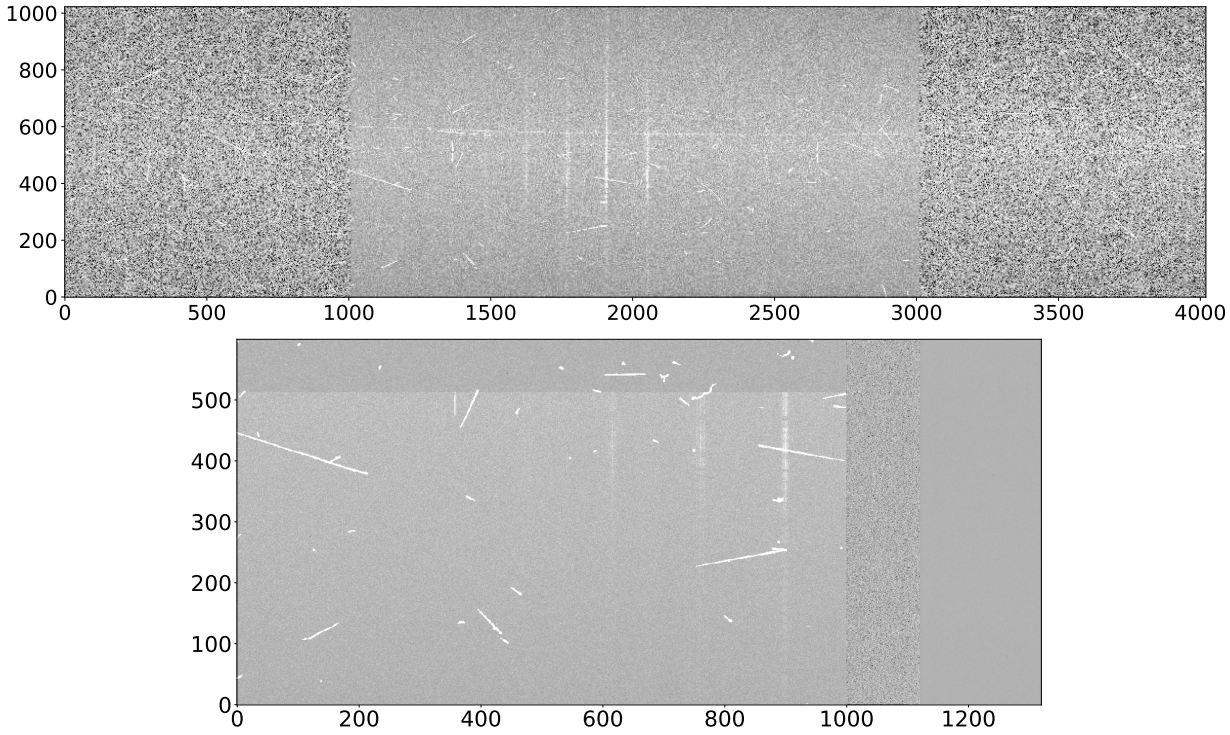

Figure 6.8: SIFS-Skipper CCD observation of quasar HB89 1159+123 using the 1/2 FoV ROI readout configuration. Top: The 1/2 FoV ROI consists of 50 repeated measurements of 1k × 2k contiguous physical pixels in the center of each AstroSkipper detector. The top panel shows the physical pixels from the four amplifier quadrants on a single AstroSkipper detector within the SIFS FoV and excludes overscan regions. The x-direction represents the SIFS spatial dimension over the SIFS FoV ($\sim$ 2k pixels per amplifier, $\sim$ 4k pixels for the detector frame) and the y-direction is the spectral dimension (512 pixels per amplifier, $\sim$ 1k for the detector frame). This configuration was used to observe QSOs with sub-electron readout noise covering a focal plane region of 4k × 2k pixels. Bottom: The multi-sample and overscan regions for the bottom left amplifier quadrant from the 1/2 FoV ROI shown in the top image. The multi-sample active area (1k pixels in the x-direction) is followed by a 120-pixel-wide single-sample serial overscan and a 200-pixel-wide multi-sample serial overscan. The parallel overscan is 88 pixels wide in the row direction. These overscan sections are used in image reduction.

[17] standard spectroscopic calibration stars (HD074000, HD60753, HD106252, HD101452, HD200654) for flux calibration purposes. Integration times for calibration star exposures are about 5 minutes due to the high signal counts ($> 10,000$ e^-) and are read out in single-sample configuration. Previously, we acquired spectroscopic data from these galaxy clusters using the original SIFS e2v detector to compare future science results between both data

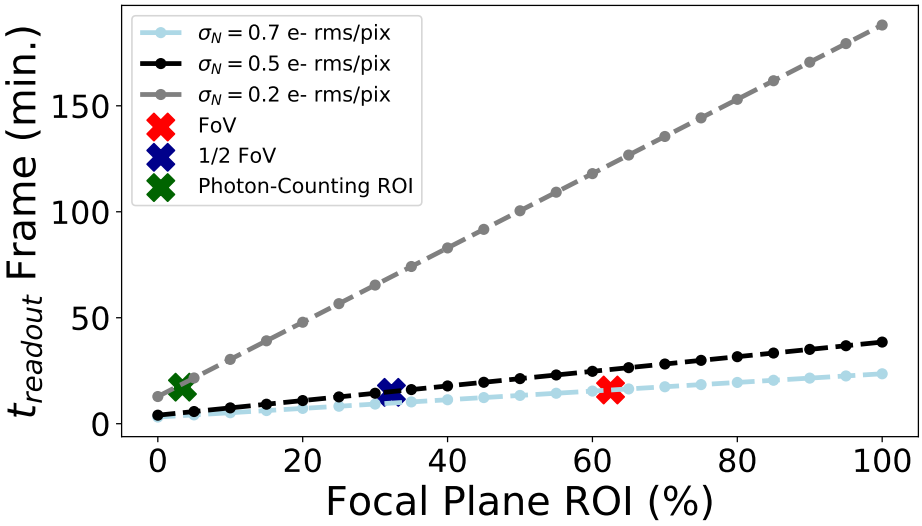

Figure 6.9: Readout time for several ROI configurations. The plot gives the expected readout time given the target noise level (sub-electron and photon counting) for different percentages of the detector readout with the target noise. We note that the rest of the FoV is read out with single-sample noise.

sets.

Emission Line Galaxy: We observed an emission line galaxy (ELG) at $z = 0.3239$ that was also observed by DESI as part of the DESI Early Data Release [166]. The O III emission line is well placed on the the SIFS FoV at $\lambda = 6628.8$ Å. This observation shows the capability of the Skipper CCDs to resolve faint spectral features and provides a validation of this technology for future spectroscopic surveys (e.g., DESI-2 [167]).

Ultra-faint Dwarf Galaxy Candide Member Star: We acquired spectroscopic data associated with a candidate member star in the periphery of the Boötes II ultra-faint dwarf galaxy identified by Pan et al. (2024). The candidate member star is relatively faint (Gaia $G \sim 19$ mag), and we plan to measure the radial velocity of this star to determine whether it is a member of Boötes II.

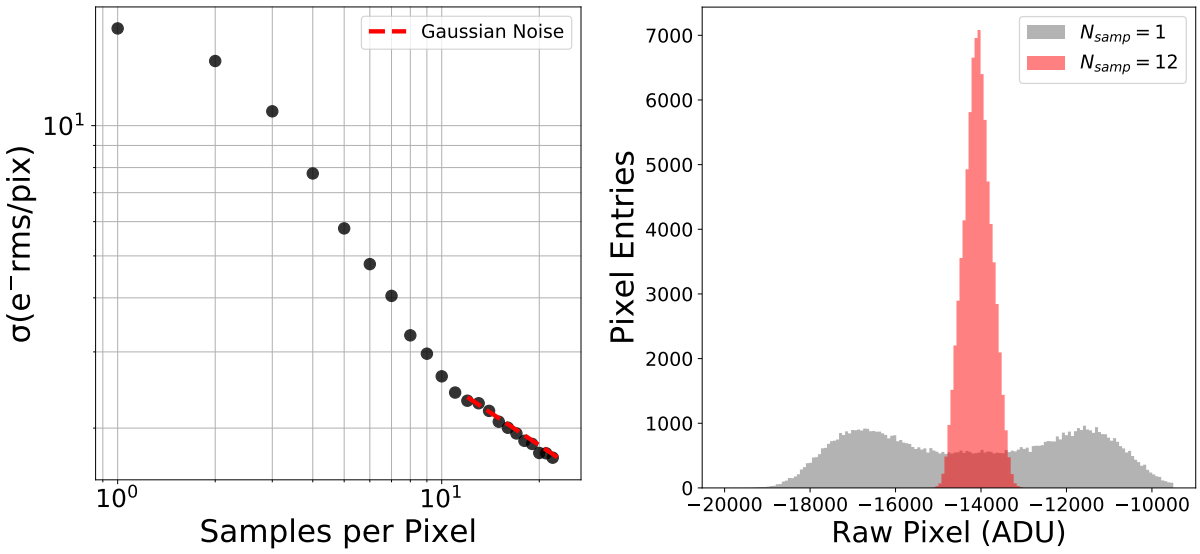

Figure 6.10: Left: Readout noise from one of the detectors affected by correlated noise as a function of the number of samples per pixel ($N_{\rm samp}$). The single-sample readout noise is $\sim 17\,{\rm e}^-$ rms/pixel but rapidly decreases with increasing $N_{\rm samp}$, reaching ~ 4.6 e$^-$ rms/pixel at $N_{\rm samp} = 7$. The theoretical Gaussian noise is recovered for $N_{\rm samp} > 12$. These detectors are able to count photons at $N_{\rm samp} = 250$. Right: The pixel distribution from the multi-sample serial overscan. For small $N_{\rm samp}$, the pixel distribution exhibits a "double-Gaussian" feature, which suggests a temporal correlation between mixed sources of noise.

6.2.2 Sub-Electron Noise Regions of Interest

We define a "full FoV" ROI that covers the entire 4k × 4k active region of SIFS focal plane array. The full FoV ROI is configured per amplifier with a contiguous active area of 512 × 2k pixels. The full FoV ROI is read out with $N_{\rm samp} = 30$, resulting in a readout noise of $\sim 0.7\,{\rm e}^-$rms/pixel while the the rest of the amplifier region (512 × 1k pixels outside the FoV) is read with $N_{\rm samp} = 1$. We use this configuration for the galaxy cluster observations and acquired five science exposures with exposure times varying from 900 to 1200 seconds.

We also define a smaller "1/2 FoV" ROI covering a 4k × 2k region of the focal plane array (excluding the parallel and serial ovserscans). The 1/2 FoV ROI consists of 512 × 1k pixels per amplifier where we achieve a noise of $\lesssim 1\,{\rm e}^-$rms/pixel with $N_{\rm samp} = 50$ measurements per pixel. The 1/2 FoV ROI enables signal to be collected from several of the brightest

fiber bundles, and this readout configuration was used to acquire data from the two QSOs, the ELG, and the Boötes II candidate member star. In the top panel of Figure 6.8, we show an observation of HB89 1159+123 using the 1/2 FoV ROI configuration; the ROI spans the entire detector in the spectral direction and ∼2k pixels in the spatial direction. In the bottom panel of Figure 6.8, we show one amplifier segment of a science image to highlight its various components. From Figure 6.9, we note that the readout time is ∼ 15 min for both FoV ROI configurations.

6.2.3 Photon-Counting Region of Interest

As a demonstration of the first on-sky photon-counting spectroscopic data collected with a Skipper CCD, we defined a "photon-counting" ROI spanning 220 pixels in the spatial direction (110 pixels per amplifier), which we sample 250 times to achieve a readout noise of ∼ 0.22 e^-rms/pix. The photon-counting ROI was used to acquire spectra from HB89 1159+123 and QSO J1621−0042. The blaze angle was chosen to center the Lyman-alpha (Ly-α) line (∼5497 Å and ∼5726 Å for the two QSOs, respectively) on a single detector. The readout time for this configuration is 17.2 min (Figure 6.9). We took one 120 s science exposure from HB89 1159+123 in order to validate noise and photon-counting performance, followed by two 60 s exposures for each QSO.

6.3 Observation Results

6.3.1 System Performance

To the best of our knowledge, these observations represent the first-ever on-sky data collected with Skipper CCDs. They demonstrated the capability of these detectors to achieve ultra-low noise and detect weak signals (e.g., resolve individual photons) under real instrument and observing scenarios. This successful demonstration of Skipper CCDs on the sky relies

not only on the demonstrated performance of the detectors [164], but also on the integrated performance of the focal plane electronics, instrument, and telescope [135]. We note two minor system issues that affected these first observations.

When integrating the Skipper CCD focal plane, we found that one pair of detectors exhibited unusually high correlated single-sample noise (~ 17 e$^-$ rms/pixel) compared to the other pair of devices (< 4.6 e$^-$ rms/pixel) [135]. Since these two detectors share clocks and biases, we attribute the source of this noise to an electronic coupling between these detectors. While we were unable to identify the precise source of this noise in the lab, we showed that this correlated noise quickly reaches nominal noise performance ($\sim 4.6\,\mathrm{e}^-$ rms/pixel) with $N_{\mathrm{samp}} = 7$. Furthermore, as shown in Figure 6.10, the Gaussian noise scaling behavior with N_{samp} is observed to recovered for $N_{\mathrm{samp}} > 12$. We measure a readout noise of $\sim 0.72\,\mathrm{e}^-$ rms/pixel and ~ 0.22 e$^-$ rms/pixel (enabling photon-counting) after $N_{\mathrm{samp}} = 50$ and $N_{\mathrm{samp}} = 250$, respectively. This multi-sample noise performance is comparable to the two unaffected devices.

During the first engineering night, we measured a shutter-open dark rate of $\mathcal{O}(10^{-1})\,\mathrm{e}^-$/pixel/s, which was attributed to stray light within the SIFS enclosure. We identified and mitigated several light sources contaminating the instrument's optical path. Science observations proceeded with an improved background rate $\sim 1.19 \times 10^{-2}$ e$^-$/pixel/s. While this remains sub-optimal, the stray light shot noise contribution can be kept to $\lesssim 2.5\,\mathrm{e}^-$ rms/pixel if the exposure time is limited to $\lesssim 600\,\mathrm{s}$ (Figure 6.11).

6.3.2 Single-Photon Counting

Single-photon counting was achieved for the first time with a Skipper CCD on the sky. We attained a readout noise of $\sim 0.22\,\mathrm{e}^-$rms/pixel over $\sim$5.4% of the SIFS FoV, enabling photon-counting in all detectors. Figures 6.12, 6.13, and 6.14 illustrate the ultra-low noise capabilities of the Skipper CCD through a sequence of readout noise configurations, ranging

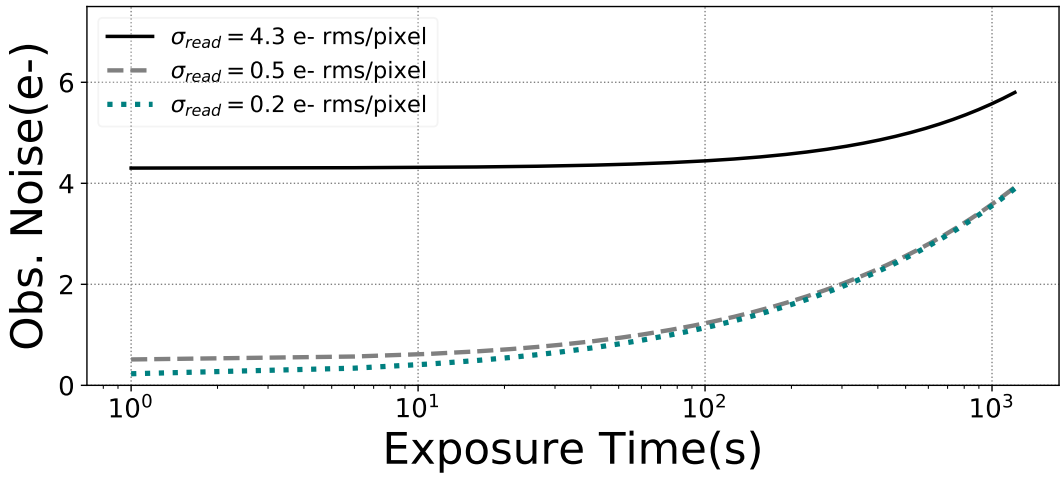

Figure 6.11: The total observation noise as a function of the exposure time. The total observation noise includes the background shot noise. In the configuration shown here, the background counts are dominated by the shutter-open dark rate. We note that for short exposure times (e.g., the $\sim 60\,\mathrm{s}$ exposure time used for some photon-counting readout configurations), the shot noise is subdominant to the readout noise.

from $N_{\mathrm{samp}} = 1$ (~ 4.6 e$^-$ rms/pixel) to $N_{\mathrm{samp}} = 250$ ($\sim 0.22\,\mathrm{e}^-$ rms/pixel). The frames in Figure 6.12 represent a 60 second exposure of the photon-counting ROI from one of the detectors, containing a bright fiber bundle which corresponds to the Ly-α emission line in HB89 1159+123. As the number of samples increases and the readout noise deceases, the line becomes increasingly visible. The reduction in the readout noise enables photon/electron counting (Figure 6.13) and the Ly-α feature becomes detectable above the noise (Figure 6.14). This is a powerful demonstration of the ultra-low noise capabilities the Skipper CCD provides. With the short exposure, we purposefully reduce the signal-level from the QSO while reducing the background contribution to the noise (< 1 e$^-$) to demonstrate the ability for the Skipper CCD to resolve spectral features contributing a few electrons.

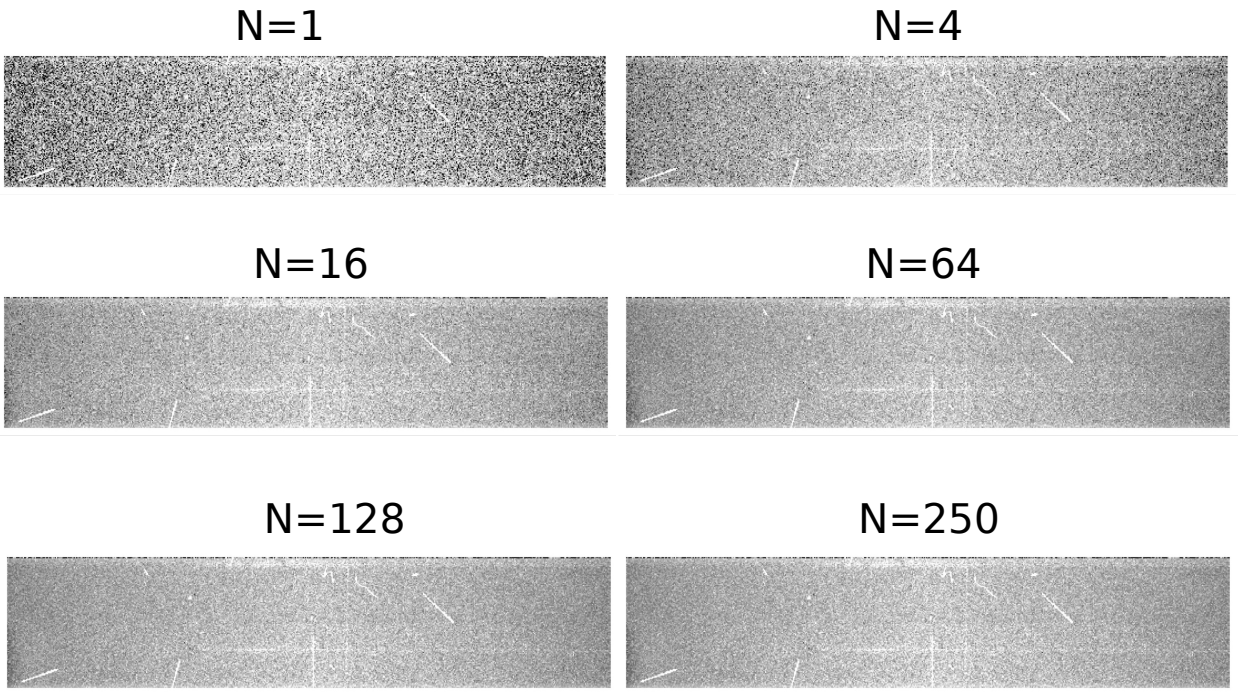

Figure 6.12: Transition between single-sample to photon-counting readout noise level for a data frame containing the Ly-α line from HB89 1159+123. Each sequence shows an increasing number of non-destructive pixel measurements and decreasing readout noise. The faint spectral trace becomes increasingly visible as the readout noise decreases. Note that the spatial and spectral axes have been flipped relative to Figures 6.7 and 6.8.

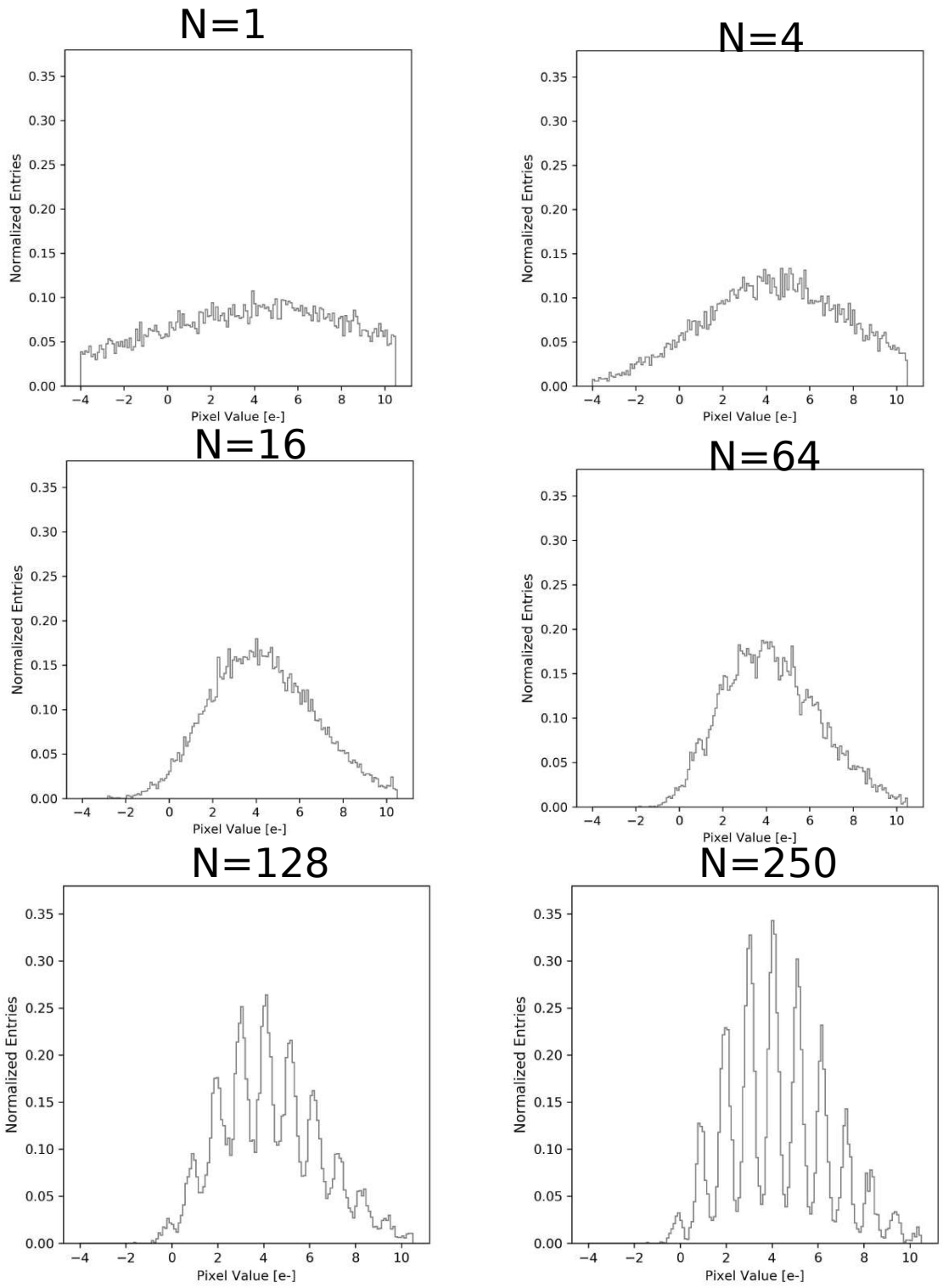

Figure 6.13: Photon-counting demonstration on the sky with the SIFS Skipper CCD focal plane. Photon resolution is achieved at 128 and 250 measurements per pixel over the ROI shown in Figure 6.12.

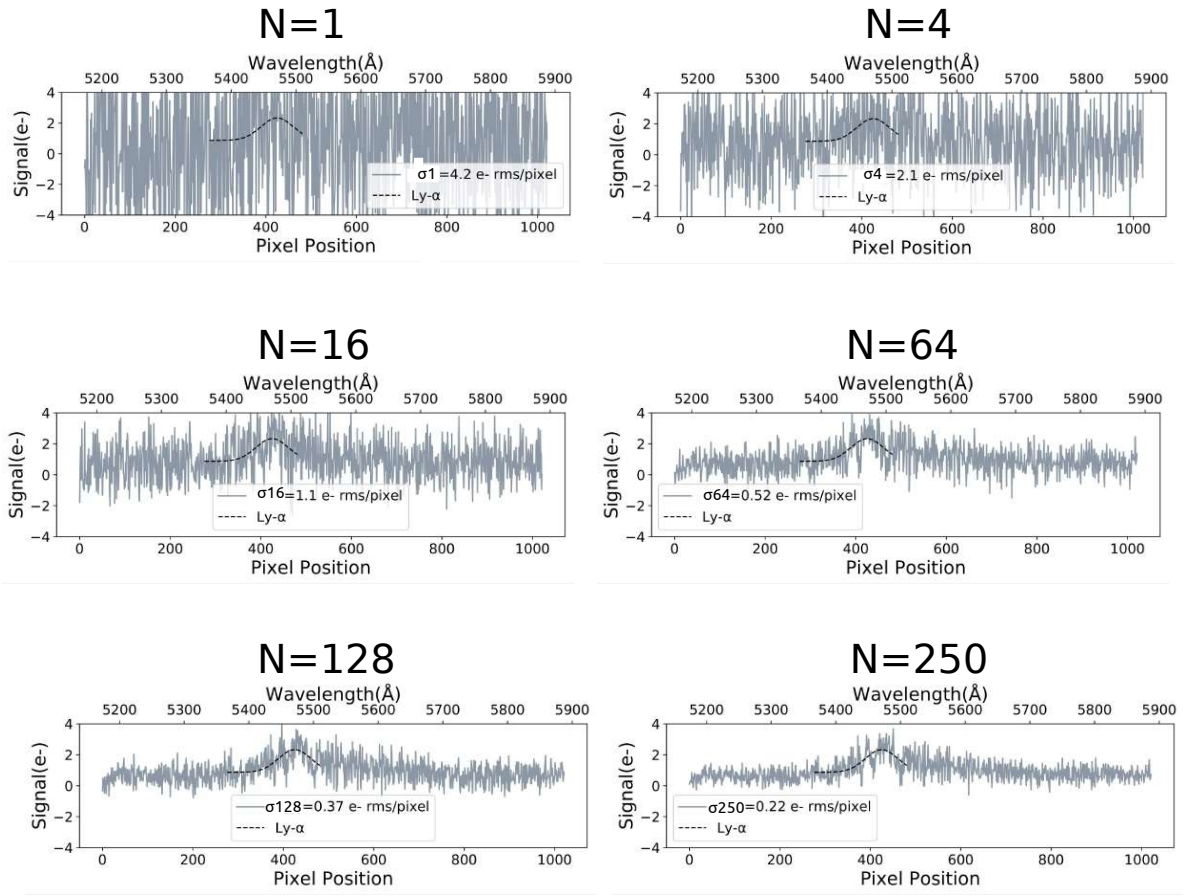

Figure 6.14: Noise reduction sequence illustrating the Ly-α line from the data frame in Figure 6.12. Of particular interest for this demonstration is the ability to resolve features of interest in the spectra. The Ly-α line is completely hidden in the readout noise for low number of samples. As the noise decreases down to the photon-counting regime, one is able to identify and precisely fit the Ly-α line.

6.3.3 Signal-to-Noise Improvement

The S/N is a measure of the ability to distinguish a signal from background noise. For faint sources in low-background observations, the readout noise can dominate the total noise in the observation, i.e.,

$$\sigma_{obs.} = \sqrt{\sigma^2_{shot} + \sigma^2_{read}} \tag{6.1}$$

where σ^2_{shot} represents the Poisson shot noise and σ_{read} is the detector's readout noise. The Poisson shot noise is calculated from the electron count rate (e^-/pixel/frame) from all sources, including CIC and the detector's "dark rate", which includes external light contamination leaking into the system. The Poisson shot noise, in contrast to the readout noise, increases with the exposure time and becomes the dominant component of the total observation noise when signal and/or background levels are high. In our current system, the background rate is sub-optimal due to issues with external light leakage. By reducing the exposure time, we can reduce the shot noise contribution from the signal and backgrounds in order to explore S/N improvements from the Skipper CCDs in the readout-noise-dominated regime. Figure 6.11 illustrates this interplay between exposure time (count level) and the readout noise. In exposures with few counts, reducing the readout noise can lead to significant gains in S/N.

Figure 6.15 shows the O III feature from the ELG for a 600 second exposure from one of the Skipper CCDs affected by correlated noise. We show that as the readout noise decreases from ~ 6 e^- rms/pixel with $N_{\rm samp} = 5$ to ~ 0.7 e^- rms/pixel after $N_{\rm samp} = 50$, the S/N increases up to 10.5, allowing for the O III emission line to be detected. In contrast, Figure 6.16 illustrates the Ly-α line from HB89 1159+123 with higher signal (~ 70 e^- on average) and a total of ~ 10 e^- contribution from the background. In this instance, the S/N stays roughly consistent because the low readout noise (~ 0.5 e^-rms/pix) is subdominant.

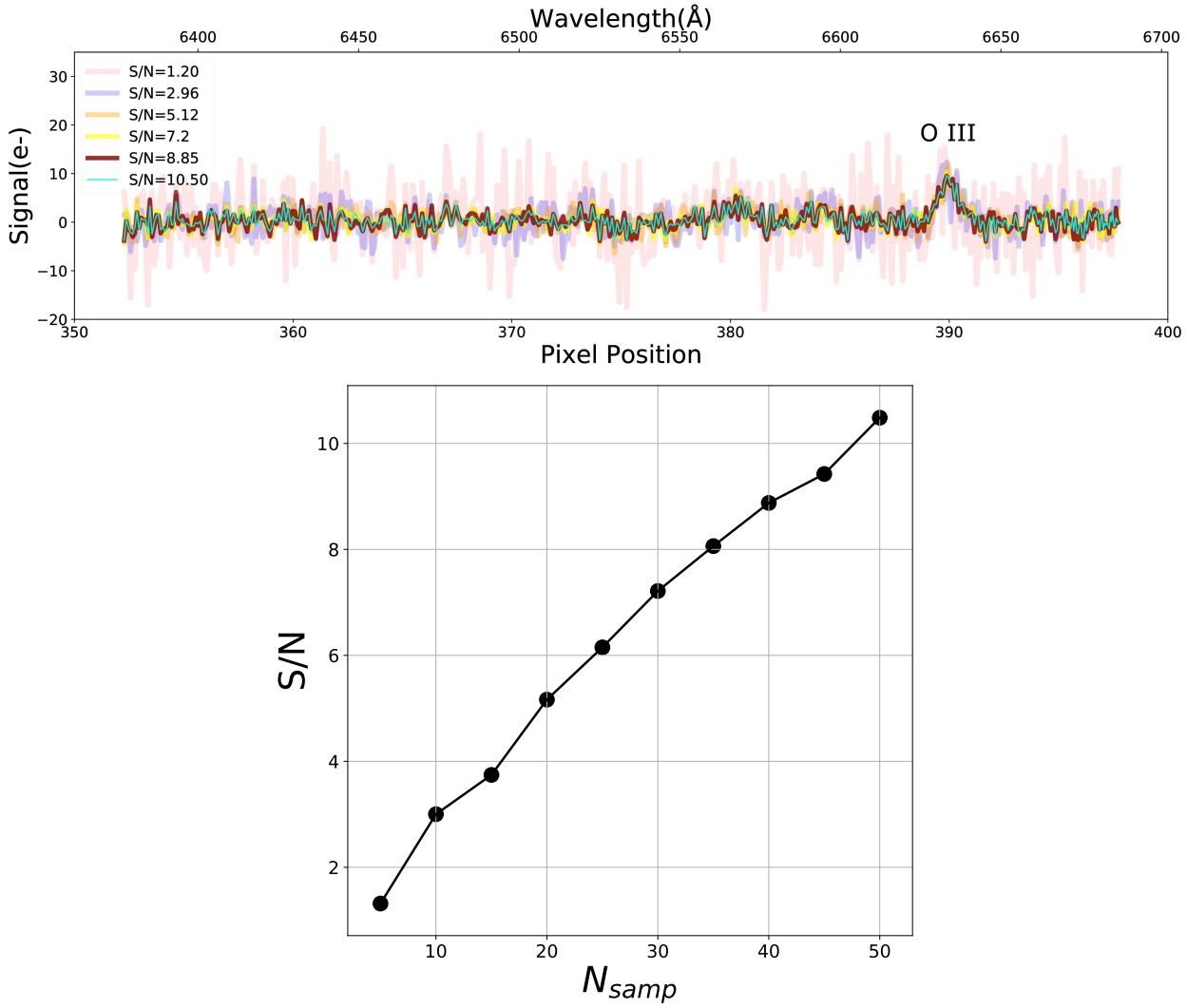

Figure 6.15: Top: Spectrum from a 600 s SIFS-Skipper CCD observation of an ELG identified in the DESI Early Data Release. The O III emission line is detected at $\lambda \sim 6628.8$ Å with different signal-to-noise ratios depending on the achieved readout noise (colored lines). Bottom: The signal-to-noise ratio as a function of $N_{\rm samp}$. In the readout-noise-dominated regime, it is possible to increase the SIFS signal-to-noise from ∼1.2 to ∼10.5 by achieving sub-electron readout noise levels. Note that this observations was taken by one of the Skipper CCDs that was affected by correlated noise.

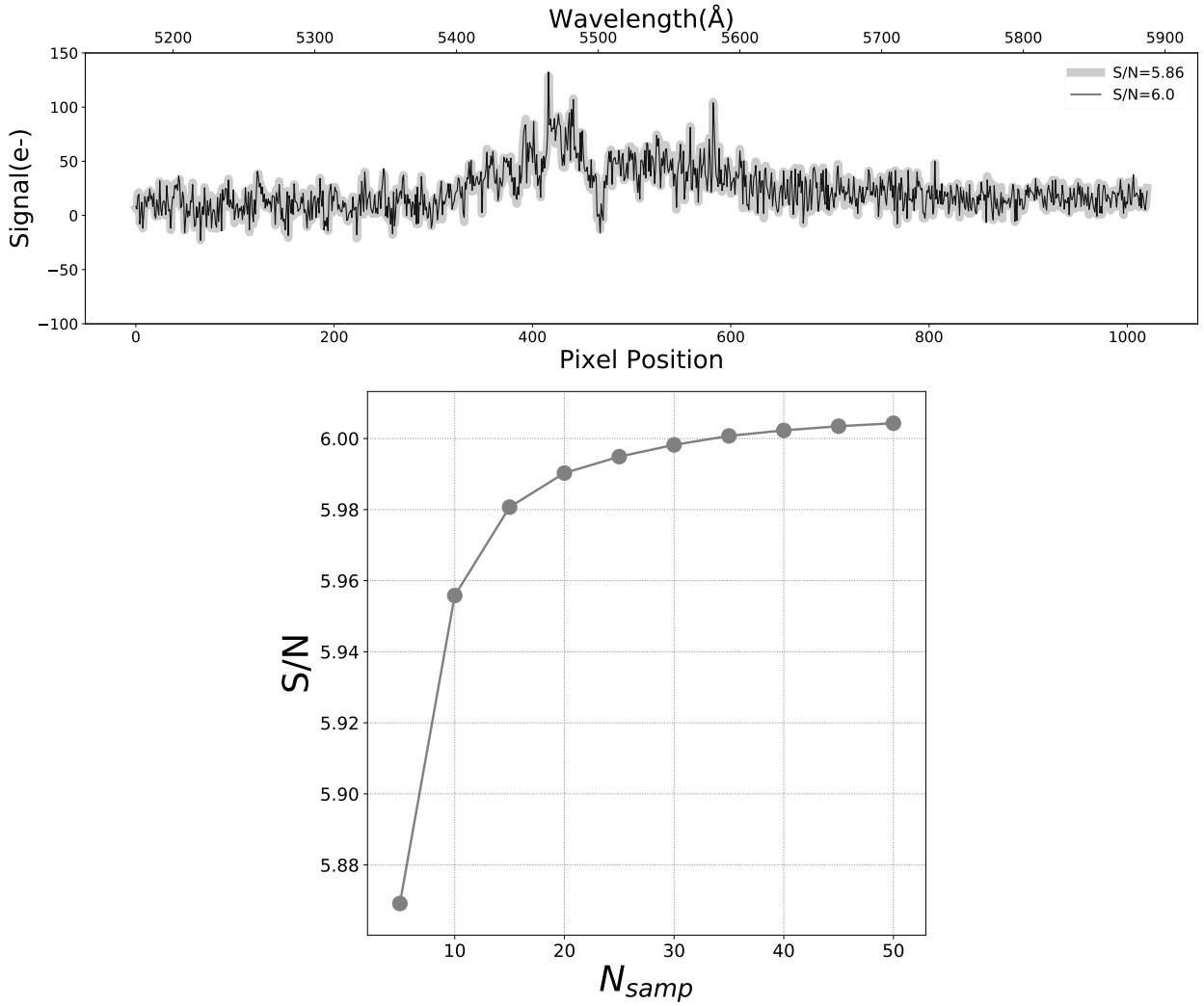

Figure 6.16: Top: High signal level ($\sim$70 e$^-$) spectrum around the Ly-α feature from a SIFS-Skipper CCD observation of QSO HB89 1159+123. Bottom: Signal-to-noise as a function of $N_{\rm samp}$ for the high signal QSO observation. The signal-to-noise improvement is minimal. The source and background contribution to the total noise is $\sim$ 10 e$^-$, which dominates the noise budget in this observation.

6.4 Summary and Planned Science

This chapter details the technology demonstration results of the first-ever on-sky testing of ultra-low noise, photon-counting Skipper CCDs at SIFS on the 4.1-m. SOAR Telescope. This experiment shows the viability of Skipper CCDs for measuring faint spectroscopic signals significantly below the noise levels in conventional scientific CCDs. We show performance parity with other astronomical CCDs, cementing the potential for using Skipper CCDs in future cosmological surveys. We demonstrated the implementation of ROIs to achieve sub-electron ($\lesssim 0.7\,\mathrm{e}^-$ rms/pixel) and photon-counting ($\sim 0.22\,\mathrm{e}^-$ rms/pixel) readout noise levels in portions of the FoV in $\lesssim$ 17 min. We note, however, that more promising alternatives, which involve modifications to the readout architecture of the detector, to minimizing readout times are in the R&D phase (See Chapter **??**).

We identified two scientific applications for the SIFS Skipper CCD science verification data: (1) we will use observations from the galaxy clusters (CL J1001+0220 and SPT-CL J2040−4451) to place new constraints on the mass of ALP DM, and (2) we use spectra from the candidate member star of the Boötes II ultra-faint dwarf galaxy to contribute to the study of the spatial distribution and DM halo of this system.

ALP Dark Matter: ALPs are a generalization of the Quantum chromodynamics (QCD) axion, initially proposed to solve the strong charge-parity (CP) problem [66, 168]. ALPs are also considered a viable DM candidate, and many efforts to search for them exploit their coupling to photons. From an astrophysics perspective, these searches aim to detect photon signals resulting from the radiative decay of ALP DM and the conversion of ALPs into photons in the presence of magnetic fields. For ALPs with masses in the electron-volt (eV) scale, the monochromatic photon emission from ALP decay falls within the optical and infrared wavelength range [19, 18]. Under the proposal SO2024A-011 ("Searching for decaying axion like particles in $z > 1.1$ galaxy clusters with SOAR/SIFS"), we have taken several science exposures of Sunyaev-Zeldovich-selected galaxy clusters (e.g., [169]) with the

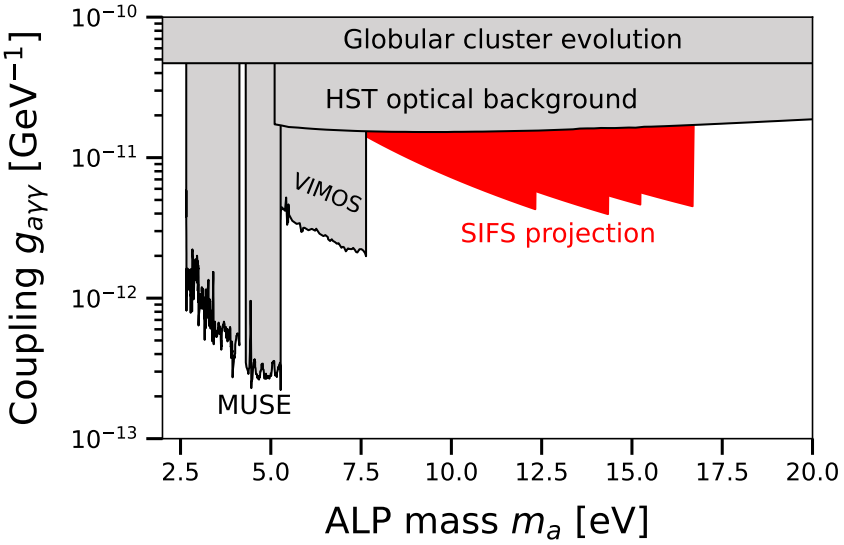

Figure 6.17: Collection of selected constraints on the ALP mass/coupling parameter space. Previous results (gray) include integral-field spectroscopic data from MUSE [18] and VIMOS [19], HST optical background [20], and stellar evolution [21]. Projected constraints from observation of galaxy clusters with SIFS are shown in red, demonstrating the advantages of low-noise detectors, as well as observations of higher-redshift clusters.

Skipper CCD focal plane prototype. These include two 1200 second exposures of the cluster CL J1001+0220 ($z \sim 2.51$ [170]) and three 900 second exposures of SPT-CL J2040−4451 ($z \sim 1.48$ [171]). For both clusters, we read out the full FoV with $N_{\mathrm{samp}} = 30$, providing $\sim$0.7 e^- rms/pixel readout noise on the two detectors not affected by the correlated noise while maintaining a manageable level of cosmic-ray contamination during read out. We show in Fig. 6.17 the expected sensitivity of these SIFS observations, compared to previous constraints from MUSE, VIMOS, and HST. (VIMOS was — and MUSE is — an integral-field spectrograph on the Very Large Telescope (VLT).) Despite the smaller diameter of SOAR compared to the VLT (4.1 m vs. 8.2 m), and the smaller FoV of SIFS compared to MUSE/VIMOS (0.03 arcmin^2 vs. 1 arcmin^2), we anticipate SIFS will deliver similar constraints on the ALP-photon coupling $g_{a\gamma\gamma}$ in a higher-mass range than has previously been probed. This is a combination of the low readout noise of the Skipper CCDs (allowing faint lines to become visible above the sky background) and observing higher-redshift galaxy

clusters (allowing photons from higher-mass — and thus faster-decaying — ALPs to redshift into the SIFS bandpass).

Boötes II Candidate Member Star: Pan et al. (2024) conducted a photometric analysis using metallicity sensitive DECam u-band imaging to identify candidate member stars in the outskirts of three MW ultra-faint dwarfs: Boötes I, Boötes II, and Segue 1. The study identify candidate member stars from derived photometric metallicities, and the authors of that work recommended spectroscopic follow-up to confirm the newly-identified candidate member stars. The SIFS-Skipper CCD system is well-suited to measure the radial velocities of these candidate member stars, allowing for unambiguous determination of their membership and extending the mapping of the stellar populations of ultra-faint dwarfs to larger distances. We acquired four 900-second exposures targeting a Boötes II candidate member star. A detailed study of this measurement is presented in the next chapter (Chapter 7).

CHAPTER 7

ASTRONOMICAL SPECTROSCOPY WITH SKIPPER CCDS

Alternative models to CDM can significantly suppress the linear matter power spectrum on small scales, suppressing the formation of smaller halos and, consequently, small galaxies. While validating these alternative models helps constrain the mechanisms responsible for structure suppression or enhancement, advancing our understanding of galaxy-halo evolution results in a more precise mapping of observables to simulations. For example, incorporating detailed baryonic physics into simulations—such as the effects of supernova feedback and tidal disruptions by massive host halos—is essential for aligning simulation predictions with observational data. Additionally, increasingly sensitive sky surveys expand the discovery potential of previously unexplored small scale parameter space, particularly those dominated by ultra-faint dwarf galaxies (UFDs) [53].

Surveys like SDSS have increased the number of known MW satellites to approximately 50. Yet, only a portion of the MW's virial volume—the region dominated by its gravitational influence—has been thoroughly surveyed. For example, SDSS covered roughly one-third of the sky and reached only about 10% of the MW's virial radius for the faintest dwarfs [72]. As a result, the current satellite count represents a lower bound, suggesting that many faint satellites likely remain undiscovered.

The abundance of UFDs is highly sensitive to any DM physics that affects the formation or survival of small halos. As such, these galaxies play a critical role in constraining various theoretical DM models (see Section 2.3). For example, the suppression of small-mass halos predicted by WDM or FDM models would reduce the number of observable satellites, providing a testable signature. In Nadler et al. (2021), a 95% confidence limit was set for the lower bound of the WDM particle mass ($m_{WDM} > 6.5$ keV). This corresponds to a maximum free-streaming length of $\lambda_{fs} \lesssim 10h^{-1}$ kpc, implying that WDM particles must have a sufficiently short free-streaming length to allow the formation of small-scale structures

such as MW satellites. If WDM particles had a longer free-streaming length, the formation of small subhalos would be suppressed, reducing the number of observable satellites and potentially creating discrepancies with CDM predictions.

The study of the kinematics of member stars in UFDs can also provide precise constraints on the distribution of DM at small scales. In particular by measuring radial velocities and velocity dispersions of member stars, one can probe the inner density profiles of DM subhalos hosting these galaxies. From the CDM perspective, UFDs are embedded in cuspy halos with steep central density profiles, such as those described by the NFW profile. These cuspy subhalos generate strong tidal forces that influence the structure and dynamics of globular cluster (GC) streams, producing streams with wider spatial extents, larger line-of-sight velocity dispersions, and higher angular momentum dispersions. In contrast, alternative DM models, such as self-interacting DM (see Section 2.3.2), predict cored subhalos with flatter inner density profiles. Such cored profiles result in weaker tidal stripping of GCs, leading to streams with narrower widths and lower velocity dispersions. Malhan et al. (2021) highlights that the line-of-sight velocity dispersions of UFDs can effectively distinguish between these DM models by revealing variations in the strength of the tidal forces acting on their stellar components. Thus, velocity dispersion profiles in UFDs can indicate whether the gravitational potential of the halo is steep or shallow, directly tying observable stellar motions to the underlying DM properties.

7.1 Motivation

Here, we focus on studying the peripheries of UFDs. Theoretical simulations suggest that UFDs are embedded in extended DM halos, and processes such as early galaxy mergers and supernova feedback may significantly shape their outer regions [173]. These peripheral regions, often extending beyond four half-light radii ($4r_h$), provide pristine environments to test DM halo properties. Stellar tracers in the outskirts of UFDs, when combined with po-

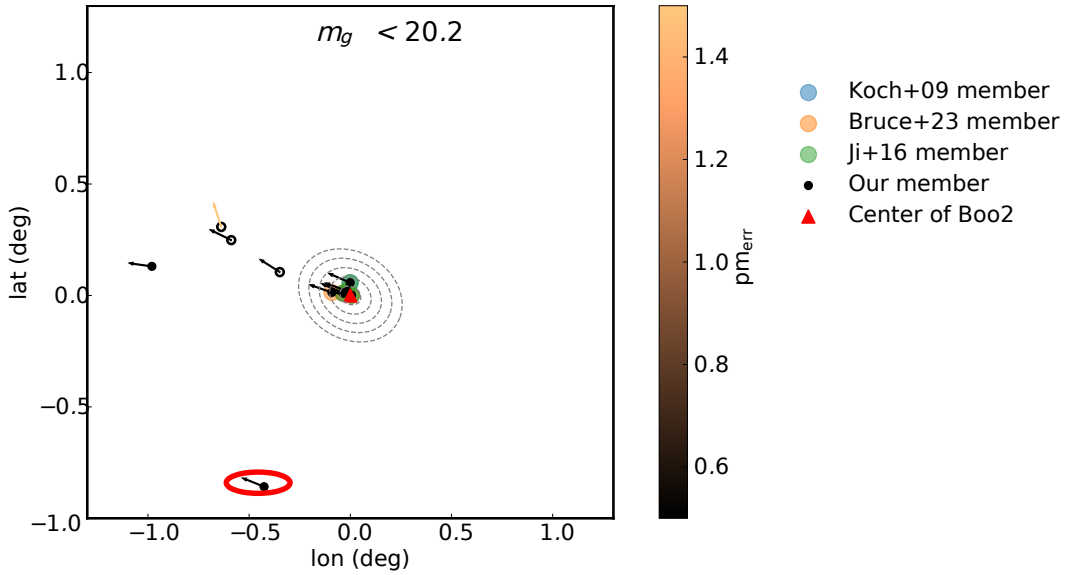

Figure 7.1: Spatial distribution of Boötes II candidate member stars with metallicities [Fe/H < -1.5]. The dashed grey ellipses represent the half-life radii (r_h). Most star in the system lie within $2r_h$; however, there are two stars (solid black points) outside $5r_h$ that could be potential members. We acquired spectra from one of these candidates (red circled star). Figure extracted from [22].

sitional and kinematic data, enable the mapping of the total mass distribution as a function of distance from the galaxy's center, offering a direct probe of the DM halo density profile. The kinematics of stars in UFDs are therefore critical for bridging the gap between observed and simulated DM halo properties, particularly at scales not well constrained by other observational probes or simulations [174]. A precise understanding of UFD formation and evolution, informed by observations of their peripheral stars, can improve models, refining DM predictions at small scales [175, 176, 177, 178]. While the central regions of UFDs have been extensively studied, the peripheries remain underexplored (e.g., [179, 22]), representing a crucial opportunity to investigate the mechanisms driving UFD evolution and the role of DM in shaping these faint galaxies.

The processes driving stars to the periphery of UFDs are not well understood. However results from both observations and simulations suggest that tidal disruptions, early UFD galaxy mergers, and stellar feedback might paly a role in relocating member stars to the

systems' outer radii. Tidal interactions with a more massive host galaxy, such as the MW, can strip stars from the core of a UFD and deposit them at greater distances. Observations strongly suggest this process for certain UFDs. For instance, Boötes I shows a larger number of candidate stars at distances beyond $4r_h$, aligning with predictions of tidal disruption [180, 181]. Early dwarf-dwarf mergers are another mechanism that may populate the peripheries of UFDs. Simulations suggest that UFDs formed at high redshift ($z \gtrsim 2$) likely experienced a handful of mergers [182]. These mergers can dynamically heat the system, forming extended stellar halos. For example, Tucana II is hypothesized to have undergone a merger during its early evolution, as evidenced by its extended stellar population reaching up to $9r_h$ [182, 179]. This spatial distribution is atypical for UFDs and suggests that mergers could play a pivotal role in shaping their structure. Bursty star formation and supernova feedback can impart significant kinetic energy to stars, dispersing them to larger radii. This mechanism is particularly effective in the low-potential wells of UFDs. For instance, Supernova-driven feedback may explain the low-density outer profiles observed in systems like Hercules and Tucana II. Feedback can result in metal-poor stars being preferentially displaced, which aligns with the metallicity gradient found in Tucana II, i.e., [Fe/H] < -3.0 compared to [Fe/H] ~ -2.62 in the core [183, 179, 184].

Pan et al. (2024) conducted a study to identify member stars in three MW UFDs: Boötes I, Boötes II, and Segue I. The study combines u-band observations from DECam with broad-band photometry from the DECam Local Volume Exploration Survey (DELVE) Data Release 2 and astrometric data from the Gaia DR3 catalog. These photometric observations are particularly well-suited for studying the outskirts of UFDs, which are sparsely populated with stars and often dominated by MW foreground stars.

The u-band is particularly useful for this task because it captures the prominent calcium (Ca II K) metal absorption line at 3933 Å, which is highly sensitive to a star's metal content. Metal-poor stars, which are common in UFDs, show stronger Ca II K absorption than

metal-rich stars. By leveraging u-band imaging with wide-field cameras such as DECam, it is possible to estimate the metallicities of all stars within the camera's field of view. Pan et al. (2024) presents the spatial distribution of candidate member stars selected based on their computed photometric metallicities for the three UFDs. In particular, for Boötes II, five candidate members are identified beyond $5r_h$. However, three of these stars are outliers on the color-magnitude diagram and may not be true members. The remaining two candidates are promising, and the authors recommend spectroscopic follow-up to confirm their membership.

Since MW foreground contamination is more likely in the outer regions of UFDs [22], it is important to determine the membership of potential candidate stars by measuring their radial velocities. As part of the observations performed with the prototype Skipper CCD focal plane at SIFS, we obtained science-quality spectra from one of the Boötes II candidate member stars that was recommended for spectroscopic follow-up. Our goal is not only to demonstrate the viability of Skipper CCDs for astronomical measurements through this technology test but also to explore scientifically significant cases using Skipper-SIFS data. We acquired four 900-second exposures from the candidate member star, utilizing the half-FOV observation configuration (see Section 6.2) with $N_{\rm samp} = 20$, achieving a readout noise of approximately 1 e^-rms/pix in the Skipper CCD focal plane ROI. The study consists on measuring the star member candidate's radial velocity from spectral absorption features (e.g., the H-α line) and determine if it is within the mean systematic radial velocity for Boötes II (-139.4$^{+1.4}_{-1.1}$ km/s) [32]. Additionally, we acquired spectra from four metal-poor stars to be used as radial velocity standards: HD 122653, BD-18 5550, Gaia DR3 2771566830179387776, and Gaia DR3 6770873387893255552. We use these standards to validate our data reduction pipeline.

7.2 Data Reduction Pipeline

We developed a data reduction pipeline to process both the science and calibration data products acquired with the SIFS-Skipper instrument. The pipeline performs two primary tasks: raw image correction and spectra extraction from science frames. Figures 7.2 and 7.3 illustrate the procedural flow for processing an image and extracting spectra. Robust image correction techniques are especially critical for this process. The science data products consist of frames with ROIs that display spatial transients along rows and columns. These transients must be efficiently removed to recover accurate, unbiased electron counts in the image. Additionally, obtaining a precise wavelength solution for the extracted spectra is crucial for accurately determining the wavelength positions of spectral features of interest. In this section, I describe the methodologies for processing raw data, deriving the wavelength solution, and extracting spectra as part of the SIFS-Skipper data reduction pipeline.

7.2.1 Image Correction

In Section 5.4.1, I briefly described the overscan subtraction method used to correct both single- and multi-sample images, where a multi-Gaussian model is applied to fit the pixel distribution for each row in the serial overscan,[1] followed by subtracting the fitted mean from each row. However, since the SIFS-Skipper data includes ROIs, this simplistic method of overscan subtraction does not effectively remove transient effects in the pixels between single- and multi-sample regions. Therefore, a more robust approach is necessary for optimal overscan subtraction in ROI images, while the simpler method can still be applied to single-sample data products, e.g., flat-fields and arc-lamp calibration frames.

The sequencer block in the LTA functions as a state machine that executes user-defined

1. Due to long readout times, environmental light leaks can lead to charge collection in the overscan pixels when they are shifted into the serial register. The presence of this charge leads to appreciable single-electron events in Skipper CCD images with sub-electron noise. We model the pixel distribution with a multi-Gaussian to accurately subtract the mean of the $0e^-$ peak.

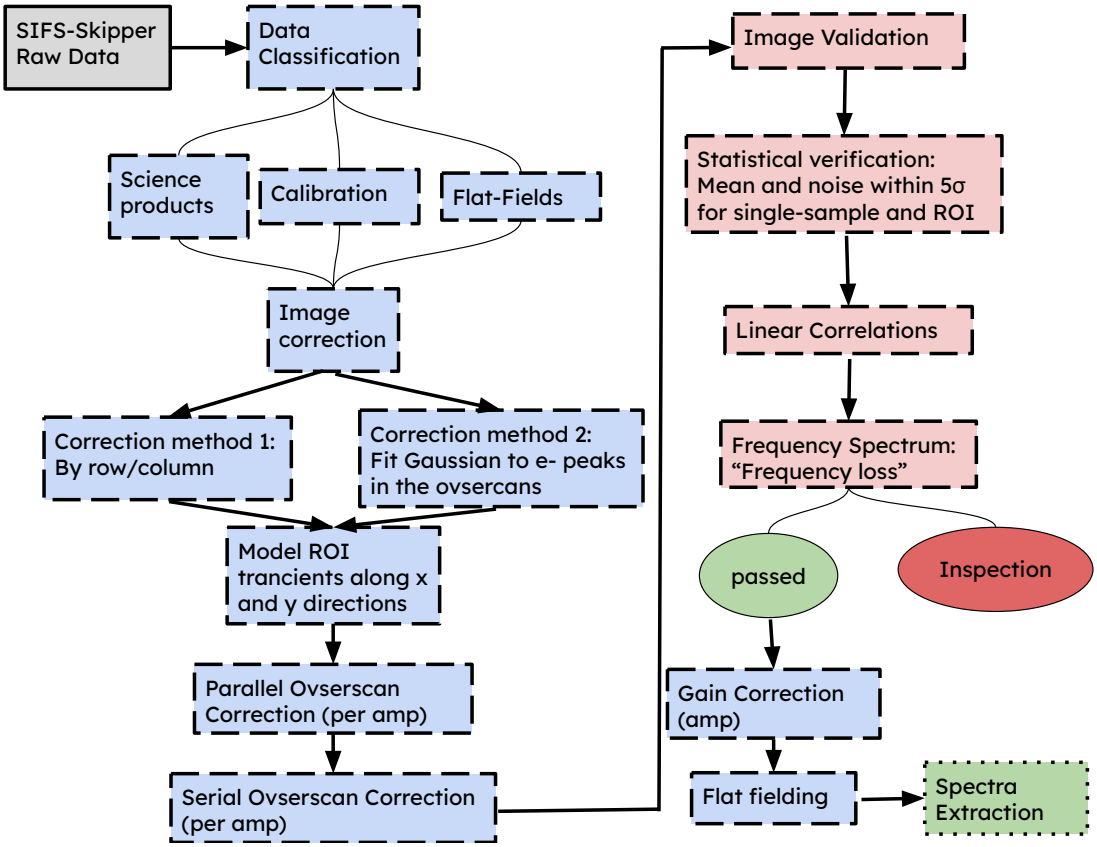

Figure 7.2: Image processing diagram. The first component of the pipeline performs image correction tasks. For a given data set, data products are first classified. Image correction proceeds with the user's choice of correction method. The algorithm models the spatial transients in ROI images and corrects for them in the parallel and serial ovserscans. The accuracy of the correction is validated by a series of tests that involved checking for noise increase and $0e^-$ shifts, introduction of linear correlations, and any other spatial patterns. Gain and flat-field (from a "combined flat") corrections are also applied.

instructions for reading each pixel on the CCD. For ROIs, the sequencer block can adaptively modify the number of measurements (N_{samp}) for each pixel based on the sensor's parameters and the current pixel being read. This information is predefined by the user in the sequencer. However, implementing "on-the-fly" changes to the pixel readout, which requires changing clock signals, introduces variations in the baseline. Because the CCD is a highly coupled device and voltage clock swings are in the order of tens of volts, abrupt changes in the clocks leads to systematic error in the determination of the pixel charge. Removing these baseline shifts rely on an accurate calibration of these transients, which depend on the ROI N_{samp},

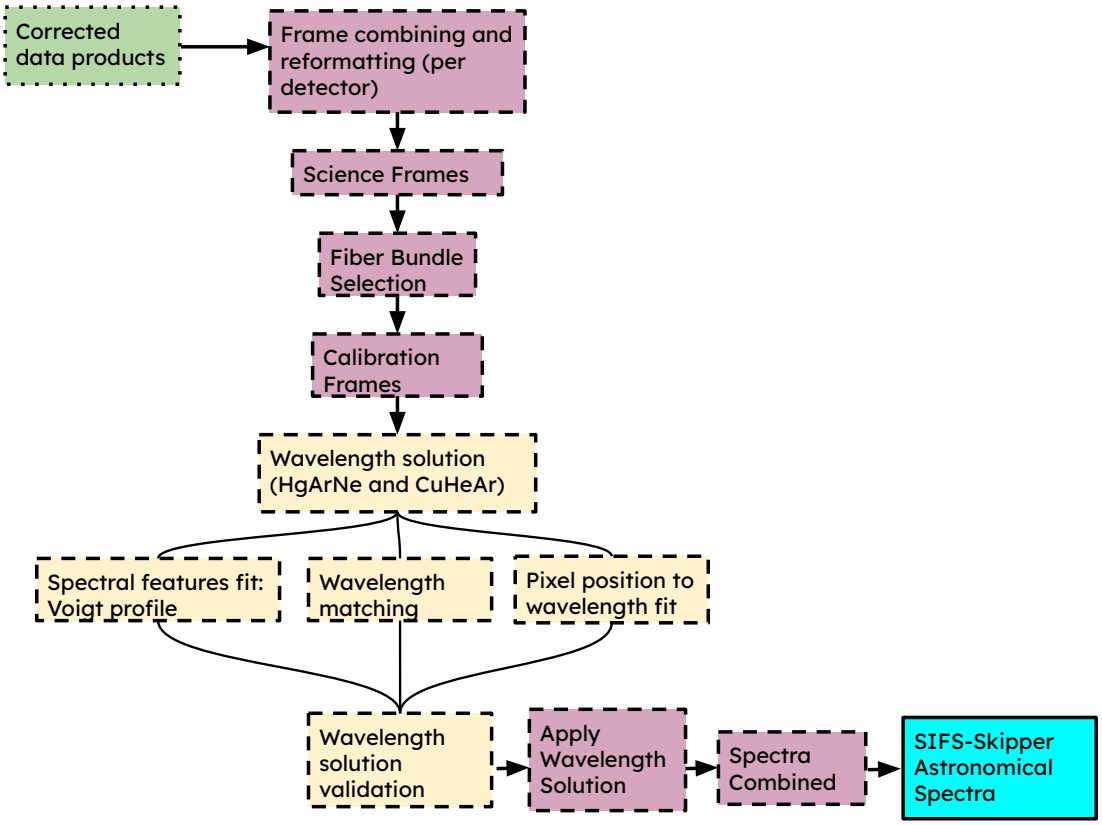

Figure 7.3: Spectral Extraction diagram. After correction of science and arc-lamp data products, these pass to the spectral extraction step in the data reduction pipeline. First, individual channels (amps) are combined in groups of four to form a "detector image" (spectra and wavelength solutions are derived on a detector by detector basis). Fiber bundles are then selected and their pixel positions are used to extract spectral lines from the arc-lamps frames. The positions of these lines are used to derive the wavelength solution. The wavelength solution is validated and then applied to the combined spectra from science frames.

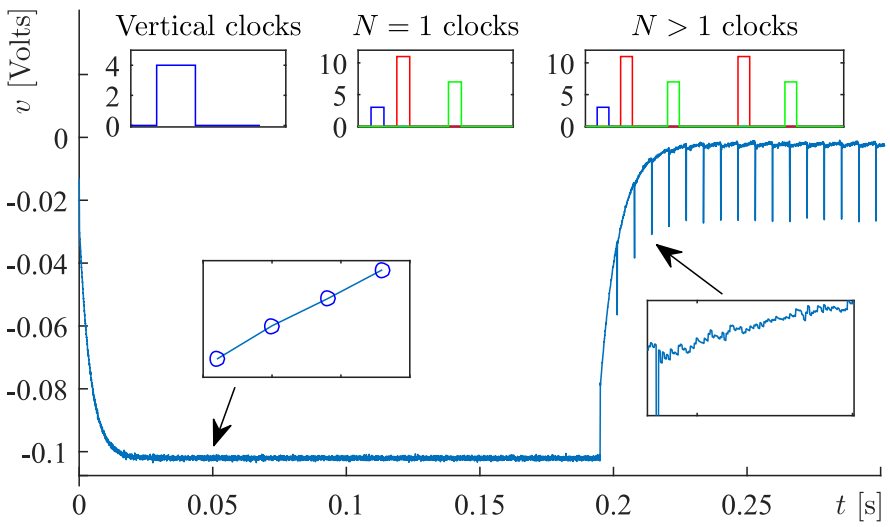

Figure 7.4: Baseline of the raw video signal. The flat signal profile (bottom left inset) corresponds to $N_{\text{samp}} = 1$. A sharp exponential transient (bottom right inset) is induced in the video signal when changing to $N_{\text{samp}} = 100$. The top insets indicate clock signals and their voltage swings Figure extracted from [23].

and the number of rows and columns being readout.

The Skipper CCD is capable of detecting charge levels as low as 2 μV per electron [23]. Thus, even minimal changes in the baseline—down to sub-parts per million—can significantly affect the accuracy of the measurements. As shown in Figure 7.4, switching the readout mode from $N_{\text{samp}} = 1$ to $N_{\text{samp}} = 100$ causes a noticeable exponential decay in the baseline, followed by a plateau. These baseline transients are orders of magnitude larger than the signal expected from individual electrons, emphasizing the critical importance of precise calibration.

Overscan Subtraction: To illustrate the procedure for bias subtraction in ROI frames, consider Figure 7.5, which shows a raw AstroSkipper image for one amplifier containing two ROIs. From left to right, the image features a single-sample region from pixel 0 to 480, followed by a multi-sample region ($N_{\text{samp}} = 20$) from pixel 480 to 1000, another single-sample region from pixel 1000 to 1200, followed by a multi-sample region from pixel 1200 to 2000, and ending with a final single-sample region that covers the remaining active area,

ending at pixel 3080.

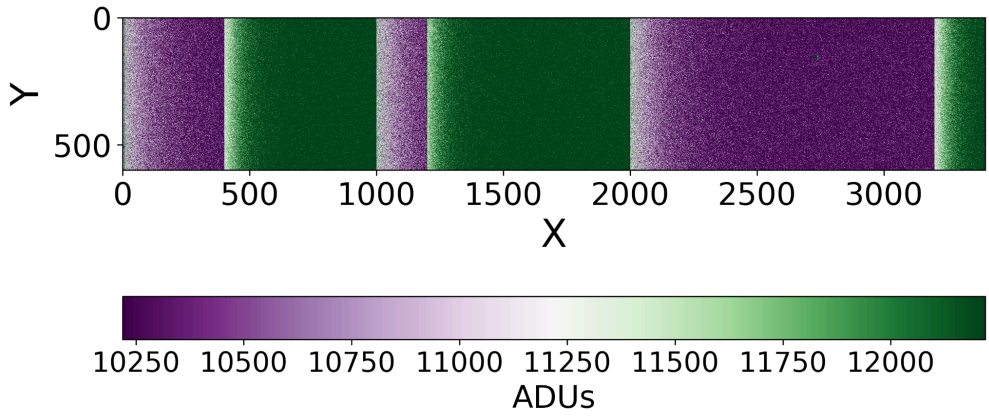

Figure 7.5: Raw AstroSkipper image for a single amplifier. The image has two ROIs with $N_{\text{samp}} = 20$. The bias level variation between the single- and multi-sample regions is ~ 2000 ADUs (~ 15 e$^-$).

There are two serial overscan regions: a single-sample region from pixel 3080 to 3200 and a multi-sample region from pixel 3200 to 3400. Note the bias level differences between regions, which exhibit a gradient that becomes uniform with increasing number of columns for each region. The bias subtraction algorithm first calculates the median value of each row in the serial single- and multi-sample overscans, applies a median filter [185], and performs a spline fit. The resulting models (as a function of row number) capture the full transient effects along the row direction for the single- and multi-sample region. These models are then used to subtract the bias shifts row by row. Figure 7.6 (Top) shows the spline fit to the bias transient in the row direction. This functional model is subtracted from the raw ROI image to get the image in Figure 7.6 (Bottom).

Serial overscan subtraction (Figure 7.6) does not fully eliminate bias shifts across the entire frame. In each row of every region, the pixel bias follows an exponential profile that reaches a steady state after ~ 100 columns. This exponential can also be modeled as a function of column number, using the parallel overscan, which extends from row 0 to row 89. The parallel overscan spans both single- and multi-sample regions, naturally capturing pixel variations across the whole image. The model (Figure 7.7, Top) is applied column by column to the

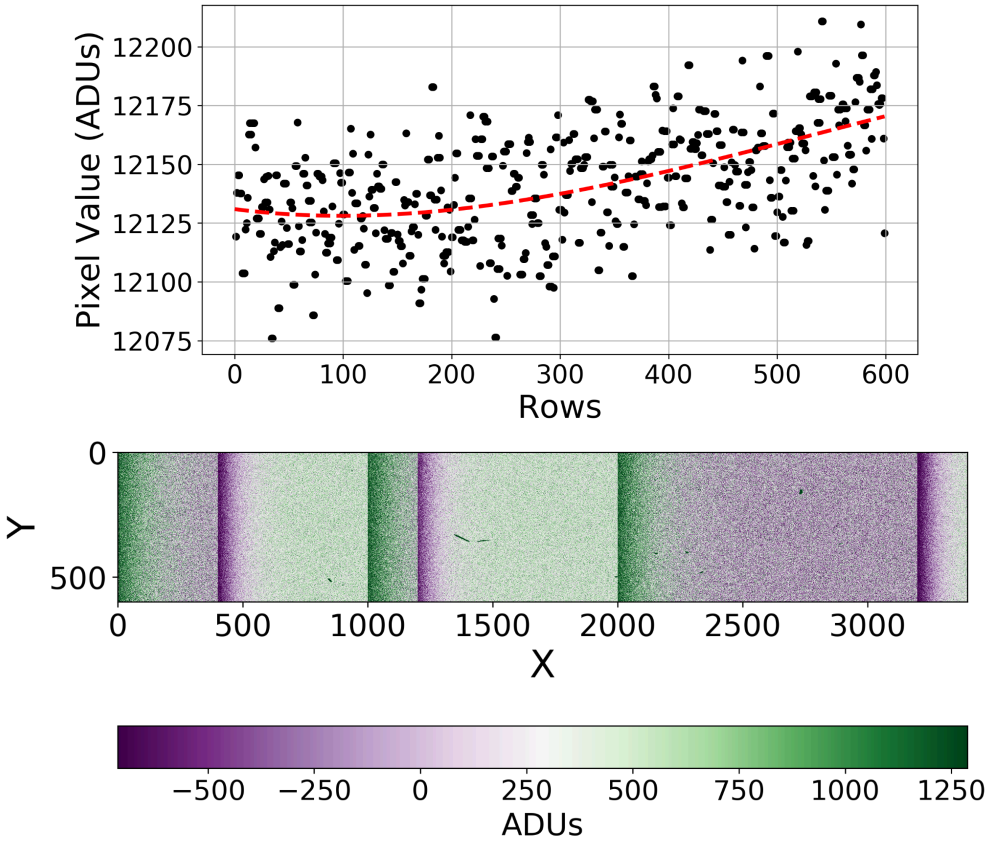

Figure 7.6: First step in the correction algorithm (Serial overscan correction). A model is derived to capture the bias shift as function of row number for for both the single- and multi-sample regions. The model is then applied to every region row by row (Bottom). Note that the image still exhibits pixel variations between regions. Subsequent steps are required to eliminate this residual.

image, resulting in an image free of transient effects (Figure 7.7, Bottom).

Image Correction Validation: In [16], we demonstrated the feasibility of capturing and eliminating pixel bias variations in ROI images using a "master bias". We collected 26 images for a specific ROI configuration and generated a sigma-clipped average from these images to correct the target image. In astronomical observations, bias frames are acquired throughout the night to create a master bias, which is then used to capture any transient effects and correct science frames. However, due to the extended readout time required for Skipper CCDs configured to achieve sub-electron readout noise, acquiring bias frames during the night is impractical. This challenge is compounded if different ROI configurations are needed, as

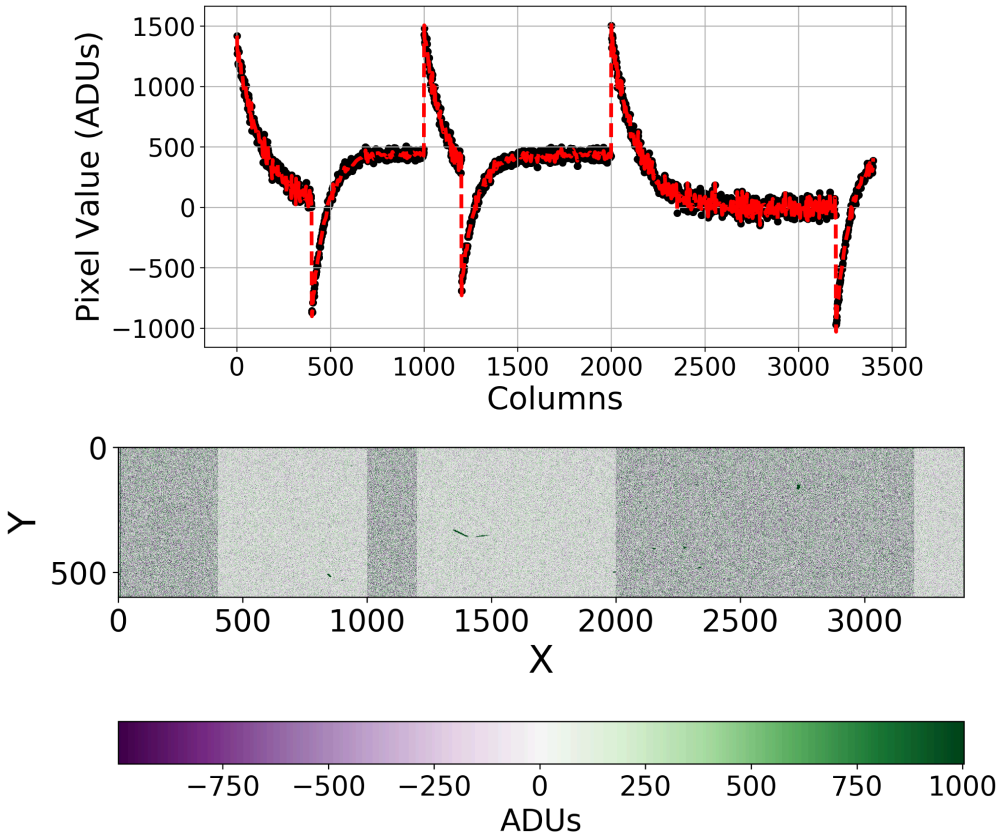

Figure 7.7: Parallel overscan correction step. The leftover pixel transient, after serial ovsrscan correction, is modeled as a function of column number, using the parallel ovsrscan (Top). After column by column correction is applied to the ROI image, all bias shifts are fully eliminated (Bottom).

each unique readout sequence would require a separate master bias. Consequently, for the SIFS-Skipper demonstration, validating our master bias-free image processing algorithm as sufficient for correcting pixel variations due to transient effects became a priority.

For each observation, we acquired bias frames (on the day before) for each ROI configuration and generated a master bias consisting of 15 individual frames. To validate our correction algorithm against the traditional master bias correction, we created residual images by applying either the master bias or our correction algorithm to individual bias frames. We then verified that the mean of the pixel distribution in the serial/parallel overscan regions is consistent with zero (within the baseline readout noise), i.e., $\mu_{fit} \pm \sigma_{fit} < \mu_{\text{baseline}} \pm \sigma_{\text{baseline}}$.

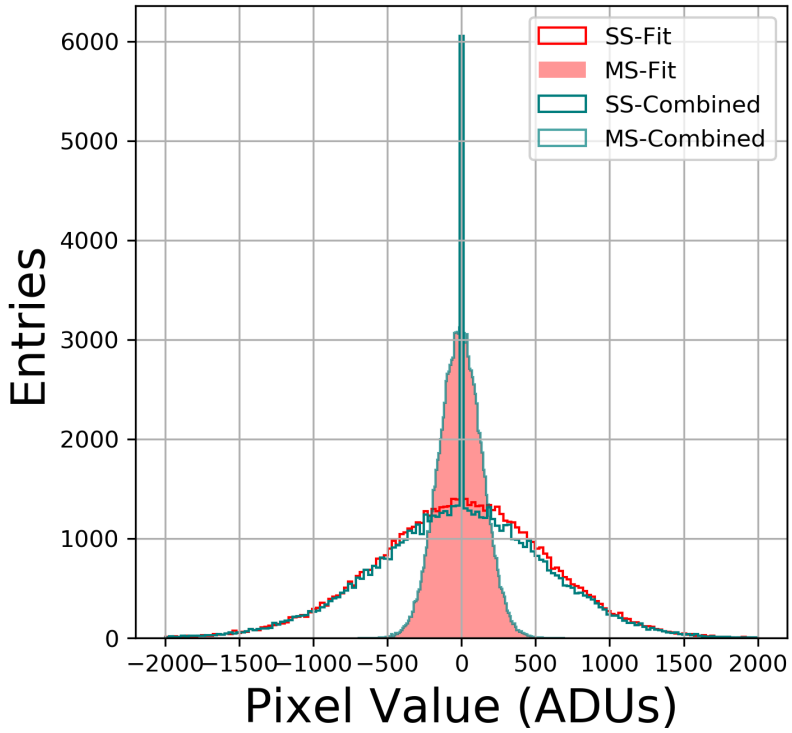

Figure 7.8: Statistical verification for the serial overscan. The pixel distributions from single-sample (SS) and multi-sample (MS) regions are shown. These correspond to images where the correction fitting algorithm (Fit) and the master bias (Combined) had been applied. Both correction methods perform similarly for all 16 amplifiers.

Additionally, we confirmed that the measured noise from each residual image (after 5σ clipping) is within 5% of the expected amplifier readout noise. This verification was performed for both the single- and multi-sample regions (Figure 7.8). This statistical validation is based on calibration products verification in the instrument signature removal (ISR) pipeline for LSST (see Malagón et al. (2024)). We confirmed that residual images from all 16 amplifiers passed this requirement.

Pixel transients in raw data products follow exponential profiles in the row and column directions. For an exponential function of the form e^{ax}, the linear approximation can be written as $1 + (ax)$. Thus, a generic method to quantify the effectiveness of both the fitting correction algorithm and the master bias method is to look for linear correlations among pixels of residual images. We compute the pixel correlation coefficients globally for the

vertical and horizontal directions as:

$$r_{xy} = \frac{\sum_{i=1}^{n}(x_i - \bar{x})(y_i - \bar{y})}{\sqrt{\sum_{i=1}^{n}(x_i - \bar{x})^2}\sqrt{\sum_{i=1}^{n}(y_i - \bar{y})^2}} \tag{7.1}$$

where the term $\sum_{i=1}^{n}(x_i - \bar{x})(y_i - \bar{y})$ represent unshifted (x_i) and shifted (y_i) pixel values, capturing how much pixel values move together when offset. The denominator of the expression normalizes this movement by the product of the standard deviations of the shifted and unshifted images. Figure 7.9 compares the two methods for image correction. As expected, the raw ROI image shows strong linear correlations in both horizontal and vertical directions due to pixel variation transients (Top). Applying either the master bias or our image correction method reduces these linear correlations in both directions, indicating that both methods perform similarly in removing pixel variations (Center and Bottom).

Frequency Domain Analysis: To capture subtle details or variations within an image that might not be apparent in the spatial domain, we compare images in the frequency domain, where patterns of repeating structures can be represented as frequency components. The discrete Fourier transform is a complex-valued function that decomposes a discrete, finite signal into its constituent frequencies, i.e., an orthogonal set of sine and cosine basis functions. The frequency representation of a 2D image is then:

$$F(u,v) = \sum_{x=0}^{M-1}\sum_{y=0}^{N-1} f(x,y)e^{-i2\pi(ux/M+vy/N)} \tag{7.2}$$

where the image size is $M \times N$, (x, y) represents the pixel coordinates in the spatial domain, $f(x, y)$ is the pixel value, and (u, v) is the complex frequency value. By computing the frequency difference, i.e., $|F_1(u, v)| - |F_2(u, v)|$, between two images, variations in structural patterns can be identified, with larger values indicating more significant discrepancies.

Additionally, we can define a "frequency loss" metric [187, 188] as the weighted difference of

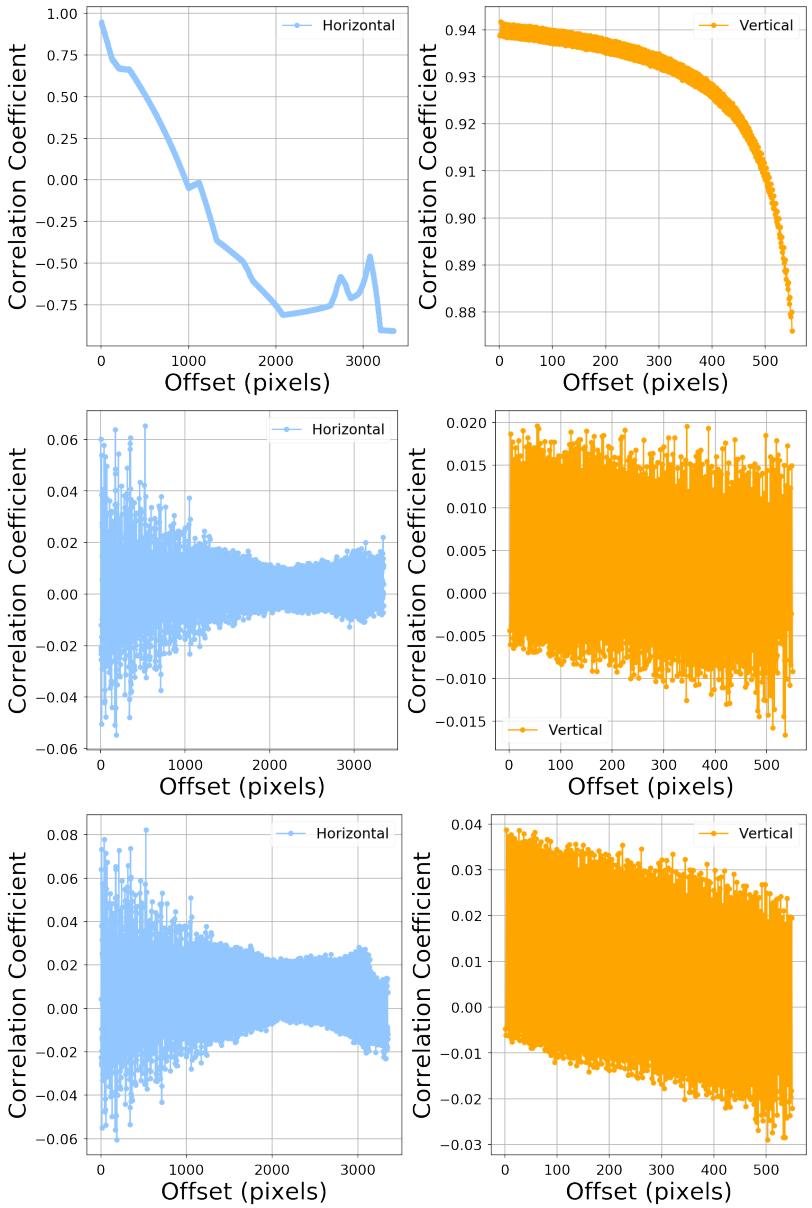

Figure 7.9: Linear correlation coefficients. Top: Raw ROI image corresponding to the Half-FoV ROI configuration. The horizontal direction (columns) show a strong positive and negative (1 and -1) linear correlation, which agrees with the alternating exponential model, e.g., Figure 7.7 (Top). The vertical direction shows a strong positive linear correlation. Center: The raw image has been corrected using the master bias. Bottom: The raw image has been corrected with the our fitting algorithm. In both instances, the linear correlations have been substantially reduced. We note that in the vertical direction there is a noticeable downward trend in the correlation coefficients. This might indicate leftover exponential residuals after image correction. However, we observe that the coefficient values are consistent with the master bias correction method (Center frame).

frequency components to quantify the overall dissimilarity between images in the frequency domain:

$$L = \frac{1}{N}\sqrt{\sum_{u,v} w(u,v)(|F_1(u,v)| - |F_2(u,v)|)^2}. \tag{7.3}$$

Here, we introduce $w(u,v)$, a weighting function that amplifies or suppresses specific frequencies. For example, a low-pass weighting, $w(u,v) = \frac{1}{u^2+v^2}$, emphasizes low frequencies or broad structures, while $w(u,v) = u^2 + v^2$ highlights high frequencies and fine details (e.g., [189]). To further compare the two image correction methods and validate our correction algorithm, we compute the frequency difference and frequency loss between ROI images corrected using each method. Figure 7.10 shows the frequency difference comparison for both correction methods with low- and high-pass filtering, and the raw image. We note that the low frequency components have been shifted to the center of the image, with higher frequencies in the outer edges for improved visual interpretation of features.

First, we examine the top and center colormap plots, which represent the frequency difference between the two image correction methods for high- and low-pass filters, respectively. The center plot emphasizes low frequencies, exhibiting a bright center spot and an overall higher discrepancy in the low-frequency component difference ($D(u,v) = |F_1(u,v)| - |F_2(u,v)|$) between the two images. This indicates differences in the smooth, broad variations between the images. In contrast, the top plot, which applies high-frequency weighting, shows darker spots near the edges, suggesting that $\sum_{u,v} D(u,v) \to 0$ and indicating small variations in fine structures, such as texture or edges, between both images.

As expected, the frequency loss value for the low-pass scheme is higher ($L \sim 110$) compared to the high-pass filtering ($L \sim 54$). We also observe vertical striping (where $v \to 0$), which suggests variations along the horizontal direction, i.e., columns. This may be interpreted as residuals from removing the strong exponential features along that direction. However, these metrics must be compared relative to each other. For example, consider the bottom plot in Figure 7.10, which shows the low-pass frequency difference between one of the corrected

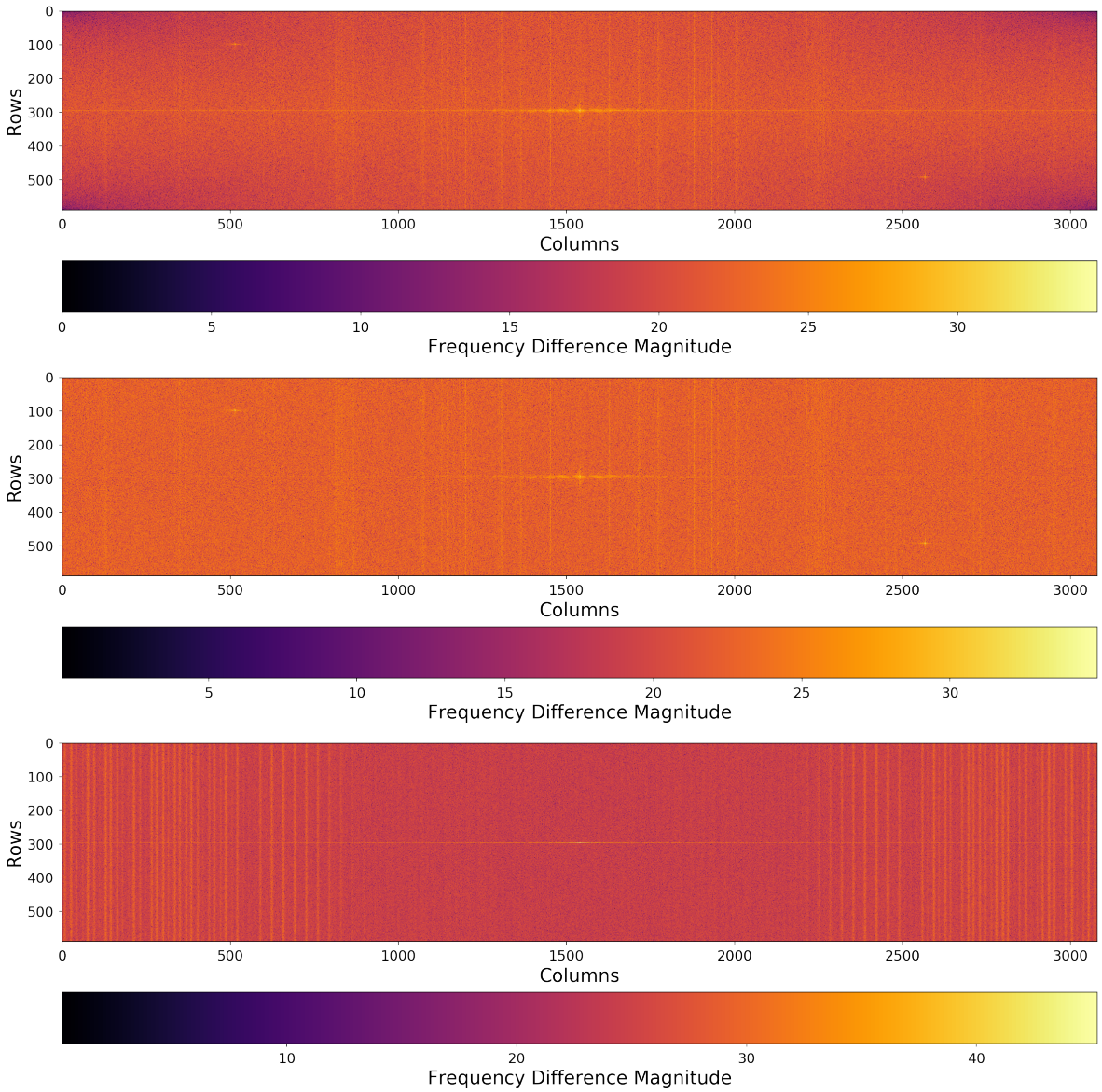

Figure 7.10: Frequency difference. Low frequency components have been shifted to the center of the images with higher frequencies in the outer edges. Top: Frequency difference for an image corrected with both the master bias and our fitting algorithm methods. Here a high-pass filter is applied, highlighting differences in the fine detail (high frequencies) between the two resulting corrected images. Center: Same as above but in this case we apply a low-pass filter to highlight differences from broad structures in the images. These would correspond to the exponential transients that cover large portions of the image. Bottom: Frequency difference for a corrected image (either method gives similar results) and a raw image using a low-pass filter. As expected the large frequency difference values across the image indicate the presence of substantial long-structure patterns in the raw image.

images (corrected either by master bias or by our correction method) and the raw image. In this case, low-frequency differences are much more pronounced in the horizontal direction, and the L score is ~ 1700—about 15 times higher than L from the two corrected images. Overall, the frequency analysis suggests that both the master bias correction and our image correction algorithm perform similarly, with only minor variations. These small differences may be attributed to the master bias being constructed from 15 different images taken at different time intervals, potentially contributing to slight variations in the master bias that are not suppressed by the averaging.

7.3 Spectral Extraction Validation

This section outlines the process for extracting spectral features from science targets, with a focus on validating the data reduction pipeline and demonstrating the robustness of the wavelength solution. As discussed in Section 7.1, our goal is to calculate the radial velocity of a Boötes II candidate member star to determine whether it belongs to the system or if it is a MW foreground star. To achieve this, we first demonstrate that the spectral pipeline, specifically the wavelength solution derivation, is reliable by using it to calculate radial velocities from standard stars' spectral absorption features, such as the H-α and H-β lines. This establishes that the pipeline can then be confidently applied to the Boötes II candidate member star.

7.3.1 Wavelength Solution and Uncertainties

The wavelength solution is the most important component of the spectral extraction procedure, as it provides a method to match the pixel position, e.g., from a spectral feature to its corresponding wavelength. The wavelength solution is derived using spectra from Mercury-Argon-Neon (HgArNe) and Copper-Helium-Argon (CuHeAr) lamps, where the wavelengths of the spectral features are precisely known. Figure 7.11 shows an image corresponding to

HgArNe calibrations; these data products are acquired as single-sample images with the high-voltage configuration, as the signal level can exceed 20,000 electrons. The curvature of the spectral lines is caused by factors such as spherical and chromatic aberrations from the lenses and grating. This curvature can be corrected by the wavelength solution, which maps each pixel position on the detector to a wavelength (for SIFS, there is 0.69 Å/pixel for the spectral modes used in the observations: 700B and 700M), compensating for the optical distortions that cause curvature.

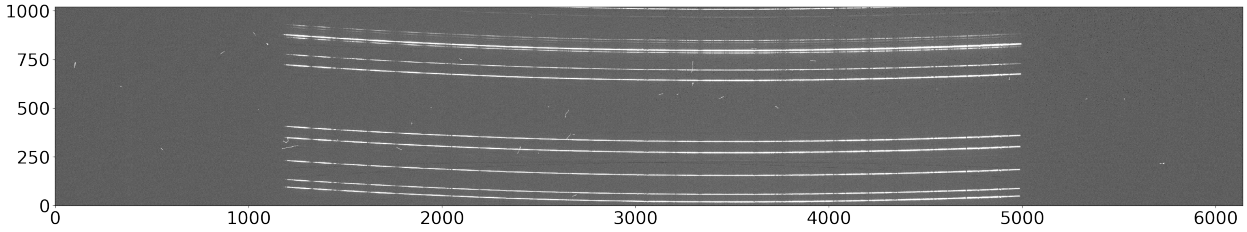

Figure 7.11: Spectral lines from the HgArNe lamp. Wavelength calibration images are taken after/before each science frame in order to account for any variation or shifts in fiber position. Note the curvature of the spectral line along the axis of the image, which needs to be corrected by the wavelength solution.

For radial velocity calculations, small variations in pixel position (and thus wavelength) translate to significant discrepancies in the calculated velocity. The radial velocity v_r is derived from the Doppler shift of the observed wavelength λ relative to a known rest wavelength λ_0:

$$v_r = \frac{\Delta\lambda}{\lambda_0} c \tag{7.4}$$

where $\Delta\lambda = \lambda_{obs} - \lambda_0$ is the observed wavelength shift, and c is the speed of light. For a given rest wavelength λ_0, small changes in $\Delta\lambda$ translate directly into changes in radial velocity, i.e., $\Delta\lambda$ is in the numerator of Eqn. 7.4. Thus, deriving a robust wavelength solution is critical for the calculation.

Now, let us explore the procedure for deriving the wavelength solution. After image correction, the pipeline identifies the fiber bundles in science frames with an average signal

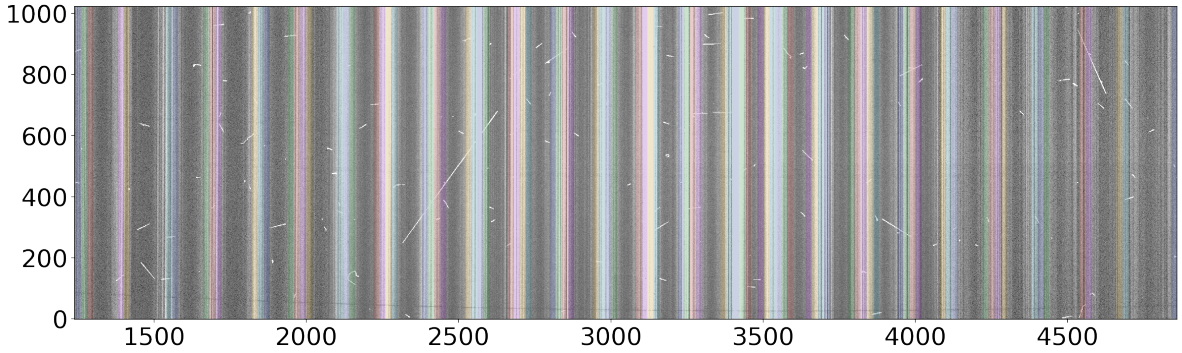

Figure 7.12: Identified spectral fiber bundles with signal level above $\sim$ 10 electrons (colored) corresponding to a science detector frame.

above $\sim$ 10 electrons per pixel and prompts the user to select the number of bundles to be extracted. For pipeline validation, we select up to 5 bundles, each spanning 20 pixels in the column direction and $\sim$ 1000 pixels in the row direction. Figure 7.12 shows a section ($\sim$4k $\times$ 1k) of a detector frame (composed of four individual amplifiers) where several bundles exceeding the required signal threshold have been identified.

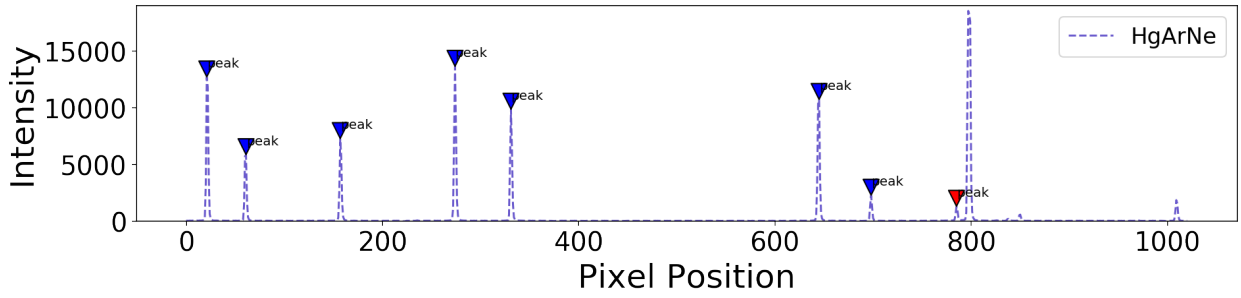

Figure 7.13: Spectral features from the HgNeAr calibration lamp image. The user selects the peaks (blue arrows) to be used for the wavelength calibration. The red arrow indicates the next peak to be selected or discarded. Each peak has a known wavelength referenced from NIST.

A wavelength solution is computed for each fiber bundle. We take the pixel coordinates from each bundle, apply them to the lamp calibration frame.(Figure 7.11), and extract the lamp spectra from that region. The user is asked to select the spectral features (peaks) to be used for the wavelength solution; these correspond to known Hg, Ar, Ne, etc., spectral lines, which wavelength has been referenced from NIST. Figure 7.13 shows the 1D spectra

from the HgArNe calibration lamp. The spectra are calculated from a collapsed 2D frame along the column direction, corresponding to a spectral bundle with ~ 20 columns . Most of the peaks are easily resolved due to the high S/N of lamp calibration products, which facilitates their identification. The wavelength calibration relies on the center positions of these lines; thus, it is important to derive a precise pixel location. To this end, we perform a Voigt profile fit to each spectral line to derive its center. The Voigt profile, the convolution of a Cauchy-Lorentz and Gaussian distributions, arises from serval physical phenomena (e.g., astrophysical spectroscopy,[2] plasma weaves, and acoustics) and it is given by [190]:

$$
\begin{aligned}
V(x) &= \int_{-\infty}^{\infty} L(x-\xi)G(\xi)\,d\xi = \frac{\omega_L/\omega_G}{\pi^{3/2}} \int_{-\infty}^{\infty} \frac{\exp -(\xi/\omega_G)^2}{(x-\xi)^2+\omega_L^2}\,d\xi \\
G(x) &= \frac{1}{\sqrt{\pi\omega_G}} \exp\left[-\left(\frac{x}{\omega_G}\right)^2\right] \\
L(x) &= \frac{1}{\pi\omega_L} \frac{\omega_L^2}{x^2+\omega_L^2}
\end{aligned}
\tag{7.5}
$$

Here $G(x)$ and $L(x)$ are the Gaussian and Lorentz profiles. ω_G and ω_L are the corresponding widths. Figure 7.14 illustrates the Voigt profile fit to one of the calibration lamp spectral lines. From the fit, we obtain the center of the distribution, which pixel position is matched to the wavelength of the line.

Generally, in an astronomical spectrograph, light is dispersed by a grating (in the case of SIFS, the VPH grating), with the resulting spectrum dispersed onto the detector. The dispersion relation can be modeled as [191]:

$$
p = p_0 + f_{cam} \tan\left[\arcsin\left(\frac{m\lambda}{\sigma} - \sin(\alpha)\right) - \beta_0\right] \tag{7.6}
$$

2. In astronomical spectroscopy, the Voigt profile arises from the convolution of two broadening mechanisms: one which produces Doppler broadening and the second one a would produce a Lorentz profile [190].

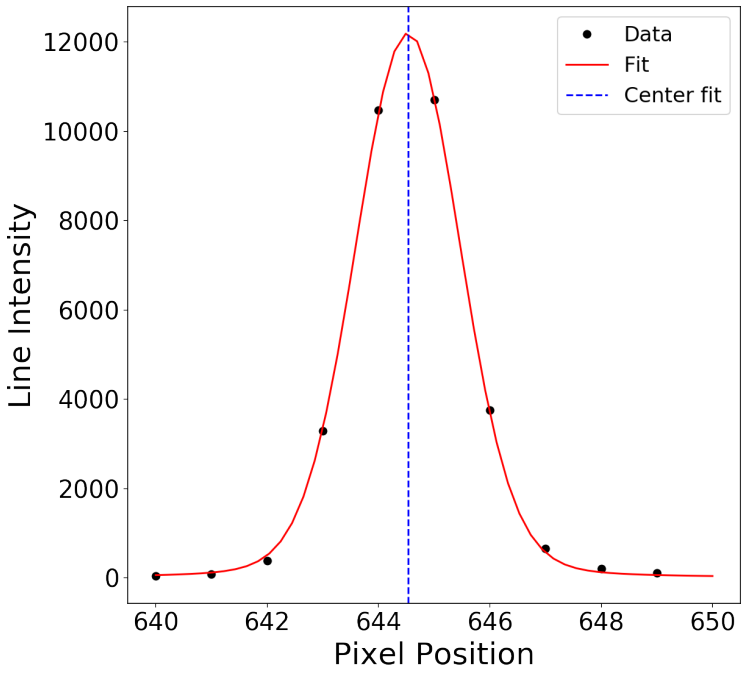

Figure 7.14: Voigt profile fit for a spectral line in the HgArNe calibration frame. The center position is used to derive the wavelength calibration.

where p is the pixel position on the detector, f_{cam}, is the effective focal length of the camera, m is the grating order, σ, is the grating spacing, α is the incident angle of light on the grating, and β_0 is the reference output angle for a specific wavelength. To capture the non-linear relationship between wavelength and the pixel position, we consider small deviations around the a central wavelength λ_0 and construct a polynomial in $(\lambda - \lambda_0)$ by Taylor expanding Eqn. 7.6.

$$p = p_0 + f_{cam}\frac{m}{\sigma\cos(\beta_0)}(\lambda - \lambda_0) + f_{cam}\frac{m^2\tan(\beta_0)}{2\sigma^2\cos^2(\beta_0)}(\lambda - \lambda_0)^2 + ... + O((\lambda - \lambda_0)^n) \quad (7.7)$$

In practice, we assume that our wavelength and pixel position data can be modeled by a polynomial of order n, where the first degree case models the primary linear dependence of p and λ while higher-order terms capture the non-linear dispersion effects. The wavelength solution is then given by the polynomial fit to the lamp spectra center pixel positions found by

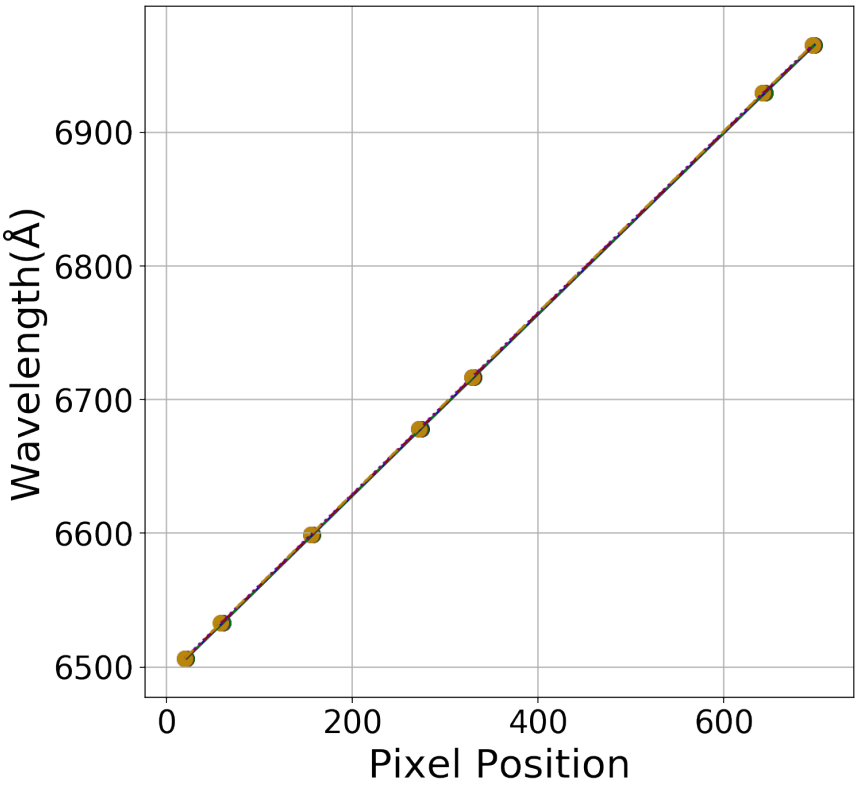

Figure 7.15: Wavelength solution. We assume a polynomial fit (e.g., Eqn. 7.7) for the lamp spectra center pixel positions and reference wavelengths. An independent fit is applied to each fiber bundle. In this case, five independent wavelength solutions are over-plotted.

the Voigt profile and the reference wavelengths. Figure 7.15 shows the wavelength solution for one of the radial velocity standard stars. Five fiber bundles were selected for this validation and a wavelength solution is derived for each bundle.

We now need to assess how well the model represents our data. Overfitting would cause the polynomial to pass through every point, thereby amplifying noise in the wavelength solution. We consider two independent uncertainties in our radial velocity measurements: systematic and statistical fitting uncertainties. The systematic uncertainties evaluate how well the polynomial models the mapping between the reference wavelengths and the pixel positions. We note that the pixel positions have associated uncertainties given by the Voigt profile fit error, i.e., the error to each pixel position data point from calibration frames is given by the shot noise. Systematic fluctuations in the data such as variations in the grating

response are inherently included in the residuals and the RMS value provides an aggregated measure of these systematic effects.

We evaluate the systematic uncertainty by examining the residuals and calculating the RMS:

$$RMS = \sqrt{\frac{1}{n-m-1}\sum_{i=1}^{n}(p_i - p(\lambda_i))^2} \tag{7.8}$$

where the factor $\frac{1}{n-m-1}$ accounts for the degrees of freedom, with n representing the number of residuals and m the degree of the polynomial fit. Consider Figure 7.16 (Top), which shows a systematic parabolic pattern in the residuals for a first-degree ($m = 1$) polynomial. The uncertainties reach up to ~ 0.3 Å, resulting in velocity uncertainties of ~ 14 km/s. This indicates that a first-degree polynomial does not adequately model the data, necessitating the inclusion of higher-order terms to improve the fidelity of the wavelength solution and capture non-linearities (e.g., Eqn. 7.7). In contrast, using a fourth-degree ($m = 4$) polynomial reduces the residuals by an order of magnitude (Figure 7.16, Bottom) compared to the first-degree fit. The quartic polynomial provides the best reduction in residuals, as fitting with a quintic polynomial does not yield further improvement.

Another component of systematic variations caused by changes in the system stability is the frame-to-frame uncertainty, which reflects any shifts in the fiber position as a result of temperature fluctuations throughout the night. To mitigate this effect, we acquire calibration lamp data products immediately before/after a science exposure. We calculate the uncertainty between consecutive pairs of calibration lamp frames by fitting Voight profiles to selected spectra features in both frames and comparing the fitted centroid to each spectral feature. Note that the error associated with the centroid is the shot noise for that particular pixel position. We observe good system stability, i.e., uncertainties associated with potential fiber shifts are < 0.1 km/s. Finally, the statistical uncertainty in the radial velocity calculation is associated with the Voight profile fit to the spectral feature of interest in the

science frame, e.g., the H-α line. Similarly, this uncertainty is given by the fitted error, which depends on the shot noise, to the centroid of the line.

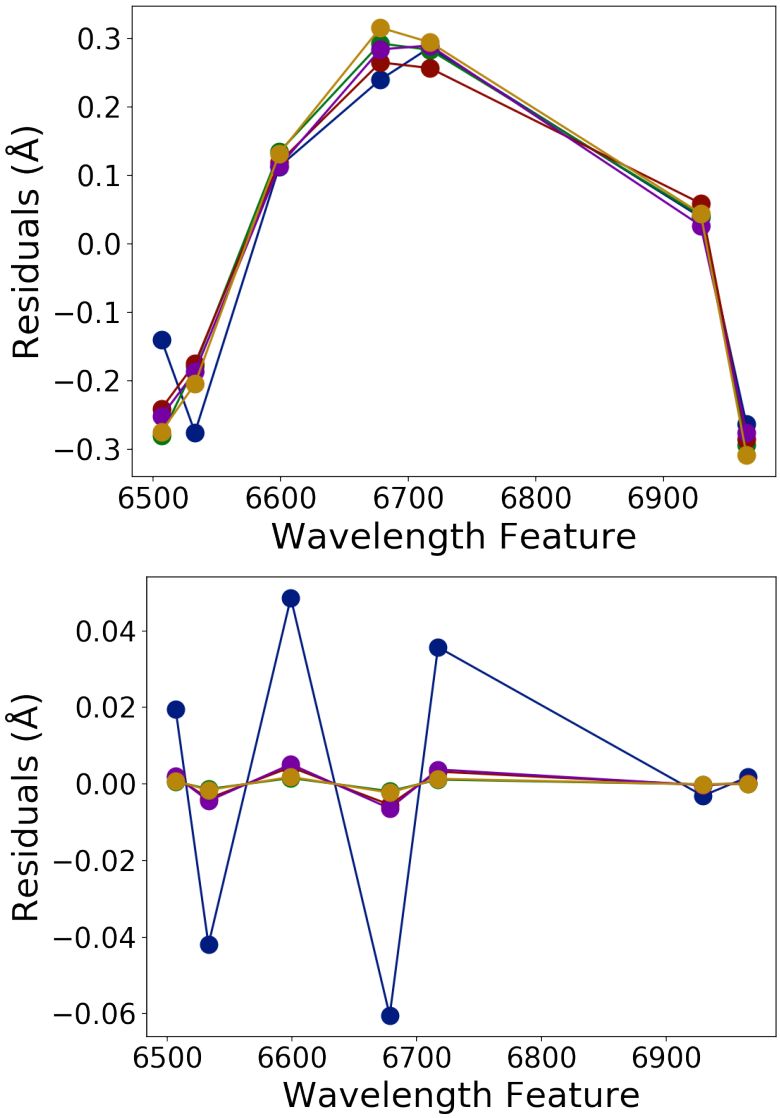

Figure 7.16: Fit residuals for the wavelength calibration. Top: The residuals show a systematic parabolic pattern for a $m = 1$ fit, indicating the inability of the model to capture non-linear behavior. Bottom: Instead, if we implement a $m = 4$ fit the residuals improved by an order of magnitude and show a consistent scatter around 0. Fitting higher order polynomials does not improve the residuals.

7.3.2 Radial Velocity Standards

As described in Section 7.1, we acquired spectra from radial velocity standard stars to validate the entire pipeline and ensure consistency in the wavelength calibration procedure. Specifically, we validate the wavelength calibration by deriving the radial velocities for BD-18 5550 and Gaia DR3 2771566830179387777 using the H-β and H-α lines. We then compare our results to the reference radial velocities for these objects from [30] and [31], respectively.

To improve the S/N, we combine the signals from five different fiber bundles, each having its own wavelength solution. The combined RMS (σ_{RMS}) is then calculated as the root mean square of all residuals across the K wavelength solutions:

$$\sigma_{RMS} = \sqrt{\frac{1}{k_{total}} \sum_{i=1}^{K} \sum_{j=1}^{k_i} RMS_{ij}^2}. \tag{7.9}$$

The frame-to-frame uncertainty is calculated independently of the wavelength solution for pairs of frames, i.e., $\sigma_{frame} = \sqrt{\frac{1}{N} \sum_{i=1}^{N} (\text{diff}_i - \mu)^2}$ where diff_i are the differences in pixel location for the pair of frames and μ is the mean of the differences. The total systematic error is then $\sigma_{sys} = \sigma_{RMS} + \sigma_{frame}$. The statistical uncertainty, σ_{stats}, is calculated for each of the fiber bundles with respect to the fitted spectral line centroid in pixel space. We assume the sources of error in our measurements are independent and thus we can write the combined uncertainty in the radial velocity measurement as:

$$\sigma_{COM} = \sqrt{\sigma_{sys}^2 + \sigma_{stats}^2}. \tag{7.10}$$

Table 7.1 lists the individual uncertainties for each of the radial velocity calculations performed here. The propagated uncertainty in the radial velocity (δv) (Eqn. 7.4) can then be expressed as:

$$\delta v = \frac{\delta\lambda}{\lambda_0} c \rightarrow \frac{\sigma_{COM}}{\lambda_0} c \tag{7.11}$$

where λ_0 is the rest wavelength (in air) of the spectral line, specifically the H-α (6562.801 Å) and H-β (4861.333 Å) lines in this case. Figure 7.17 shows the radial velocity calculated for BD-18 5550 using both the H-α and H-β lines (Top and Center), as well as the radial velocity for Gaia DR3 2771566830179387776 from the H-β line (Bottom). We note that both of the spectral lines are on different detectors and thus the spectral lines used to derive the wavelength solution vary in number per detector, resulting in different fit uncertainties. For BD-18 5550 we calculate -126.05 ± 2.02 km/s and -125.35 ± 1.54 km/s from the H-β and H-α lines, respectively. The referenced radial velocity for this star is -125.08 ± 0.25 km/s [30]. The first calculated radial velocity value shows the largest discrepancy compared to the reference velocity at -0.97 ± 2.04 km/s. However, this difference remains within less than 1σ. For Gaia DR3 2771566830179387776, we calculate -85.73 ± 2.19 km/s and the referenced value is -85.86 ± 0.42 km/s [31]. There is no statistical significance between both values with a difference of 0.13 ± 2.23 km/s. To account for the motion of the observer relative to the barycenter of the solar system, our radial velocity measurements have a barycentric correction.

Object Name	RMS (km/s)	Frame-to-Frame(km/s)	Stat. (km/s)	σ_{COM}
BD-18 H-β	1.03	0.66	1.11	2.02
BD-18 H-α	0.79	0.66	0.52	1.54
Gaia DR3 27... H-β	1.02	0.73	1.32	2.19
Boötes II star H$-\alpha$	0.56	0.60	1.59	1.97
Boötes II star Mg-triplet	1.53	0.60	1.15	2.42

Table 7.1: Uncertainties in radial velocity measurements for standard stars and the Boötes II candidate member star. The total systematic uncertainty is given by the RMS and frame-to-frame uncertainties. We assume the systematic and statistical uncertainties are independent. The combined uncertainty, σ_{COM}, is calculated with Eqn. 7.10

7.4 Boötes II Candidate Member Star

After validating the data processing and spectral extraction pipeline, we apply the same procedures to calculate the radial velocity of the Boötes II candidate member star. First, we extract the H$-\alpha$ spectra from the corresponding detector image (Figure 7.18, Top), calculate the radial velocity, and derive the combined uncertainty from RMS, frame-to-frame, and statistical errors. We find a value of $v_r = 177.88 \pm 1.79$ km/s, which is consistent with the value derived from one of the magnesium triplet lines, with a rest-frame in-air wavelength of 5183.604 Å ($v_r = 177.09 \pm 2.0$ km/s). We note that the H$-\alpha$ velocity calculation is considered the primary result as it utilizes more calibration lamp spectral lines to construct the wavelength solution. The bottom panel in Figure 7.18 shows the Voigt profile fit to one of the magnesium triplet lines.

The radial velocity calculated for the candidate member star is highly inconsistent with the Boötes II mean systematic radial velocity ($-139.4^{+1.4}_{-1.1}$ km/s). This discrepancy suggests that the star is unlikely to be a member of Boötes II and is more plausibly a foreground star within the MW. More specifically, we compare our calculated radial velocity to the MW halo star velocity distribution in Brown et al. (2010), Figure 2. This distribution assumes a Galactic rest-frame. Transforming our redial velocity to the Galactocentric frame, we obtain $\sim$ 182.30 km/s which is consistent with the kinematic characteristics of MW halo stars. The MW halo star population exhibits a velocity dispersion of 106 km/s, with $\gtrsim$ 5% of stars having $v_r \gtrsim 180$ km/s [192]. In addition to the radial velocity calculation, metallicity measurements of the candidate member star can provide further insight into whether the star's kinematic and compositional characteristics align with those of other metal-poor MW halo stars (e.g., [193, 194]).

7.4.1 Outlook: UFD Science

We demonstrated the capability for the SIFS-Skipper instrument to make precise radial velocity measurements, even for faint stars ($mag < 20.2$), showcasing its potential for studying the kinematics of stars in UFDs. Probing the kinematics at the periphery of UFDs is particularly important, as these regions contain stars whose motions are most sensitive to the underlying dark matter distribution and tidal interactions. However, observational challenges, such as low surface brightness, necessitate high-sensitivity detector technologies paired with advanced spectroscopic capabilities. Future surveys can address these challenges by utilizing high-multiplexed multi-object spectrographs (MOS), which can collect spectra for large samples of stars simultaneously. The effectiveness of such instruments will depend on key parameters, including the telescope's collecting area, the field of view, the number of fibers, and the spectrograph's resolution and sensitivity. For instance, the proposed Maunakea Spectroscopic Explorer (MSE) plans to use a 12.5-meter telescope equipped with more than 4000 fibers distributed over a 1.52 $\deg^2$ field of view. This configuration will enable the simultaneous acquisition of high-quality spectra from thousands of objects, vastly increasing the efficiency of kinematic surveys for faint stellar populations [195].

The synergy between future MOS instruments and LSST will be transformative for the study of UFDs and their DM subhalos. While LSST will identify numerous UFDs, MOS instruments will provide the necessary spectral follow-up to probe DM subhalos down to $10^5 M_\odot$ [196]. High-resolution MOS such as MSE, with spectral resolutions ranging from R$\sim 5,000$ to $30,000$, will enable velocity measurements with precision better than 1 km/s. This level of accuracy is critical for detecting subtle kinematic features, such as velocity gradients, dispersion profiles, and signatures of tidal disruption, which are essential for robust modeling of DM density profiles in UFDs and for directly testing alternative DM theories like WDM and FDM [197].

For instance, Guerra et al. (2023) provides a detailed analysis demonstrating the power of

stellar kinematics in constraining DM density profiles. The study shows that obtaining radial velocities for approximately 1,000 stars in a UFD can constrain the enclosed mass within the galaxy's effective radius to within 5%. Furthermore, combining radial velocity data with proper motion measurements for $\sim 10,000$ stars is necessary to distinguish between cuspy and cored DM profiles at the 1σ confidence level. This underscores the need for instruments with exceptional sensitivity to detect the faintest UFDs and to probe thousands of stellar members for membership confirmation and detailed matter distribution mapping. The ability of future MOS to provide comprehensive spectral follow-up for LSST-identified UFDs will be critical to improve DM predictions at small scales.

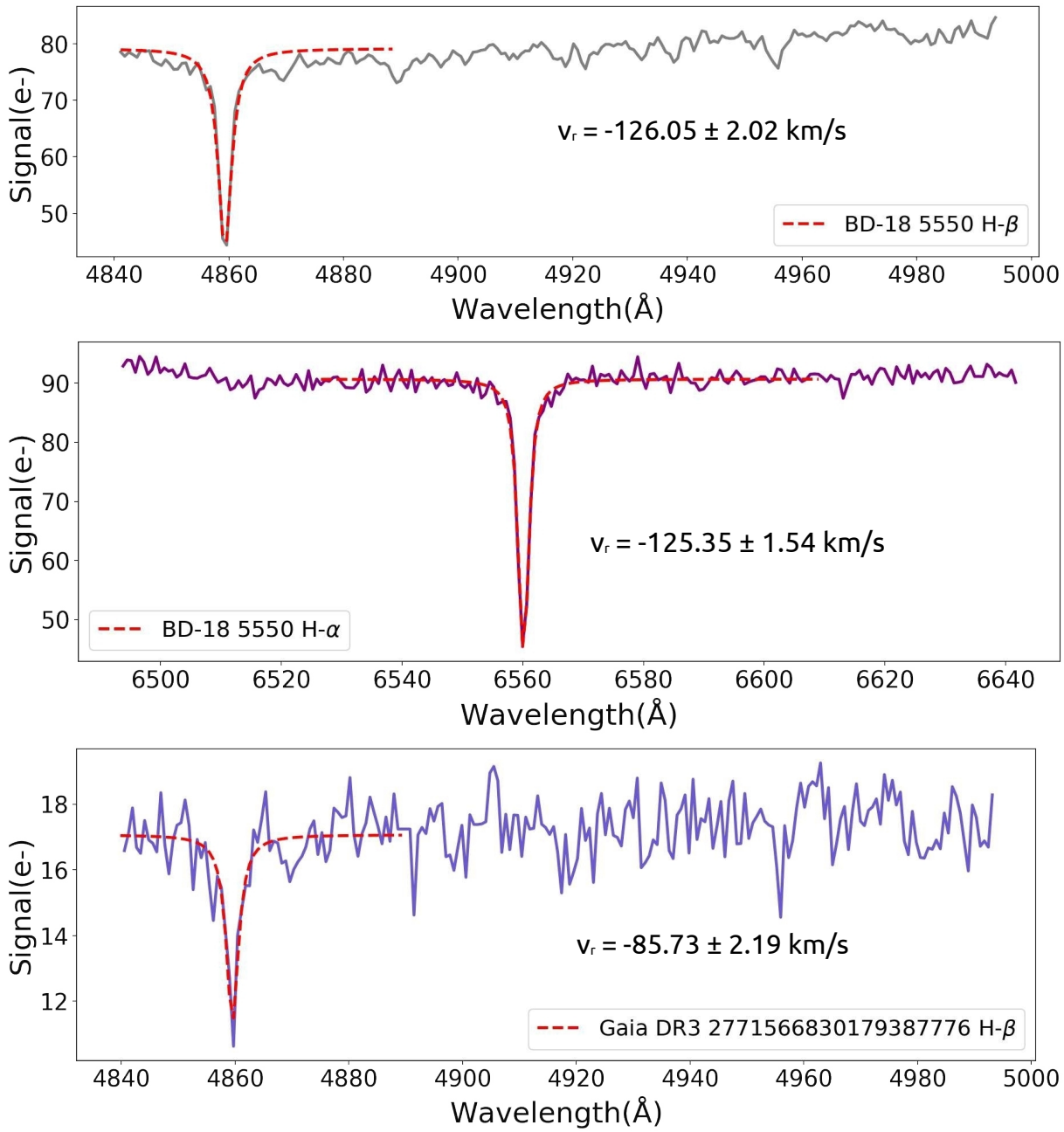

Figure 7.17: Radial velocity standard stars spectra for the H-β and H-α lines. Top: BD-18 5550 H$-\beta$ spectra. We calculate $v_r = -126.05 \pm 2.02$ km/s. The referenced radial velocity value is -125.08 ± 0.25 km/s. The two values agree well within the uncertainties, i.e., $\Delta v = -0.97 \pm 2.04$ km/s. Center: We calculate $v_r = -125.35 \pm 1.54$ km/s for the same star from the H$-\alpha$ line. Bottom: $v_r = -85.73 \pm 1.67$ km/s for the Gaia DR3 2771566830179387776 star. These values pose no significant statistical variations from the referenced radial velocities. We validate the entire pipeline and show that our spectral extraction method gives reasonable answers.

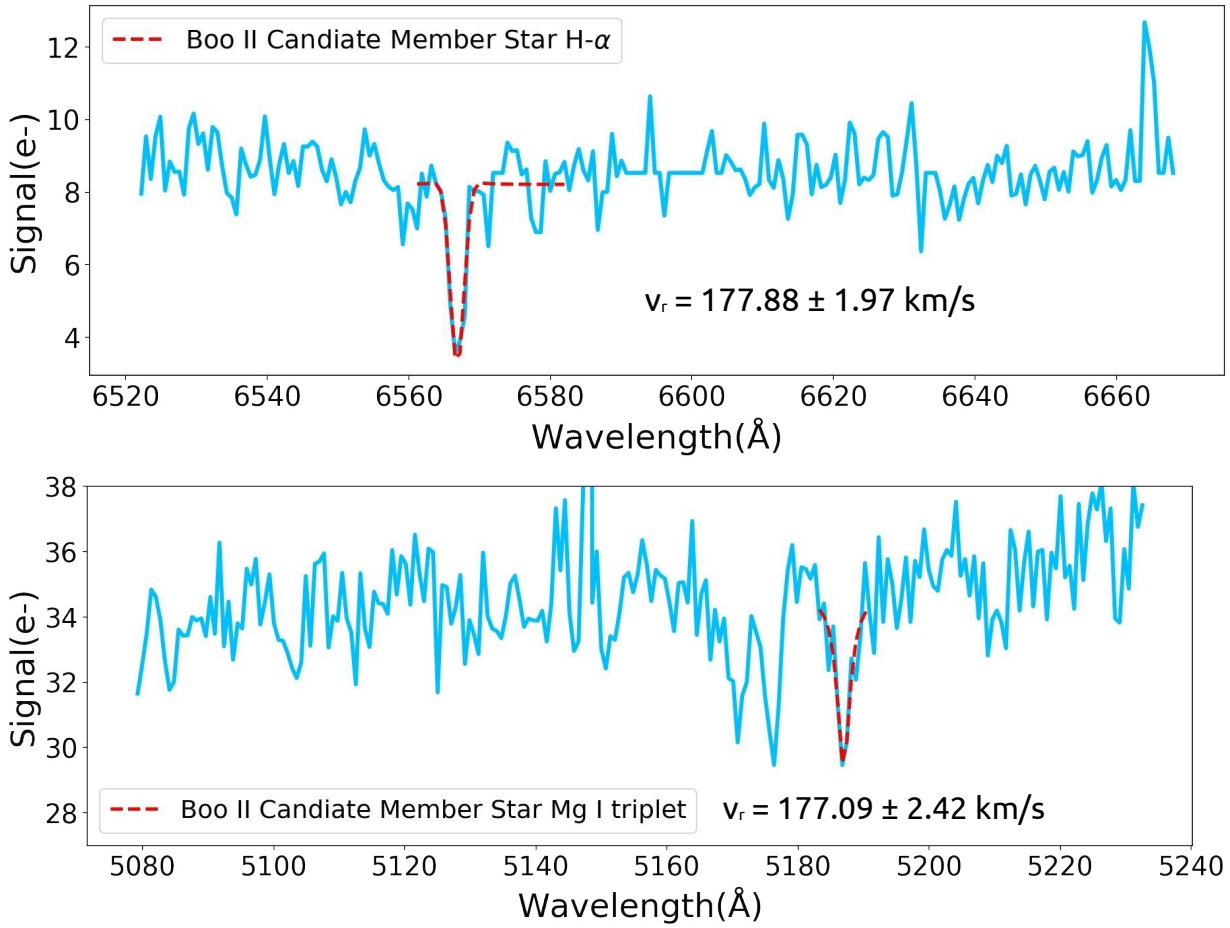

Figure 7.18: Top: Boötes II candidate member star H$-\alpha$ spectra. Bottom: Spectra of the magnesium triplet. We show the Voigt profile fit to one of the magnesium lines. Radial velocities are derived following the same procedures as in the pipeline validation with radial velocity standards.

CHAPTER 8

OUTLOOK: MAS CCDS

The multiple-amplifier sensing (MAS) CCD implements a chain of interspersed floating-gate amplifiers along the serial register (see Figure 8.1) [24]. Each amplifier provides a statistically independent measurement of the charge packet after the charge has been measured by M amplifiers, each measurement can be averaged to achieve a reduction in the readout noise:

$$\sigma_{eff} = \frac{\sigma_1}{\sqrt{(N \times M)}} \tag{8.1}$$

where σ_{eff} is the effective readout noise achieved with M amplifiers, σ_1 is the nominal readout noise and N is the number of non-destructive reads performed by each of the M amplifiers. The readout time for a MAS device with N_{row} (number of rows) and N_{col} (number columns) as described by Holland (2023) is,

$$t_{\text{readout}} = N_{row}(t_n + t_V), \tag{8.2}$$

where t_V is the time to clock the charge from the active area to the serial register, i.e., the time for vertical clocking (analog to t_V in Eqn. 5.1 for a conventional Skipper) and t_n is the time required to read n pixels in a row, which is equivalent to the total number of columns in the active area [199, 200, 201],

$$t_n = k_{\text{ext}} t_{\text{shift}} + M(k_{\text{inter}} t_{\text{shift}} + N t_{\text{pix}} + (n-1)(t_{\text{shift}}) + N t_{\text{pix}}). \tag{8.3}$$

Here k_{ext} is the number of extended serial pixels, k_{inter} are the pixels between amplifiers, t_{shift} is the time needed to shift the charge one serial pixel, and t_{pix} is the time to compute a pixel value (CDS). The first two terms in Eqn. 8.3 are shared with the readout of a conventional Skipper (the time to read the first pixel) and the third term only applies to the

MAS, i.e., the time to read all subsequent pixels through all M amplifiers. Functionally, the readout time scaling-factor between MAS and Skipper CCDs is dominated by the inverse of M.

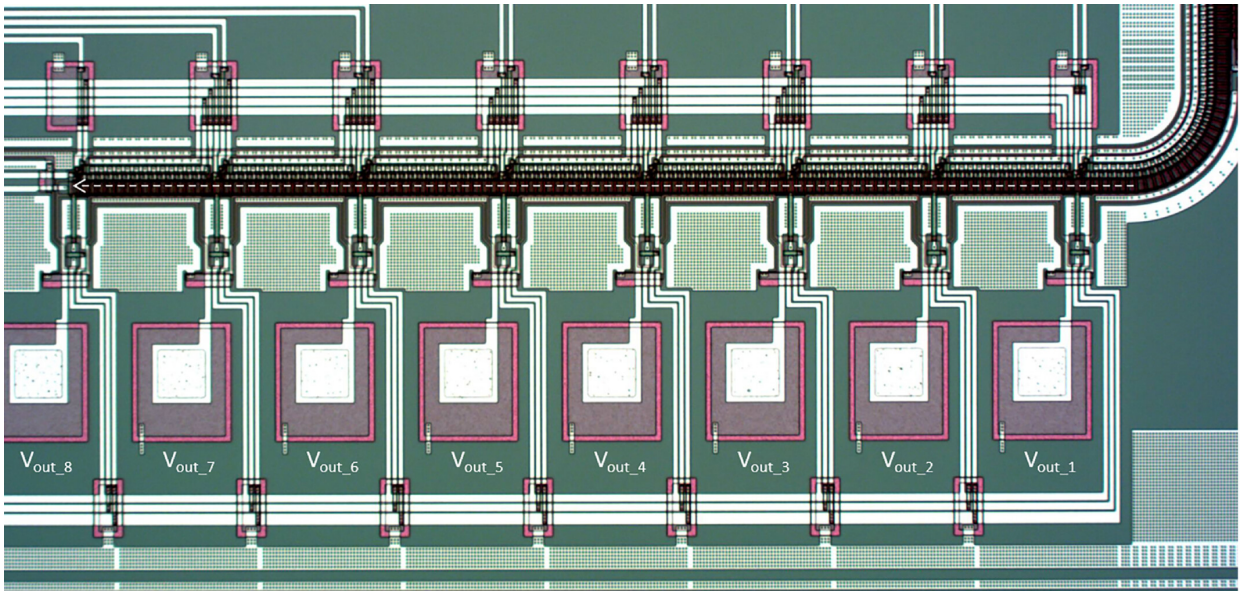

Figure 8.1: Picture of the output region of a MAS CCD with 8 independent floating-gate (skipper) amplifiers, labeled V_{out}_1 to V_{out}_8. For a scale reference, the aluminum bond pads (white squares in the image above the labels) are 100 μm $\times$ 100 μm. As the charge is move from the active region to the serial register, charge packets are measured independently by each of the MAS amplifiers, providing a factor of $\frac{1}{\sqrt{M}}$ (where M is the number of amplifiers) after averaging. Picture adapted from [24].

More practically, let us explore the performance gains possible with MAS CCDs over conventional Skipper CCDs. When comparing MAS and Skipper devices in the context of astronomical observations, it is crucial to consider the trade-off between S/N and total observation time, which includes both the exposure ($t_{\rm exp}$) and readout time ($t_{\rm readout}$). The maximum improvement in the S/N depends on the co-optimization of $t_{\rm exp}$ and $t_{\rm readout}$. For example, time spent reading out the detector could alternatively be used for collecting more photons, and optimizing $t_{\rm exp}$ is essential to ensure the observations remain in a readout noise-dominated regime, where S/N $\propto t_{\rm exp}$. The observation time, $t_{\rm obs}$, is defined as the sum of $t_{\rm readout}$ and $t_{\rm exp}$ and can be written as:

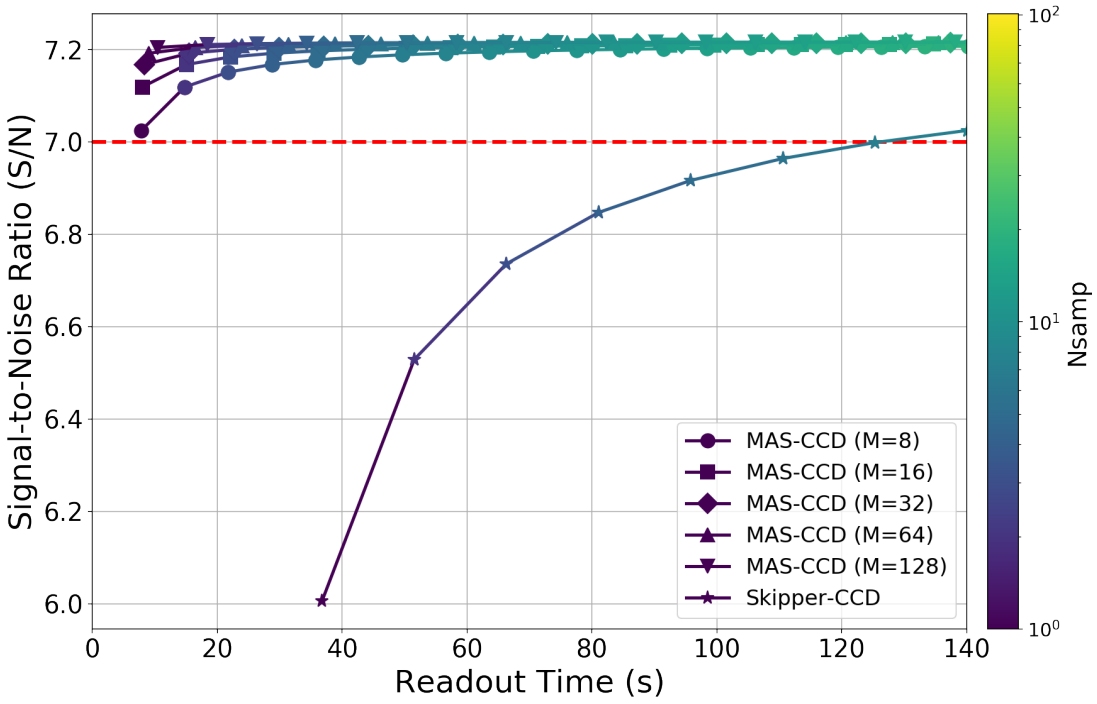

Figure 8.2: S/N as a function of readout time. The S/N is calculated for both a conventional Skipper CCD and MAS devices with increasing number of amplifiers. A typical SIFS observation is assumed with a fixed exposure time of 20 min. and a 20% ROI from 4k $\times$ 4k devices. We compare the time at which each configuration reaches a S/N of ~ 7. Mas devices reach S/N $\gtrsim 7$ in 8 seconds while the Skipper CCD requires 125 seconds which is equivalent to $N_{\rm samp} = 8$.

$$t_{\rm obs} = t_{\rm exp} + (1-f)t_{\rm readout} + fN_{\rm samp}t_{\rm readout}. \tag{8.4}$$

Here, f represents the fraction of the detector being read out with low read noise, i.e., the ROI. First, we compare the readout time of MAS devices and a conventional Skipper CCD to achieve a target S/N ~ 7, assuming a fixed exposure time of 20 minutes—a typical observation scheme for SIFS. Using the signal and background rates outlined in Table 4.1 and a 20% ROI on 4k $\times$ 4k devices (for both MAS and Skipper CCDs), we calculate the S/N with Eqn. 4.5. The corresponding readout times for Skipper and MAS devices are determined using Eqns. 5.1 and 8.2, respectively.

For MAS devices, the readout time depends on Eqn. 8.3, where the operational timing

parameters are $t_{\rm pix} = 10.3$ μs, $t_{\rm shift} = 1$ μs, $t_{\rm kext} = 27$ μs, and $t_{\rm int} = 16$ μs, based on typical lab testing conditions. Figure 8.2 illustrates the S/N as a function of readout time for the conventional Skipper CCD and MAS devices with increasing numbers of amplifiers. The results show that a 8-channle ($M = 8$) MAS CCD achieves S/N $\gtrsim 7$ with a read noise of $\lesssim 1$ e$^-$ rms/pix in 8 seconds, from a single-read across all 8 amplifiers. We assume a single-sample readout noise of 3.5 e$^-$rms/pix for MAS and Skipper devices. In contrast, the Skipper CCD requires 125 seconds to reach the same S/N, due to the need to perform 8 non-destructive reads per pixel, increasing its readout time by a factor of ~ 15 compared to the MAS device. Notably, $M = 8$ amplifiers is sufficient, as further increasing the number of amplifiers does not significantly improve the S/N for this specific observational setup.

Next, for the same SIFS observation configuration, described above, we explore the reduction in total observation time ($t_{\rm exp} + t_{\rm readout}$) to reach a fixed S/N = 7. $t_{\rm exp}$ can be calculated from Eqn. 4.5 as $at_{\rm exp}^2 + bt_{\rm exp} + c$ where $a = (R_{\rm src} + N)^2$, $b = -(S/N)^2 \times (R_{\rm src} + R_{\rm bkg} + R_{\rm dark}) \times N$ and $c = -(S/N)^2 \times t_{\rm readout}^2 \times N$. Figure 8.3 (Top) shows the relative time per exposure as a function of readout noise. The dashed-gray line is the baseline observation performance achieved by a conventional Skipper CCD operating with a read noise of 3.5e$^-$rms/pix and $N_{\rm samp} = 1$. The Skipper CCD (black curve) configuration can achieve a $\sim 20\%$ improvement in sensitivity at a readout noise of ~ 1.1e$^-$rms/pix, requiring $N_{\rm samp} = 10$. Both MAS configurations result in a $\sim 30\%$ improvement in the observation time, achieving sub-electron noise ($\lesssim 0.6$) with a single-read.

In Figure 8.3 (Bottom), we investigate the potential observation time improvements for the Inamori-Magellan Areal Camera and Spectrograph (IMACS) on the 6.5-m Magellan-Baade telescope [202]. IMACS is a high resolution ($\lambda/\Delta\lambda \sim 11,000$), wide-field, multi-purpose imaging spectrograph. The instrument has been extensively used in UFDs studies, e.g., the spectroscopic analysis of Eridanus IV and Centaurus I [203]. Here we assume a similar observational configuration as in the SIFS case, i.e., 4k $\times$ 4k devices, a 20% ROI for

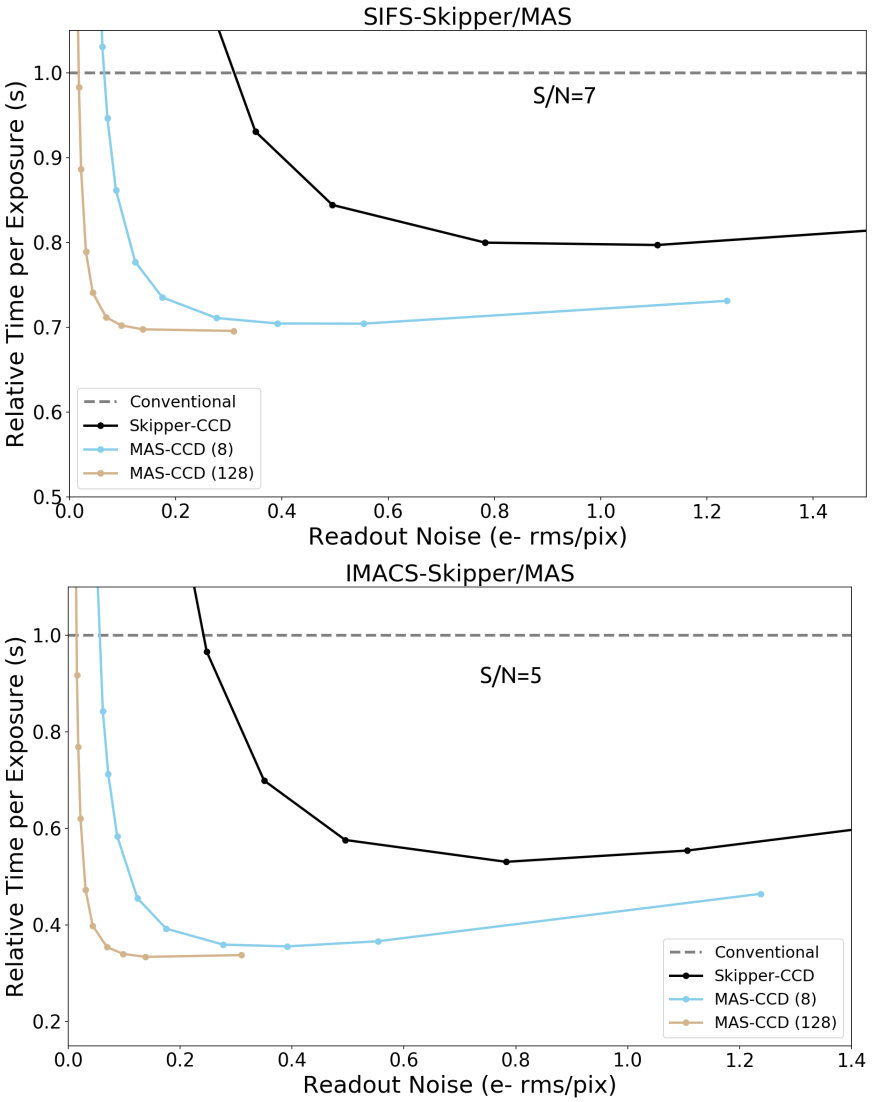

Figure 8.3: Relative observation time per exposure as a function of detector readout noise. The observation time is normalized to the baseline detector configuration (dashed-gray line in both plots), which is assumed to be a Skipper CCD operating with $N_{\rm samp} = 1$ and $\sigma_1 = 3.5{\rm e}^-{\rm rms/pix}$. Top: Skipper and MAS ($M = 8$ and $M = 128$) comparison. MAS devices outperform the conventional Skipper CCD by a $\gtrsim 10\%$ increase in observation efficiency when targeting S/N=7 at SIFS. Bottom: Skipper and MAS comparison for IMACS. While the conventional Skipper cuts the nominal observation time (baseline detector configuration) by $\sim 47\%$ at a readout noise of $\sim 0.78{\rm e}^-{\rm rms/pix}$, the MAS CCD can improve the instrument's efficiency by as much as $\sim 65\%$, resulting in lower observation times to reach S/N=5.

both Skipper and MAS CCDs, and the baseline configuration (dashed-gray line) consisting of a Skipper CCD with $N_{\rm samp} = 1$. We observe that MAS devices can improve the observation

efficiency by $\sim 65\%$. When comparing MAS ($M = 8$ and $M = 128$) to the conventional Skipper, the MAS advantage remains at $\sim 19\%$ efficiency improvement. These measurements assume a fixed S/N = 5 (typical S/N reached in IMACS observations for faint targets, e.g., UFD member stars [27]).

With IMACS, we also explore the potential sensitivity enhancements to faint UFD member stars enabled by MAS CCDs. We base our analysis on the observational parameters outlined by Li et al. (2017), who observed member stars of the MW satellite Eridanus II using IMACS in the z-band. Their observations achieved a S/N ~ 5 for stars of magnitude 22 with an exposure time of 40 minutes. For this study, we assume a fixed exposure time of 40 minutes and calculate the S/N for stars with magnitudes ranging from 21.5 to 25 in the z-band. This analysis aims to assess the faintest sources to which an IMACS instrument equipped with MAS CCDs could remain sensitive. Figure 8.4 presents contour maps showing S/N performance as a function of star magnitude and the readout time for a conventional Skipper CCD and MAS CCDs with $M = 8$ and $M = 128$. For stars with magnitudes $m \gtrsim 23$, MAS devices achieve S/N ~ 5 within readout times $\lesssim 0.5$ minutes, whereas the Skipper system achieves only S/N $\lesssim 4$ for the same conditions. For even fainter stars ($23.5 \leq m \leq 24$), the Skipper CCD loses sensitivity entirely, while MAS devices maintain S/N $\gtrsim 2$.

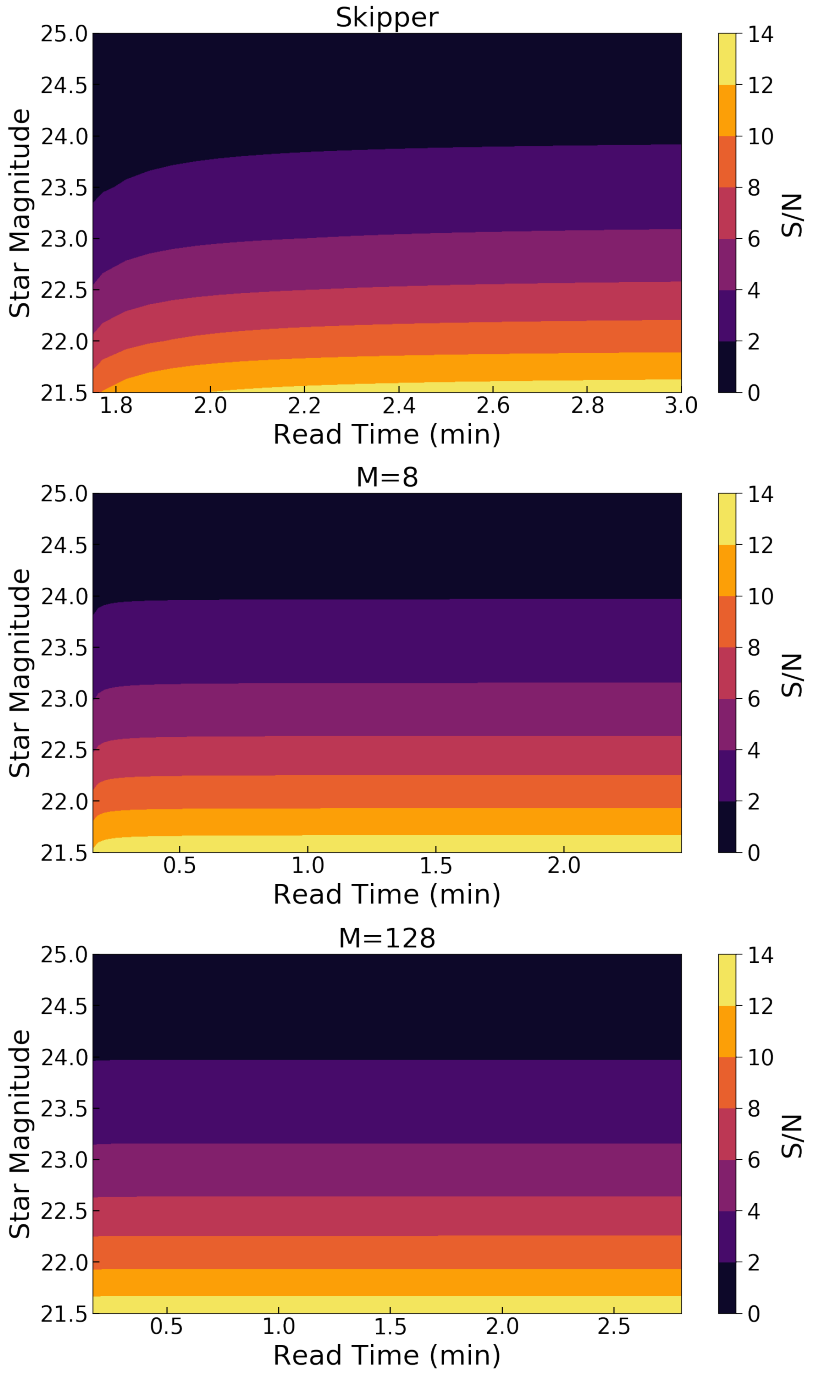

Figure 8.4: Comparison of the sensitivity to faint UFD stars between Skipper and MAS devices, assuming IMACS observations in the z-band. The three contour map plots show S/N bands for stars with magnitudes between 21.5 and 25; the exposure time is kept fixed at 40 minutes. For stars with magnitudes ~ 23, MAS devices ($M = 8$ and $M = 128$) achieve S/N ~ 5 while the Skipper system only reaches S/N $\lesssim 4$. For fainter stars, magnitudes $\gtrsim 23.5$, MAS devices retain sensitivity (S/N $\gtrsim 2$), while the Skipper CCD losses sensitivity entirely.

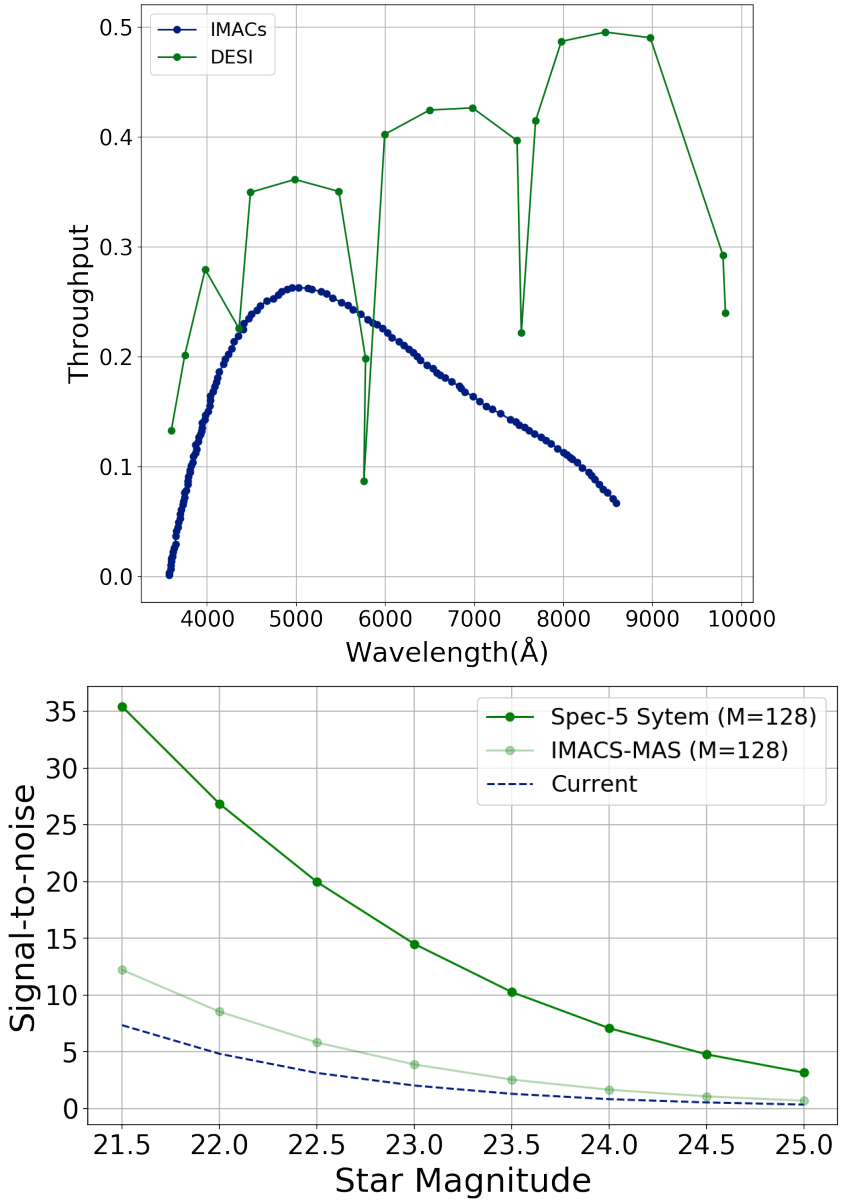

Figure 8.5: DESI and IMACS spectrographs throughput and sensitivity increase to faint stars from a Stage 5 survey. Top: Throughput for the IMACS and DESI spectrographs, extracted from [25] and [26], respectively. Measurements are not corrected for atmospheric effects. Bottom: Projections for the Spec-S5 system consisting of a thick ($\sim 250\mu$m) $M = 128$ MAS CCD (bright green curve). We take the baseline IMACS signal rate (0.00416e$^-$rms/pix) for observations of faint UFD stars at $\sim$ 8400 Å [27] and rescale it assuming a 6-m telescope mirror and the DESI throughput at $\sim$ 8400 Å. This measurement is compared to both the current IMACS configuration and an IMACS-MAS ($M = 128$, thin, blue-optimized MAS CCD). Notable, We note a factor of $\gtrsim 5$ improvement in the Spec-S5 system compared to the current IMACS system for all star magnitudes. Furthermore, for stars with magnitudes $\gtrsim 23$, the Spec-S5 system achieves a factor of $\gtrsim 4$ improvement in S/N compared to the IMACS-MAS system, highlighting the synergy between a stage-of-the-art spectrograph and ultra-low noise detectors.

Demonstrating that the Skipper CCD provides a meaningful advantage in S/N and efficiency for signal-starved observations was an important first step to motivate further technology development. The MAS CCD represents a critical improvement to the conventional Skipper architecture, enabling a substantial reduction in the readout time required to achieve sub-electron readout noise. In this work, we show that observations with conventional Skipper CCDs necessarily required the implementation of ROIs in order to significantly reduce readout times. However, MAS CCD can provide sub-electron noise in large detector areas without the readout time penalty. Overcoming the Skipper CCD's readout time limitation for astronomy not only enhances overall observation efficiency but, more importantly, facilitates the adoption of the technology, unlocking the potential to explore new parameter spaces and conduct novel cosmological measurements.

A Stage 5 spectroscopic survey (see Section 2.5.5) could benefit significantly from implementing ultra-low noise detectors such as the MAS CCD, providing increased sensitivity to the faintest objects. As an example, we consider the sensitivity to faint UFD stars from a Spec-S5 system consisting of a thick ($\sim 250\mu$m), 128-channel ($M = 128$) MAS CCD. Note that the thick CCD will result in higher efficiency at red wavelengths (see Section 3.2.3) compared to the current IMACS blue-optimized CCD [25]. The Spec-S5 system performance is compared to the current IMACS configuration with a conventional CCD operating with a noise of ~ 5 e^-rms/pix [25] and to an IMACS-MAS system (assuming the current spectrograph's throughput and a thin, blue-optimized $M = 128$ MAS CCD). We first assume the baseline signal rate for IMACS (0.00416 $e^-pix^{-1}s^{-1}$ [27]) and make projections of the expected signal, assuming realistic specifications for a Spec-S5 system, i.e., a 6-m. class telescope, and the DESI spectrographs' total throughput. Functionally, we scale the IMACS signal rate by the telescope size, and the spectrograph throughput (from Figure 8.5, Top) at the observation's target wavelength of ~ 8400 Å (for the Calcium Triplet spectral lines [27]).

Figure 8.5 (Bottom) illustrates the theoretical sensitivity improvements for stars with

magnitudes ranging from 21.5 to 25. Additionally, this study highlights the synergy between efficient spectrographs and ultra-low noise detectors in a Spec-S5 system. Notably, for stars with magnitudes $m \gtrsim 23$, the Spec-S5 system (bright-green curve) achieves a factor of $\gtrsim 4$ improvement in S/N compared to the IMACS-MAS system (light-green curve). Furthermore, the Spec-S5 system, incorporating the DESI spectrograph's performance, provides a factor of $\gtrsim 5$ increase in S/N across all star magnitudes when compared to the current IMACS configuration (blue curve). This study also demonstrates the importance of pairing state-of-the-art spectrographs with highly efficient, ultra-low readout noise detectors.

CHAPTER 9

SUMMARY

This work marks the first successful development, optimization, and demonstration of ultra-low noise, photon-counting Skipper CCD technology, pioneering its application in cosmology. Future large-scale cosmological surveys, especially those aimed at probing cosmic expansion and elucidating the nature of DM by observing both the most distant objects and the dynamics and distribution of the faintest objects within the MW, require novel detector technology with a broad sensitivity range. Skipper CCDs present a promising candidate for enabling such scientific exploration in next-generation cosmological surveys. Here, we have demonstrated the first astronomical spectroscopic measurements conducted with Skipper CCDs operating in the sub-electron and photon-counting regimes. These results confirm the technological maturity of Skipper CCDs for cosmology, enabling sensitivity improvements and scientifically relevant measurements.

We conducted early characterization measurements of a small-format R&D Skipper CCD processed for astronomy. Our results demonstrated that the detector could achieve a QE $> 75\%$ across the wavelength range of 450 nm to 900 nm. Additionally, we explored the full dynamic range of the detector, spanning from the photon-counting regime to signal levels around 30,000 electrons. This comprehensive analysis allowed us to determine key detector characteristics, such as the gain, and to confirm the detector's linear response across its entire dynamic range. Collaboration with NOIRLab was crucial in enabling a focused effort to leverage these initial findings and develop a full prototype Skipper CCD focal plane, consisting of four 6k $\times$ 4k Skipper CCDs.

Exploring the S/N improvements in the readout noise-dominated regime—critical for observing faint astronomical objects—was a primary objective of the on-sky demonstration with Skipper CCDs. Given the low signal throughput of SIFS (see Table 4.1), we predicted a $\sim$30% improvement in instrument efficiency achievable with Skipper CCDs operating at

a minimum readout noise of 0.7 e^-rms/pix. We packaged eight astronomy-grade Skipper CCDs, leveraging tools and methods developed for DECam and DESI detector packaging. The readout system was designed to include four synchronized LTAs, each configured to read out 16 amplifiers across the entire focal plane array. Additionally, we repurposed a spare SIFS Dewar to house the Skipper array and designed a custom preamplifier to provide pre-amplification and route all 16 outputs.

In Bloch et al. (2024), the SENSEI collaboration reported a new unprecedentedly low single-electron event rate ($1.39 \pm 0.11 \times 10^{-5}$ e^-/pix/day) for a Skipper CCD. While low background rates are achievable with Skipper CCDs, these depend on the operation parameters and environment of the detector. For astronomical applications, the Skipper CCD needs to operate in a completely different regime. Extensive efforts were made to understand the observation requirements and optimize the Skipper CCD for such requirements. For instance, we optimized operational voltages to reach full-well capacities $> 40,000$ e^- and reduced CIC to ~ 3 e^-/pixel/frame in this operational regime. We concluded that the trade off between CIC and full-well capacity needed careful treatment, leading us to operate the detectors dynamically where observations were conducted with a full-well capacity of $\sim 10,000$ with a CIC rate of ~ 1 e^-/pixel/frame while calibration products were acquired with the highest full-well configuration. Table 5.1 summarizes characterization results for the astronomy-optimized Skipper CCDs, confirming that they meet or exceed the performance of other back-illuminated, thick, astronomy CCDs (e.g., QE, DC, CTI, charge diffusion, and non-linearity). Additionally, we implemented novel methods that rely on charge quantization to measure detector non-linearities in the photon-counting, low signal regime.

The observation strategy with Skipper CCDs at SIFS focused on reducing readout times. The S/N improvements from minimizing readout noise are significant only in low-background conditions, as longer readout times increase the impact of shot noise from light leaks and contamination from cosmic rays (see Eqn. 4.5). The readout time was optimized as a

function of the integration time for the CDS and the readout noise. This approach allowed us to reduce the pixel read time from ~ 200 μs/pixel to $\sim 40\mu$s/pixel for a single amplifier while maintaining a readout noise upper limit $\lesssim 4.3$ e$^-$rms/pix. Moreover, the use of ROIs enabled us to maintain total readout times under 20 minutes for all observations.

We demonstrated sub-electron (< 0.7 e$^-$rms/pix) and photon-counting (~ 0.2 e$^-$rms/pix) readout noise for the first time in astronomical spectroscopy with silicon CCDs. Targeting high-redshift astronomical objects (i.e., faint quasars and emission-line galaxies), resulted in S/N improvements from ~ 1.2—with a nominal detector noise of ~ 17 e$^-$rms/pix (see Section 6.3.1)—to ~ 10.5 by achieving sub-electron readout noise levels.

The acquisition of spectra from the Boötes II candidate member star leveraged sub-electron noise ($\lesssim 1$ e$^-$rms/pix) from the Skipper CCD to perform relevant measurements for near-field cosmology. UFDs such as Boötes II can be pristine environments to study DM microphysics since their luminous mass is subdominant compared to the DM halo. For instance, studying the periphery regions of these objects allows us to probe the mechanisms of DM halo-UFD evolution, e.g., mergers and tidal disruption. The study of the Boötes II candidate member star sought to contribute to mapping the UFD's matter distribution. This study motivated the development of a robust pipeline to process SIFS-Skipper data, derive a wavelength solution, and extract the spectra. The validation of the pipeline with radial velocity standard stars confirms the reliability of our image correction algorithm and wavelength solution, i.e., calculated radial velocity values are consistent with the reference values. These same procedures were applied to the Boötes II candidate member star to derive its radial velocity from the H$-\alpha$ ($v_r = 177.88 \pm 1.97$ km/s) and one of the Mg-triplet lines ($v_r = 177.09 \pm 2.42$ km/s). Radial velocity values were consistent with the candidate member star being a MW foreground star.

Results from the on-sky demonstration affirm the technological maturity and scientific viability of Skipper CCDs for astronomical spectroscopy, highlighting their potential for

integration into future Stage 5 spectroscopic surveys. However, addressing the primary limitation of Skipper CCDs—long readout times—is crucial for broader adoption. To this end, continued development efforts are underway, such as the MAS CCD, to explore alternative CCD readout architectures that can significantly reduce readout time while preserving readout noise tuneability. Technology demonstrations such as the focus of this work, contribute to the Skipper technology maturation, building an astronomy/cosmology-dedicated platform of ultra-low noise, photon-counting detectors for the next generation of large cosmological surveys. In this context, testing new detector technology such as the Skipper CCD for the first time on the sky marks a seminal achievement in astronomical instrumentation.

APPENDIX A

A PREDICTIVE FRAMEWORK FOR STELLAR STREAM GAPS

Here, I outline the work I undertook to build a framework, based on the foundational work by Erkal et al. [28, 205, 29], to statistically predict the number of gaps expected from different DM models. Although this work was not published, it reached a stage where the findings are compelling and could be of interest for a future publication. It is also worth noting that the stellar stream research described here, while more theoretical in nature compared to the primary focus of this thesis, is intrinsically connected to the development of improved astronomical instrumentation. Precise models that predict observables (e.g., the statistical distribution of DM at small scales) coupled to astronomical detectors that are sensitive to the faintest signals are critical in developing the next generation of cosmic surveys.

A.0.1 Gap Evolution: A Qualitative Description

Let us assume an unperturbed stellar stream in a circular orbit within an arbitrary spherical potential. Now, consider a subhalo passing near or through the stream, gravitationally perturbing the stream's particles (i.e., cold stars) and pulling them toward the point of closest approach. These perturbations are strongest near the subhalo, and different parts of the stream experience varying velocity "kicks" depending on their proximity to the subhalo. These kicks can be decomposed into three components: perpendicular to the stream's orbital plane, along the radial direction from the host, and along the stream's orbit. Among these, kicks along the orbit have the most significant impact because they impart the largest change in kinetic energy to the stars. This change alters the radial extent of their orbits and, consequently, their orbital periods.

In astrophysical potentials, the orbital period increases with radius. Particles kicked in

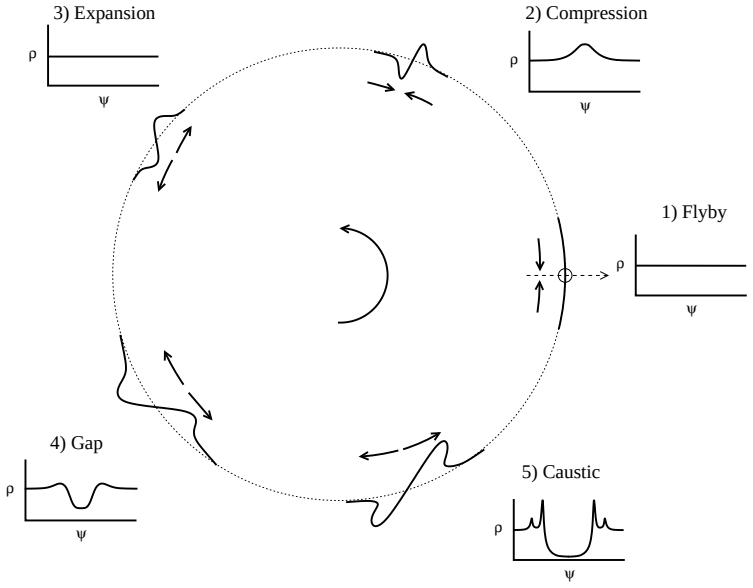

Figure A.1: Diagram of a stream gap creation and evolution. The dotted line denotes the direction of the stream motion, the solid lines show the point of closest approach. At each stage of gape evolution, the graphs illustrate density (ρ) as a function of the angle on the sky (ψ) from the perspective of an observer at the center of the galaxy. (1) Unperturbed stream with uniform density. (2) Compression of stream's particles to point of closest approach. (3) Changes in orbital period: particles kicked along their orbital direction gain kinetic energy, leading to a longer orbital period, which causes them to fall behind the impact point. particles kicked in the opposite direction lose kinetic energy, resulting in a shorter orbital period, causing them to move ahead of the impact point. As a result, compression is reversed. (4) Over time, the particles that were previously pulled together near the point of closest approach begin to spread out, forming an under-dense gap. (5) Expansion continues and eventually particles overtake each other, forming caustics. Figure extracted from [28].

the direction of their orbit gain kinetic energy, resulting in a longer orbital period, which causes them to lag behind the subhalo's impact point. Conversely, particles receiving a kick opposite to their orbital direction lose kinetic energy, shortening their orbital period, and allowing them to race ahead of the subhalo's impact point.

Velocity kicks induced by the subhalo lead to the formation of under-dense regions around the point of closest approach, signaling the creation of a gap in the stellar stream. Initially, during the *compression* phase, there is a density enhancement as particles are pulled toward the point of contact with the perturber. This density enhancement can be quantified as

$f = \rho/\rho_0 > 1$, where ρ represents the stream density at the perturbation point and ρ_0 is the density of the unperturbed stream. After approximately one orbital period, the *expansion* phase follows ($f \leq 1$) as particles begin to move apart, resulting in a discernible gap in the stream. Since the magnitude of the velocity kick varies depending on the position along the stream, particles at different locations will gradually start to overtake one another. Over time, this differential motion leads to the *caustic* phase, where particles pile up on either side of the gap, creating density enhancements at the edges of the under-dense region. Figure A.1 qualitatively illustrates the process of a stream gap evolution.

A.0.2 Stream-Halo Kinematics

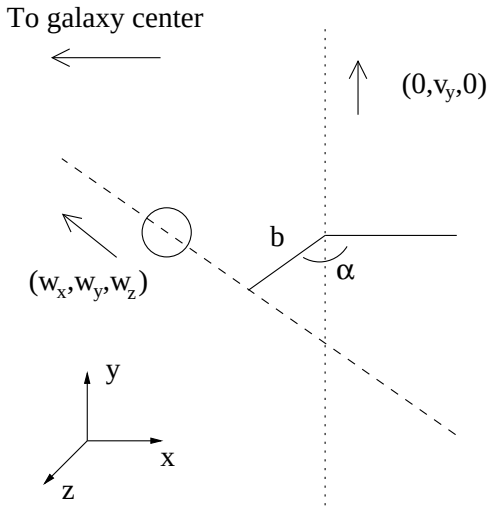

Figure A.2: The geometry for the stream-halo interaction. The dotted line represents the stream and the dashed line is the halo's path. The interaction occurs in the $x - y$ where b is the point of closet approach. Figure taken from [28].

Now, we consider the arbitrary geometry for a stream-subhalo interaction illustrated in Figure A.2. For a detailed definition of this geometrical interpretation readers can reference Erkal and Belokurov (2015). Here, we use this framework to derive important stream and subhalo parameters. The stream is oriented in the y-direction with x in the radial direction, and z perpendicular to the orbital plane. We then assume the stream moves with velocity

$(0, v_y = \sqrt{r_0 \partial_r \Phi(r)}, 0)$ where $\Phi(r)$ is an arbitrary spherical gravitational potential, and r_0 is the radius of the stream's circular orbit. The subhalo moves in an arbitrary direction with velocity (w_x, w_y, w_z) and makes a closest approach at $(b_x, 0, b_z)$, i.e., the closest approach occurs in the $x-z$ plane with the origin on the stream. We can then parametrize the impact parameter and the subhalo velocity as $b = \sqrt{b_x^2 + b_z^2}$ and $w_\perp = \sqrt{w_x^2 + w_z^2}$ since the impact parameter and the point of closest approach are orthogonal. The magnitude of the relative velocity can be defined as $w = \sqrt{w_\parallel^2 + w_\perp^2}$, where $v_\parallel = v_y - w_y$.

The above expression defines the velocity components for a single interaction between a subhalo and a stellar stream. However, to predict gaps resulting from a population of subhalos—i.e., to create realizations where a distribution of subhalos interacts with the stream across a given phase space—we must consider the distribution of subhalo velocities. First, the relative velocity distribution $w_\parallel$ is written as

$$P(w_\parallel | b_{max}) = \frac{1}{\sqrt{2\pi\sigma^2}} \exp\left(-\frac{(w_\parallel + v_s)^2}{s\sigma^2}\right) \tag{A.1}$$

here b_{max} is the the radius of the volume from which subhalos enter[1] and perturb the stream and v_s is the velocity of the stream (i.e., $v_y \equiv v_s$). We then write the distribution for $w_\perp$ as

$$P(w_\perp | b_{max}) = \sqrt{\frac{2}{\pi}} \frac{w_\perp^2}{\sigma^3} \exp\left(-\frac{w_\perp^2}{2\sigma^2}\right). \tag{A.2}$$

We defined the impact parameter as the distance of the closest approach between the path of the subhalo and the track of the stream. Thus, the distribution of impact parameters is a three-dimensional calculation of the distances between two lines: the subhalo's path and the stream's orbit. In this context, the distribution of these minimum distances is uniform, i.e., $P(b|b_{max})$ is uniformly distributed between 0 and b_{max}.

1. One can consider an imaginary cylindrical volume around a 1D stream moving with v_s. Subhalos with radial velocity v_r will enter within b_{max} of the stream. See Figure 1 in [29].

A.0.3 Stream Gap Framework Definition

The statistical framework to predict the number of gaps in stellar streams relies on the geometry, kinematic distributions, and assumptions described above. However, a key difference from previous work (e.g., [29]) is the inclusion of a generalized impulse approximation treatment. A fully general treatment of gravitational encounters is extremely complex, and numerical simulations are often the preferred method to handle such problems. Nonetheless, in the impulsive limit, where the encounter velocity is much larger than the internal velocity of the stream, the impulse approximation applies, allowing for an analytical approach. In this scenario, the displacement of stars during the stream-halo interaction can be ignored, and the velocity change in the system can be computed as [206]:

$$\Delta \boldsymbol{v} = -\int \nabla \Phi \; dt \tag{A.3}$$

where Φ is the gravitational potential from the perturber.

Now let us consider the dynamics of a close encounter in a mutually unbound system: a point in the stellar stream and the pertuber with relative velocity $w_{||}$ and impact parameter b. For sufficiently fast encounters, the mutual deflection of the stream and the perturber from their original orbits due to gravitational interaction is small. Thus, the orbits of both the stream and the subhalo can be approximated as straight lines during the encounter. Note that we had defined the origin on the stream; the position of a point in the stream is then given by $\boldsymbol{r}$, the center of mass of the perturber is given by $\boldsymbol{R}$ and the relative positions between $\boldsymbol{r}$ and $\boldsymbol{R}$ is given by $\boldsymbol{R_P} = \boldsymbol{R} - \boldsymbol{r}$. The gravitational potential due to the perturber at the impact point on the stream $\boldsymbol{r} = (x, y, z)$ is a function of the distance to the particle from its center, $R_P = |\boldsymbol{R} - \boldsymbol{r}| = \sqrt{x^2 + (b-y)^2 + (z-wt)^2}$. The acceleration of the stream particle due to the perturbing force is given by:

$$\boldsymbol{a} = -\nabla\Phi = \frac{1}{R_P}\frac{d\Phi}{dR_P}[-x\hat{x} + (b-y)\hat{y} - (z-wt)\hat{z}]. \tag{A.4}$$

Now, focusing on the net velocity change of the stream particle in the $x-y$ plane, we can express the instantaneous velocity change as:

$$\Delta v = \int_{-\infty}^{\infty} dt\boldsymbol{a} \propto I(s)[-x\hat{x} + (b-y)\hat{y}], \tag{A.5}$$

where $s^2 = x^2 + (b-y)^2$ and the impulse function $I(s)$ is defined as:

$$I(s) = \int_0^{\infty} d\zeta \frac{1}{R_P}\frac{d\Phi}{dR_P} \tag{A.6}$$

with $\zeta = wt - z$ [206].

The formulation defined above provides a formalism for calculating the velocity kicks imparted to the stars in the stream by a nearby perturber and depends on the impact parameter and the relative motion between the stream and the perturber. It is important to note the advantage of implementing a fully generalized impulse approximation, which is evident when considering Eqn. A.6, the impulse function. $I(s)$ encodes information about the detailed density profile of the pertuber. A fundamental characteristic of a DM halo is its density profile, which describes how the mass is distributed within the halo as a function of distance from its center [207, 208]. Despite the complex and dynamic processes involved in halo formation—such as mergers, accretion, and gravitational interactions—N-body simulations (e.g., [209]) have consistently shown that the mass distributions of DM halos tend to settle into equilibrium profiles that follow a common functional form across different halo masses. The density profile of the halo directly impacts the gravitational potential, which influences the orbit of stars, galaxies, or other material within the halo. Consequently, it affects the dynamics of any external object, such as a stellar stream, that interacts with the halo.

In Erkal et al. (2016), the stream gap modeling assumes a Plummer sphere halo density profile. The Plummer profile is defined as [210]:

$$\rho(r) = \frac{3M_P}{4\pi r_P^3}\left(1 + \frac{r^2}{r_P^2}\right)^{-5/2} \tag{A.7}$$

where M is the mass of the perturber, r_P is the Plummer scale radius (in this case the pertuber or halo scale radius) and r is the radial distance from the center of the halo. The Plummer gravitational potential can be derived from Poisson's equation (i.e., $\nabla^2\Phi(r) = 4\pi G\rho(r)$) and takes the form:

$$\Phi_{Plummer}(r) = -\frac{GM_P}{r^2 + r_P^2}. \tag{A.8}$$

In this work, we implement the Navarro-Frenk- White (NFW) density profile. The NFW profile is one of the most widely used density profiles to provide a spherically averaged description of the mass distribution within a DM halo. The NFW profile is a two-parameter model (or one-parameter at fixed mass) that describes how density declines with distance from the halo center. Mathematically, the density profile is given by [211]:

$$\rho(r) = \frac{\rho_s}{\frac{r}{r_P}\left(1 + \frac{r}{r_P}\right)^2} \tag{A.9}$$

where ρ_s is a characteristic density and r_P is the scale radius, corresponding to the radius at which the logarithmic slope of the density profile, $\frac{d\ln\rho(r)}{d\ln r}$, equals -2. This means that inside r_P, the density falls off more steeply, while outside it, the profile gradually transitions to a more extended outer halo. Similarly, one can solve the Poisson's equation to obtain the potential associated with the NFW profile.

$$\Phi_{NFW}(r) = -\frac{GM_P}{r}\ln\left(1 + \frac{r}{r_P}\right) \tag{A.10}$$

In the case of the NFW profile, another important parameter used to define the shape of a halo is the concentration parameter (c), which quantifies how centrally concentrated the DM is within the halo. The concentration parameter is defined as the ratio of the virial radius (r_{vir})—which effectively marks the outer boundary of the halo, where the mean density is $\sim$ 200 times the critical density of the universe—to the scale radius (r_P), i.e., $c = \frac{r_{vir}}{r_P}$. The concentration parameter is not constant but instead exhibits a dependence on both the halo mass and redshift. Typically, more massive halos have lower concentrations, while halos at higher redshifts are also less concentrated due to their earlier formation times. This dependence is described by the concentration-mass relation [212, 213, 214, 215]. M_P in Eqn. A.10 is then the mass of a NFW halo, which is defined in terms of the concentration parameter c as $M_P = \frac{M_{vir}}{f(c)}$ where M_{vir} is the viral mass or M_{200} (the mass contained within a sphere where the average density is $\sim$200 times the critical density of the universe (ρ_{crit}) at a given redshift) and $f(c) = \ln(1+c) - \frac{c}{(1+c)}$ [206].

Now that we have defined the halo and stream properties and assumptions, we need a model to quantify the effect of each encounter to assess the detectability of a gap and thus compute the distribution of gaps from realizations of subhalos interacting with a stellar stream. A complete and detailed derivation of stream gap properties, i.e., the depth and size can be found in Erkal and Belokurov (2015). Here, I present the key expressions used in this analysis. First the gap depth is defined as $f \equiv \rho/\rho_0$ or

$$\frac{\rho}{\rho_0} = \left(1 + \frac{4-\gamma^2}{\gamma^2}\frac{\omega_\perp^2}{\omega^3}\frac{2GM_P}{b^2+r_P^2}t\right)^{-1} \tag{A.11}$$

where γ is related to the subhalo gravitation potential (e.g., $\Phi_{NFW}(r)$):

$$\gamma^2 = 3 + r\partial_r^2\Phi(r). \tag{A.12}$$

The expected number of gaps is computed for gaps deeper than a certain density threshold

$f < f_{cut}$, which defines the detectability limit for gaps. It is important to note that this framework assumes that the gap depths and widths are considered from the perspective of an observer at the center of the Galaxy. A heliocentric perspective might indicate that a gap is smaller or larger depending on the distance to the stream. The gap might also appear foreshortened if its orientation is not perpendicular to the line of sight [29].

The structure and size of a stream gap are controlled by the velocity kicks imparted to the stream during stream-halo interaction. The width of the gap, $\Psi_{\rm gap}$, can be computed using the following expression:

$$\Delta\Psi_{\rm gap} = 1 + \frac{2tGM_P w_\perp^2}{rw^3}\left(I(s) + \frac{\psi_0 \frac{dI(s)}{ds} r^2 w_\perp^2}{r_c w^2}\right) \tag{A.13}$$

where $r_c = \sqrt{b^2 + \frac{r^2\psi_0^2 w_\perp^2}{w^2}}$ and $\psi_0 = \frac{y}{b}$ describes the initial distance between a point along the stream and the point of closest approach, where y is the perpendicular distance along the stream, and b is the impact parameter. These expressions describe the average time evolution of the gap's density and size, enabling the rapid computation of the gap properties following an interaction. By integrating over key parameters such as the impact parameter, subhalo velocity, and the time of impact, one can predict the distribution of gaps formed in a stellar stream due to flybys.

A.0.4 Framework Implementation Results

Here, I describe the procedures for creating stream-halo realizations and computing the resulting gap properties. The gap distribution prediction is tested using the properties of the Palomar 5 (Pal 5) stellar stream [216], which can be found in Table A.1 along with five other cold MW streams that are good candidates for testing this framework. To begin the simulation, we first assign the subhalo kinematic properties, specifically the parallel and perpendicular velocities, using the appropriate velocity distributions (Eqns. A.1 and A.3)

for subhalos within b_{max}. We then draw the impact parameter from a uniform distribution $P(b|b_{max}) = \frac{1}{b_{max}}$.

Stream	$\Delta\phi_{\rm helio}$	$\Delta\phi_{\rm GC}$	$l_{\rm stream}$	$r_{\rm helio}$	$r_{\rm GC}$	Age
Pal 5	**22°**	**29°**	**9 kpc**	**23 kpc**	**19 kpc**	**3.4 Gyr**
GD-1	63°	32°	9 kpc	7.3-9.1 kpc	13.5-15 kpc	3-5 Gyr
Tri/Psc	35°	17°	12 kpc	35 kpc	40 kpc	9.3 Gyr
ATLAS	20°	16°	6 kpc	20 kpc	22-23 kpc	2.1 Gyr
Phoenix	15°	11°	4 kpc	17.5 kpc	18-19 kpc	1.8 Gyr
Styx	53°	64°	50 kpc	45 kpc	45-50 kpc	18.5 Gyr

Table A.1: Properties of cold MW stellar streams. For this work, we test the gap predicting framework with the Pal 5 Stream. The gap predicting framework is fully generalized and thus the rest of the streams are good candidates for future implementations. The stream properties are extracted from [29].

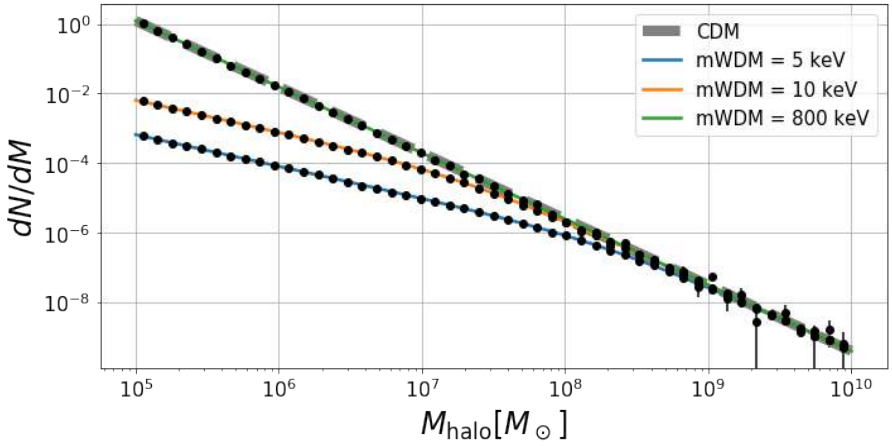

Figure A.3: Subhalo mass functions for CDM and different WDM models. In the halo-stream interaction realizations, the subhalo mass is drawn from the appropriate SHMF (i.e., CDM or WDM) via the inverse CDF method. Mass values are overplotted on the corresponding DM model (solid lines).

The mass for each subhalo is drawn from the subhalo mass function (SHMF), which describes the number distribution of subhalos as a function of their mass. For CDM, the SHMF is taken to be a power-law fit to the subhalo population from the Aquarius simulation [217, 218]:

$$\left(\frac{dN}{dM}\right)_{CDM} = 3.26 \times 10^{-5} \left(\frac{M}{2.57 \times 10^7 M_\odot}\right)^{-1.9} M_\odot^{-1}. \tag{A.14}$$

To sample the mass, we construct a comulative distribution function, which is numerically approximated as $CDF_i = \sum_{j=0}^{i} \Delta M \frac{dN}{dM_j}$ where $\Delta M = \frac{M_{min} - M_{max}}{\text{steps}}$. In this case we create subhalos with mass ranges between $10^5 M_\odot - 10^9 M_\odot$. Additionally, it is possible to parameterize the SHMF to account for WDM models, which suppress the formation of small subhalos. We implement Schutz (2020) robust parametrization of the WDM SHMF, derived from analyses of stellar streams (i.e., Pal5 and GD-1) and counts of classical MW satellites:

$$\left(\frac{dN}{dM}\right)_{WDM} = \left(1 + \gamma \frac{M_{hm}}{M}\right)^{-\beta} \left(\frac{dN}{d \ln M}\right)_{CDM} \tag{A.15}$$

where the best fit in the Aquarius simulations is $\gamma = 2.7$ and $\beta = 0.99$. Figure A.3 illustrates subhalo mass values drawn using the inverse CDF method from both CDM and WDM models.

To test this generalized formalism for predicting the number of gaps caused by DM perturbers on stellar streams (in this case Pal 5), we first replicate the results from Erkal et al. (2016) by constructing realizations of a population of ΛCDM subhalos and calculating the gap depth and width, assuming a Plummer sphere density profile. In this analysis, we consider subhalos with masses in the range $10^5 - 10^9 M_\odot$, as subhalos below this mass range produce velocity kicks that are too small to cause significant density depletion in the stellar stream. Specifically, we impose a cutoff for subhalos that produce velocity kicks $\Delta v < 0.1$, as motivated by the simulations in [29], which show that such low velocity produces insufficient gap depths. Figure A.4 illustrates the expected distribution of gap sizes for various density thresholds.

We successfully replicated the expected gap size distribution, demonstrating that a fully generalized treatment of gap property calculations via the impulse approximation is capable

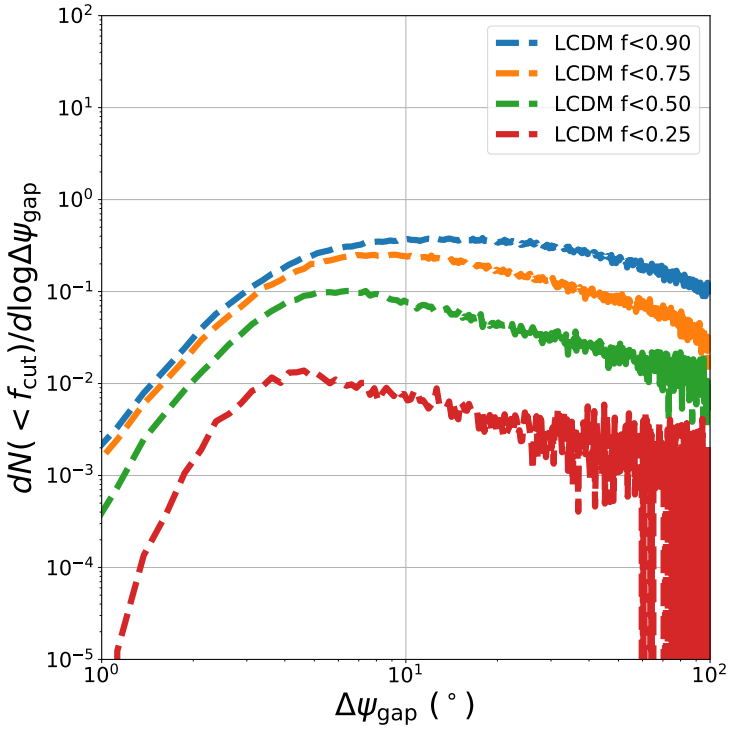

Figure A.4: Gap size distribution for different density thresholds f. The gap sizes and dpeths are calculated from a population of ΛCDM subhalos with a mass range $10^5 - 10^9 M_\odot$. Calculations assumed a Plummer potential.

of recovering the expected gap sizes for subhalos with a Plummer potential. This result offers valuable insights. For instance, we observe that the peak of the distribution strongly depends on the density threshold. For a feasible gap depth of $f < 0.75$, the characteristic gap scale is on the order of several degrees, suggesting that such gaps have significant discovery potential as observable features in stellar streams. For shallower gaps (e.g., $f < 0.25$), there is a wide range of gap sizes, with larger gap sizes dominating the distribution. In contrast, deeper gaps tend to be dominated by smaller gap sizes which are created by low-mass subhalos. This somewhat counterintuitive result arises due to the requirement of a minimum velocity kick for gap formation. For deep gaps, the necessary velocity kick can be satisfied by both low- and high-mass subhalos. However, since low-mass subhalos are more numerous, they dominate the formation of small gaps. On the other hand, for shallow gaps, many low-mass subhalos produce negligible velocity kicks, which leads to a larger contribution from more

massive subhalos.

Following the first validation of the stream gap prediction framework, we now construct realizations of a ΛCDM population of NFW subhalos. As previously indicated, the NFW potential (i.e., Eqn. A.10) depends on the pertuber mass M_P, which in turn depends on the concentration parameter (c). Therefore, when simulating NFW subhalos, in addition to drawing the subhalo mass, we assign a concentration to each subhalo, given by:

$$c_{NFW}(M_{vir}) = \exp\left[c_6\left(\frac{M_{fs}}{M_{vir}}\right)^{1/3}\right]\sum_{i=0}^{5} c_i\left[\ln\left(\frac{M_{vir}}{h^{-1}M_{\odot}}\right)\right] \tag{A.16}$$

where c_i are dimensionless constants (their values come from the best fits to simulation data [219]) and the free-stream mass scale is given by $M_{fs} = \frac{4\pi}{3}(\frac{2\pi}{k_{fs}})^3\rho_{\text{mean}} \sim 7.3 \times 10^{-6}M_{\odot}$ for a typical CDM model particle with mass 100 GeV. [2] The concentration mass-relation described by Eqn. A.16 is based on a high resolution multi-zoom simulation with 30 orders of magnitude in mass and resolving power of internal structure down to Earth-mass halos [219].

Figure A.5 (Left) shows the comparison between the gap size distributions for Plummer and NFW subhalos, revealing important qualitative differences that hint at quantifiable observable distinctions in gap characteristics. For example, in the case of the Plummer model, the gap size distribution peaks at $\sim 7^{\circ}$, whereas for the NFW model, it peaks at $\sim 15^{\circ}$. On average, NFW subhalos might produce slightly larger gaps, potentially enhancing gap detectability. Another important difference is the suppression of small gap sizes (corresponding to low-mass subhalos) and the suppression of large gaps ($> 15^{\circ}$), which are produced by larger-mass subhalos. This behavior can be attributed to the concentration effects inherent in the NFW profile. The concentration-mass relation decreases with halo mass (e.g, Figure

2. M_{fs} depends on the free-streaming scale (k_{fs}) which indicates the process of kinetic decoupling of CDM particles which is characterized by damping of small-scale perturbations. The free-streaming scale at matter-radiation equality, k_{fs}, can be expressed as $k_{fs} \sim \frac{1.7\times10^6}{\text{Mpc}}\frac{(m/100\text{GeV})^{1/2}(T_{kd}/30MeV)^{1/2}}{1+\ln(T_{kd}/30MeV)/19.2}$ [220]. Here m is the DM particle mass and T_{kd} is the DM kinematic decoupling temperature (see Section 2.3.2).

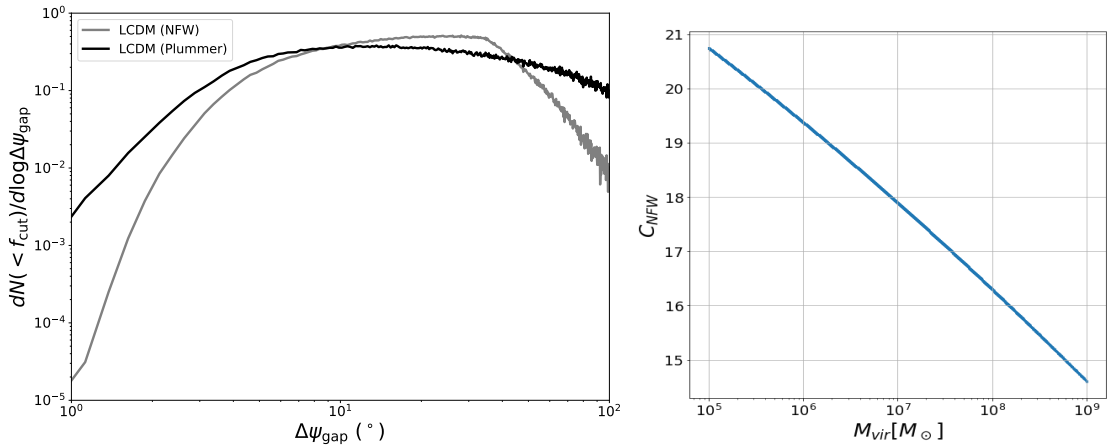

Figure A.5: Left: the gap size distribution produced by a realization of ΛCDM subhalos with NFW and Plummer gravitational potentials. The distributions correspond to $f < 0.90$. Calculations are made with $10^5 - 10^9 M_\odot$ subhalos. In the NFW case, there is a suppression of small gaps, i.e., gaps produced by low-mass pertubers and a sharp cut-off of gaps $> 15°$ produced by the most massive subahlos. These differences in gap sizes between NFW and Plummer subhalos are due to concentration effects in the NFW case. Right: the concetration-mass relation for NFW halos as described by Eqn. A.16.

A.5, Right), and thus, smaller halos are more concentrated. For highly concentrated halos, a significant portion of their mass is concentrated near the center, reducing the mass distributed in the outer regions. This leads to a smaller effective cross-section, which in turn reduces the gravitational influence on the stellar stream, reducing the number of perturbers that produce appreciable gaps. In contrast, larger halos in the NFW model tend to have lower concentrations, meaning they are more diffuse. These halos might therefore produce weaker density perturbations, suppressing the formation of the largest gaps compared to the Plummer model, where the more uniform mass distribution could lead to higher number of large gaps produced by massive halos.

To calculate the gap size distribution for different WDM models, we follow the same established framework procedures to assign subhalo parameters. One key distinction is the concentration-mass relation for WDM. As we have explored, in WDM scenarios, the delayed onset of structure formation affects the assembly history of DM halos, suppressing their concentration. As such, one can write the WDM in terms of the CDM concentration with a

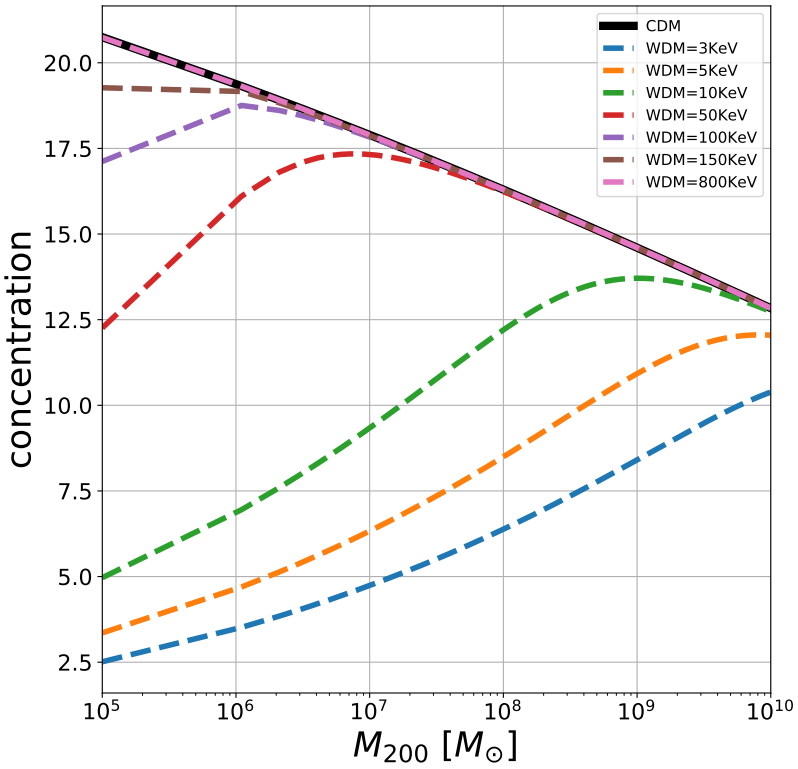

Figure A.6: The concentration-mass relation for the WDM models, as described by Eqn. A.17, explored in the simulations alongside the CDM concentration for comparison.

"suppression" factor [221]:

$$c_{WDM} = (c_{CDM})\,(1+z)^{\beta(z)} \left(1 + 60\frac{M_{hm}}{M_{200}}\right)^{-0.17} \tag{A.17}$$

where z is the redshift, $\beta(z) = 0.026z - 0.04$ and $M_{hm} = 3 \times 10^8 \left(\frac{m_{WDM}}{3.3keV}\right)^{-3.33} M_\odot$ is the half-mode mass defined in terms of the length scale where the transfer function between CDM and WDM power spectra drops to one-half. Figure A.6 shows the concentration for the various WDM simulated models alongside the CDM concentration.

In figure A.7 (Top), we present the gap size distributions for different WDM models. We observe a sharp cut-off for larger gaps, similar to that seen in the CDM case. As expected WDM models with larger DM particle (e.g., $m_{WDM} > 200$ keV) match the CDM gap size distribution. By integrating the gap size distribution curves, we can estimate the total

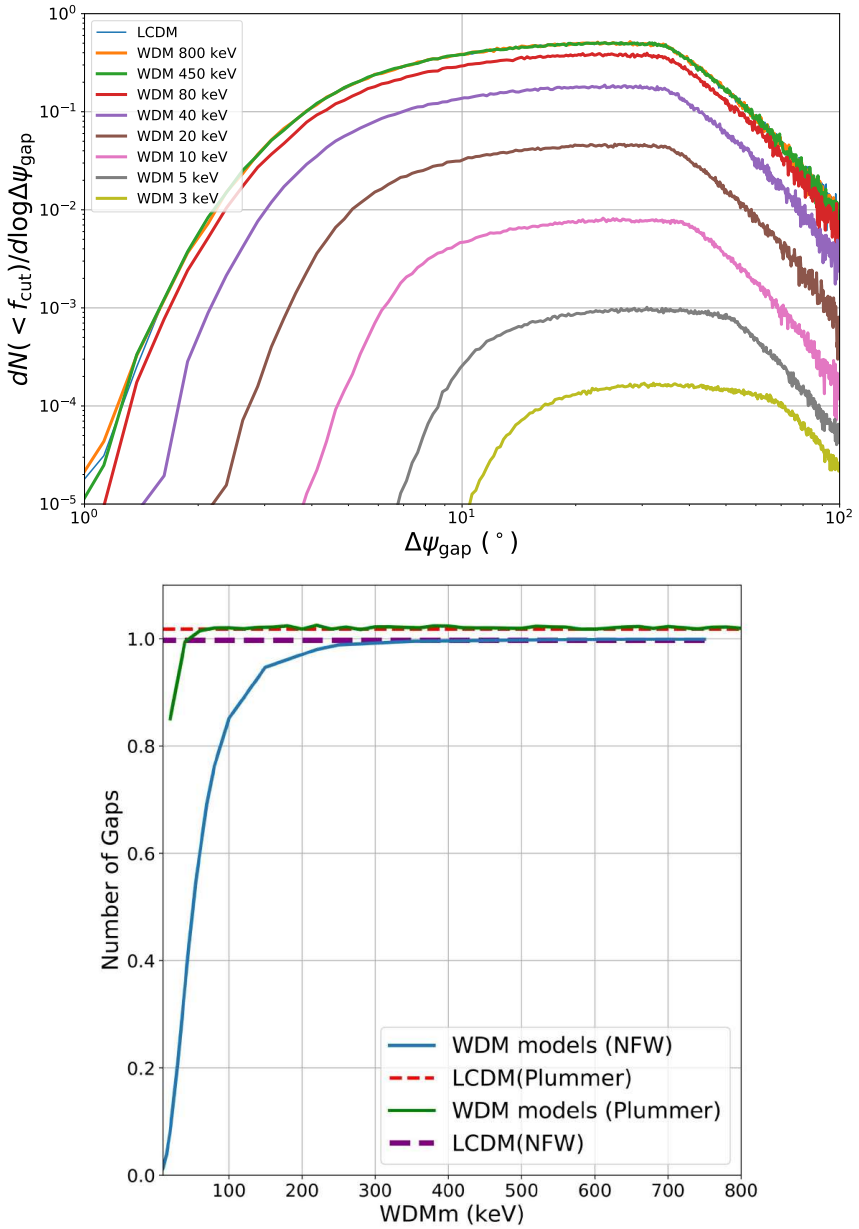

Figure A.7: Top: Gap size distributions for different realizations of WDM models. As expected, there is a pronounced suppression of all gap sizes, i.e., subhalo suppression, for WDM models with $m_{WDM} \lesssim 80$ keV. Bottom: The total number of gaps for various WDM models assuming both Plummer and NFW potentials. The CDM (Plummer and NFW) expected gaps are plot for reference. These calculations assume the properties of the Pal 5 stream in Table A.1.

number of gaps—independent of size—for each DM model. Figure A.7 (Bottom) shows the total number of gaps as a function of the WDM particle mass, with the number of gaps

predicted by CDM (Plummer) and CDM (NFW) also displayed for comparison. These gap size calculations are made with a gap depth threshold of $f < 0.9$. We find that, for both CDM cases, we would expect to observe ~ 1 gap in Pal 5. In contrast, WDM models predict fewer than one gap for $m_{WDM} < 200$ keV in the NFW case and $m_{WDM} < 50$ keV in the Plummer case.

A.0.5 Outlook: Stellar Streams

Here, I have outlined a formalism to predict the number of gaps in stellar streams caused by DM perturbers. The modeling tools rely on the generalized impulse approximation to calculate the velocity kicks imparted on the stars by DM halos, and subsequently characterize the resulting density perturbations that evolve into observable gaps with measurable depth and width. Furthermore, the generalized definition of this framework allows to test different DM models such as WDM and compare gap size and depth predictions with CDM. The results of this work may serve as a qualitative guide for targeted searches for stream gaps in astronomical surveys.

Of particular interest are the results presented in Figures A.5 and A.7, which highlight the observable differences between gaps caused by Plummer and NFW subhalos. For example, the NFW gap size distribution predicts that gaps as large as 15° can be produced in Pal 5, indicating that gap searches should focus on identifying gaps larger than $\sim 1^\circ$. Another important conclusion is that alternative DM models predict noticeable differences in the expected number of gaps compared to CDM. For instance, LSST is expected to precisely measure dozens of stellar streams, providing much stronger constraints on DM models. At the 10-year LSST depth, ΛCDM predicts the observation of 17 gaps in total across the 13 Dark Energy Survey streams reported by Shipp et al. (2018). Observing fewer than 6 gaps would be inconsistent with ΛCDM at a confidence level of 99.9%[50].

Current efforts are underway to increase the sample of stellar streams in the MW. For

example, Gaia [223] has led to the discovery and characterization of more than a hundred stellar streams, a tenfold increase compared to pre-Gaia knowledge. Furthermore, Gaia has provided accurate stream kinematics, including proper motions and orbit constraints, which have clarified the origins and paths of these streams. These proper motions also facilitated more effective spectroscopic follow-up observations, allowing deeper study of these streams. Stellar streams have now become key gravitational probes within the MW's halo, helping to map the DM distribution. Over the next decade with the advent of larger and more capable cosmological surveys, the Galactic stellar streams are expected to be fully mapped, and in conjunction with observable predictions from models, more robust constraints on DM can be placed [224].

REFERENCES

[1] John Kormendy and Ralf Bender. Supermassive black holes do not correlate with dark matter halos of galaxies. *Nature*, 469:377–80, 01 2011. doi:10.1038/nature09695.

[2] Douglas Clowe, Maruša Bradač, Anthony H. Gonzalez, Maxim Markevitch, Scott W. Randall, Christine Jones, and Dennis Zaritsky. A direct empirical proof of the existence of dark matter*. *The Astrophysical Journal*, 648(2):L109, aug 2006. doi:10.1086/508162. URL https://dx.doi.org/10.1086/508162.

[3] Planck Collaboration. Planck 2018 results - vi.cosmological parameters. *AA*, 2020. doi:10.1051/0004-6361/201833910. URL https://doi.org/10.1051/0004-6361/201833910.

[4] The Dark Energy Survey Collaboration. The dark energy camera (decam), 2024. URL https://www.darkenergysurvey.org/the-des-project/instrument/the-camera/.

[5] David J. Schlegel and et al. A spectroscopic road map for cosmic frontier: Desi, desi-ii, stage-5. 9 2022. doi:10.2172/1887254. URL https://www.osti.gov/biblio/1887254.

[6] Ross F Chun. A high voltage charge-coupled device (ccd) controller asic for the large synoptic survey telescope (lsst). 2010. URL https://api.semanticscholar.org/CorpusID:55527678.

[7] J. R. Janesick. *Scientific Charge Coupled Devices*. SPIE Publications, 2001.

[8] Javier Tiffenberg, Miguel Sofo-Haro, Alex Drlica-Wagner, Rouven Essig, Yann Guardincerri, Steve Holland, Tomer Volansky, and Tien-Tien Yu. Single-electron and single-photon sensitivity with a silicon Skipper CCD. *Phys. Rev. Lett.*, 119(13):131802, 2017. doi:10.1103/PhysRevLett.119.131802.

[9] Guillermo Fernández Moroni, Juan Estrada, Gustavo Cancelo, Stephen E Holland, Eduardo E Paolini, and H Thomas Diehl. Sub-electron readout noise in a skipper CCD fabricated on high resistivity silicon. *Experimental Astronomy*, 34(1):43–64, July 2012.

[10] S.E. Holland, K.S. Dawson, and et al. Fabrication of back-illuminated, fully depleted charge-coupled devices. *Nuclear Instruments and Methods in Physics Research Section A: Accelerators, Spectrometers, Detectors and Associated Equipment*, 579(2):653–657, 2007. ISSN 0168-9002. doi:https://doi.org/10.1016/j.nima.2007.05.265. URL https://www.sciencedirect.com/science/article/pii/S0168900207011564. Proceedings of the 6th "Hiroshima" Symposium on the Development and Application of Semiconductor Detectors.

[11] Vanessa B. P. Macanhan, Fernando G. Santoro, and et al. Mechanical design of SIFS SOAR integral field unit spectrograph. In Ian S. McLean, Suzanne K. Ramsay, and Hideki Takami, editors, *Ground-based and Airborne Instrumentation for Astronomy III*, volume 7735, pages 2439 – 2445. International Society for Optics and Photonics, SPIE, 2010. doi:10.1117/12.856593. URL https://doi.org/10.1117/12.856593.

[12] H. Thomas Diehl, Robert Angstadt, and et al. Characterization of DECam focal plane detectors. In David A. Dorn and Andrew D. Holland, editors, *High Energy, Optical, and Infrared Detectors for Astronomy III*, volume 7021, page 702107. International Society for Optics and Photonics, SPIE, 2008. doi:10.1117/12.790053. URL https://doi.org/10.1117/12.790053.

[13] Guillermo Fernández Moroni, Juan Estrada, Gustavo Cancelo, Stephen E. Holland, Eduardo E. Paolini, and H. Thomas Diehl. Sub-electron readout noise in a Skipper CCD fabricated on high resistivity silicon. *Experimental Astronomy*, 34(1):43–64, July 2012. doi:10.1007/s10686-012-9298-x.

[14] Pierre Astier, Pierre Antilogus, Claire Juramy, Rémy Le Breton, Laurent Le Guillou, Eduardo Sepulveda, and The Dark Energy Science Collaboration. The shape of the photon transfer curve of ccd sensors. *A&A*, 629:A36, 2019. doi:10.1051/0004-6361/201935508. URL https://doi.org/10.1051/0004-6361/201935508.

[15] William R. Coulton, Robert Armstrong, Kendrick M. Smith, Robert H. Lupton, and David N. Spergel. Exploring the Brighter-fatter Effect with the Hyper Suprime-Cam. AJ, 155(6):258, June 2018. doi:10.3847/1538-3881/aac08d.

[16] Alex Drlica-Wagner, Edgar Marrufo Villalpando, Judah O'Neil, Juan Estrada, Stephen Holland, Noah Kurinsky, Ting Li, Guillermo Fernandez Moroni, Javier Tiffenberg, and Sho Uemura. Characterization of skipper CCDs for cosmological applications. In Andrew D. Holland and James Beletic, editors, *X-Ray, Optical, and Infrared Detectors for Astronomy IX*, volume 11454, page 114541A. International Society for Optics and Photonics, SPIE, 2020. doi:10.1117/12.2562403. URL https://doi.org/10.1117/12.2562403.

[17] Ralph C. Bohlin, Karl D. Gordon, and P.-E. Tremblay. Techniques and review of absolute flux calibration from the ultraviolet to the mid-infrared. *Publications of the Astronomical Society of the Pacific*, 126(942):711, 2014. doi:10.1086/677655. URL https://dx.doi.org/10.1086/677655.

[18] Marco Regis, Marco Taoso, Daniel Vaz, Jarle Brinchmann, Sebastiaan L. Zoutendijk, Nicolas F. Bouché, and Matthias Steinmetz. Searching for light in the darkness: Bounds on alp dark matter with the optical muse-faint survey. *Physics Letters B*, 814: 136075, 2021. ISSN 0370-2693. doi:https://doi.org/10.1016/j.physletb.2021.136075. URL https://www.sciencedirect.com/science/article/pii/S0370269321000150.

[19] Daniel Grin, Giovanni Covone, Jean-Paul Kneib, Marc Kamionkowski, Andrew Blain, and Eric Jullo. Telescope search for decaying relic axions. *Phys. Rev. D*, 75:105018, 2007. doi:10.1103/PhysRevD.75.105018. URL https://link.aps.org/doi/10.1103/PhysRevD.75.105018.

[20] P. Carenza, G. Lucente, and E. Vitagliano. Probing the blue axion with cosmic optical background anisotropies. *Phys. Rev. D*, 107(8):083032, 2023. doi:10.1103/PhysRevD.107.083032.

[21] M. J. Dolan, F. J. Hiskens, and R. R. Volkas. Advancing globular cluster constraints on the axion-photon coupling. *J. Cosmol. Astropart. Phys.*, 10:096, 2022. doi:10.1088/1475-7516/2022/10/096.

[22] Yue Pan, Anirudh Chiti, Alex Drlica-Wagner, Alexander P. Ji, Ting S. Li, Guilherme Limberg, Douglas L. Tucker, and Sahar Allam. Stellar Metallicities from DECam *u*-band Photometry: A Study of Milky Way Ultra-Faint Dwarf Galaxies. *submitted to Astrophys. J.*, art. arXiv:2404.08054, 2024. doi:10.48550/arXiv.2404.08054.

[23] Fernando Chierchie, Guillermo Fernandez Moroni, Leandro Stefanazzi, Eduardo Paolini, Javier Tiffenberg, Juan Estrada, Gustavo Cancelo, and Sho Uemura. Smart readout of nondestructive image sensors with single photon-electron sensitivity. *Phys. Rev. Lett.*, 127:241101, Dec 2021. doi:10.1103/PhysRevLett.127.241101. URL https://link.aps.org/doi/10.1103/PhysRevLett.127.241101.

[24] S.E. Holland. Fully depleted charge-coupled device design and technology development. *Astron.Nachr./AN, e20230072*, 2023. doi:https://doi.org/10.1002/asna.20230072.

[25] Las Campanas Observatory. *IMACS User Manual*, n.d. URL https://www.lco.cl/technical-documentation/imacs-user-manual/. Retrieved from https://www.lco.cl/technical-documentation/imacs-user-manual/.

[26] DESI Collaboration, B Abareshi, J Aguilar, S Ahlen, and et al. Overview of the instrumentation for the dark energy spectroscopic instrument. *The Astronomical Journal*, 164(5):207, October 2022.

[27] T. S. Li, J. D. Simon, and et al. (DES Collaboration). Farthest Neighbor: The Distant Milky Way Satellite Eridanus II. *The Astrophysical Journal*, 838(1):8, mar 2017. doi:10.3847/1538-4357/aa6113. URL https://dx.doi.org/10.3847/1538-4357/aa6113.

[28] Denis Erkal and Vasily Belokurov. Forensics of subhalo–stream encounters: the three phases of gap growth. *Monthly Notices of the Royal Astronomical Society*, 450(1): 1136–1149, 04 2015. ISSN 0035-8711. doi:10.1093/mnras/stv655. URL https://doi.org/10.1093/mnras/stv655.

[29] Denis Erkal, Vasily Belokurov, Jo Bovy, and Jason L. Sanders. The number and size of subhalo-induced gaps in stellar streams. *Monthly Notices of the Royal Astronomical*

Society, 463(1):102–119, 08 2016. ISSN 0035-8711. doi:10.1093/mnras/stw1957. URL https://doi.org/10.1093/mnras/stw1957.

[30] SIMBAD Astronomical Database. Bd -18 5550. https://simbad.cds.unistra.fr/simbad/sim-basic?Ident=BD+%E2%80%9418%C2%B05550. Accessed: 2024-11-05.

[31] Gaia Collaboration. Gaia DR3 2771566830179387776. https://gea.esac.esa.int/archive/. Accessed: 2024-11-05.

[32] Jordan Bruce, Ting S. Li, Andrew B. Pace, Mairead Heiger, Ying-Yi Song, and Joshua D. Simon. Spectroscopic analysis of milky way outer halo satellites: Aquarius ii and boötes ii. *The Astrophysical Journal*, 950(2):167, jun 2023. doi:10.3847/1538-4357/acc943. URL https://dx.doi.org/10.3847/1538-4357/acc943.

[33] Henrietta S. Leavitt and Edward C. Pickering. Periods of 25 Variable Stars in the Small Magellanic Cloud. *Harvard College Observatory Circular*, 173:1–3, March 1912.

[34] V. M. Slipher. Nebulae. *Proceedings of the American Philosophical Society*, 56:403–409, January 1917.

[35] Edwin Hubble. A relation between distance and radial velocity among extra-galactic nebulae. *Proceedings of the National Academy of Science*, 15(3):168–173, March 1929. doi:10.1073/pnas.15.3.168.

[36] A. A. Penzias and R. W. Wilson. A Measurement of Excess Antenna Temperature at 4080 Mc/s. ApJ, 142:419–421, July 1965. doi:10.1086/148307.

[37] A. Friedman. On the curvature of space. *Z. Phys.*, 10:377–386, 1922. doi:10.1007/BF01332580.

[38] Abbé G. Lemaître. A Homogeneous Universe of Constant Mass and Increasing Radius accounting for the Radial Velocity of Extra-galactic Nebulæ. *Monthly Notices of the Royal Astronomical Society*, 91(5):483–490, 03 1931. ISSN 0035-8711. doi:10.1093/mnras/91.5.483. URL https://doi.org/10.1093/mnras/91.5.483.

[39] H. P. Robertson. Kinematics and World-Structure. ApJ, 82:284, November 1935. doi:10.1086/143681.

[40] A. G. Walker. On milne's theory of world-structure. *Proceedings of the London Mathematical Society*, s2-42(1):90–127, 1937. doi:https://doi.org/10.1112/plms/s2-42.1.90. URL https://londmathsoc.onlinelibrary.wiley.com/doi/abs/10.1112/plms/s2-42.1.90.

[41] L. Page, G. Hinshaw, and et al. Three-year wilkinson microwave anisotropy probe (wmap) observations: Polarization analysis. *The Astrophysical Journal Supplement Series*, 170(2):335, jun 2007. doi:10.1086/513699. URL https://dx.doi.org/10.1086/513699.

[42] Shadab Alam, Marie Aubert, and et al. Avila, Santiago. Completed sdss-iv extended baryon oscillation spectroscopic survey: Cosmological implications from two decades of spectroscopic surveys at the apache point observatory. *Phys. Rev. D*, 103:083533, Apr 2021. doi:10.1103/PhysRevD.103.083533. URL https://link.aps.org/doi/10.1103/PhysRevD.103.083533.

[43] F. Zwicky. Die Rotverschiebung von extragalaktischen Nebeln. *Helvetica Physica Acta*, 6:110–127, January 1933.

[44] F. Zwicky. On the Masses of Nebulae and of Clusters of Nebulae. ApJ, 86:217, October 1937. doi:10.1086/143864.

[45] James Binney and Scott Tremaine. *Galactic Dynamics*. Princeton University Press, Princeton, NJ, 2nd edition, 2008.

[46] Vera C. Rubin and Jr. Ford, W. Kent. Rotation of the Andromeda Nebula from a Spectroscopic Survey of Emission Regions. ApJ, 159:379, February 1970. doi:10.1086/150317.

[47] V. C. Rubin, Jr. Ford, W. K., and N. Thonnard. Rotational properties of 21 SC galaxies with a large range of luminosities and radii, from NGC 4605 (R=4kpc) to UGC 2885 (R=122kpc). ApJ, 238:471–487, June 1980. doi:10.1086/158003.

[48] Matthias Bartelmann. Gravitational lensing. *Classical and Quantum Gravity*, 27(23): 233001, November 2010. ISSN 1361-6382. doi:10.1088/0264-9381/27/23/233001. URL http://dx.doi.org/10.1088/0264-9381/27/23/233001.

[49] Prasenjit Saha, Dominique Sluse, Jenny Wagner, and Liliya L. R. Williams. Essentials of strong gravitational lensing, 2024. URL https://arxiv.org/abs/2401.04165.

[50] Alex Drlica-Wagner, Yao-Yuan Mao, Susmita Adhikari, and et al. Probing the fundamental nature of dark matter with the large synoptic survey telescope, 2019. URL https://arxiv.org/abs/1902.01055.

[51] D. J. Fixsen. The temperature of the cosmic microwave background. *The Astrophysical Journal*, 707(2):916, nov 2009. doi:10.1088/0004-637X/707/2/916. URL https://dx.doi.org/10.1088/0004-637X/707/2/916.

[52] Dan Hooper. *Particle cosmology and Astrophysics*. Princeton University Press, Princeton, 2024.

[53] A. Drlica-Wagner, K. Bechtol, and et al. (DES Collaboration). Milky way satellite census i. the observational selection function for milky way satellites in des y3 and pan-starrs dr1. *The Astrophysical Journal*, 893(1):47, apr 2020. doi:10.3847/1538-4357/ab7eb9. URL https://dx.doi.org/10.3847/1538-4357/ab7eb9.

[54] Pablo Villanueva-Domingo, Nickolay Y. Gnedin, and Olga Mena. Warm dark matter and cosmic reionization. *The Astrophysical Journal*, 852(2):139, jan 2018. doi:10.3847/1538-4357/aa9ff5. URL https://dx.doi.org/10.3847/1538-4357/aa9ff5.

[55] Paul Bode, Jeremiah P. Ostriker, and Neil Turok. Halo formation in warm dark matter models. *The Astrophysical Journal*, 556(1):93, jul 2001. doi:10.1086/321541. URL https://dx.doi.org/10.1086/321541.

[56] James S. Bullock and Michael Boylan-Kolchin. Small-scale challenges to the λcdm paradigm. *Annual Review of Astronomy and Astrophysics*, 55(Volume 55, 2017):343–387, 2017. ISSN 1545-4282. doi:https://doi.org/10.1146/annurev-astro-091916-055313. URL https://www.annualreviews.org/content/journals/10.1146/annurev-astro-091916-055313.

[57] Alexander Merle and Aurel Schneider. Production of sterile neutrino dark matter and the 3.5 kev line. *Physics Letters B*, 749:283–288, 2015. ISSN 0370-2693. doi:https://doi.org/10.1016/j.physletb.2015.07.080. URL https://www.sciencedirect.com/science/article/pii/S0370269315006000.

[58] S Bhargava, P A Giles, and et al. The XMM Cluster Survey: new evidence for the 3.5-keV feature in clusters is inconsistent with a dark matter origin. *Monthly Notices of the Royal Astronomical Society*, 497(1):656–671, 06 2020. ISSN 0035-8711. doi:10.1093/mnras/staa1829. URL https://doi.org/10.1093/mnras/staa1829.

[59] Eric D. Carlson, Marie E. Machacek, and Lawrence J. Hall. Self-interacting Dark Matter. ApJ, 398:43, October 1992. doi:10.1086/171833.

[60] David N. Spergel and Paul J. Steinhardt. Observational evidence for self-interacting cold dark matter. *Phys. Rev. Lett.*, 84:3760–3763, Apr 2000. doi:10.1103/PhysRevLett.84.3760. URL https://link.aps.org/doi/10.1103/PhysRevLett.84.3760.

[61] Ayuki Kamada, Manoj Kaplinghat, Andrew B. Pace, and Hai-Bo Yu. Self-interacting dark matter can explain diverse galactic rotation curves. *Phys. Rev. Lett.*, 119:111102, Sep 2017. doi:10.1103/PhysRevLett.119.111102. URL https://link.aps.org/doi/10.1103/PhysRevLett.119.111102.

[62] David Wittman, Nathan Golovich, and William A. Dawson. The mismeasure of mergers: Revised limits on self-interacting dark matter in merging galaxy clusters. *The Astrophysical Journal*, 869(2):104, dec 2018. doi:10.3847/1538-4357/aaee77. URL https://dx.doi.org/10.3847/1538-4357/aaee77.

[63] Tao Ren, Anna Kwa, Manoj Kaplinghat, and Hai-Bo Yu. Reconciling the diversity and uniformity of galactic rotation curves with self-interacting dark matter. *Phys. Rev. X*, 9:031020, Aug 2019. doi:10.1103/PhysRevX.9.031020. URL https://link.aps.org/doi/10.1103/PhysRevX.9.031020.

[64] Laura Sagunski, Sophia Gad-Nasr, Brian Colquhoun, Andrew Robertson, and Sean Tulin. Velocity-dependent self-interacting dark matter from groups and clusters of galaxies. *Journal of Cosmology and Astroparticle Physics*, 2021(01):024, jan 2021. doi:10.1088/1475-7516/2021/01/024. URL https://dx.doi.org/10.1088/1475-7516/2021/01/024.

[65] Susmita Adhikari, Arka Banerjee, Kimberly K. Boddy, Francis-Yan Cyr-Racine, Harry Desmond, Cora Dvorkin, Bhuvnesh Jain, Felix Kahlhoefer, Manoj Kaplinghat, Anna Nierenberg, Annika H. G. Peter, Andrew Robertson, Jeremy Sakstein, and Jesús Zavala. Astrophysical tests of dark matter self-interactions, 2022. URL https://arxiv.org/abs/2207.10638.

[66] R. D. Peccei and Helen R. Quinn. CP conservation in the presence of pseudoparticles. *Phys. Rev. Lett.*, 38:1440–1443, Jun 1977. doi:10.1103/PhysRevLett.38.1440. URL https://link.aps.org/doi/10.1103/PhysRevLett.38.1440.

[67] P. Sikivie and Q. Yang. Bose-einstein condensation of dark matter axions. *Phys. Rev. Lett.*, 103:111301, Sep 2009. doi:10.1103/PhysRevLett.103.111301. URL https://link.aps.org/doi/10.1103/PhysRevLett.103.111301.

[68] Aravind Natarajan and Pierre Sikivie. Inner caustics of cold dark matter halos. *Phys. Rev. D*, 73:023510, Jan 2006. doi:10.1103/PhysRevD.73.023510. URL https://link.aps.org/doi/10.1103/PhysRevD.73.023510.

[69] Eric Armengaud, Nathalie Palanque-Delabrouille, Christophe Yèche, David J. E. Marsh, and Julien Baur. Constraining the mass of light bosonic dark matter using SDSS Lyman-α forest. *Monthly Notices of the Royal Astronomical Society*, 471 (4):4606–4614, 07 2017. ISSN 0035-8711. doi:10.1093/mnras/stx1870. URL https://doi.org/10.1093/mnras/stx1870.

[70] Peter Behroozi, Risa H Wechsler, Andrew P Hearin, and Charlie Conroy. UniverseMachine: The correlation between galaxy growth and dark matter halo assembly from $z = 0 - 10$. *Monthly Notices of the Royal Astronomical Society*, 488(3): 3143–3194, 05 2019. ISSN 0035-8711. doi:10.1093/mnras/stz1182. URL https://doi.org/10.1093/mnras/stz1182.

[71] P. Jethwa, D. Erkal, and V. Belokurov. The upper bound on the lowest mass halo. *Monthly Notices of the Royal Astronomical Society*, 473(2):2060–2083, 09 2017. ISSN 0035-8711. doi:10.1093/mnras/stx2330. URL https://doi.org/10.1093/mnras/stx2330.

[72] Stacy Y. Kim, Annika H. G. Peter, and Jonathan R. Hargis. Missing satellites problem: Completeness corrections to the number of satellite galaxies in the milky way are consistent with cold dark matter predictions. *Phys. Rev. Lett.*, 121:211302, Nov 2018. doi:10.1103/PhysRevLett.121.211302. URL https://link.aps.org/doi/10.1103/PhysRevLett.121.211302.

[73] Volker Bromm and Naoki Yoshida. The first galaxies. *Annual Review of Astronomy and Astrophysics*, 49(Volume 49, 2011):373–407, 2011. ISSN 1545-4282. doi:https://doi.org/10.1146/annurev-astro-081710-102608. URL https://www.annualreviews.org/content/journals/10.1146/annurev-astro-081710-102608.

[74] Joss Bland-Hawthorn, Ralph Sutherland, and David Webster. Ultrafaint dwarf galaxies—the lowest-mass relics from before reionization. *The Astrophysical Journal*, 807 (2):154, jul 2015. doi:10.1088/0004-637X/807/2/154. URL https://dx.doi.org/10.1088/0004-637X/807/2/154.

[75] Risa H. Wechsler and Jeremy L. Tinker. The connection between galaxies and their dark matter halos. *Annual Review of Astronomy and Astrophysics*, 56(Volume 56, 2018):435–487, 2018. ISSN 1545-4282. doi:https://doi.org/10.1146/annurev-astro-081817-051756. URL https://www.annualreviews.org/content/journals/10.1146/annurev-astro-081817-051756.

[76] K. Bechtol, A. Drlica-Wagner, E. Balbinot, et al., and (The DES Collaboration). Eight new milky way companions discovered in first-year dark energy survey data. *The Astrophysical Journal*, 807(1):50, jun 2015. doi:10.1088/0004-637X/807/1/50. URL https://dx.doi.org/10.1088/0004-637X/807/1/50.

[77] Sergey E. Koposov, Vasily Belokurov, Gabriel Torrealba, and N. Wyn Evans. Beasts of the southern wild: Discovery of nine ultra faint satellites in the vicinity of the magellanic clouds. *The Astrophysical Journal*, 805(2):130, may 2015. doi:10.1088/0004-637X/805/2/130. URL https://dx.doi.org/10.1088/0004-637X/805/2/130.

[78] A. Drlica-Wagner, K. Bechtol, E. S. Rykoff, et al., and (The DES Collaboration). Eight ultra-faint galaxy candidates discovered in year two of the dark energy survey. *The Astrophysical Journal*, 813(2):109, nov 2015. doi:10.1088/0004-637X/813/2/109. URL https://dx.doi.org/10.1088/0004-637X/813/2/109.

[79] Daisuke Homma, Masashi Chiba, and et al. A new milky way satellite discovered in the subaru/hyper suprime-cam survey. *The Astrophysical Journal*, 832(1):21, nov 2016. doi:10.3847/0004-637X/832/1/21. URL https://dx.doi.org/10.3847/0004-637X/832/1/21.

[80] Daisuke Homma, Masashi Chiba, and et al. Searches for new Milky Way satellites from the first two years of data of the Subaru/Hyper Suprime-Cam survey: Discovery of Cetus III. *Publications of the Astronomical Society of Japan*, 70(SP1):S18, 07 2017. ISSN 0004-6264. doi:10.1093/pasj/psx050. URL https://doi.org/10.1093/pasj/psx050.

[81] LSST Science Collaboration. Lsst science book, version 2.0, 2009. URL https://arxiv.org/abs/0912.0201.

[82] Ioana Ciucă, Daisuke Kawata, and et al. A Gaia DR2 search for dwarf galaxies towards Fermi-LAT sources: implications for annihilating dark matter. *Monthly Notices of the Royal Astronomical Society*, 480(2):2284–2291, 07 2018. ISSN 0035-8711. doi:10.1093/mnras/sty1994. URL https://doi.org/10.1093/mnras/sty1994.

[83] Mariah Baker and Beth Willman. Charting unexplored dwarf galaxy territory with rr lyrae. *The Astronomical Journal*, 150(5):160, nov 2015. doi:10.1088/0004-6256/150/5/160. URL https://dx.doi.org/10.1088/0004-6256/150/5/160.

[84] Jorge Peñarrubia. Fluctuations of the gravitational field generated by a random population of extended substructures. *Monthly Notices of the Royal Astronomical Society*, 474(2):1482–1498, 11 2017. ISSN 0035-8711. doi:10.1093/mnras/stx2773. URL https://doi.org/10.1093/mnras/stx2773.

[85] Ana Bonaca and David W. Hogg. The information content in cold stellar streams. *The Astrophysical Journal*, 867(2):101, nov 2018. doi:10.3847/1538-4357/aae4da. URL https://dx.doi.org/10.3847/1538-4357/aae4da.

[86] Ana Bonaca, David W. Hogg, Adrian M. Price-Whelan, and Charlie Conroy. The spur and the gap in gd-1: Dynamical evidence for a dark substructure in the milky way halo. *The Astrophysical Journal*, 880(1):38, jul 2019. doi:10.3847/1538-4357/ab2873. URL https://dx.doi.org/10.3847/1538-4357/ab2873.

[87] Paul Menker and Andrew Benson. Advancing stellar streams as a dark matter probe – i: Evolution of the cdm subhalo population, 2024. URL https://arxiv.org/abs/2406.11989.

[88] Joo Heon Yoon, Kathryn V. Johnston, and David W. Hogg. Clumpy streams from clumpy halos: Detecting missing satellites with cold stellar structures. *The Astrophysical Journal*, 731(1):58, mar 2011. doi:10.1088/0004-637X/731/1/58. URL https://dx.doi.org/10.1088/0004-637X/731/1/58.

[89] Niv Drory, Guillermo A. Blanc, Kathryn Kreckel, and et al. The sdss-v local volume mapper (lvm): Scientific motivation and project overview, 2024. URL https://arxiv.org/abs/2405.01637.

[90] T. M. C. Abbott, M. Adamow, M. Aguena, and et al. Dark energy survey: A 2.1 *Phys. Rev. D*, 110:063515, Sep 2024. doi:10.1103/PhysRevD.110.063515. URL https://link.aps.org/doi/10.1103/PhysRevD.110.063515.

[91] DESI Collaboration, A. G. Adame, J. Aguilar, S. Ahlen, and et al. The early data release of the dark energy spectroscopic instrument. *The Astronomical Journal*, 168 (2):58, jul 2024. doi:10.3847/1538-3881/ad3217. URL https://dx.doi.org/10.3847/1538-3881/ad3217.

[92] Donald G. York, J. Adelman, Jr. John E. Anderson, and et al. The sloan digital sky survey: Technical summary. *The Astronomical Journal*, 120(3):1579, sep 2000. doi:10.1086/301513. URL https://dx.doi.org/10.1086/301513.

[93] Joshua A. Frieman, Bruce Bassett, Andrew Becker, and at al. The sloan digital sky survey-ii supernova survey: Technical summary. *The Astronomical Journal*, 135(1): 338, dec 2007. doi:10.1088/0004-6256/135/1/338. URL https://dx.doi.org/10.1088/0004-6256/135/1/338.

[94] Brian Yanny, Constance Rockosi, Heidi Jo Newberg, and et al. Segue: A spectroscopic survey of 240,000 stars with g = 14–20. *The Astronomical Journal*, 137(5):4377, apr 2009. doi:10.1088/0004-6256/137/5/4377. URL https://dx.doi.org/10.1088/0004-6256/137/5/4377.

[95] Predehl, P., Andritschke, R., Arefiev, V., and et al. The erosita x-ray telescope on srg. *å*, 647:A1, 2021. doi:10.1051/0004-6361/202039313. URL https://doi.org/10.1051/0004-6361/202039313.

[96] Andrés Almeida, Scott F. Anderson, Maria Argudo-Fernández, and et al. The eighteenth data release of the sloan digital sky surveys: Targeting and first spectra from sdss-v. *The Astrophysical Journal Supplement Series*, 267(2):44, aug 2023. doi:10.3847/1538-4365/acda98. URL https://dx.doi.org/10.3847/1538-4365/acda98.

[97] Nicholas P. Konidaris, Niv Drory, and et al. SDSS-V local volume mapper instrument: overview and status. In Christopher J. Evans, Julia J. Bryant, and Kentaro Motohara, editors, *Ground-based and Airborne Instrumentation for Astronomy VIII*, volume 11447, page 1144718. International Society for Optics and Photonics, SPIE, 2020. doi:10.1117/12.2557565. URL https://doi.org/10.1117/12.2557565.

[98] Brenna Flaugher. The dark energy survey. *Int. J. Mod. Phys. A*, 20(14):3121–3123, June 2005.

[99] Dark Energy Survey Collaboration:, T. Abbott, F. B. Abdalla, J. Aleksić, and et al. The Dark Energy Survey: more than dark energy – an overview. *Monthly Notices of the Royal Astronomical Society*, 460(2):1270–1299, 03 2016. ISSN 0035-8711. doi:10.1093/mnras/stw641. URL https://doi.org/10.1093/mnras/stw641.

[100] I. Sevilla-Noarbe, K. Bechtol, M. Carrasco Kind, et al., and (DES Collaboration). Dark energy survey year 3 results: Photometric data set for cosmology. *The Astrophysical Journal Supplement Series*, 254(2):24, may 2021. doi:10.3847/1538-4365/abeb66. URL https://dx.doi.org/10.3847/1538-4365/abeb66.

[101] M. Vincenzi, D. Brout, P. Armstrong, and et al. The dark energy survey supernova program: Cosmological analysis and systematic uncertainties, 2024. URL https://arxiv.org/abs/2401.02945.

[102] DES Collaboration: T. M. C. Abbott, M. Acevedo, and et al. The dark energy survey: Cosmology results with $\sim$ 1500 new high-redshift type ia supernovae using the full 5 yr data set. *The Astrophysical Journal Letters*, 973(1):L14, oct 2024. doi:10.3847/2041-8213/ad6f9f. URL https://dx.doi.org/10.3847/2041-8213/ad6f9f.

[103] B. Flaugher, H. T. Diehl, K. Honscheid, T. M. C. Abbott, et al., and (The DES Collaboration). The dark energy camera. *The Astronomical Journal*, 150(5):150, oct 2015. doi:10.1088/0004-6256/150/5/150. URL https://dx.doi.org/10.1088/0004-6256/150/5/150.

[104] S.E. Holland, D.E. Groom, N.P. Palaio, R.J. Stover, and Mingzhi Wei. Fully depleted, back-illuminated charge-coupled devices fabricated on high-resistivity silicon. *IEEE Transactions on Electron Devices*, 50(1):225–238, 2003. doi:10.1109/TED.2002.806476.

[105] Kyle Dawson, James Annis, and et al. Next-generation spectroscopic surveys with desi. 2020. URL https://www.snowmass21.org/docs/files/summaries/CF/SNOWMASS21-CF6_CF4_Dawson-041.pdf. Snowmass2021 Letter of Interest.

[106] Michael E. Levi, Lori E. Allen, and et al. The dark energy spectroscopic instrument (desi), 2019. URL https://arxiv.org/abs/1907.10688.

[107] Paul Martini, Stephen Bailey, and et al. Overview of the Dark Energy Spectroscopic Instrument. In Christopher J. Evans, Luc Simard, and Hideki Takami, editors, *Ground-based and Airborne Instrumentation for Astronomy VII*, volume 10702, page 107021F. International Society for Optics and Photonics, SPIE, 2018. doi:10.1117/12.2313063. URL https://doi.org/10.1117/12.2313063.

[108] A. G. Adame and et al. DESI 2024 III: Baryon Acoustic Oscillations from Galaxies and Quasars. 4 2024.

[109] Željko Ivezić, Steven M. Kahn, J. Anthony Tyson, and et al. Lsst: From science drivers to reference design and anticipated data products. *The Astrophysical Journal*, 873(2): 111, mar 2019. doi:10.3847/1538-4357/ab042c. URL https://dx.doi.org/10.3847/1538-4357/ab042c.

[110] A. Roodman, A. Rasmussen, A. Bradshaw, and at al. LSST camera verification testing and characterization. In Julia J. Bryant, Kentaro Motohara, and Joël R. D. Vernet, editors, *Ground-based and Airborne Instrumentation for Astronomy X*, volume 13096, page 130961S. International Society for Optics and Photonics, SPIE, 2024. doi:10.1117/12.3019698. URL https://doi.org/10.1117/12.3019698.

[111] Yousuke Utsumi, Pierre Antilogus, Pierre Astier, and et al. LSST Camera focal plane optimization. In Andrew D. Holland and Kyriaki Minoglou, editors, *X-Ray, Optical, and Infrared Detectors for Astronomy XI*, volume 13103, page 131030W. International Society for Optics and Photonics, SPIE, 2024. doi:10.1117/12.3019117. URL https://doi.org/10.1117/12.3019117.

[112] David J. Schlegel, Juna A. Kollmeier, Greg Aldering, and et al. The megamapper: A stage-5 spectroscopic instrument concept for the study of inflation and dark energy, 2022. URL https://arxiv.org/abs/2209.04322.

[113] David J. Schlegel, Juna A. Kollmeier, Greg Aldering, and et al. Astro2020 apc white paper: The megamapper: a z $>$ 2 spectroscopic instrument for the study of inflation and dark energy, 2019. URL https://arxiv.org/abs/1907.11171.

[114] W. S. Boyle and G. E. Smith. Charge coupled semiconductor devices. *The Bell System Technical Journal*, 49(4):587–593, 1970. ISSN 0005-8580. doi:10.1002/j.1538-7305.1970.tb01790.x.

[115] George E. Smith. Nobel lecture: The invention and early history of the ccd. *Rev. Mod. Phys.*, 82:2307–2312, Aug 2010. doi:10.1103/RevModPhys.82.2307. URL https://link.aps.org/doi/10.1103/RevModPhys.82.2307.

[116] Mykhaylo Evstigneev. *Introduction to Semiconductor Physics and Devices*. Springer Cham, 2022. doi:https://doi.org/10.1007/978-3-031-08458-4.

[117] Chul-Ho Lee, Gwan-Hyoung Lee, Arend M van der Zande, Wenchao Chen, Yilei Li, Minyong Han, Xu Cui, Ghidewon Arefe, Colin Nuckolls, Tony F Heinz, Jing Guo, James Hone, and Philip Kim. Atomically thin p–n junctions with van der waals heterointerfaces. *Nature Nanotechnology*, 9(9):676–681, September 2014.

[118] Gustavo I. Cancelo et al. Low Threshold Acquisition controller for Skipper CCDs. *J. Astron. Telesc. Instrum. Syst.*, 7(1):015001, 2021. doi:10.1117/1.JATIS.7.1.015001.

[119] Dobromir P. Dobrev and Tatyana D. Neycheva. Correlated multiple sampling techniques for sensor signal conditioning. In *2020 XXIX International Scientific Conference Electronics (ET)*, pages 1–4, 2020. doi:10.1109/ET50336.2020.9238159.

[120] C.J. Bebek, J.H. Emes, D.E. Groom, S. Haque, S.E. Holland, A. Karcher, W.F. Kolbe, J.S. Lee, N.P. Palaio, and G. Wang. Ccd development for the dark energy spectroscopic instrument. *Journal of Instrumentation*, 10(05):C05026, may 2015. doi:10.1088/1748-0221/10/05/C05026. URL https://dx.doi.org/10.1088/1748-0221/10/05/C05026.

[121] J. R. Janesick, T. Elliott, A. Dingizian, R. A. Bredthauer, and C. E. Chandler. New advancements in charge-coupled device technology - Sub-electron noise and 4096 $\times$ 4096 pixel CCDs. *SPIE*, 1242:223–237, 1990.

[122] C. E. Chandler, R. A. Bredthauer, J. R. Janesick, J. A. Westphal, and J. E. Gunn. Sub-electron noise charge coupled devices. *SPIE*, 1242:238–251, 1990.

[123] D.D. Wen. Design and operation of a floating gate amplifier. *IEEE Journal of Solid-State Circuits*, 9(6):410–414, 1974. doi:10.1109/JSSC.1974.1050535.

[124] Michael Crisler, Rouven Essig, Juan Estrada, Guillermo Fernandez, Javier Tiffenberg, Miguel Sofo Haro, Tomer Volansky, and Tien-Tien Yu. Sensei: First direct-detection constraints on sub-gev dark matter from a surface run. *Phys. Rev. Lett.*, 121:061803, Aug 2018. doi:10.1103/PhysRevLett.121.061803. URL https://link.aps.org/doi/10.1103/PhysRevLett.121.061803.

[125] Liron Barak, Itay M. Bloch, and et al. Sensei: Direct-detection results on sub-gev dark matter from a new skipper ccd. *Phys. Rev. Lett.*, 125:171802, Oct 2020. doi:10.1103/PhysRevLett.125.171802. URL https://link.aps.org/doi/10.1103/PhysRevLett.125.171802.

[126] Alexis Aguilar-Arevalo, Fabricio Alcalde Bessia, and et al. The oscura experiment, 2022.

[127] Brenda A. Cervantes-Vergara, Santiago Perez, and et al. Skipper-CCD sensors for the Oscura experiment: requirements and preliminary tests. *Journal of Instrumentation*, 18(8):P08016, August 2023. doi:10.1088/1748-0221/18/08/P08016.

[128] Mark A. Skinner, David N. Burrows, Gordon P. Garmire, Ralph Porter Kraft, David H. Lumb, and John A. Nousek. CUBIC: laboratory testing of 'thin poly' CCDs. In Oswald H. W. Siegmund, editor, *EUV, X-Ray, and Gamma-Ray Instrumentation for Astronomy IV*, volume 2006, pages 258 – 264. International Society for Optics and Photonics, SPIE, 1993. doi:10.1117/12.162838. URL https://doi.org/10.1117/12.162838.

[129] A. C. de Oliveira, L. S. de Oliveira, and et al. The SOAR integral field unit spectrograph optical design and IFU implementation. In Eli Atad-Ettedgui and Dietrich Lemke, editors, *Modern Technologies in Space- and Ground-based Telescopes and Instrumentation*, volume 7739, pages 1646 – 1657. International Society for Optics and Photonics, SPIE, 2010. doi:10.1117/12.857698. URL https://doi.org/10.1117/12.857698.

[130] Jacques R. D. Lepine, Antonio Cesar de Oliveira, and et al. SIFUS: SOAR integral field unit spectrograph. In Masanori Iye and Alan F. M. Moorwood, editors, *Instrument Design and Performance for Optical/Infrared Ground-based Telescopes*, volume 4841, pages 1086 – 1095. International Society for Optics and Photonics, SPIE, 2003. doi:10.1117/12.461977. URL https://doi.org/10.1117/12.461977.

[131] III Palumbo, Michael L., Sheila J. Kannappan, Elaine M. Frazer, Kathleen D. Eckert, Dara J. Norman, Luciano Fraga, Bruno C. Quint, Philippe Amram, Claudia Mendes de Oliveira, Ashley S. Bittner, Amanda J. Moffett, David V. Stark, Mark A. Norris, Nathaniel T. Cleaves, and Derrick S. Carr. Linking compact dwarf starburst galaxies in the RESOLVE survey to downsized blue nuggets. MNRAS, 494(4):4730–4750, June 2020. doi:10.1093/mnras/staa899.

[132] Patrí cia da Silva, R B Menezes, and J E Steiner. The nuclear region of NGC 613 – i. multiwavelength analysis. *Monthly Notices of the Royal Astronomical Society*, 492(4): 5121–5140, jan 2020. doi:10.1093/mnras/staa007. URL https://doi.org/10.1093%2Fmnras%2Fstaa007.

[133] Gregory Derylo, H. Thomas Diehl, and Juan Estrada. 0.250mm-thick CCD packaging for the Dark Energy Survey Camera array. In *Society of Photo-Optical Instrumentation Engineers (SPIE) Conference Series*, volume 6276 of *Society of Photo-*

Optical Instrumentation Engineers (SPIE) Conference Series, page 627608, 2006. doi:10.1117/12.672505.

[134] Alistair R. Walker, Maxime Boccas, Marco Bonati, Ramon Galvez, Manual Martinez, Patricio Schurter, Ricardo E. Schmidt, Michael C. Ashe, Francisco Delgado, and Roberto Tighe. SOAR Optical Imager. In Masanori Iye and Alan F. M. Moorwood, editors, *Instrument Design and Performance for Optical/Infrared Ground-based Telescopes*, volume 4841, pages 286 – 294. International Society for Optics and Photonics, SPIE, 2003. doi:10.1117/12.457977. URL https://doi.org/10.1117/12.457977.

[135] M Bonati, Braulio Cancino, Peter Moore, et al. Skipper ccd mosaic on the soar integral field spectrograph. In *Society of Photo-Optical Instrumentation Engineers (SPIE) Conference Series*, volume this volume of *Society of Photo-Optical Instrumentation Engineers (SPIE) Conference Series*, 2024.

[136] Gustavo Cancelo, Claudio Chavez, Fernando Chierchie, Juan Estrada, Guillermo Fernandez Moroni, Eduardo Emilio Paolini, Miguel Sofo Haro, Angel Soto, Leandro Stefanazzi, Javier Tiffenberg, Ken Treptow, Neal Wilcer, and Ted Zmuda. Low Threshold Acquisition controller for Skipper CCDs. pages 86–91, 2020. doi:10.1109/CAE.2019.8709274.

[137] Gustavo I. Cancelo, Claudio Chavez, Fernando Chierchie, Juan Estrada, Guillermo Fernandez-Moroni, Eduardo E. Paolini, Miguel Sofo Haro, Angel Soto, Leandro Stefanazzi, Javier Tiffenberg, Ken Treptow, Neal Wilcer, and Ted J. Zmuda. Low threshold acquisition controller for Skipper charge-coupled devices. *Journal of Astronomical Telescopes, Instruments, and Systems*, 7(1):1 – 19, 2021. doi:10.1117/1.JATIS.7.1.015001. URL https://doi.org/10.1117/1.JATIS.7.1.015001.

[138] Liron Barak, Itay M. Bloch, Ana Botti, Mariano Cababie, Gustavo Cancelo, Luke Chaplinsky, Fernando Chierchie, Michael Crisler, Alex Drlica-Wagner, Rouven Essig, Juan Estrada, Erez Etzion, Guillermo Fernandez Moroni, Daniel Gift, Stephen E. Holland, Sravan Munagavalasa, Aviv Orly, Dario Rodrigues, Aman Singal, Miguel Sofo Haro, Leandro Stefanazzi, Javier Tiffenberg, Sho Uemura, Tomer Volansky, and Tien-Tien Yu. Sensei: Characterization of single-electron events using a skipper charge-coupled device. *Phys. Rev. Appl.*, 17:014022, Jan 2022. doi:10.1103/PhysRevApplied.17.014022. URL https://link.aps.org/doi/10.1103/PhysRevApplied.17.014022.

[139] C.J. Bebek, J.H. Emes, D.E. Groom, S. Haque, S.E. Holland, P.N. Jelinsky, A. Karcher, W.F. Kolbe, J.S. Lee, N.P. Palaio, D.J. Schlegel, G. Wang, R. Groulx, R. Frost, J. Estrada, and M. Bonati. Status of the ccd development for the dark energy spectroscopic instrument. *Journal of Instrumentation*, 12(04):C04018, apr 2017. doi:10.1088/1748-0221/12/04/C04018. URL https://dx.doi.org/10.1088/1748-0221/12/04/C04018.

[140] D. E. Groom, S. Haque, S. E. Holland, and W. F. Kolbe. Quantum efficiency modeling for a thick back-illuminated astronomical CCD. *Journal of Applied Physics*, 122(5): 055301, 08 2017. ISSN 0021-8979. doi:10.1063/1.4986506. URL https://doi.org/10.1063/1.4986506.

[141] M. Bonati, J. Estrada, A. Castaneda, and P. Hernandez. Fully automated detector testbench. In Juan C. Guzman and Jorge Ibsen, editors, *Software and Cyberinfrastructure for Astronomy VI*, volume 11452, pages 290 – 302. International Society for Optics and Photonics, SPIE, 2020. doi:10.1117/12.2559203. URL https://doi.org/10.1117/12.2559203.

[142] Edgar Marrufo Villalpando, Alex Drlica-Wagner, Marco Bonati, Abhishek Bakshi, Vanessa Bawden de Paula Macanhan, Braulio Cancino, Gregory E. Derylo, Juan Estrada, Guillermo Fernandez Moroni, Luciano Fraga, Stephen Holland, Michelle J. Jonas, Agustín Lapi, Peter Moore, Andrés A. Plazas Malagón, Leandro Stefanazzi, and Javier Tiffenberg. Design of a Skipper CCD focal plane for the SOAR Integral Field Spectrograph. In Andrew D. Holland and James Beletic, editors, *X-Ray, Optical, and Infrared Detectors for Astronomy X*, volume 12191, page 121910U. International Society for Optics and Photonics, SPIE, 2022. doi:10.1117/12.2629475. URL https://doi.org/10.1117/12.2629475.

[143] G. M. Bernstein, T. M. C. Abbott, S. Desai, D. Gruen, R. A. Gruendl, M. D. Johnson, H. Lin, F. Menanteau, E. Morganson, E. Neilsen, K. Paech, A. R. Walker, W. Wester, B. Yanny, and (DES Collaboration). Instrumental response model and detrending for the dark energy camera. *Publications of the Astronomical Society of the Pacific*, 129 (981):114502, sep 2017. doi:10.1088/1538-3873/aa858e. URL https://dx.doi.org/10.1088/1538-3873/aa858e.

[144] Dario Rodrigues, Kevin Andersson, and et al. Absolute measurement of the fano factor using a skipper-ccd. *Nuclear Instruments and Methods in Physics Research Section A: Accelerators, Spectrometers, Detectors and Associated Equipment*, 1010: 165511, 2021. ISSN 0168-9002. doi:https://doi.org/10.1016/j.nima.2021.165511. URL https://www.sciencedirect.com/science/article/pii/S0168900221004964.

[145] S. M. Tulloch and V. S. Dhillon. On the use of electron-multiplying CCDs for astronomical spectroscopy. MNRAS, 411(1):211–225, February 2011. doi:10.1111/j.1365-2966.2010.17675.x.

[146] Liron Barak, Itay M. Bloch, Mariano Cababie, Gustavo Cancelo, Luke Chaplinsky, Fernando Chierchie, Michael Crisler, Alex Drlica-Wagner, Rouven Essig, Juan Estrada, Erez Etzion, Guillermo Fernandez Moroni, Daniel Gift, Sravan Munagavalasa, Aviv Orly, Dario Rodrigues, Aman Singal, Miguel Sofo Haro, Leandro Stefanazzi, Javier Tiffenberg, Sho Uemura, Tomer Volansky, and Tien-Tien Yu. SENSEI: Direct-Detection Results on sub-GeV Dark Matter from a New Skipper-CCD. *Phys. Rev. Lett.*, 125:arXiv:2004.11378, 2020.

[147] Gillian Kyne, Erika T. Hamden, Nicole Lingner, Patrick Morrissey, Shouleh Nikzad, and D. Christopher Martin. The faint intergalactic-medium red-shifted emission balloon: future UV observations with EMCCDs. In Andrew D. Holland and James Beletic, editors, *High Energy, Optical, and Infrared Detectors for Astronomy VII*, volume 9915, page 991507. International Society for Optics and Photonics, SPIE, 2016. doi:10.1117/12.2232879. URL https://doi.org/10.1117/12.2232879.

[148] Olivier Daigle, Claude Carignan, Jean-Luc Gach, Christian Guillaume, Simon Lessard, Charles-Anthony Fortin, and Sébastien Blais-Ouellette. Extreme faint flux imaging with an emccd. *Publications of the Astronomical Society of the Pacific*, 121(882):866–884, 2009. ISSN 00046280, 15383873. URL http://www.jstor.org/stable/10.1086/605449.

[149] Olivier Daigle, Pierre-Olivier Quirion, and Simon Lessard. The darkest EMCCD ever. In Andrew D. Holland and David A. Dorn, editors, *High Energy, Optical, and Infrared Detectors for Astronomy IV*, volume 7742, page 774203. International Society for Optics and Photonics, SPIE, 2010. doi:10.1117/12.856405. URL https://doi.org/10.1117/12.856405.

[150] Ashlee N. Wilkins and et al. Characterization of a photon counting emccd for space-based high contrast imaging spectroscopy of extrasolar planets. In Andrew D. Holland and James Beletic, editors, *High Energy, Optical, and Infrared Detectors for Astronomy VI*. SPIE, July 2014. doi:10.1117/12.2055346. URL http://dx.doi.org/10.1117/12.2055346.

[151] Mark Downing, Dietrich Baade, Peter Sinclaire, Sebastian Deiries, and Fabrice Christen. CCD riddle: a) signal vs time: linear; b) signal vs variance: non-linear. In David A. Dorn and Andrew D. Holland, editors, *High Energy, Optical, and Infrared Detectors for Astronomy II*, volume 6276, page 627609. International Society for Optics and Photonics, SPIE, 2006. doi:10.1117/12.671457. URL https://doi.org/10.1117/12.671457.

[152] S E Holland, C J Bebek, W F Kolbe, and J S Lee. Physics of fully depleted ccds. *Journal of Instrumentation*, 9(03):C03057, mar 2014. doi:10.1088/1748-0221/9/03/C03057. URL https://dx.doi.org/10.1088/1748-0221/9/03/C03057.

[153] D. Gruen, G. M. Bernstein, M. Jarvis, B. Rowe, V. Vikram, A. A. Plazas, and S. Seitz. Characterization and correction of charge-induced pixel shifts in DECam. *Journal of Instrumentation*, 10(5):C05032, May 2015. doi:10.1088/1748-0221/10/05/C05032.

[154] C. Lage, A. Bradshaw, and J. A. Tyson. Measurements and simulations of the brighter-fatter effect in CCD sensors. *Journal of Instrumentation*, 12(3):C03091, March 2017. doi:10.1088/1748-0221/12/03/C03091.

[155] Pierre Astier and Nicolas Regnault. Correction of the brighter-fatter effect on the CCDs of hyper suprime-cam. *Astronomy & Astrophysics*, 670:A118, feb 2023. doi:10.1051/0004-6361/202245407. URL https://doi.org/10.1051%2F0004-6361%2F202245407.

[156] Satoshi Miyazaki, Yutaka Komiyama, and et al. Hyper Suprime-Cam: System design and verification of image quality. *Publications of the Astronomical Society of Japan*, 70(SP1):S1, 09 2017. ISSN 0004-6264. doi:10.1093/pasj/psx063. URL https://doi.org/10.1093/pasj/psx063.

[157] H.M. Schmid. Astronomical Imaging and Spectroscopy with CCD detectors. In *Astronomical Imaging and Spectroscopy with CCD detectors*. ETH Zurich, Institute for Particle Physics and Astrophysics, 2012. URL https://ethz.ch/content/dam/ethz/special-interest/phys/particle-physics/quanz-group-dam/documents-old-s-and-p/Courses/vp-asl-astro/CCDobservations.pdf.

[158] James Bosch, Yusra AlSayyad, and et al. An overview of the lsst image processing pipelines, 2018.

[159] David Lawrence, Paul O'Connor, James Frank, and Peter Takacs. Model-independent characterization of charge diffusion in thick fully depleted ccds. *Publications of the Astronomical Society of the Pacific*, 123(907):1100, aug 2011. doi:10.1086/661948. URL https://dx.doi.org/10.1086/661948.

[160] Carlos Blanco, Yonatan Kahn, Benjamin Lillard, and Samuel D. McDermott. Dark matter daily modulation with anisotropic organic crystals. *Phys. Rev. D*, 104:036011, Aug 2021. doi:10.1103/PhysRevD.104.036011. URL https://link.aps.org/doi/10.1103/PhysRevD.104.036011.

[161] Tiffany M. Borders, Peter R. McCullough, and Sylvia M. Baggett. Wfc3 tv3 testing: Quantum yield of the uvis ccds. 2010. URL https://api.semanticscholar.org/CorpusID:10355073.

[162] K. Ramanathan and N. Kurinsky. Ionization yield in silicon for ev-scale electron-recoil processes. *Phys. Rev. D*, 102:063026, Sep 2020. doi:10.1103/PhysRevD.102.063026. URL https://link.aps.org/doi/10.1103/PhysRevD.102.063026.

[163] S. M. Baggett, J. W. MacKenty, R. A. Kimble, T. Borders, B. Hilbert, S. Deustua, V. Kozhurina-Platais, K. S. Long, A. Riess, R. Gilliland, R. J. Hill, and J. Kalirai. WFC3 detectors: on-orbit performance. In Jacobus M. Oschmann Jr., Mark C. Clampin, and Howard A. MacEwen, editors, *Space Telescopes and Instrumentation 2010: Optical, Infrared, and Millimeter Wave*, volume 7731, page 773138. International Society for Optics and Photonics, SPIE, 2010. doi:10.1117/12.857642. URL https://doi.org/10.1117/12.857642.

[164] Edgar Marrufo Villalpando, Alex Drlica-Wagner, Andrés A. Plazas Malagón, Abhishek Bakshi, Marco Bonati, Julia Campa, Braulio Cancino, Claudio R. Chavez, Juan Estrada, Guillermo Fernandez Moroni, Luciano Fraga, Manuel E. Gaido, Stephen Holland, Rachel Hur, Michelle Jonas, Peter Moore, and Javier Tiffenberg. Characterization and optimization of skipper ccds for the soar integral field spectrograph. *Publications of the Astronomical Society of the Pacific*, 136(4):045001, 2024. doi:10.1088/1538-3873/ad2865. URL https://dx.doi.org/10.1088/1538-3873/ad2865.

[165] López, S., D'Odorico, V., Ellison, S. L., Becker, G. D., Christensen, L., Cupani, G., Denney, K. D., Pâris, I., Worseck, G., Berg, T. A. M., Cristiani, S., Dessauges-Zavadsky, M., Haehnelt, M., Hamann, F., Hennawi, J., Iršič, V., Kim, T.-S., López, P., Lund Saust, R., Ménard, B., Perrotta, S., Prochaska, J. X., Sánchez-Ramírez, R., Vestergaard, M., Viel, M., and Wisotzki, L. XQ-100: A legacy survey of one hundred $3.5 \lesssim z \lesssim 4.5$ quasars observed with VLT/X-shooter. *A&A*, 594:A91, 2016. doi:10.1051/0004-6361/201628161. URL https://doi.org/10.1051/0004-6361/201628161.

[166] DESI Collaboration. The Early Data Release of the Dark Energy Spectroscopic Instrument. *submitted to AJ*, art. arXiv:2306.06308, 2023. doi:10.48550/arXiv.2306.06308.

[167] David J. Schlegel, Simone Ferraro, and et al. A spectroscopic road map for cosmic frontier: Desi, desi-ii, stage-5, 2022.

[168] R. D. Peccei and Helen R. Quinn. Constraints imposed by CP conservation in the presence of pseudoparticles. *Phys. Rev. D*, 16:1791–1797, 1977. doi:10.1103/PhysRevD.16.1791. URL https://link.aps.org/doi/10.1103/PhysRevD.16.1791.

[169] N. Huang, L. E. Bleem, and et al. Galaxy Clusters Selected via the Sunyaev–Zel'dovich Effect in the SPTpol 100-square-degree Survey. *AJ*, 159(3):110, 2020. doi:10.3847/1538-3881/ab6a96. URL https://dx.doi.org/10.3847/1538-3881/ab6a96.

[170] T. Wang et al. Discovery of a galaxy cluster with a violently starbursting core at $z = 2.506$. *Astrophys. J.*, 828(1):56, 2016. doi:10.3847/0004-637X/828/1/56.

[171] M. B. Bayliss et al. SPT-CL J2040-4451: An SZ-selected galaxy cluster at $z = 1.478$ with significant ongoing star formation. *Astrophys. J.*, 794(1):12, 2014. doi:10.1088/0004-637X/794/1/12.

[172] E. O. Nadler, A. Drlica-Wagner, and et al. Constraints on dark matter properties from observations of milky way satellite galaxies. *Phys. Rev. Lett.*, 126:091101, Mar 2021. doi:10.1103/PhysRevLett.126.091101. URL https://link.aps.org/doi/10.1103/PhysRevLett.126.091101.

[173] Khyati Malhan, Monica Valluri, and Katherine Freese. Probing the nature of dark matter with accreted globular cluster streams. *Monthly Notices of the Royal Astronomical Society*, 501(1):179–200, 11 2020. ISSN 0035-8711. doi:10.1093/mnras/staa3597. URL https://doi.org/10.1093/mnras/staa3597.

[174] Xiaowei Ou, Anirudh Chiti, Nora Shipp, Joshua D. Simon, Marla Geha, Anna Frebel, Mohammad K. Mardini, Denis Erkal, and Lina Necib. Signatures of tidal disruption of the hercules ultra-faint dwarf galaxy, 2024. URL https://arxiv.org/abs/2403.00921.

[175] Jorge Sánchez Almeida, Ignacio Trujillo, and Angel R. Plastino. The stellar distribution in ultrafaint dwarf galaxies suggests deviations from the collisionless cold dark matter paradigm. *The Astrophysical Journal Letters*, 973(1):L15, sep 2024. doi:10.3847/2041-8213/ad66bc. URL https://dx.doi.org/10.3847/2041-8213/ad66bc.

[176] Erminia Calabrese and David N. Spergel. Ultra-light dark matter in ultra-faint dwarf galaxies. *Monthly Notices of the Royal Astronomical Society*, 460(4):4397–4402, 05 2016. ISSN 0035-8711. doi:10.1093/mnras/stw1256. URL https://doi.org/10.1093/mnras/stw1256.

[177] Neal Dalal and Andrey Kravtsov. Excluding fuzzy dark matter with sizes and stellar kinematics of ultrafaint dwarf galaxies. *Phys. Rev. D*, 106:063517, Sep 2022. doi:10.1103/PhysRevD.106.063517. URL https://link.aps.org/doi/10.1103/PhysRevD.106.063517.

[178] Ivan Esteban, Annika H. G. Peter, and Stacy Y. Kim. Milky way satellite velocities reveal the dark matter power spectrum at small scales, 2024. URL https://arxiv.org/abs/2306.04674.

[179] Anirudh Chiti, Anna Frebel, Joshua D. Simon, Denis Erkal, Laura J. Chang, Lina Necib, Alexander P. Ji, Helmut Jerjen, Dongwon Kim, and John E. Norris. An extended halo around an ancient dwarf galaxy. *Nature Astronomy*, 5(4):392–400, April 2021. ISSN 2397-3366. doi:10.1038/s41550-020-01285-w. URL https://doi.org/10.1038/s41550-020-01285-w.

[180] Andrew B. Pace, Denis Erkal, and Ting S. Li. Proper motions, orbits, and tidal influences of milky way dwarf spheroidal galaxies. *The Astrophysical Journal*, 940(2):136, nov 2022. doi:10.3847/1538-4357/ac997b. URL https://dx.doi.org/10.3847/1538-4357/ac997b.

[181] Elisa A. Tau, A. Katherina Vivas, and Clara E. Martínez-Vázquez. Extended stellar populations in ultrafaint dwarf galaxies. *The Astronomical Journal*, 167(2):57, jan 2024. doi:10.3847/1538-3881/ad1509. URL https://dx.doi.org/10.3847/1538-3881/ad1509.

[182] Alis Deason, Andrew Wetzel, and Shea Garrison-Kimmel. Satellite dwarf galaxies in a hierarchical universe: The prevalence of dwarf–dwarf major mergers. *The Astrophysical Journal*, 794(2):115, sep 2014. doi:10.1088/0004-637X/794/2/115. URL https://dx.doi.org/10.1088/0004-637X/794/2/115.

[183] Coral Wheeler, Philip F Hopkins, Andrew B Pace, Shea Garrison-Kimmel, Michael Boylan-Kolchin, Andrew Wetzel, James S Bullock, Dušan Kereš, Claude-André Faucher-Giguère, and Eliot Quataert. Be it therefore resolved: cosmological simulations of dwarf galaxies with 30 solar mass resolution. *Monthly Notices of the Royal Astronomical Society*, 490(3):4447–4463, 2019. ISSN 0035-8711. doi:10.1093/mnras/stz2887. URL https://doi.org/10.1093/mnras/stz2887.

[184] Anirudh Chiti, Anna Frebel, Alexander P. Ji, Mohammad K. Mardini, Xiaowei Ou, Joshua D. Simon, Helmut Jerjen, Dongwon Kim, and John E. Norris. Detailed chemical abundances of stars in the outskirts of the tucana ii ultrafaint dwarf galaxy. *The Astronomical Journal*, 165(2):55, jan 2023. doi:10.3847/1538-3881/aca416. URL https://dx.doi.org/10.3847/1538-3881/aca416.

[185] Sebastián A. Villar, Sebastián Torcida, and Gerardo G. Acosta. Median filtering: A new insight. *J. Math. Imaging Vis.*, 58(1):130–146, May 2017. ISSN 0924-9907. doi:10.1007/s10851-016-0694-0. URL https://doi.org/10.1007/s10851-016-0694-0.

[186] Andrés A. Plazas Malagón, Chris Waters, Alex Broughton, Eli Rykoff, Agnès Ferté, Merlin Fisher-Levine, and Robert Lupton. Instrument signature removal and calibration products for the rubin legacy survey of space and time, 2024. URL https://arxiv.org/abs/2404.14516.

[187] Liming Jiang, Bo Dai, Wayne Wu, and Chen Change Loy. Focal frequency loss for image reconstruction and synthesis, 2021. URL https://arxiv.org/abs/2012.12821.

[188] Bilel Benjdira, Anas M. Ali, and Anis Koubaa. Guided frequency loss for image restoration, 2023. URL https://arxiv.org/abs/2309.15563.

[189] Duvvuri Kavya, Kunisetty Jaswanth, Savarala Chethana, P. Shruti, and Jayan Sarada. Comparative analysis of image denoising using different filters. In Deepak Gupta, Ashish Khanna, Siddhartha Bhattacharyya, Aboul Ella Hassanien, Sameer Anand, and Ajay Jaiswal, editors, *International Conference on Innovative Computing and Communications*, pages 271–284, Singapore, 2023. Springer Nature Singapore. ISBN 978-981-19-2535-1.

[190] G. Pagnini and R. K. Saxena. A note on the voigt profile function, 2008. URL https://arxiv.org/abs/0805.2274.

[191] Eikonal Optics. Spectrometer wavelength calibration: Theory. 2024. URL https://eikonaloptics.com/blogs/tutorials/spectrometer-wavelength-calibration-theory. Accessed: 10, 20, 2024.

[192] Warren R. Brown, Margaret J. Geller, Scott J. Kenyon, and Antonaldo Diaferio. Velocity dispersion profile of the milky way halo. *The Astronomical Journal*, 139(1):59, nov 2009. doi:10.1088/0004-6256/139/1/59. URL https://dx.doi.org/10.1088/0004-6256/139/1/59.

[193] K Youakim, E Starkenburg, N F Martin, G Matijevič, D S Aguado, C Allende Prieto, A Arentsen, P Bonifacio, R G Carlberg, J I González Hernández, V Hill, G Kordopatis, C Lardo, J F Navarro, P Jablonka, R Sánchez Janssen, F Sestito, G F Thomas, and K Venn. The pristine survey – viii. the metallicity distribution function of the milky way

halo down to the extremely metal-poor regime. *Monthly Notices of the Royal Astronomical Society*, 492(4):4986–5002, 01 2020. ISSN 0035-8711. doi:10.1093/mnras/stz3619. URL https://doi.org/10.1093/mnras/stz3619.

[194] S. Salvadori, A. Ferrara, R. Schneider, E. Scannapieco, and D. Kawata. Mining the galactic halo for very metal-poor stars. *Monthly Notices of the Royal Astronomical Society: Letters*, 401(1):L5–L9, 01 2010. ISSN 1745-3925. doi:10.1111/j.1745-3933.2009.00772.x. URL https://doi.org/10.1111/j.1745-3933.2009.00772.x.

[195] Andrew Sheinis, Samuel C. Barden, Jennifer Sobeck, and the MSE Team. The maunakea spectroscopic explorer: Thousands of fibers, infinite possibilities. *Astronomische Nachrichten*, 344(8-9):e20230108, 2023. doi:https://doi.org/10.1002/asna.20230108. URL https://onlinelibrary.wiley.com/doi/abs/10.1002/asna.20230108.

[196] The MSE Science Team, Carine Babusiaux, Maria Bergemann, and et al. The detailed science case for the maunakea spectroscopic explorer, 2019 edition, 2019. URL https://arxiv.org/abs/1904.04907.

[197] Sukanya Chakrabarti, Alex Drlica-Wagner, Ting S. Li, Neelima Sehgal, Joshua D. Simon, Simon Birrer, Duncan A. Brown, Rebecca Bernstein, Alberto D. Bolatto, Philip Chang, Kyle Dawson, Paul Demorest, Daniel Grin, David L. Kaplan, Joseph Lazio, Jennifer Marshall, Eric J. Murphy, Scott Ransom, Brant E. Robertson, Rajeev Singh, Anže Slosar, Tommaso Treu, Yu-Dai Tsai, and Benjamin F. Williams. Snowmass2021 cosmic frontier white paper: Observational facilities to study dark matter, 2022. URL https://arxiv.org/abs/2203.06200.

[198] Juan Guerra, Marla Geha, and Louis E. Strigari. Forecasts on the dark matter density profiles of dwarf spheroidal galaxies with current and future kinematic observations. *The Astrophysical Journal*, 943(2):121, feb 2023. doi:10.3847/1538-4357/aca8a5. URL https://dx.doi.org/10.3847/1538-4357/aca8a5.

[199] Ana M. Botti, Brenda A. Cervantes-Vergara, Claudio R. Chavez, Fernando Chierchie, Alex Drlica-Wagner, Juan Estrada, Guillermo Fernandez Moroni, Stephen E. Holland, Blas Junior Irigoyen Gimenez, Agustin J. Lapi, Edgar Marrufo Villalpando, Miguel Sofo Haro, Javier Tiffenberg, and Sho Uemura. Single-quantum measurement with a multiple-amplifier sensing charge-coupled device. *IEEE Transactions on Electron Devices*, 71(6):3732–3738, 2024. doi:10.1109/TED.2024.3392711.

[200] Agustin J. Lapi, Blas J. Irigoyen Gimenez, Miqueas E. Gamero, Claudio R. Chavez Blanco, Fernando Chierchie, Guillermo Fernandez-Moroni, Stephen Holland, Ana M. Botti, Brenda A. Cervantes-Vergara, Javier Tiffenberg, and Juan Estrada. Sixteen multiple-amplifier sensing charge-coupled devices and characterization techniques targeting the next generation of astronomical instruments, 2024. URL https://arxiv.org/abs/2405.19505.

[201] Kenneth W. Lin, Armin Karcher, Julien Guy, Stephen E. Holland, William F. Kolbe, Peter E. Nugent, Alex Drlica-Wagner, Ana M. Botti, and Javier Tiffenberg. Multi-amplifier sensing charge-coupled devices for next generation spectroscopy. *Publications of the Astronomical Society of the Pacific*, 136(9):095002, sep 2024. doi:10.1088/1538-3873/ad716c. URL https://dx.doi.org/10.1088/1538-3873/ad716c.

[202] Alan Dressler, Bruce Bigelow, Tyson Hare, Brian Sutin, Ian Thompson, Greg Burley, Harland Epps, Augustus Oemler, Alan Bagish, Christoph Birk, Ken Clardy, Steve Gunnels, Daniel Kelson, Stephen Shectman, and David Osip. Imacs: The inamori-magellan areal camera and spectrograph on magellan-baade. *Publications of the Astronomical Society of the Pacific*, 123(901):288, feb 2011. doi:10.1086/658908. URL https://dx.doi.org/10.1086/658908.

[203] M. E. Heiger, T. S. Li, A. B. Pace, J. D. Simon, A. P. Ji, A. Chiti, C. R. Bom, J. A. Carballo-Bello, J. L. Carlin, W. Cerny, Y. Choi, A. Drlica-Wagner, D. J. James, C. E. Martínez-Vázquez, G. E. Medina, B. Mutlu-Pakdil, M. Navabi, N. E. D. Noël, J. D. Sakowska, G. S. Stringfellow, and (DELVE Collaboration). Reading between the (spectral) lines: Magellan/imacs spectroscopy of the ultrafaint dwarf galaxies eridanus iv and centaurus i. *The Astrophysical Journal*, 961(2):234, jan 2024. doi:10.3847/1538-4357/ad0cf7. URL https://dx.doi.org/10.3847/1538-4357/ad0cf7.

[204] Itay M. Bloch, Ana M. Botti, and et al. Sensei at snolab: Single-electron event rate and implications for dark matter, 2024. URL https://arxiv.org/abs/2410.18716.

[205] Denis Erkal and Vasily Belokurov. Properties of dark subhaloes from gaps in tidal streams. *Monthly Notices of the Royal Astronomical Society*, 454(4):3542–3558, 10 2015. ISSN 0035-8711. doi:10.1093/mnras/stv2122. URL https://doi.org/10.1093/mnras/stv2122.

[206] Uddipan Banik and Frank C van den Bosch. A fully general, non-perturbative treatment of impulsive heating. *Monthly Notices of the Royal Astronomical Society*, 502(1):1441–1455, 01 2021. ISSN 0035-8711. doi:10.1093/mnras/stab092. URL https://doi.org/10.1093/mnras/stab092.

[207] Mücket, J. P. and Hoeft, M. Density profile asymptotes at the centre of dark matter halos. *AA*, 404(3):809–814, 2003. doi:10.1051/0004-6361:20030549. URL https://doi.org/10.1051/0004-6361:20030549.

[208] Catherine E Fielder, Yao-Yuan Mao, Andrew R Zentner, Jeffrey A Newman, Hao-Yi Wu, and Risa H Wechsler. Illuminating dark matter halo density profiles without subhaloes. *Monthly Notices of the Royal Astronomical Society*, 499(2):2426–2444, 09 2020. ISSN 0035-8711. doi:10.1093/mnras/staa2851. URL https://doi.org/10.1093/mnras/staa2851.

[209] Raul E Angulo and Oliver Hahn. Large-scale dark matter simulations. *Living Reviews in Computational Astrophysics*, 8(1):1, February 2022.

[210] H. C. Plummer. On the Problem of Distribution in Globular Star Clusters: (Plate 8.). *Monthly Notices of the Royal Astronomical Society*, 71(5):460–470, 03 1911. ISSN 0035-8711. doi:10.1093/mnras/71.5.460. URL https://doi.org/10.1093/mnras/71.5.460.

[211] Julio F. Navarro, Carlos S. Frenk, and Simon D. M. White. A universal density profile from hierarchical clustering. *The Astrophysical Journal*, 490(2):493, dec 1997. doi:10.1086/304888. URL https://dx.doi.org/10.1086/304888.

[212] Risa H. Wechsler, James S. Bullock, Joel R. Primack, Andrey V. Kravtsov, and Avishai Dekel. Concentrations of dark halos from their assembly histories. *The Astrophysical Journal*, 568(1):52, mar 2002. doi:10.1086/338765. URL https://dx.doi.org/10.1086/338765.

[213] J. C. Muñoz-Cuartas, A. V. Macciò, S. Gottlöber, and A. A. Dutton. The redshift evolution of Λ cold dark matter halo parameters: concentration, spin and shape. *Monthly Notices of the Royal Astronomical Society*, 411(1):584–594, 01 2011. ISSN 0035-8711. doi:10.1111/j.1365-2966.2010.17704.x. URL https://doi.org/10.1111/j.1365-2966.2010.17704.x.

[214] Francisco Prada, Anatoly A. Klypin, Antonio J. Cuesta, Juan E. Betancort-Rijo, and Joel Primack. Halo concentrations in the standard Λ cold dark matter cosmology. *Monthly Notices of the Royal Astronomical Society*, 423(4):3018–3030, 07 2012. ISSN 0035-8711. doi:10.1111/j.1365-2966.2012.21007.x. URL https://doi.org/10.1111/j.1365-2966.2012.21007.x.

[215] Aaron A. Dutton and Andrea V. Macciò. Cold dark matter haloes in the Planck era: evolution of structural parameters for Einasto and NFW profiles. *Monthly Notices of the Royal Astronomical Society*, 441(4):3359–3374, 05 2014. ISSN 0035-8711. doi:10.1093/mnras/stu742. URL https://doi.org/10.1093/mnras/stu742.

[216] C. J. Grillmair. Detection of a 60°-long dwarf galaxy debris stream. *The Astrophysical Journal*, 645(1):L37, jun 2006. doi:10.1086/505863. URL https://dx.doi.org/10.1086/505863.

[217] V. Springel, J. Wang, M. Vogelsberger, A. Ludlow, A. Jenkins, A. Helmi, J. F. Navarro, C. S. Frenk, and S. D. M. White. The Aquarius Project: the subhaloes of galactic haloes. *Monthly Notices of the Royal Astronomical Society*, 391(4):1685–1711, 12 2008. ISSN 0035-8711. doi:10.1111/j.1365-2966.2008.14066.x. URL https://doi.org/10.1111/j.1365-2966.2008.14066.x.

[218] Katelin Schutz. Subhalo mass function and ultralight bosonic dark matter. *Phys. Rev. D*, 101:123026, Jun 2020. doi:10.1103/PhysRevD.101.123026. URL https://link.aps.org/doi/10.1103/PhysRevD.101.123026.

[219] J Wang, S Bose, C S Frenk, L Gao, A Jenkins, V Springel, and S D M White. Universal structure of dark matter haloes over a mass range of 20 orders of magnitude. *Nature*, 585(7823):39–42, September 2020.

[220] Anne M. Green, Stefan Hofmann, and Dominik J. Schwarz. The power spectrum of SUSY-CDM on subgalactic scales. *Monthly Notices of the Royal Astronomical Society*, 353(3):L23–L27, 09 2004. ISSN 0035-8711. doi:10.1111/j.1365-2966.2004.08232.x. URL https://doi.org/10.1111/j.1365-2966.2004.08232.x.

[221] Daniel Gilman, Simon Birrer, Anna Nierenberg, Tommaso Treu, Xiaolong Du, and Andrew Benson. Warm dark matter chills out: constraints on the halo mass function and the free-streaming length of dark matter with eight quadruple-image strong gravitational lenses. *Monthly Notices of the Royal Astronomical Society*, 491(4): 6077–6101, 12 2019. ISSN 0035-8711. doi:10.1093/mnras/stz3480. URL https://doi.org/10.1093/mnras/stz3480.

[222] N. Shipp, A. Drlica-Wagner, E. Balbinot, et al., and (The DES Collaboration). Stellar streams discovered in the dark energy survey. *The Astrophysical Journal*, 862(2):114, jul 2018. doi:10.3847/1538-4357/aacdab. URL https://dx.doi.org/10.3847/1538-4357/aacdab.

[223] Gaia Collaboration. The gaia mission. *å*, 595:A1, 2016. doi:10.1051/0004-6361/201629272. URL https://doi.org/10.1051/0004-6361/201629272.

[224] Ana Bonaca and Adrian M. Price-Whelan. Stellar streams in the gaia era, 2024. URL https://arxiv.org/abs/2405.19410.

[225] Jaswant K. Yadav, J. S. Bagla, and Nishikanta Khandai. Fractal dimension as a measure of the scale of homogeneity: The scale of homogeneity. *Monthly Notices of the Royal Astronomical Society*, pages no–no, April 2010. ISSN 1365-2966. doi:10.1111/j.1365-2966.2010.16612.x. URL http://dx.doi.org/10.1111/j.1365-2966.2010.16612.x.

[226] Erik Holmberg. On the Clustering Tendencies among the Nebulae. ApJ, 92:200, September 1940. doi:10.1086/144212.

[227] Xiangwei Zhang, Bingqiu Chen, Pinjian Chen, Jiarui Sun, and Zhijia Tian. The rotation curve and mass distribution of M31. *Monthly Notices of the Royal Astronomical Society*, 528(2):2653–2666, 01 2024. ISSN 0035-8711. doi:10.1093/mnras/stae025. URL https://doi.org/10.1093/mnras/stae025.

[228] R. K. Sachs and A. M. Wolfe. Perturbations of a Cosmological Model and Angular Variations of the Microwave Background. ApJ, 147:73, January 1967. doi:10.1086/148982.

[229] Wayne Hu and Scott Dodelson. Cosmic microwave background anisotropies. *Annual Review of Astronomy and Astrophysics*, 40(Volume 40, 2002):171–216, 2002. ISSN 1545-4282. doi:https://doi.org/10.1146/annurev.astro.40.060401.093926. URL https:

//www.annualreviews.org/content/journals/10.1146/annurev.astro.40.060401.093926.

[230] Particle Data Group, P A Zyla, R M Barnett, J Beringer, and et al. Review of Particle Physics. *Progress of Theoretical and Experimental Physics*, 2020(8):083C01, 08 2020. ISSN 2050-3911. doi:10.1093/ptep/ptaa104. URL https://doi.org/10.1093/ptep/ptaa104.

[231] S. Basak, A. Ganguly, K. Haris, S. Kapadia, A. K. Mehta, and P. Ajith. Constraints on compact dark matter from gravitational wave microlensing. *The Astrophysical Journal Letters*, 926(2):L28, feb 2022. doi:10.3847/2041-8213/ac4dfa. URL https://dx.doi.org/10.3847/2041-8213/ac4dfa.

[232] Scott Tremaine and James E. Gunn. Dynamical role of light neutral leptons in cosmology. *Phys. Rev. Lett.*, 42:407–410, Feb 1979. doi:10.1103/PhysRevLett.42.407. URL https://link.aps.org/doi/10.1103/PhysRevLett.42.407.

[233] C. Firmani, E. D'Onghia, V. Avila-Reese, G. Chincarini, and X. Hernández. Evidence of self-interacting cold dark matter from galactic to galaxy cluster scales. *Monthly Notices of the Royal Astronomical Society*, 315(3):L29–L32, 07 2000. ISSN 0035-8711. doi:10.1046/j.1365-8711.2000.03555.x. URL https://doi.org/10.1046/j.1365-8711.2000.03555.x.

[234] Mark Vogelsberger, Amina Helmi, Volker Springel, Simon D. M. White, Jie Wang, Carlos S. Frenk, Adrian Jenkins, Aaron Ludlow, and Julio F. Navarro. Phase-space structure in the local dark matter distribution and its signature in direct detection experiments. *Monthly Notices of the Royal Astronomical Society*, 395(2):797–811, 04 2009. ISSN 0035-8711. doi:10.1111/j.1365-2966.2009.14630.x. URL https://doi.org/10.1111/j.1365-2966.2009.14630.x.

[235] Miguel Rocha, Annika H. G. Peter, James S. Bullock, Manoj Kaplinghat, Shea Garrison-Kimmel, Jose Oñorbe, and Leonidas A. Moustakas. Cosmological simulations with self-interacting dark matter – I. Constant-density cores and substructure. *Monthly Notices of the Royal Astronomical Society*, 430(1):81–104, 01 2013. ISSN 0035-8711. doi:10.1093/mnras/sts514. URL https://doi.org/10.1093/mnras/sts514.

[236] Yonit Hochberg, Eric Kuflik, Tomer Volansky, and Jay G. Wacker. Mechanism for thermal relic dark matter of strongly interacting massive particles. *Phys. Rev. Lett.*, 113:171301, Oct 2014. doi:10.1103/PhysRevLett.113.171301. URL https://link.aps.org/doi/10.1103/PhysRevLett.113.171301.

[237] Mattias Blennow, Stefan Clementz, and Juan Herrero-Garcia. Self-interacting inelastic dark matter: a viable solution to the small scale structure problems. *Journal of Cosmology and Astroparticle Physics*, 2017(03):048, mar 2017. doi:10.1088/1475-7516/2017/03/048. URL https://dx.doi.org/10.1088/1475-7516/2017/03/048.

[238] Felix Kahlhoefer, Kai Schmidt-Hoberg, Mads T. Frandsen, and Subir Sarkar. Colliding clusters and dark matter self-interactions. *Monthly Notices of the Royal Astronomical Society*, 437(3):2865–2881, 11 2013. ISSN 0035-8711. doi:10.1093/mnras/stt2097. URL https://doi.org/10.1093/mnras/stt2097.

[239] Ran Huo, Manoj Kaplinghat, Zhen Pan, and Hai-Bo Yu. Signatures of self-interacting dark matter in the matter power spectrum and the cmb. *Physics Letters B*, 783:76–81, 2018. ISSN 0370-2693. doi:https://doi.org/10.1016/j.physletb.2018.06.024. URL https://www.sciencedirect.com/science/article/pii/S0370269318304726.

[240] Francis-Yan Cyr-Racine and Kris Sigurdson. Cosmology of atomic dark matter. *Phys. Rev. D*, 87:103515, May 2013. doi:10.1103/PhysRevD.87.103515. URL https://link.aps.org/doi/10.1103/PhysRevD.87.103515.

[241] Francis-Yan Cyr-Racine, Roland de Putter, Alvise Raccanelli, and Kris Sigurdson. Constraints on large-scale dark acoustic oscillations from cosmology. *Phys. Rev. D*, 89:063517, Mar 2014. doi:10.1103/PhysRevD.89.063517. URL https://link.aps.org/doi/10.1103/PhysRevD.89.063517.

[242] Laura G. van den Aarssen, Torsten Bringmann, and Christoph Pfrommer. Is dark matter with long-range interactions a solution to all small-scale problems of Λ cold dark matter cosmology? *Phys. Rev. Lett.*, 109:231301, Dec 2012. doi:10.1103/PhysRevLett.109.231301. URL https://link.aps.org/doi/10.1103/PhysRevLett.109.231301.

[243] Alan H. Guth, Mark P. Hertzberg, and C. Prescod-Weinstein. Do dark matter axions form a condensate with long-range correlation? *Phys. Rev. D*, 92:103513, Nov 2015. doi:10.1103/PhysRevD.92.103513. URL https://link.aps.org/doi/10.1103/PhysRevD.92.103513.

[244] Yashar Hezaveh, Neal Dalal, Gilbert Holder, Theodore Kisner, Michael Kuhlen, and Laurence Perreault Levasseur. Measuring the power spectrum of dark matter substructure using strong gravitational lensing. *Journal of Cosmology and Astroparticle Physics*, 2016(11):048, nov 2016. doi:10.1088/1475-7516/2016/11/048. URL https://dx.doi.org/10.1088/1475-7516/2016/11/048.

[245] Ana Diaz Rivero, Francis-Yan Cyr-Racine, and Cora Dvorkin. Power spectrum of dark matter substructure in strong gravitational lenses. *Phys. Rev. D*, 97:023001, Jan 2018. doi:10.1103/PhysRevD.97.023001. URL https://link.aps.org/doi/10.1103/PhysRevD.97.023001.

[246] D Bayer, S Chatterjee, L V E Koopmans, S Vegetti, J P McKean, T Treu, C D Fassnacht, and K Glazebrook. Probing sub-galactic mass structure with the power spectrum of surface-brightness anomalies in high-resolution observations of galaxy–galaxy strong gravitational lenses. II. Observational constraints on the subgalactic matter power spectrum. *Monthly Notices of the Royal Astronomical Society*, 523(1):

1310–1325, 05 2023. ISSN 0035-8711. doi:10.1093/mnras/stad1402. URL https://doi.org/10.1093/mnras/stad1402.

[247] Risa H. Wechsler and Jeremy L. Tinker. The connection between galaxies and their dark matter halos. *Annual Review of Astronomy and Astrophysics*, 56(1):435–487, 2018. doi:10.1146/annurev-astro-081817-051756. URL https://doi.org/10.1146/annurev-astro-081817-051756.

[248] Francis-Yan Cyr-Racine, Charles R. Keeton, and Leonidas A. Moustakas. Beyond subhalos: Probing the collective effect of the universe's small-scale structure with gravitational lensing. *Phys. Rev. D*, 100:023013, Jul 2019. doi:10.1103/PhysRevD.100.023013. URL https://link.aps.org/doi/10.1103/PhysRevD.100.023013.

[249] H. Abdallah, R. Adam, F. Aharonian, and et al. Search for dark matter signals towards a selection of recently detected des dwarf galaxy satellites of the milky way with h.e.s.s. *Phys. Rev. D*, 102:062001, Sep 2020. doi:10.1103/PhysRevD.102.062001. URL https://link.aps.org/doi/10.1103/PhysRevD.102.062001.

[250] Roni Harnik, Joachim Kopp, and Pedro A. N. Machado. Exploring nu Signals in Dark Matter Detectors. *JCAP*, 1207:026, 2012. doi:10.1088/1475-7516/2012/07/026.

[251] A. Aguilar-Arevalo et al. Results of the engineering run of the Coherent Neutrino Nucleus Interaction Experiment (CONNIE). *JINST*, 11(07):P07024, 2016. doi:10.1088/1748-0221/11/07/P07024.

[252] N. Abgrall et al. New limits on Bosonic Dark Matter, Solar Axions, Pauli Exclusion Principle Violation, and Electron Decay from the Majorana Demonstrator. *Phys. Rev. Lett.*, 118(16):161801, 2017. doi:10.1103/PhysRevLett.118.161801.

[253] E. Armengaud et al. Measurement of the cosmogenic activation of germanium detectors in EDELWEISS-III. *Astropart. Phys.*, 91:51–64, 2017. doi:10.1016/j.astropartphys.2017.03.006.

[254] R. Agnese et al. Projected Sensitivity of the SuperCDMS SNOLAB experiment. *Phys. Rev.*, D95(8):082002, 2017. doi:10.1103/PhysRevD.95.082002.

[255] A. Aguilar-Arevalo et al. Measurement of radioactive contamination in the high-resistivity silicon CCDs of the DAMIC experiment. *JINST*, 10(08):P08014, 2016. doi:10.1088/1748-0221/10/08/P08014.

[256] G. Angloher et al. Results on light dark matter particles with a low-threshold CRESST-II detector. *Eur. Phys. J.*, C76(1):25, 2016. doi:10.1140/epjc/s10052-016-3877-3.

[257] Chris Kouvaris and Josef Pradler. Probing sub-GeV Dark Matter with conventional detectors. *Phys. Rev. Lett.*, 118(3):031803, 2017. doi:10.1103/PhysRevLett.118.031803.

[258] Rouven Essig, Tomer Volansky, and Tien-Tien Yu. New Constraints and Prospects for sub-GeV Dark Matter Scattering off Electrons in Xenon. 2017.

[259] Rouven Essig, Aaron Manalaysay, Jeremy Mardon, Peter Sorensen, and Tomer Volansky. First Direct Detection Limits on sub-GeV Dark Matter from XENON10. *Phys. Rev. Lett.*, 109:021301, 2012. doi:10.1103/PhysRevLett.109.021301.

[260] Rouven Essig, Jeremy Mardon, and Tomer Volansky. Direct Detection of Sub-GeV Dark Matter. *Phys. Rev.*, D85:076007, 2012. doi:10.1103/PhysRevD.85.076007.

[261] Teresa Marrodán Undagoitia and Ludwig Rauch. Dark matter direct-detection experiments. *J. Phys.*, G43(1):013001, 2016. doi:10.1088/0954-3899/43/1/013001.

[262] Yonit Hochberg, Tongyan Lin, and Kathryn M. Zurek. Absorption of light dark matter in semiconductors. *Phys. Rev.*, D95(2):023013, 2017. doi:10.1103/PhysRevD.95.023013.

[263] Itay M. Bloch, Rouven Essig, Kohsaku Tobioka, Tomer Volansky, and Tien-Tien Yu. Searching for Dark Absorption with Direct Detection Experiments. 2016.

[264] Rouven Essig, Marivi Fernandez-Serra, Jeremy Mardon, Adrian Soto, Tomer Volansky, and Tien-Tien Yu. Direct Detection of sub-GeV Dark Matter with Semiconductor Targets. *JHEP*, 05:046, 2016. doi:10.1007/JHEP05(2016)046.

[265] Amelio, G. F. and Tompsett, M. F. and Smith, G. E. Experimental verification of the charge coupled device concept. *Bell Syst. Tech. J.*, 49:593–600, 1970.

[266] McLean, I. *Electronic Imaging in Astronomy Detectors and Instrumentation*. Springer-Praxis, 2nd edition, 2008.

[267] H. M. Wey and W. Guggenbuhl. An Improved Correlated Double Sampling Circuit for Low Noise Charge-Coupled Devices. *IEEE Transactions on Circuits and Systems*, 37(12):1559–1565, 1990. ISSN 00984094. doi:10.1109/31.101279.

[268] Guillermo Fernandez Moroni, Juan Estrada, Gustavo Cancelo, Stephen E. Holland, Eduardo E. Paolini, and H. Thomas Diehl. Sub-electron readout noise in a Skipper CCD fabricated on high resistivity silicon. *Exper. Astron.*, 34:43–64, 2012. doi:10.1007/s10686-012-9298-x.

[269] J. R. Janesick. Ultra low-noise charge coupled device. *United States Patent*, US: 5,250,824, 1993. Filing date Aug 29, 1990.

[270] D.D. Wen. Design and operation of a floating gate amplifier. *IEEE Journal of Solid-State Circuits*, 9(6):410–414, 1974. doi:10.1109/JSSC.1974.1050535.

[271] Guillermo Fernandez Moroni, Juan Estrada, Eduardo E. Paolini, Gustavo Cancelo, Javier Tiffenberg, and Jorge Molina. Charge Coupled Devices for detection of coherent neutrino-nucleus scattering. *Phys. Rev.*, D91(7):072001, 2015. doi:10.1103/PhysRevD.91.072001.

[272] DAMIC Collaboration. DAMIC at SNOLAB. *TAUP*, 2013.

[273] Ian S. Mclean, Brenna L. Flaugher, Timothy M.C. Abbott, Robert Angstadt, Jim Annis, et al. Status of the Dark Energy Survey Camera (DECam) project. *Ground-based and Airborne Instrumentation for Astronomy IV*, 8446:844611–844611–15, 2012. doi:10.1117/12.926216.

[274] B. Flaugher et al. The Dark Energy Camera. *Astron. J.*, 150:150, 2015. doi:10.1088/0004-6256/150/5/150.

[275] James Janesick and John Tower. Particle and Photon Detection: Counting and Energy Measurement. *Sensors*, 16(5):688, 2016. doi:10.3390/s16050688. URL `http://www.mdpi.com/1424-8220/16/5/688/htm`.

[276] J. M. Hum, A. P. Siegel, F. M. Pavalko, and R. N. Day. Monitoring biosensor activity in living cells with fluorescence lifetime imaging microscopy. *Int J Mol Sci.*, 13:14385–14400. doi:10.3390/ijms131114385.

[277] A. Aguilar-Arevalo et al. First Direct Detection Constraints on eV-Scale Hidden Photon Dark Matter with DAMIC at SNOLAB. *Submitted to: Phys. Rev. Lett.*, 2016.

[278] A. Aguilar-Arevalo et al. Search for low-mass WIMPs in a 0.6 kg day exposure of the DAMIC experiment at SNOLAB. *Phys. Rev. D*, 94(8):082006, 2016. doi:10.1103/PhysRevD.94.082006.

[279] Alexis Aguilar-Arevalo et al. Exploring low-energy neutrino physics with the Coherent Neutrino Nucleus Interaction Experiment. Phys. Rev. D, 100(9):092005, 2019. doi:10.1103/PhysRevD.100.092005.

[280] Brendan Crill and Nick Siegler. Exoplanet Exploration Program Technology Plan Appendix. 2017. URL `https://exoplanets.nasa.gov/system/internal_resources/details/original/449_2017_ExEP_Technology_Plan_Appendix_Rev_B_Cleared.pdf`.

[281] Brendan Crill and Nick Siegler. Exoplanet Exploration Program Technology Plan Appendix. 2019. URL `https://exoplanets.nasa.gov/internal_resources/1123/`.

[282] Brendan P. Crill and Nicholas Siegler. Space technology for directly imaging and characterizing exo-Earths. In *Society of Photo-Optical Instrumentation Engineers (SPIE) Conference Series*, volume 10398 of *Society of Photo-Optical Instrumentation Engineers (SPIE) Conference Series*, page 103980H, 2017. doi:10.1117/12.2275697.

[283] National Research Council. *New Worlds, New Horizons in Astronomy and Astrophysics*. The National Academies Press, 2010. doi:10.17226/12951.

[284] C.J. Bebek, J.H. Emes, D.E. Groom, S. Haque, S.E. Holland, A. Karcher, W.F. Kolbe, J.S. Lee, N.P. Palaio, and G. Wang. Ccd development for the dark energy spectroscopic instrument. *Journal of Instrumentation*, 10(05):C05026, 2015. URL `http://stacks.iop.org/1748-0221/10/i=05/a=C05026`.

[285] S. Shaklan, M. Levine, M. Foote, M. Rodgers, M. Underhill, L. Marchen, and D. Klein. The AFTA coronagraph instrument. In *Techniques and Instrumentation for Detection of Exoplanets VI*, volume 8864 of *Proc. SPIE*, page 886415, 2013. doi:10.1117/12.2024560.

[286] P. O'Connor. Crosstalk in multi-output ccds for lsst. *Journal of Instrumentation*, 10 (05):C05010, 2015. URL `http://stacks.iop.org/1748-0221/10/i=05/a=C05010`.

[287] Peter W. Graham, David E. Kaplan, Surjeet Rajendran, and Matthew T. Walters. Semiconductor Probes of Light Dark Matter. *Phys. Dark Univ.*, 1:32–49, 2012. doi:10.1016/j.dark.2012.09.001.

[288] Samuel K. Lee, Mariangela Lisanti, Siddharth Mishra-Sharma, and Benjamin R. Safdi. Modulation Effects in Dark Matter-Electron Scattering Experiments. *Phys. Rev.*, D92 (8):083517, 2015. doi:10.1103/PhysRevD.92.083517.

[289] Haipeng An, Maxim Pospelov, and Josef Pradler. Dark Matter Detectors as Dark Photon Helioscopes. *Phys. Rev. Lett.*, 111:041302, 2013. doi:10.1103/PhysRevLett.111.041302.

[290] Haipeng An, Maxim Pospelov, Josef Pradler, and Adam Ritz. Direct Detection Constraints on Dark Photon Dark Matter. *Phys. Lett.*, B747:331–338, 2015. doi:10.1016/j.physletb.2015.06.018.

[291] J. Angle et al. A search for light dark matter in XENON10 data. *Phys. Rev. Lett.*, 107:051301, 2011. doi:10.1103/PhysRevLett.110.249901, 10.1103/PhysRevLett.107.051301. [Erratum: Phys. Rev. Lett.110,249901(2013)].

[292] Gerhard Lutz, Matteo Porro, Stefan Aschauer, Stefan Wölfel, and Lothar Strüder. *Sensors*, 16(5):608, 2016. ISSN 1424-8220. doi:10.3390/s16050608. URL `http://www.mdpi.com/1424-8220/16/5/608`.

[293] Miguel Haro, Guillermo Moroni, Javier Tiffenberg, Gustavo Cancelo, Juan Estrada, Xavier Bertou, and Eduardo Paolini. Taking the CCDs to the ultimate performance for low threshold experiments. *PoS*, ICHEP2016:278, 2016. doi:10.22323/1.282.0278.

[294] M. S. Haro, G. Cancelo, G. F. Moroni, X. Bertou, J. Tiffenberg, E. Paolini, and J. Estrada. Measurement of the read-out noise of fully depleted thick ccds. In *2016 Argentine Conference of Micro-Nanoelectronics, Technology and Applications (CAMTA)*, pages 11–16, 2016. doi:10.1109/CAMTA.2016.7574083.

[295] C.J. Bebek, J.H. Emes, D.E. Groom, S. Haque, S.E. Holland, P.N. Jelinsky, A. Karcher, W.F. Kolbe, J.S. Lee, N.P. Palaio, D.J. Schlegel, G. Wang, R. Groulx, R. Frost, J. Estrada, and M. Bonati. Status of the ccd development for the dark energy spectroscopic instrument. *Journal of Instrumentation*, 12(04):C04018, 2017. URL `http://stacks.iop.org/1748-0221/12/i=04/a=C04018`.

[296] D. Doering, N. Andresen, D. Contarato, P. Denes, J. M. Joseph, P. McVittie, J. P. Walder, J. Weizeorick, and B. Zheng. High speed, direct detection 1k frame-store ccd sensor for synchrotron radiation. In *2011 IEEE Nuclear Science Symposium Conference Record*, pages 1840–1845, 2011. doi:10.1109/NSSMIC.2011.6154370.

[297] Steve Holland. Fabrication of detectors and transistors on high-resistivity silicon. *Nuclear Instruments and Methods in Physics Research Section A: Accelerators, Spectrometers, Detectors and Associated Equipment*, 275(3):537 – 541, 1989. ISSN 0168-9002. doi:http://dx.doi.org/10.1016/0168-9002(89)90741-9. URL `http://www.sciencedirect.com/science/article/pii/0168900289907419`.

[298] S. E. Holland, D. E. Groom, N. P. Palaio, R. J. Stover, and Mingzhi Wei. Fully depleted, back-illuminated charge-coupled devices fabricated on high-resistivity silicon. *IEEE Transactions on Electron Devices*, 50(1):225–238, 2003. ISSN 0018-9383. doi:10.1109/TED.2002.806476.

[299] Sol M. Gruner. Charge-coupled device area x-ray detectors. *Review of Scientific Instruments*, 73:2815, 2002. doi:http://dx.doi.org/10.1063/1.1488674.

[300] CJS Damerell, FJM Farley, AR Gillman, and FJ Wickens. Charge-coupled devices for particle detection with high spatial resolution. *Nuclear Instruments and Methods in Physics Research*, 185(1-3):33–42, 1981.

[301] R. Agnese et al. New Results from the Search for Low-Mass Weakly Interacting Massive Particles with the CDMS Low Ionization Threshold Experiment. *Phys. Rev. Lett.*, 116 (7):071301, 2016. doi:10.1103/PhysRevLett.116.071301.

[302] C. E. Aalseth et al. CoGeNT: A Search for Low-Mass Dark Matter using p-type Point Contact Germanium Detectors. *Phys. Rev.*, D88:012002, 2013. doi:10.1103/PhysRevD.88.012002.

[303] Ben G.; Sanjay Banerjee Streetman. Solid state electronic devices. *Prentice Hall*, 2005.

[304] C. A. Klein. Bandgap Dependence and Related Features of Radiation Ionization Energies in Semiconductors. *Journal of Applied Physics*, 39:2029–2038, 1968. doi:10.1063/1.1656484.

[305] M. H. White, D. R. Lampe, F. C. Blaha, and I. A. Mack. Characterization of surface channel ccd image arrays at low light levels. *IEEE Journal of Solid-State Circuits*, 9 (1):1–12, 1974. ISSN 0018-9200. doi:10.1109/JSSC.1974.1050448.

[306] J. Barreto et al. Direct Search for Low Mass Dark Matter Particles with CCDs. *Phys.Lett.*, B711:264–269, 2012. doi:10.1016/j.physletb.2012.04.006.

[307] Peter Sorensen. Electron train backgrounds in liquid xenon dark matter search detectors are indeed due to thermalization and trapping. 2017.

[308] Orr Abramoff et al. SENSEI: Direct-Detection Constraints on Sub-GeV Dark Matter from a Shallow Underground Run Using a Prototype Skipper-CCD. *Phys. Rev. Lett.*, 122(16):161801, 2019. doi:10.1103/PhysRevLett.122.161801.

[309] Michael Crisler, Rouven Essig, Juan Estrada, Guillermo Fernandez, Javier Tiffenberg, Miguel Sofo-Haro, Tomer Volansky, and Tien-Tien Yu. SENSEI: First Direct-Detection Constraints on sub-GeV Dark Matter from a Surface Run. *Phys. Rev. Lett.*, 121(6): 061803, 2018. doi:10.1103/PhysRevLett.121.061803.

[310] Dario Rodrigues, Kevin Andersson, Mariano Cababie, Andre Donadon, Ana Botti, Gustavo Cancelo, Juan Estrada, Guillermo Fernandez-Moroni, Ricardo Piegaia, Matias Senger, Miguel Sofo Haro, Leandro Stefanazzi, Javier Tiffenberg, and Sho Uemura. Absolute measurement of the Fano factor using a Skipper-CCD. *arXiv e-prints*, art. arXiv:2004.11499, 2020.

[311] Pierre Astier, Pierre Antilogus, Claire Juramy, Rémy Le Breton, Laurent Le Guillou, and Eduardo Sepulveda. The shape of the photon transfer curve of CCD sensors. A&A, 629:A36, 2019. doi:10.1051/0004-6361/201935508.

[312] G. Derylo, J. Estrada, B. Flaugher, J. Hamilton, D. Kubik, K. Kuk, and V. Scarpine. Surface cleaning of CCD imagers using an electrostatic dissipative formulation of First Contact polymer. In *Advanced Optical and Mechanical Technologies in Telescopes and Instrumentation*, volume 7018 of *Society of Photo-Optical Instrumentation Engineers (SPIE) Conference Series*, page 701858, 2008. doi:10.1117/12.789654.

[313] A. A. Plazas, G. M. Bernstein, and E. S. Sheldon. On-Sky Measurements of the Transverse Electric Fields' Effects in the Dark Energy Camera CCDs. PASP, 126 (942):750, 2014. doi:10.1086/677682.

[314] DESI Collaboration, Amir Aghamousa, Jessica Aguilar, Steve Ahlen, et al. The DESI Experiment Part I: Science,Targeting, and Survey Design. *arXiv e-prints*, art. arXiv:1611.00036, 2016.

[315] DESI Collaboration, Amir Aghamousa, Jessica Aguilar, Steve Ahlen, et al. The DESI Experiment Part II: Instrument Design. *arXiv e-prints*, art. arXiv:1611.00037, 2016.

[316] National Research Council. *New Worlds, New Horizons in Astronomy and Astrophysics*. National Academies Press, 2010. ISBN 9780309186858. doi:10.17226/12951. URL `https://doi.org/10.17226/12951`.

[317] H. Thomas Diehl et al. Characterization of DECam focal plane detectors. In David A. Dorn and Andrew D. Holland, editors, *High Energy, Optical, and Infrared Detectors for Astronomy III*, volume 7021 of *Society of Photo-Optical Instrumentation Engineers (SPIE) Conference Series*, page 702107, 2008. doi:10.1117/12.790053.

[318] Stuart Shaklan, Marie Levine, Marc Foote, Michael Rodgers, Michael Underhill, Luis Marchen, and Dan Klein. The AFTA coronagraph instrument. In Stuart Shaklan,

editor, *Techniques and Instrumentation for Detection of Exoplanets VI*, volume 8864 of *Society of Photo-Optical Instrumentation Engineers (SPIE) Conference Series*, page 886415, 2013. doi:10.1117/12.2024560.

[319] Steven Tingay. High-cadence optical transient searches using drift scan imaging I: Proof of concept with a pre-prototype system. PASA, 37:e015, April 2020. doi:10.1017/pasa.2020.7.

[320] Michael W. Richmond, Masaomi Tanaka, and et al. An optical search for transients lasting a few seconds. PASJ, 72(1):3, February 2020. doi:10.1093/pasj/psz120.

[321] D. Kubik, R. Alvarez, and et al. Automated characterization of CCD detectors for DECam. In Ian S. McLean, Suzanne K. Ramsay, and Hideki Takami, editors, *Ground-based and Airborne Instrumentation for Astronomy III*, volume 7735 of *Society of Photo-Optical Instrumentation Engineers (SPIE) Conference Series*, page 77355C, July 2010. doi:10.1117/12.864472.

[322] Beverly J. LaMarr, Gregory Y. Prigozhin, Eric D. Miller, Carolyn Thayer, Marshall W. Bautz, Richard Foster, Catherine E. Grant, Andrew Malonis, Barry E. Burke, Michael Cooper, Kevan Donlon, and Christopher Leitz. Measurement and simulation of charge diffusion in a small-pixel charge-coupled device. *Journal of Astronomical Telescopes, Instruments, and Systems*, 8(1):1 – 19, 2022. doi:10.1117/1.JATIS.8.1.016004. URL `https://doi.org/10.1117/1.JATIS.8.1.016004`.

[323] Philip Massey and Margaret M. Hanson. Astronomical Spectroscopy. In Terry D. Oswalt and Howard E. Bond, editors, *Planets, Stars and Stellar Systems. Volume 2: Astronomical Techniques, Software and Data*, page 35. 2013. doi:10.1007/978-94-007-5618-2_2.

[324] III Palumbo, Michael L, Sheila J Kannappan, Elaine M Frazer, Kathleen D Eckert, Dara J Norman, Luciano Fraga, Bruno C Quint, Philippe Amram, Claudia Mendes de Oliveira, Ashley S Bittner, Amanda J Moffett, David V Stark, Mark A Norris, Nathaniel T Cleaves, and Derrick S Carr. Linking compact dwarf starburst galaxies in the RESOLVE survey to downsized blue nuggets. *Monthly Notices of the Royal Astronomical Society*, 494(4):4730–4750, 04 2020. ISSN 0035-8711. doi:10.1093/mnras/staa899. URL `https://doi.org/10.1093/mnras/staa899`.

[325] Fernando Chierchie, Guillermo Fernandez Moroni, Leandro Stefanazzi, Eduardo Paolini, Javier Tiffenberg, Juan Estrada, Gustavo Cancelo, and Sho Uemura. Smart readout of nondestructive image sensors with single photon-electron sensitivity. *Physical Review Letters*, 127(24), dec 2021. doi:10.1103/physrevlett.127.241101. URL `https://doi.org/10.1103%2Fphysrevlett.127.241101`.

[326] Fernando Chierchie, Guillermo Fernandez Moroni, Leandro Stefanazzi, Claudio Chavez, Eduardo Paolini, Gustavo Cancelo, Miguel Sofo Haro, Javier Tiffenberg, Juan Estrada, and Sho Uemura. Smart-readout of the Skipper-CCD: Achieving Sub-electron

Noise Levels in Regions of Interest. *arXiv e-prints*, art. arXiv:2012.10414, December 2020.

[327] D. Tanoglidis, A. Drlica-Wagner, and et al. Shadows in the Dark: Low-surface-brightness Galaxies Discovered in the Dark Energy Survey. ApJS, 252(2):18, February 2021. doi:10.3847/1538-4365/abca89.

[328] Johnny P. Greco, Andy D. Goulding, Jenny E. Greene, Michael A. Strauss, Song Huang, Ji Hoon Kim, and Yutaka Komiyama. A Study of Two Diffuse Dwarf Galaxies in the Field. ApJ, 866(2):112, October 2018. doi:10.3847/1538-4357/aae0f4.

[329] Liron Barak, Itay M. Bloch, and et al. SENSEI: Characterization of single-electron events using a skipper charge-coupled device. *Physical Review Applied*, 17(1), jan 2022. doi:10.1103/physrevapplied.17.014022. URL `https://doi.org/10.1103%2Fphysrevapplied.17.014022`.

[330] Kyle Dawson, Chris Bebek, John Emes, Steve Holland, Sharon Jelinsky, Armin Karcher, William Kolbe, Nick Palaio, Natalie Roe, Juhi Saha, Koki Takasaki, and Guobin Wang. Radiation Tolerance of Fully-Depleted P-Channel CCDs Designed for the SNAP Satellite. *IEEE Transactions on Nuclear Science*, 55(3):1725–1735, June 2008. doi:10.1109/TNS.2008.919262.

[331] Lakeshore. Cryogenic-wire. `https://www.lakeshore.com/products/categories/specification/temperature-products/cryogenic-accessories/cryogenic-wire`.

[332] Charles E. Chandler, Richard A. Bredthauer, James R. Janesick, and James A. Westphal. Sub-electron noise charge-coupled devices. In Morley M. Blouke, editor, *Charge-Coupled Devices and Solid State Optical Sensors*, volume 1242, pages 238 – 251. International Society for Optics and Photonics, SPIE, 1990. doi:10.1117/12.19457. URL `https://doi.org/10.1117/12.19457`.

[333] Michael C. Ashe, Marco Bonati, and Steven Heathcote. ArcVIEW: a LabVIEW-based astronomical instrument control system. In Hilton Lewis, editor, *Advanced Telescope and Instrumentation Control Software II*, volume 4848, pages 508 – 518. International Society for Optics and Photonics, SPIE, 2002. doi:10.1117/12.461433. URL `https://doi.org/10.1117/12.461433`.

[334] Astrophysics and space science library, editors. *Scientific Detectors for Astronomy, The beginning of a New Era*, volume 300, chapter IV, ISPI's software - an application of the ArcVIEW system, pages 427–430. Kluwer Academic Publishers, 2005.

[335] J. P. D. Gow, N. J. Murray, A. D. Holland, and D. Burt. Proton Damage Comparison of an e2v Technologies n-channel and p-channel CCD204. *IEEE Transactions on Nuclear Science*, 61(4):1843–1848, August 2014. doi:10.1109/TNS.2014.2298254.

[336] Daniel Wood, David J. Hall, Jason Gow, Jesper Skottfelt, Neil J. Murray, Konstantin Stefanov, and Andrew D. Holland. Evolution and Impact of Defects in a p-Channel

CCD After Cryogenic Proton-Irradiation. *IEEE Transactions on Nuclear Science*, 64 (11):2814–2821, November 2017. doi:10.1109/TNS.2017.2756019.

[337] Jason P. D. Gow, Daniel Wood, Neil J. Murray, David Burt, David J. Hall, Ben Dryer, and Andrew D. Holland. Postirradiation behavior of p-channel charge-coupled devices irradiated at 153 K. *Journal of Astronomical Telescopes, Instruments, and Systems*, 2 (2):026001, 2016. doi:10.1117/1.JATIS.2.2.026001. URL `https://doi.org/10.1117/1.JATIS.2.2.026001`.

[338] A. J. Lapi, F. Chierchie, G. Fernandez Moroni, L. Stefanazzi, E. Paolini, J. Estrada, A. Drlica-Wagner, E. Marrufo Villalpando, and Javier Tiffenberg. Fast readout of the Skipper CCD for astronomy and quantum imaging. In Andrew D. Holland and James Beletic, editors, *X-Ray, Optical, and Infrared Detectors for Astronomy X*, volume 12191, page 121910V. International Society for Optics and Photonics, SPIE, 2022. doi:10.1117/12.2631791. URL `https://doi.org/10.1117/12.2631791`.

[339] D. Wen, J. Early, C. Kim, and G. Amelio. A distributed floating-gate amplifier in charge-coupled devices. In *1975 IEEE International Solid-State Circuits Conference. Digest of Technical Papers*, volume XVIII, pages 24–25, 1975. doi:10.1109/ISSCC.1975.1155402.

[340] Pierre Astier and Nicolas Regnault. Correction of the brighter-fatter effect on the CCDs of Hyper Suprime-Cam. A&A, 670:A118, February 2023. doi:10.1051/0004-6361/202245407.

[341] Ana M. Botti, Brenda A. Cervantes-Vergara, Claudio R. Chavez, Fernando Chierchie, Alex Drlica-Wagner, Juan Estrada, Guillermo Fernandez Moroni, Stephen E. Holland, Blas J. Irigoyen Gimenez, Agustin J. Lapi, Edgar Marrufo Villalpando, Miguel Sofo Haro, Javier Tiffenberg, and Sho Uemura. Fast Single-Quantum Measurement with a Multi-Amplifier Sensing Charge-Coupled Device. *arXiv e-prints*, art. arXiv:2308.09822, August 2023. doi:10.48550/arXiv.2308.09822.

[342] A. A. Plazas, C. Shapiro, R. Smith, E. Huff, and J. Rhodes. Laboratory measurement of the brighter-fatter effect in an h2rg infrared detector. *Publications of the Astronomical Society of the Pacific*, 130(988):065004, apr 2018. doi:10.1088/1538-3873/aab820. URL `https://dx.doi.org/10.1088/1538-3873/aab820`.

[343] Christopher M. Hirata and Ami Choi. Brighter-fatter effect in near-infrared detectors. i. theory of flat autocorrelations. *Publications of the Astronomical Society of the Pacific*, 132(1007):014501, dec 2019. doi:10.1088/1538-3873/ab44f7. URL `https://dx.doi.org/10.1088/1538-3873/ab44f7`.

[344] Ioannis Argyriou, Craig Lage, George H. Rieke, Danny Gasman, Jeroen Bouwman, Jane Morrison, Mattia Libralato, Daniel Dicken, Bernhard R. Brandl, Javier Álvarez Márquez, Alvaro Labiano, Michael Regan, and Michael E. Ressler. The brighter-fatter effect in the jwst miri si:as ibc detectors i. observations, impact on science, and modelling, 2023.

[345] F. Chierchie, C.R. Chavez, M. Sofo Haro, G. Fernandez Moroni, B.A. Cervantes-Vergara, S. Perez, J. Estrada, J. Tiffenberg, S. Uemura, and A. Botti. First results from a multiplexed and massive instrument with sub-electron noise skipper-ccds. *Journal of Instrumentation*, 18(01):P01040, jan 2023. doi:10.1088/1748-0221/18/01/P01040. URL `https://dx.doi.org/10.1088/1748-0221/18/01/P01040`.

[346] G. Fernandez-Moroni, R. Harnik, P. A. N. Machado, I. Martinez-Soler, Y. F. Perez-Gonzalez, D. Rodrigues, and S. Rosauro-Alcaraz. The physics potential of a reactor neutrino experiment with Skipper-CCDs: searching for new physics with light mediators. *Journal of High Energy Physics*, 2022(2):127, February 2022. doi:10.1007/JHEP02(2022)127.

[347] L.K Townsley, P.S Broos, J.A Nousek, and G.P Garmire. Modeling charge transfer inefficiency in the chandra advanced ccd imaging spectrometer. *Nuclear Instruments and Methods in Physics Research Section A: Accelerators, Spectrometers, Detectors and Associated Equipment*, 486(3):751–784, 2002. ISSN 0168-9002. doi:https://doi.org/10.1016/S0168-9002(01)02156-8. URL `https://www.sciencedirect.com/science/article/pii/S0168900201021568`.

[348] Yoshiaki Kanemaru, Jin Sato, and et al. Experimental studies on the charge transfer inefficiency of ccd developed for the soft x-ray imaging telescope xtend aboard the xrism satellite. *Nuclear Instruments and Methods in Physics Research Section A: Accelerators, Spectrometers, Detectors and Associated Equipment*, 984:164646, 2020. ISSN 0168-9002. doi:https://doi.org/10.1016/j.nima.2020.164646. URL `https://www.sciencedirect.com/science/article/pii/S0168900220310433`.

[349] A. M. Botti, S. Uemura, G. Fernandez Moroni, L. Barak, M. Cababie, R. Essig, E. Etzion, D. Rodrigues, N. Saffold, M. Sofo Haro, J. Tiffenberg, and T. Volansky. Constraints on the electron-hole pair creation energy and Fano factor below 150 eV from Compton scattering in a skipper CCD. Phys. Rev. D, 106(7):072005, October 2022. doi:10.1103/PhysRevD.106.072005.

[350] Andrés A. Plazas Malagón, Charles Shapiro, Ami Choi, and Chris Hirata. Spot-Based Measurement of the Brighter-Fatter Effect on a Roman Space Telescope H4RG Detector and Comparison with Flat-Field Data. *arXiv e-prints*, art. arXiv:2310.01920, October 2023.

[351] Guillermo Fernández Moroni, Juan Estrada, Eduardo E. Paolini, Gustavo Cancelo, and H. Thomas Diehl. Achieving sub-electron readout noise in skipper ccds. In *2011 Argentine School of Micro-Nanoelectronics, Technology and Applications*, pages 1–6, 2011.

[352] Nick J. Mostek, Christopher J. Bebek, Armin Karcher, William F. Kolbe, Natalie A. Roe, and Jonathan Thacker. Charge trap identification for proton-irradiated p+ channel CCDs. In Andrew D. Holland and David A. Dorn, editors, *High Energy, Optical, and Infrared Detectors for Astronomy IV*, volume 7742, page 774216. Interna-

tional Society for Optics and Photonics, SPIE, 2010. doi:10.1117/12.855936. URL https://doi.org/10.1117/12.855936.

[353] Adam Snyder and Aaron Roodman. Investigation of deferred charge effects in Large Synoptic Survey Telescope ITL sensors. *Journal of Astronomical Telescopes, Instruments, and Systems*, 5:041509, October 2019. doi:10.1117/1.JATIS.5.4.041509.

[354] Bernard J. Rauscher, S. E. Holland, Emily Kan, Daniel Kelly, Laddawan Miko, D. Brent Mott, and Augustyn Waczynski. Radiation tolerant, photon counting, visible, and near-IR detectors for space coronagraphs. In Laura E. Coyle, Shuji Matsuura, and Marshall D. Perrin, editors, *Space Telescopes and Instrumentation 2022: Optical, Infrared, and Millimeter Wave*, volume 12180 of *Society of Photo-Optical Instrumentation Engineers (SPIE) Conference Series*, page 1218065, August 2022. doi:10.1117/12.2628961.

[355] I. Arnquist, N. Avalos, and et al. First Constraints from DAMIC-M on Sub-GeV Dark-Matter Particles Interacting with Electrons. Phys. Rev. Lett., 130(17):171003, April 2023. doi:10.1103/PhysRevLett.130.171003.

[356] Ashlee N. Wilkins, Michael W. McElwain, and et al. Characterization of a photon counting EMCCD for space-based high contrast imaging spectroscopy of extrasolar planets. In Andrew D. Holland and James Beletic, editors, *High Energy, Optical, and Infrared Detectors for Astronomy VI*, volume 9154, page 91540C. International Society for Optics and Photonics, SPIE, 2014. doi:10.1117/12.2055346. URL https://doi.org/10.1117/12.2055346.

[357] Matthew G. Walker, Mario Mateo, Edward W. Olszewski, Jorge Peñarrubia, N. Wyn Evans, and Gerard Gilmore. A universal mass profile for dwarf spheroidal galaxies? *Astrophys. J.*, 704(2):1274, 2009. doi:10.1088/0004-637X/704/2/1274. URL https://dx.doi.org/10.1088/0004-637X/704/2/1274.

[358] Ferah Munshi, Alyson M. Brooks, Charlotte Christensen, Elaad Applebaum, Kelly Holley-Bockelmann, Thomas R. Quinn, and James Wadsley. Dancing in the dark: Uncertainty in ultrafaint dwarf galaxy predictions from cosmological simulations. *Astrophys. J.*, 874(1):40, 2019. doi:10.3847/1538-4357/ab0085. URL https://dx.doi.org/10.3847/1538-4357/ab0085.

[359] Stephen E. Holland. Fully depleted charge-coupled device design and technology development. *Astronomische Nachrichten*, 344(8-9):e20230072, 2023. doi:https://doi.org/10.1002/asna.20230072. URL https://onlinelibrary.wiley.com/doi/abs/10.1002/asna.20230072.

[360] DESI Collaboration. The early data release of the dark energy spectroscopic instrument, 2023. URL https://zenodo.org/record/7964161.

[361] Sandrine Perruchot, Pierre-Éric Blanc, and et al. Testing the 10 spectrograph units for DESI: approach and results. In Christopher J. Evans, Julia J. Bryant, and Kentaro

Motohara, editors, *Ground-based and Airborne Instrumentation for Astronomy VIII*, volume 11447, page 1144786. International Society for Optics and Photonics, SPIE, 2020. doi:10.1117/12.2561275. URL https://doi.org/10.1117/12.2561275.

[362] Coral Wheeler, Jose Oñorbe, James S. Bullock, Michael Boylan-Kolchin, Oliver D. Elbert, Shea Garrison-Kimmel, Philip F. Hopkins, and Dušan Kereš. Sweating the small stuff: simulating dwarf galaxies, ultra-faint dwarf galaxies, and their own tiny satellites. *Monthly Notices of the Royal Astronomical Society*, 453(2):1305–1316, 08 2015. ISSN 0035-8711. doi:10.1093/mnras/stv1691. URL https://doi.org/10.1093/mnras/stv1691.

[363] Elisa G. M. Ferreira. Ultra-light dark matter. *The Astronomy and Astrophysics Review*, 29(1):7, 2021. ISSN 1432-0754. doi:10.1007/s00159-021-00135-6. URL https://doi.org/10.1007/s00159-021-00135-6.

[364] Joshua D. Simon. The Faintest Dwarf Galaxies. ARA&A, 57:375–415, August 2019. doi:10.1146/annurev-astro-091918-104453.